LEABHARLANN CHOLÁISTE NA TRÍONÓIDE, BAILE ÁTHA CLIATH | TRINITY COLLEGE LIBRARY DUBLIN
Ollscoil Átha Cliath | The University of Dublin

Terms and Conditions of Use of Digitised Theses from Trinity College Library Dublin

Copyright statement

All material supplied by Trinity College Library is protected by copyright (under the Copyright and Related Rights Act, 2000 as amended) and other relevant Intellectual Property Rights. By accessing and using a Digitised Thesis from Trinity College Library you acknowledge that all Intellectual Property Rights in any Works supplied are the sole and exclusive property of the copyright and/or other IPR holder. Specific copyright holders may not be explicitly identified. Use of materials from other sources within a thesis should not be construed as a claim over them.

A non-exclusive, non-transferable licence is hereby granted to those using or reproducing, in whole or in part, the material for valid purposes, providing the copyright owners are acknowledged using the normal conventions. Where specific permission to use material is required, this is identified and such permission must be sought from the copyright holder or agency cited.

Liability statement

By using a Digitised Thesis, I accept that Trinity College Dublin bears no legal responsibility for the accuracy, legality or comprehensiveness of materials contained within the thesis, and that Trinity College Dublin accepts no liability for indirect, consequential, or incidental, damages or losses arising from use of the thesis for whatever reason. Information located in a thesis may be subject to specific use constraints, details of which may not be explicitly described. It is the responsibility of potential and actual users to be aware of such constraints and to abide by them. By making use of material from a digitised thesis, you accept these copyright and disclaimer provisions. Where it is brought to the attention of Trinity College Library that there may be a breach of copyright or other restraint, it is the policy to withdraw or take down access to a thesis while the issue is being resolved.

Access Agreement

By using a Digitised Thesis from Trinity College Library you are bound by the following Terms & Conditions. Please read them carefully.

I have read and I understand the following statement: All material supplied via a Digitised Thesis from Trinity College Library is protected by copyright and other intellectual property rights, and duplication or sale of all or part of any of a thesis is not permitted, except that material may be duplicated by you for your research use or for educational purposes in electronic or print form providing the copyright owners are acknowledged using the normal conventions. You must obtain permission for any other use. Electronic or print copies may not be offered, whether for sale or otherwise to anyone. This copy has been supplied on the understanding that it is copyright material and that no quotation from the thesis may be published without proper acknowledgement.

Micromechanical modelling of normal, drug treated and osteoporotic bone using Scanning Acoustic Microscopy and Finite Element Analysis

Patrick Michel Wulliamoz

A dissertation submitted to the University of Dublin for the degree of:

Doctor in Philosophy

Trinity College Dublin

Supervisor

Dr. Patrick J. Prendergast

External Examiner
Prof. Marie Christine Ho Ba Tho

Internal Examiner
Prof. David Taylor

December 2011

TRINITY COLLEGE
2 4 MAY 2013
LIBRARY DUBLIN

Thesis 9953

Declaration

I declare that this thesis has not been submitted as an exercise for a degree at this or any other university and it is entirely my own work.

I agree to deposit this thesis in the open access institutional repository or allow the Library to do so on my behalf, subject to Irish Copyright Legislation and Trinity College Library conditions of use and acknowledgement.

Summary

Ultrasonic methods were exclusively used to image cortical bone at high resolutions. A scanning acoustic microscope was used at a frequency of 150 MHz giving a resolution of 20μm. Images were taken of ovine bone samples from the "Bone for Life" PRTLI funded project. These were available in three types; ovariectomised (OVX), control (CON) and ovariectomised drug treated (OVX-ZOL). These samples exhibit changes in bone due to estrogen withdrawal. These samples were available at two time points; 12 months (OVX n=6, CON n=6), and 31 months (OVX-ZOL n=3, OVX, n=3, CON n=3). The images of cortical bone microstructure captured by SAM were converted into representations of Young's modulus values across the bone samples. Three areas were chosen randomly in each sample for analysis using Finite Element Analysis (FEA). A physiological strain of 1500 μ strain was applied. The resulting stresses and strain were analysed for each sample type.

It was found that the year 1 sample types (OVX and CON) had the same means and standard deviations for Young's modulus, equivalent stress and strain. They also shared the same distributions (p value= 0.28, Anderson Darling K test, Young's Modulus).

For year 2 CON and OVX-ZOL samples had similar distributions for Young's modulus, stress and strain (p value= 0.49, Anderson Darling K test Young's Modulus) . None of the other sample types shared a common distribution for Young's modulus, equivalent stress or strain.

In comparing the distributions of OVX-ZOL with the CON sample types, it is evident for the year 2 samples that the anti-resorptive bisphosphonate drug (Zoledronic acid) has maintained bone properties, as measured by SAM, to a state similar to that of the disease free control samples.

The methods developed in this study can evaluate the tissue level micro-mechanical environment of cortical bone allowing an estimation to be made of the alteration of that environment by disease processes such as estrogen withdrawal induced osteoporosis. Evaluation can also be made of the effectiveness of drug treatments for osteoporosis.

Acknowledgements

I would like to thank my supervisor Prof. Patrick Prendergast for his patience and guidance during the long gestation of this work. I would also like to thank my colleagues at the RCSI for their help with the samples used in this project. Particularly Oran Kennedy, Orlaith Brennan, Clive Lee and Fergal O'Brien and of course Peter Mauer for the use of his ovine bone samples. Anthony Staines provided much needed wisdom and insight into appropriate use of statistical methods in this project. I would also like to thank Tony Compagno and the team at the Tyndall Institute Cork for help with the SAM imaging. I would also like to extend my gratitude to my colleagues at DIT Bolton St. for their helpful advice and support, especially Barry Duignan. I would also like to extend a warm thank you to my friends and family for their support, especially Jennifer.

Access to the Scanning Acoustic Microscope was funded by the SFI National Access Program at Tyndall Institute, Lee Maltings, Cork. (NAP 53, NAP227 and NAP361). Funding was also supplied by the DIT Fee support scheme. The samples used in this research come from the "Bone for life" PRTLI funded Research Program.

Publications, Presentations and Posters.

P.M. Wulliamoz, O. Kennedy, O. Brennan, F.J. O'Brien, T.C. Lee, S.M. Rackard, P.J. Prendergast, "Micromechanical modelling of bone using scanning acoustic microscopy and finite element analysis", Finite Element Modelling in Biomechanics and Mechanobiology, Proceedings of the 2007 Summer Workshop of the European Society of Biomechanics, Trinity College, Dublin, 26-28 August 2007, 1 page abstract and poster.

P. M. Wulliamoz, O. Kennedy, O. Brennan, F.J. O'Brien, T.C.Lee, S. M. Rackard , P. J. Prendergast, "Micromechanical modelling of bone using scanning acoustic microscopy and finite element analysis". Bioengineering in Ireland Conference, January 25-26, 2008, Radisson Hotel, Sligo (2008), 1 page abstract and oral presentation.

P.M.Wulliamoz, O.Kennedy, O.Brennan, F.J.O'Brien, T.C.Lee, S.M.Rackard, P.J.Prendergast, "Micromechanical modelling of bone using scanning acoustic microscopy and finite element analysis" 8th International Symposium on Computer Methods in Biomechanics and Biomedical Engineering CMBBE 2008 Sheraton Hotel and SPA, Porto, Portugal, 27th February-1st March 2008(2008), 6 page paper and oral presentation.

P.M.Wulliamoz, O.Kennedy, O.Brennan, F.J.O'Brien, T.C.Lee, S.M.Rackard, P.J.Prendergast, "Finite Element Micromechanical Models of Cortical Bone" Irish Society for Scientific & Engineering Computation, Irish Mechanics Society, Joint Symposium on Advances in Mechanics, 15th and 16th May 2008, University College Dublin (2008), 1 page abstract and oral presentation.

Contents

DECLARATION I

SUMMARY II

ACKNOWLEDGEMENTS III

PUBLICATIONS, PRESENTATIONS AND POSTERS. IV

CONTENTS V

LIST OF FIGURES IX

LIST OF TABLES XVI

NOMENCLATURE XIX

1 INTRODUCTION 1

1.1 Osteoporosis and its Societal Cost 2

1.2 Diagnosis and treatment of Osteoporosis 2

1.3 Bone Biomechanics 3
1.3.1 Bone mechano-sensivity 3
1.3.2 Ultrasonics applied to bone 6
1.3.3 Finite Element Analysis (FEA) of cortical bone microstructures. 6

1.4 Combining Ultrasonics and FEA 7

1.5 Statement of Research Hypothesis 8

2 LITERATURE REVIEW 9

2.1 Bone 10
2.1.1 Introduction 10
2.1.2 Bone as a Tissue 10
2.1.3 Cortical Bone 11
2.1.4 Osteoporosis 23
2.1.5 Mechanobiology 27
2.1.6 Conclusion 39

2.2 Review of "Bone For Life" study. 41
2.2.1 Aims of study 41
2.2.2 Description of methods applied 41
2.2.3 Discussion of main findings 42

2.3 Basic Ultrasonic principles applied to cortical bone 44

2.3.1 Reflection and refraction 48
2.3.2 Dispersion 49
2.3.3 Kramers-Kronig Relations. 49
2.3.4 Attenuation and absorption 49
2.3.5 Tissue penetration 54
2.3.6 Scattering 55
2.3.7 Speed of sound. 56
2.3.8 Assessment of mechanical and physical properties 57
2.3.9 Conclusion 61

2.4 Scanning Acoustic Microscopy 64
2.4.1 A scan imaging 65
2.4.2 C scan Imaging 66
2.4.3 Time of Flight measurement 67
2.4.4 Scanning Acoustic Microscopy applied to cortical bone 67
2.4.5 Conclusion 75

2.5 Computational simulation of cortical bone microstructure and remodelling. 76
2.5.1 The Finite Element method. 76
2.5.2 Application of Finite Element Analysis to the assessment of stresses and strain at the tissue level in bone. 79
2.5.3 Validation of the FE models 81
2.5.4 Conclusion 82

3 METHODS 83

3.1 Introduction 84

3.2 Sourcing of Cortical Bone Samples 84

3.3 Sample Preparation 84

3.4 Ovine Cortical Bone samples 84
3.4.1 Statement of the experimental objectives: 84

3.5 Ultrasonic equipment. 87

3.6 Experimental procedure. 89
3.6.1 Calibration 90
3.6.2 Data gates on Sonix SAM machine: 94
3.6.3 Surface roughness and surface undulation issues 95

3.7 Image analysis 96
3.7.1 Regression Analysis 96
3.7.2 Focus Correction using Time of Flight estimation 97
3.7.3 Selection of appropriate averaging size. 103
3.7.4 Uncertainty analysis of image processing pipeline 105

3.8 FE Analysis 105
3.8.1 Input images: 105
3.8.2 Modelling Assumptions. 106
3.8.3 Material Models 106
3.8.4 Element type 106
3.8.5 Loads and constraints 106
3.8.6 Results Required: 107

3.9 Statistical Analysis Procedures: 107
3.9.1 Descriptive Statistics Required 108
3.9.2 Statistical inference test applied to results: 108

3.10 Conclusions 110

4 RESULTS 111

4.1 Experimental Results 112
4.1.1 SAM images 112
4.1.2 Acoustic lens characterisation 115
4.1.3 Calibration 116
4.1.4 SAM Images 118

4.2 Processed Results 122
4.2.1 Finite Element Analysis Results Plots 122

4.3 Descriptive Statistics 124
4.3.1 Young's Modulus 124
4.3.2 Equivalent Stress 131
4.3.3 Equivalent Strain 137

4.4 Inferential Statistics 144
4.4.1 Young's Modulus 145
4.4.2 Equivalent Stress 147
4.4.3 Equivalent Strain 149

4.5 Concluding Statement on results. 150

5 DISCUSSION 151

5.1 Discussion of research outcomes 152
5.1.1 Research Objectives 152
5.1.2 Research Background 152
5.1.3 Research outcomes 156

5.2 Discussion of experimental techniques and results processing. 159
5.2.1 Bone for Life Samples 159
5.2.2 Limitations of methods used 160

5.3 Consequences of Research Findings 165
5.3.1 Clinical Consequences 165
5.3.2 Biomechanical consequences 165

5.4 Future Work. 169

6 CONCLUSIONS 171

7 APPENDICES 173

7.1 Matlab Code for Image Processing 174
7.1.1 Year 1 samples 174
7.1.2 Year 2 samples 185

7.2 ANSYS Macro for generating FE models 194

7.3 SAM Reflectance Images 214
7.3.1 11th December 2009 215
7.3.2 30th September 2011 216

7.4 Sample Preparation Procedure 217

7.5 Ultrasonic Tranducers 218
7.5.1 Piezoelectricity and transducer design 218
7.5.2 Bandwidth of transducer 219
7.5.3 Ultrasonic field beam characteristics 220

7.6 References 229

List of Figures

Figure 1 Simplified structure of cortical bone (Adapted from (Fung 1993)) 1

Figure 2 Schematic representation of the feedback control loop responsible for remodelling in cortical bone. 4

Figure 3 Combined modelling and remodelling effects on bone strength and "mass.'" The horizontal line at the bottom of this graph suggests typical peak bone strain from zero on the left, to the fracture strain on the right (Fx), plus the locations of the remodelling, modelling, and microdamage thresholds (MESr, MESm, MESp). The horizontal axis represents no net gains or losses of bone strength or "mass." The lower dotted line curve suggests how remodelling removes and weakens bone where strain stay in or below the MESr range, but otherwise begins maintaining bone and bone strength. The upper dashed line curve suggests how modelling begins to increase bone strength and "mass," where strain enter or exceed the MESm range. The dashed outlines suggest the combined effects. At and beyond the MESp range, woven bone formation drifts usually replace lamellar bone formation drifts. Fx - the fracture strain near 25,000 microstrain. At the top: DW disuse window; AW adapted window or "comfort zone" as in normally adapted adults; MOW = mild overload window as in growing mammals including children; POW pathologic overload window) In the nearly flat "comfort zone" or adapted window between the MESr and MESm, bone strength and "mass" change little as typical peak strain change. In children, increasing weight and muscle strength shift bone strain towards the MESm. From: (Frost 1997a) 5

Figure 4 Microstructural strain field overlaid on a digital micrograph of a cortical bone specimen that was loaded to a macroscopic strain of 1500 μ strain in the horizontal direction. Each color represents a specific level of maximum principal strain as indicated by the legend. The local microstructural strain field is highly heterogeneous and strain is found to localize around osteocyte lacunae as well as between lacunae. Magnification 500x. From: (Nicolella et al. 2006) 7

Figure 5 Hierarchical structural organization of bone: (a) cortical and cancellous bone; (b) osteons with Haversian systems; (c) lamellae; (d) collagen fiber assemblies of collagen fibrils; (e) bone mineral crystals, collagen molecules, and non-collagenous proteins (Rho et al. 1998). 14

Figure 6(A) Composite elastic modulus bounds for stiff fibre reinforcement (solid line) and particle composite (dashed line), expressed in terms of the volume fraction of the stiff phase, together with illustrations of the corresponding physical structures (black represents the stiff phase). (B) Experimental data for the elastic modulus (E) versus mineral concentration (volume fraction, V_f) of PMMA-embedded bone samples (Oyen et al. 2008). 18

Figure 7 A two-level micromechanical model of osteonal cortical bone (Dong et al. 2006) 19

Figure 8 Comparison of measured tan δ (loss tangent) for longitudinal cut bone (Garner et al. 2000) 23

Figure 9. Scanning electron micrograph of a group of osteocytes, isolated from embryonic chicken calvariae, after 3 days of culture as monolayer. The cells have re-established a cellular network by moving away from each other and making thin, branching cell processes that connect with those of neighbouring cells. The cell in the upper left corner is an osteoblast (Burger et al. 1999b). 29

Figure 10 A confocal microscopy image of a crack and three osteocytes (solid arrows). The crack (A) has travelled through the lacuna of one osteocyte (B), which appears to have remained intact. The majority of the cell processes are broken by the crack, but some processes seem to cross the crack faces (circle) (Hazenberg et al. 2006). 32

Figure 11 Schematic representation of a Basic Multicellular Unit. This collection of specialised cells removes old bone and lays down new bone (Taylor et al. 2007). 34

Figure 12 DW, AW, MOW and POW refer to the disuse adaptive, mild overload and pathologic overload windows respectively. MES stands for minimally effective strain, which are the setpoints separating the various windows: MESr is disuse remodelling threshold, MESm is the bone modelling threshold and MESp is the microdamage threshold. Fx is the bone's fracture strength. Note that the setpoints are not given precise values in the Mechanostat to account for individual variability as the setpoints are hypothesised to be genetically determined (Mulvihill et al. 2008) 37

Figure 13 (a)Intracortical porosity as measured by MicroCT at a resolution of 8 microns. (b) Stiffness from compact bone samples as measured by tensile testing (Kennedy et al. 2009). 43

Figure 14 Diagram of types of refraction and reflection perpendicular, oblique and oblique beyond critical angle present at liquid solid interface (Laugier 1999). 48
Figure 15 BUA can be found by using a phantom with a known attenuation mechanism an comparing it to an unknown such as a piece of bone (Njeh 1999a). 52
Figure 16 Comparison of empirical equations for relating Acoustic Reflectance R and Elastic Stiffness C_{33} (Shieh et al. 1995; Raum et al. 2006a) 59
Figure 17 Relationship between acoustic impedance, mass density, and elastic stiffness for different materials (Raum 2008). 61
Figure 18 Scanning acoustic microscope. The acoustic lens (A) scans over the sample (B) in a raster fashion building up an acoustic image of the samples (Raum 2003). 64
Figure 19 A-scan plot with amplitude on Y axis and time on X axis. (From Sonix (2005)) 66
Figure 20 C-Scan Image of cortical bone at various resolutions. From (Raum et al. 2004). 66
Figure 21 Eight node quadrilateral element showing the global coordinate system (x,y) and the local element coordinate system (s,t) with natural coordinates. Node i in (s,t) coordinates is (-1,-1) for example. This element has mid-side nodes m,n,o and p(Image adapted from (ANSYS 2004)) 77
Figure 22 Illustration of 2x2 integration points. The integral is evaluated at the locations of the black dots shown on the element above for Gaussian Quadrature. The natural coordinates (s,t)are shown, adapted from (Felippa 2011) 78
Figure 23 Images of strain in cortical bone samples taken by the stereoimaging technique (Nicolella 2001). An image is taken of sample with no load applied, this is then compared with an image taken with load applied. An algorithm is used to detect differences in displacement in sample. These are converted to strains which are shown on the image on the left hand side. 81
Figure 24 Ultrasonic lateral resolution for lens in Table 12 for a range of frequencies. 87
Figure 25: Normalised plot of Amplitude Vs. TOF (Time of Flight). The peak amplitude is at 8.94μsec for this lens. The Ultrasonic beam has a focal zone which is defined as the area each side of the peak where amplitude drops to 50% of maximum (-6dB). In this region a maximum lateral resolution of 20μm is achieved. The values shown are for the V3849 transducer. All measurements taken at 20dB attenuation. 88

Figure 26 Sample 67 and Sample 58A unprocessed SAM images 1 pixel=25μm. Note features such as osteons, cement lines and Haversian canals can be observed.....90
Figure 27 Calibration curve for Poly Carbonate, Poly Vinyl Chloride & Quartz. (20dB attenuation).....91
Figure 28 Plot of Normalised Measured Amplitude Vs. TOF in μsec. Both the Bone and calibration samples are shown on this graph. There is a good correlation between these two data sets. Note that the error increases to the left of the focus peak as time of flight decreases. 93
Figure 29 Plot of Normalised Measured experimental Amplitude Vs. TOF μSec. Curves are shown for both bone and calibration materials. These are normalised so they can be displayed on the same plot.....94
Figure 30 Sonix Machine Data gates. The horizontal axis is TOF in μsec. The vertical axis is the amplitude of the signal. From (Sonix 2005). 95
Figure 31 Points on Image with known focus. (Sample 4A) 96
Figure 32 Sample 4A shown before (on left) and after (on right) regression analysis. ..97
Figure 33 Flowchart 1 Image Processing Pipeline.....99
Figure 34 Flowchart 2 Image Processing Pipeline.....100
Figure 35 Averaging applied to original SAM image to account to surface undulations. 102
Figure 36 The relationship between the Young's Modulus and averaging area for a range of averaging areas. There are 18 sub samples for CONY1, OVXY1 and 12 for OVX-ZOLY1. Each sub sample has 5151 pixels.....104
Figure 37 FFT frequency domain plot from 0 to 70 pixels. An area of a SAM Image was chosen (25110 pixels). This consisted of the raw unprocessed image data. This data was taken from sample 15. 104
Figure 38 Loads and constraints on analysed section. 107
Figure 39 Screenshoot from SAM, showing image of sample 4b.Showing the acquired SAM image top left , The A-scan for the point shown with water path (WP) and amplitude is displayed in the top right. 113
Figure 40 Input Image for Sample 4b. Acoustic Reflectance R, 15x15 averaging. Area shown in black at bottom right of image is out of focus.....114
Figure 41 Lens characteristic curves for Bone, Quartz, PVC and PC. (11-12-2009)...115
Figure 42 Calibration curve relating measured acoustic reflectance to actual acoustic reflectance. (20dB attenuation) (11-12-2009).....117

Figure 43Raw SAM image of Sample 67 showing location of sub-image 1. 122
Figure 44(A) Raw unprocessed sub-image sample 67, (B) Young's Modulus (GPa) values assigned to FE model, (C) Equivalent strain, (D) Equivalent stress (MPa). 123
Figure 45 Boxplots of Young's modulus (GPa) for Year 1 (top) and Year 2 (bottom) Samples.Within the year 1 data there is little variation in mean and standard deviation between sample types. Within the year 2 data ovariectomised samples have a greater value of standard deviation when compared to controls. 126
Figure 46 Year 1 and year 2 individual sample histograms. Within the year 1 histograms the distributions between and within sample types are similar. For the year 2 samples, comparing the distributions of ovariectomised sample types with control samples types, the ovariectomised samples have fatter tails to the left of the mean of the distribution. 127
Figure 47 Year 1 and Year 2 Histograms for each sample type. Each sample type shown is made up of the pooled data from each sample. For year 1 sample types the distributions are overlapping. Within year 2 sample types control and drug treated ovariectomised samples have similar distributions, conversely the ovariectomised sample type has a different distribution, having larger tails when compared with controls 129
Figure 48 Year 1 and Year 2 Empirical cumulative density function. The zeros have been removed from the empirical cumulative density function plots shown above to avoid distorting the distributions observed. 130
Figure 49 Boxplots of Equivalent stress (MPa) for year 1 (top) and year 2 (bottom) Samples. Within the year 1 data there is little variation in mean and standard deviation between sample types. Within the year 2 data ovariectomised samples have a greater value of standard deviation when compared to controls. 132
Figure 50 Year 1 and year 2 individual sample histograms. Equivalent stress (MPa). Within the year 1 histograms the distributions between and within sample types are similar. For the year 2 samples, comparing the distributions of ovariectomised sample types with control samples types, the ovariectomised samples have fatter tails to the left of the mean of the distribution. 133
Figure 51 Year 1 and year 2 Histograms for each sample type. Equivalent stress (MPa). Each sample type shown is made up of the pooled data from each sample. For year 1 sample types the distributions are overlapping. Within year 2 sample types

control and drug treated ovariectomised samples have similar distributions, conversely the ovariectomised sample type has a different distribution, having larger tails when compared with controls. 135
Figure 52 Year 1 and year 2 Empirical cumulative density function Equivalent stress (MPa). The zeros have been removed from the empirical cumulative density function plots shown above to avoid distorting the distributions observed. 136
Figure 53 Boxplots of Equivalent strain for year 1 and year 2 Samples. .Within the year 1 data there is little variation in the standard deviation between sample types. Within the year 2 data ovariectomised samples have a greater value of standard deviation when compared to controls..... 139
Figure 54 Year 1 and year 2 individual sample histograms. Equivalent strain. Within the year 1 histograms the distributions between and within sample types are similar. For the year 2 samples, comparing the distributions of ovariectomised sample types with control samples types, the ovariectomised samples have fatter tails to the left of the mean of the distribution. 140
Figure 55 Year 1 and year 2 Histograms for each sample type. Equivalent strain. Each sample type shown is made up of the pooled data from each sample. For year 1 sample types the distributions are overlapping. Within year 2 sample types control and drug treated ovariectomised samples have similar distributions, conversely the ovariectomised sample type has a different distribution, having larger tails when compared with controls. 142
Figure 56 Year 1 and year 2 empirical cumulative density function. Equivalent strain. The zero values have been removed to avoid distortion and allow easier comparison between the sample type distributions..... 143
Figure 57 Calculated TOF Vs. Actual TOF orthogonal regression analysis. We can see there is a strong correlation between the measured TOF and the calculated TOF. Note a steady increase in the scatter of points from focus (right hand side of graph) to out of focus (left hand side). 161
Figure 58 An interpretation of the altered distribution of strains, when compared to controls, due to osteoporosis. Diagram (A) above shows normal bone exposed to a physiological strain $\varepsilon_{applied}$. The distribution can be divided into a disuse window where bone can be resorbed, an adaptive window where no targeted remodelling takes place and a mild overload window where bone formation will occur. The most extreme situation to the right is where bone is resorbed due to it being

damaged. Diagram (B) shows the strain distribution in osteoporotic bone. Comparing it with normal bone it has a fatter tail region to the left of the distribution. This can be interpreted that for a given disuse window and physiological strain load more area of bone in osteoporotic bone is at risk of resorption than in normal bone. Diagram (C) is the combined strain-adaptive remodelling and damage simulated resorption algorithm using the ON/OFF remodelling concept (Mulvihill et al. 2010). 167
Figure 59 Basic structure of an ultrasonic transducer (Goldstein 2000) 219
Figure 60 Schematic of an ultrasonic transducer showing the near and far field regions. 221
Figure 61 Schematic showing the far field region of ultrasonic transducer. 221
Figure 62 Schematic showing the relative amplitude as a function of distance from the transducer. 222
Figure 63 Schematic of maximum resolution being a function of beam width. 223
Figure 64 Comparison of transducers with different transducer diameters. The effect of higher frequency is to reduce the size of the narrow field. 224
Figure 65 Geometry of a focussed transducer(Passmann 1994) 226
Figure 66 Top left: Lateral Resolution Depending on Center-Frequency and F-Number. Top right: Penetration Depth Depending on Center-Frequency and F-Number. Bottom left: Axial Resolution Depending on Bandwidth. Bottom right: Useable Depth Range for Imaging Depending on Center-Frequency and F-Number(Passmann 1993) 228

List of Tables

Table 1 Typical Properties of cortical bone, (From Ashman et al., 1984) 11
Table 2 Levels of hierarchy found in bone, adapted from (Dulgar 2007). 16
Table 3 "Bone for Life"animal group, initial animal numbers (Lee et al. 2004). 42
Table 4 Ultrasonic frequency required to image various constituent parts of cortical bone. Adapted from (Lakes et al. 1986). 53
Table 5 Attenuations for various biological materials (Laugier 1999). 54
Table 6 Typical depth achievable at various frequencies for cortical bone 55
Table 7 Summary of representative studies on cortical bone using SAM, showing the increasing sophistication of the techniques (Increased resolution) and technologies applied to imaging cortical bone both quantitatively and qualitatively. 68
Table 8 Typical physical values of bone samples (Raum et al. 2006a). 74
Table 9 Sample types available in study. 85
Table 10 Number of samples in statistical analysis. Each sub image has 5151 pixels. .. 85
Table 11 Year 1 and year 2 Samples imaged by SAM, Y1 and Y2 indicate year 1 and year 2 samples respectively. CON refers to bone samples which come from control sheep, OVX refers to samples from ovariectomised sheep and OVX-ZOL refers to bone samples from sheep which have been ovariectomised and subsequently administered Zoledronic acid. 86
Table 12 Transducer details (From Sonix correspondence) 87
Table 13 Materials used for calibration 91
Table 14 Averaging in mm^2 for each increment. Note an osteon has area of about $6.25x10^{-2} mm^2$. 103
Table 15 Breakdown of error sources for image processing pipeline. 105
Table 16 Measured acoustic reflectance for calibration materials. (20dB attenuation). (11-12-2009) 116
Table 17 Unprocessed SAM images, Control year 1 samples (CONY1) imaged on the 11th December 2009. 118
Table 18 Unprocessed SAM images, ovariectomised year 1 samples (OVXY1) imaged on the 11th December 2009. 119
Table 19 Unprocessed SAM images. Samples in left column are control year2 (CONY2). Samples in the right column are the ovariectomised year 2 samples (OVXY2). Imaged on the 30th September 2011 120

Table 20 Unprocessed SAM images, ovariectomised year 2 bone samples (OVX-ZOLY2). Imaged on the 30 9 2011 121
Table 21 Young's Modulus (GPa) data for year 1 and year 2 samples. 124
Table 22 Equivalent stress (MPa) Data for year 1 and year 2 samples. 131
Table 23 Equivalent strain data for year 1 and year 2 samples. 137
Table 24 Two sample t test: Young's modulus for year 1 and year 2 comparison. 145
Table 25 Two sided K-S test for Young's modulus. No removal of zeros (1000 points sample) 146
Table 26 Two sided ADK test for Young's modulus. No removal of zeros (1000 random points from each sample type) 146
Table 27 Combined ADK test for Young's modulus. No removal of zeros (1000 random points from each sample type) Null hypothesis at least one sample type shares a common distribution. 146
Table 28 Two sample t test: Equivalent stress for year 1 and year 2 comparison. 147
Table 29 2 sided K-S test Equivalent Stress. No removal of zeros 1000 point sample 148
Table 30 Two sided ADK test for Equivalent Stress. No removal of zeros (1000 random points from each sample type) 148
Table 31 Combined ADK test for Equivalent stress. No removal of zeros (1000 random points from each sample type) 148
Table 32 2 sided K-S test Equivalent Strain. No removal of zeros, 1000 point sample. 149
Table 33 Two sided ADK test for Equivalent Strain. No removal of zeros, 1000 point sample. 149
Table 34 Combined ADK test for Young's modulus. No removal of zeros, 1000 point sample. 150
Table 35 Results of Orthogonal Regression for a 15x15 averaging areas for focus correction algorithm. If the measuring methods are equivalent then the confidence intervals for the slope should include 1 and the intercept should include 0. 160
Table 36 Variation of acoustic Impedance of water with temperature. 161
Table 37 An estimate of the errors in the image processing of samples from raw SAM images to finite element models. 163
Table 38 Flat transducers typical properties 224
Table 39 Equations describing the F number, lateral and axial resolution of a focused transducer. 226

Table 40 Typical values for laterial resolution and penetration depth of a transducer for a range of ultrasonic frequencies.....227

Nomenclature

A/D Analogue to digital.

BMC Bone mineral content

BMD Bone mineral density.

BUA Broadband Ultrasound Attenuation.

C_{33} Stiffness coefficient in principle direction of loading of bone.

CON Control sheep bone samples

CT Computer Tomography

DEXA Dual-energy X-ray absorptiometry

E_3 Young's Modulus in the principle direction of loading of bone.

FE Finite Element method.

K-K Kramers Kronig relations.

OS Osteoporosis

OVX Ovariectomised sheep bone samples.

OVX+ZOL Ovariectomised drug treated sheep bone samples

QUS Quantitative Ultrasound.

R Acoustic Reflectance.

RF Radio Frequency.

SAM Scanning Acoustic Microscopy.

SOS Speed of sound.

StDev Statistical term, Standard deviation

US Ultrasound.

V(z) Technique for finding velocities of sound in a material by the interference of shear and longitudinal waves independent of sample thickness.

v_{bar} Bar velocity using bar approximation.

v_L Longitudinal sound velocity.

Z Acoustic Impedance.

ZOL Same meaning as **OVX+ZOL** Ovariectomised drug treated sheep bone samples

θ_c Critical angle.

λ Wavelength.

ν Poisson's Ratio,

ρ Density

1 Introduction

Bone is a living multi-scale hierarchical composite material capable of self repair. The three constituent elements of this composite are: an organic form of a calcium ceramic known as hydroxyapatite (HAP), collagen, and water (Fung 1993). These elements are organised into a micron scale structure known as a mineralised collagen fibril. This is the basic building block of bone (Mann *et al.* 1999). The combination of a hard brittle HAP and soft ductile collagen results in a heterogeneous structure that is strong and hard but also maintains some flexibility (Doblaré *et al.* 2002). As with many engineering composites it displays properties such as low density and good fracture toughness (Weiner *et al.* 1999).

There are many forms of bone found in the body each with properties suited to their function. The lamellar form of bone can be thought of as the "concrete" of the bone family of materials. This is perhaps the most complex form and is most common in humans. It is found in a variety of forms in the human skeleton. In cortical bone this form can be found in the concentric ring structure of an osteon in Haversian bone, see Figure 1. Approximately 80%, by mass, of the human skeleton is made up of cortical bone (Jee 2001). This form of bone has low porosity (about 5%) and contains only microscopic channels and is the principal focus of this study.

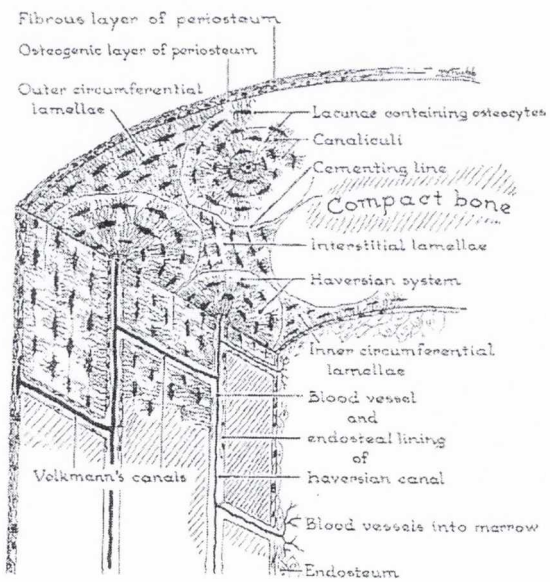


Figure 1 Simplified structure of cortical bone (Adapted from (Fung 1993))

In order to understand the complexity of bone as a material, it is useful to consider the the dimension of hierarchy. Bone has at least seven levels of organisation from the nano-meter scale HAP crystals and collagen to the whole bone. Structures within these levels give rise to macroscopic forms of bone such as Haversian, cancellous and plexiform bone. As a consequence of diseases, such as osteoporosis, the pattern and orientation of these fibril arrays could change. These changes could have an impact on the ultimate strength and fracture toughness of the affected bone. Disease processes such as osteoporosis can be understood in terms of how they effect changes to bone at these hierarchical levels of organisation.

1.1 Osteoporosis and its Societal Cost

As populations in western societies age, osteoporosis is becoming a major health issue. In Ireland, the fracture rates for females aged 50 and over are 407 per 100,000. Assuming a stable incidence rate, and due to an aging population the number of fractures occurring on an annual basis is expected to double by 2026 (Dodds *et al.* 2009). In 2000, there were an estimated 4 million new fractures across Europe with osteoporotic fractures estimated at 3.79 million of which 0.89 million were hip fractures (Johnell *et al.* 2006). The total direct costs were estimated at €31.7 billion and by 2050 this cost could rise to €76.7 billion based on the expected demographic changes in Europe (Kanis *et al.* 2005). This situation leads to unsustainable increases in the costs of healthcare provision. There is an increased risk of mortality as a result of osteoporosis. Patients are at increased risk of premature death for many years after a fragility-related hip fracture. For instance, during the first year after fracture, mortality rates range from 8.4% to 36% (Abrahamsen *et al.* 2009). The best treatment for osteoporosis is prevention by early detection and intervention. Any treatments or insights into how bone architecture and structure change due to the effects of osteoporosis will help paint a more comprehensive picture of the pathology of the disease and create further opportunities for successful intervention.

1.2 Diagnosis and treatment of Osteoporosis

The international reference standard for the description of osteoporosis in postmenopausal women, and in men aged 50 years or more, is a femoral neck BMD of 2.5 standard deviations or more below the young female adult mean, using normative data from the NHANES reference database of Caucasian women aged 20–29 years. Although the reference standard for the description of osteoporosis is BMD at the

femoral neck, other central sites (e.g. lumbar spine, total hip) can be used for diagnosis in clinical practice (Anonymous 2007).

DEXA has been the standard clinical test in the diagnosis of osteoporosis, but it must be noted that it measures bone quantity (BMD) and it does not assess bone quality. Bone quality can be defined as how the composition and structure of bone determines its strength (Seeman *et al.* 2006). Bone quality is also an important determinant of bone fracture risk. Considering the hierarchical dimension of bone, DEXA only assess the amount of mineral present in the mineralised collagen fibril. It does not assess how this material is organised at the higher hierarchies of bone such as in the lamellae or the osteon.

Drug treatment is an effective method in the treatment of osteoporosis. Third generation bisphosphonates such as Zoledronic acid (Novartis, Basel, Switzerland) are highly effective in halting the deterioration of bone by inhibiting the action of bone cells called osteoclasts responsible for resorption of bone. A small yearly dose is sufficient in adult humans to significantly reduce fracture risk (Reid *et al.* 2002).

1.3 Bone Biomechanics

1.3.1 Bone mechano-sensivity

Mechano-sensitivity is the ability of bone to detect mechanical loading and generate some signal which will initiate a response such as modelling or remodelling. The principle candidate (Cowin *et al.* 1991) for this role is the osteocyte. It is the most plentiful cell in cortical bone and it is embedded throughout the matrix. It is known that osteocytes locked away in lacunae are in contact with surrounding cells through cell processes.

By applying classical control theory concepts (See Figure 2) to targeted bone remodelling, the process can be thought of in simple terms as a closed loop feedback system. The sensing and comparison element is the osteocyte and their interconnected processes. The control element being the cascade of chemical and hormonal signals triggered by a departure from a comfortable range of physiological strain and the process element is action of the basic multicellular units (BMUs) in removing old bone and laying down new bone. There is also a disuse strain level below which bone is removed and not replaced.

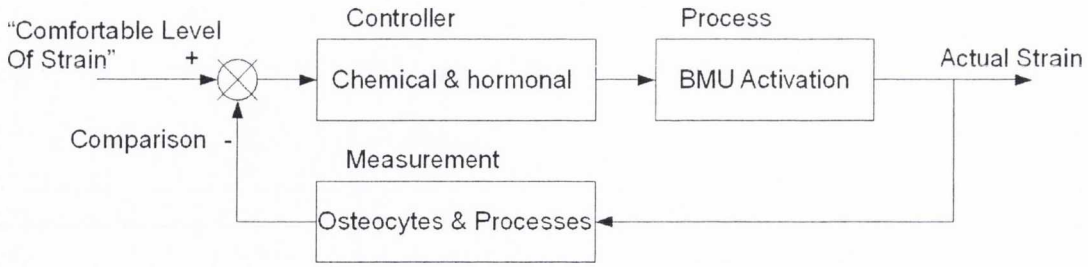


Figure 2 Schematic representation of the feedback control loop responsible for remodelling in cortical bone.

If these cells are the principle transducers of load history in bone then what happens to this mechanism as a result of disease such as osteoporosis? It is known that osoteocytes have a chemical receptor for oestrogen and the effect of oestrogen on females during puberty has the effect of increasing the percentage of bone mass as a proportion of lean weight as compared to males (Schiessl *et al.* 1998). It would seem logical to infer that the reverse is happening at menopause. Estrogen withdrawal could have the effect of modifying the strain at which bone cells responds by initiating bone remodelling.

Incorporating such ideas, Frost (Frost 1997a; Frost 2004) developed the mechano-stat model of bone modelling and remodelling. He postulated that below 100 microstrain, resorption occurs in normal bone. The effect of estrogen withdrawal, as experienced at menopause is to raise this threshold, thus bone will be resorbed at, for example <200 microstrain, instead of 100. This will lead to a reduction of bone mass. This concept and others relating to the Mechanostat theory are described in Figure 3.

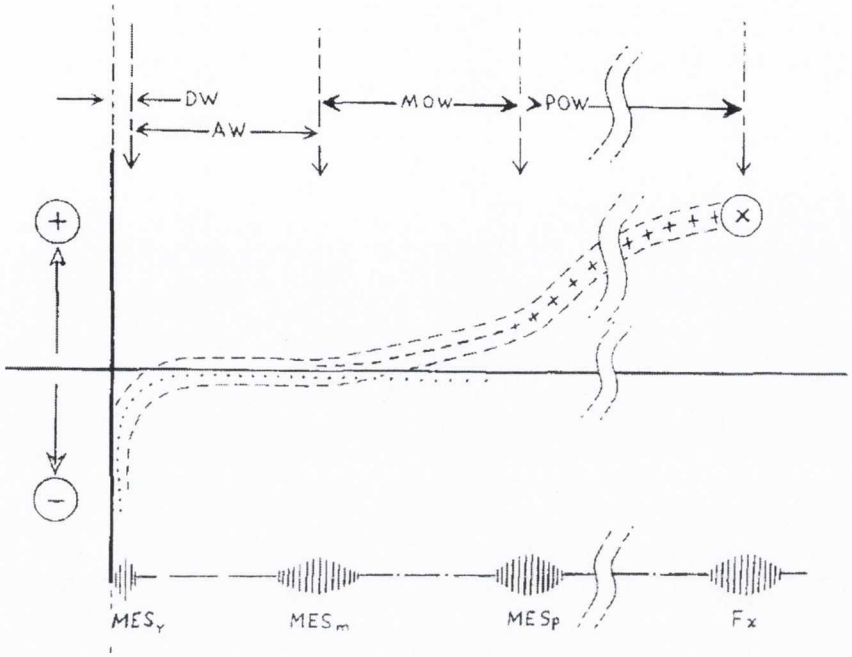


Figure 3 Combined modelling and remodelling effects on bone strength and "mass."' The horizontal line at the bottom of this graph suggests typical peak bone strain from zero on the left, to the fracture strain on the right (Fx), plus the locations of the remodelling, modelling, and microdamage thresholds (MESr, MESm, MESp). The horizontal axis represents no net gains or losses of bone strength or "mass." The lower dotted line curve suggests how remodelling removes and weakens bone where strain stay in or below the MESr range, but otherwise begins maintaining bone and bone strength. The upper dashed line curve suggests how modelling begins to increase bone strength and "mass," where strain enter or exceed the MESm range. The dashed outlines suggest the combined effects. At and beyond the MESp range, woven bone formation drifts usually replace lamellar bone formation drifts. Fx - the fracture strain near 25,000 microstrain. At the top: DW disuse window; AW adapted window or "comfort zone" as in normally adapted adults; MOW = mild overload window as in growing mammals including children; POW pathologic overload window) In the nearly flat "comfort zone" or adapted window between the MESr and MESm, bone strength and "mass" change little as typical peak strain change. In children, increasing weight and muscle strength shift bone strain towards the MESm. From: (Frost 1997a)

When micro-structural changes occur in cortical bone, they have consequences for the mechanical stimuli generated in the tissues. These micro-structural changes, and the way they alter the strain environment of the bone microstructure, is thought to affect the way bone cells sense the need to lay down or resorb matrix (Cowin *et al.* 1991; Burger *et al.* 1999a). It is well known that bone tissue adapts its structure to its mechanical load environment. Bone is a living tissue and it is has a mechano-sensory apparatus which

has the ability to sense mechanical loading and damage (Burger *et al.* 1999b). Changes in bone microstructure brought about by osteoporosis could change the distribution of stimuli within the tissue and could fundamentally affect mechano-sensitive cell response (Mulvihill *et al.* 2008).

1.3.2 Ultrasonics applied to bone

In-vivo ultrasound methods have the capability to give more insight into the changes that occur in cortical bone due to osteoporosis than the traditional DEXA method (Njeh 1999b). An ultrasonic technique known as Scanning Acoustic Microscopy (SAM) can be used to image bone samples *in-vitro*. This technique can build up an image of the acoustic properties of a bone sample across its surface.

1.3.3 Finite Element Analysis (FEA) of cortical bone microstructures.

Based on an idealised Haversian structure, the effects of damage in an osteon have been examined by (Prendergast *et al.* 1996). The resulting alterations in the local micro-structural stress and strain environment were estimated using FEA. It was found that the strain concentration that resulted could be sufficient to stimulate the bone remodelling mechanism (Hogan 1992).

A parametric three dimensional finite element study of the effect of physiological strain on the strain environment in and around the lacunae was carried out. It was found that for a variety of possible material and physical configurations of lacunae, strain amplification was predicted to be in the region of three (Bonivtch *et al.* 2007).

More recently, studies (Abdel-Wahab *et al.* 2011; Mischinski *et al.* 2011) have investigated the crack propagation in representative finite element models of Haversian bone microstructures. These studies found that the fracture properties of the osteons were more important to influencing crack propagation paths than the elastic modulus of the osteon.

Nicolella *et al.* developed a method of experimentally determining the strain environment in a sample of cortical bone using machine vision (See Figure 4). A sample of bone was loaded on a tensile testing machine. The sample was then imaged at two increments of loading. The images were then processed to determine the relative displacements in the images and hence the strain. This method offers a way of confirming the conclusions of the finite element method approach. It was found that

structures such as lacunae in the osteon act as strain concentrators with an average concentration factor of 1.1 to 3.8 (Nicolella *et al.* 2006).

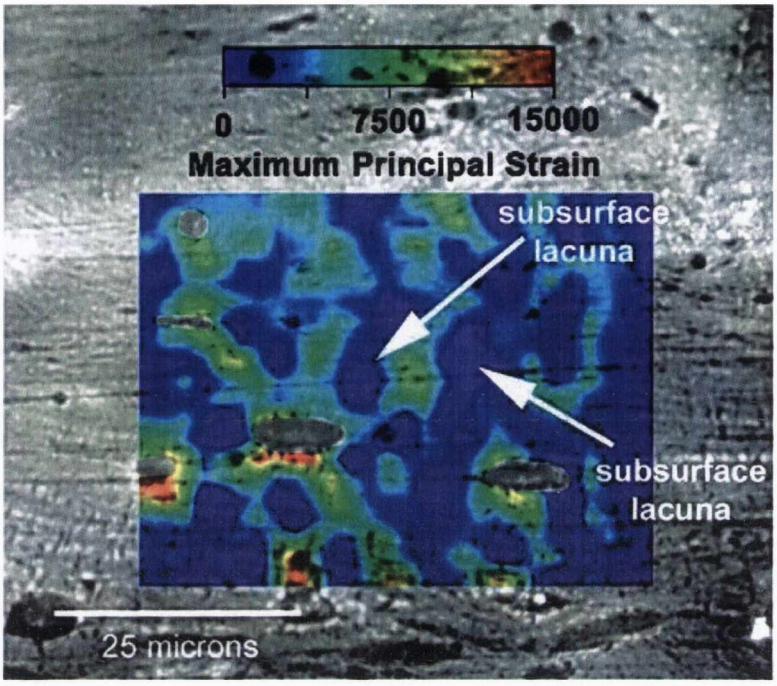


Figure 4 Microstructural strain field overlaid on a digital micrograph of a cortical bone specimen that was loaded to a macroscopic strain of 1500 μ strain in the horizontal direction. Each color represents a specific level of maximum principal strain as indicated by the legend. The local microstructural strain field is highly heterogeneous and strain is found to localize around osteocyte lacunae as well as between lacunae. Magnification 500x. From: (Nicolella et al. 2006)

1.4 Combining Ultrasonics and FEA

Ultrasonic methods, such as scanning acoustic microscopy, have been proven to accurately measure mechanical stiffness C_{33} of cortical bone at resolutions of up to eight micrometers (Shieh *et al.* 1995; Chandelier 2004; Raum *et al.* 2006a). The properties of individual lamellae at ultrasonic frequencies of 1GHz can be determined. At lower frequencies (5-10 MHz) mechanical properties can be measured at the macro scale at resolutions of 1-5mm. Whilst ultrasonic methods can measure mechanical properties such as stiffness (C_{33}) how can we assess the strain environment experienced by the mechano-sensory system of bone?

One method is to use the two dimensional maps of mechanical stiffness generated by SAM to create finite element models. Each pixel in an image can be represented by a

finite element with appropriate stiffness. Appropriate boundary conditions and physiological loading can be applied and the strain environment evaluated. Many researchers have estimated the strain around representative models of cortical bone micro-structure but they lacked exact values for stiffness in their finite element models (Prendergast *et al.* 1996; Bonivtch *et al.* 2007; Abdel-Wahab *et al.* 2011; Mischinski *et al.* 2011).With more realistic finite element models it will be possible to assess the strain environment of actual bone samples (Raum *et al.* 2006a).

1.5 Statement of Research Hypothesis

The author's hypothesis is that the process of osteoporosis changes the magnitude and distribution of stresses and strain in cortical bone tissue, and this could drive the pathology through altered cell responses. One way that this could happen is if ovariectomy leading to osteoporosis, triggers a change in the bone remodelling strain set point threshold for resorption. This in turn has a structural consequence for bone which further alters future cell responses to load. If the hypothesis is corroborated it will be possible to quantify this response and understand how the process proceeds over time. These insights will be invaluable to further understanding and developing treatments for osteoporosis. It will also show the benefit of applying computational simulation techniques (Finite Element Analysis) to the study of the strain field in bone microstructure which is difficult if not impossible to undertake using experimental methods. This allows comparison of bone types, for example bone from ovariectomised sheep compared to control samples. Direct comparison of the strain environments between sample types can be made.

2 Literature Review

2.1 Bone

2.1.1 Introduction

On average 18% of the body weight of a human is made up of bone. Its main functions are to:

- Contribute to body shape and form
- Provide mechanical support and sites for muscle attachment for locomotion.
- Provide protection for various organs such as those in the rib cage.
- Act as a calcium and phosphate reserve for the metabolic pathways associated with mineral homeostasis.

2.1.2 Bone as a Tissue

Bone is a composite material made up of 65% mineral, 35% organic matrix, cells and water. The mineral phase of bone is composed of hydroxyapatite, $Ca_{10}(PO_4)(OH)_2$, and it is in the form of small crystals in the shape of small rods and plates intertwined between the collagen fibres. The hydroxyapatite contains apatite crystals that are very stiff but brittle (Young's modulus: $165GN/m^2$). Also present in the mineral are constituents such as magnesium, fluoride, carbonate and strontium (Fung 1993). The water phase facilitates the interactions between the HAP phase and the collagen phases (Broz *et al.* 1995).

Subsequent to the creation of new bone structural units (BSUs) a process is started, which over time, adds organic hydroxyapatite to the lamellar structure of bone. This process is known as biomineralisation. The most basic processes in biomineralisation operate at the nanometer length scales and involve proteins and/or other macromolecules directly in controlling the nucleation, growth, and inhibition of the mineral phase (Mann *et al.* 1999).

The organic matrix is made up of 90% collagen and 10% non-collagenous proteins. Collagen is a softer, more elastic and ductile material with a much lower Young's modulus of $1.24\ GN/m^2$. The combination of the hard and brittle hydroxyapatite with the soft and ductile collagen yields a special heterogeneous structure that is strong and hard but also maintains flexibility.

2.1.3 Cortical Bone

Cortical bone is a dense, solid mass with only microscopic channels. Approximately 80% of the skeletal mass in the adult skeleton system is cortical bone, which forms the outer wall of all bones and is largely responsible for the supportive and protective function of the skeleton (Jee 2001). These mechanical properties do not solely depend on the composition of the bone but also on the structure of the bone i.e. geometric shape of components; bond between fibres and matrix and bonds at points of contacts of fibres (See Table 1).

E_1	12 MPa
E_2	13.4 MPa
E_3	20 MPa
G_{12}	4.53 MPa
G_{13}	5.61 MPa
G_{23}	6.23 MPa
ν_{12}	0.376
ν_{13}	0.222
ν_{23}	0.235
ν_{21}	0.422
ν_{31}	0.371
ν_{32}	0.35
ρ	1875-1950kg/m3
UTS	124±1.1 MPa

Table 1 Typical Properties of cortical bone, (From Ashman et al., 1984)

2.1.3.1 Bone Structure

Bone is really a family of materials in which the basic building block is the mineralised collagen fibril. The lamellar bone structure is perhaps the most complex. It is also the most common form in humans (Mann *et al.* 1999).

Osteon or Haversian system: Osteons form approximately two thirds of cortical bone volume; the remaining one third is made up of the interstitial bone composed of the remnants of past generations of osteons, and subperiosteal/subendosteal circumferential

lamellae. A typical osteon is cylindrical in shape, about 200μm to 250μm in diameter, with up to 30 concentric layers (lamellae) of bone approximately 5μm thick. Surrounding the outer border of each osteon is a cement line approximately 1-2μm thick, which is a mineralised matrix deficient in hydroxyapatite crystals. It functions as a weak interface between osteonal lamellae and interstial lamellae and could increase the fracture toughness of bone by arresting crack growth (Dong *et al.* 2004). The cement layer is only found in secondary bone.

At the middle of each osteon lies a Haversian canal. This cavity is approximately aligned to the long axis of the bone. It contains capillaries and nerves and is up to 50μm in diameter.

Volkmann's Canals: Transverse cavities connect Haversian canals to each other and to the outside surfaces of the bone through a branching network. The canals also contain blood vessels and probably nerves.

Resorption Cavities: Temporary spaces created by osteoclasts in the initial stage of remodelling and are approximately 200μm in diameter (Martin 1998).

The Lamellar Structure: This could be thought of as the "concrete" of the bone family of materials. A lamellar unit is composed of five sub-layers. Each sub-layer is an array of aligned mineralised collagen fibrils. The orientations of these arrays differ in each sub-layer with respect to both collagen fibril axes and crystal layers (Mann et al. 1999).

This structure appears to have the benefit of resisting weaknesses that can occur due to micro-damage and fatigue. For example, during testing it has been observed that osteonal bone never breaks into two distinct pieces after catastrophic failure, the two sides always remained attached. This may be a key survival benefit as bone can only heal if the two fractured parts are in close proximity (Weiner *et al.* 1999).

Cortical bone is also observed in other forms such as woven and plexiform. Woven bone is found at the site of a fracture undergoing healing. The collagen fibres are randomly organised and loosely packed. This is a result of the speed at which it is laid down.

Plexiform bone is found in rapidly growing animals such as cows and sheep. In contrast to woven bone it must be able to offer increased mechanical support for longer periods of time. Plexiform bone arises from mineral buds which firstly grow perpendicular and then parallel to the outer bone surface. This growth pattern produces a brick like

structure characteristic of plexiform bone. Each brick is about 125μm across. Plexiform bone have greater stiffness than primary or secondary cortical bone, but it lacks the crack arresting properties which would make it suitable for more active structures such as those found in dogs and humans (Martin 1998).

2.1.3.2 Hierarchical structure

Bone has a complex hierarchical structure, see Figure 5. The fundamental building blocks are extremely small plate-shaped crystals of apatite a few hundred Angstroms long and 20-30 Angstroms thick. They are arranged in parallel layers within a collagenous framework. At the next hierarchical level these mineral filled fibrils are all organised into a 3D structure which makes up a single layer or lamellae of bone a few microns thick. The organisation of the 3D structure from one lamellae to the next has different orientations of fibrils. This further enhances the strength and fracture toughness of the bone. These lamellae are then part of a higher level of organisation known as osteons. Compact bone is made up of many of these osteons arranged approximately perpendicular to the principle axis of the bone. Between the osteons is a type of bone known as interstitial bone. Overall bone is a remarkable ordered material from the molecular to the macroscopic scale (Weiner *et al.* 1992). (See Figure 5)

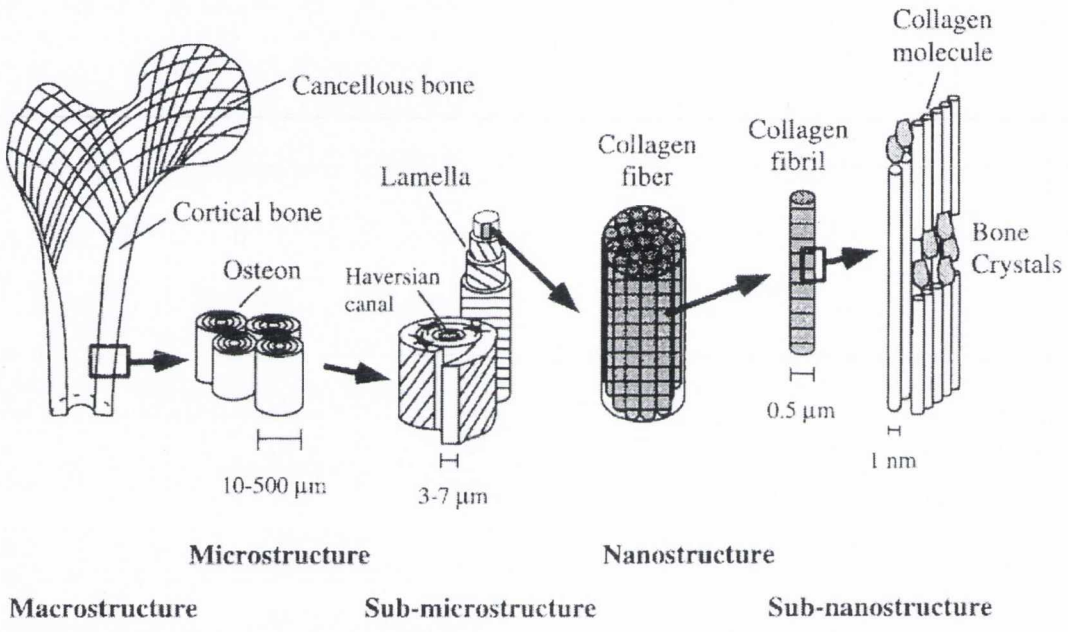
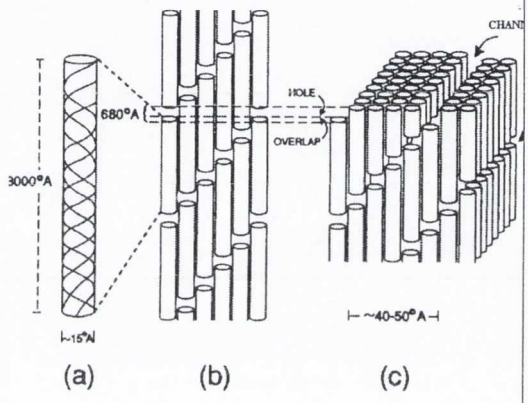
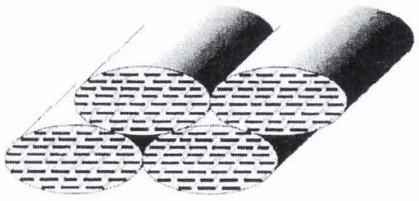


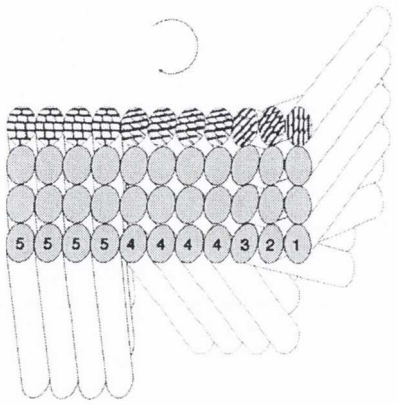
Figure 5 Hierarchical structural organization of bone: (a) cortical and cancellous bone; (b) osteons with Haversian systems; (c) lamellae; (d) collagen fiber assemblies of collagen fibrils; (e) bone mineral crystals, collagen molecules, and non-collagenous proteins (Rho et al. 1998).

Hierarchy can be thought of as the third dimension of bone. There are several levels to this hierarchy, see Table 2 below.

Level	Description	Diagram
1	**Molecular Building Blocks:** **Mineral:** Dahllite, a carbonated apatite ceramic, chemically identical to hydroxyapatite. Plate shaped nano-crystal 50x36x2.5nm. Young's modulus 165GPa (Fung 1993). **Protein:** Type I Collagen, fibres woven into the form of a cylinder 80-300nm x1.5nm. Tangent modulus 1.24GPa. (Fung 1993). **Water:** Important component in the mechanical properties of bone.	
2	**Mineralised Collagen Fibril Basic Building Block of Bone:** **Fibrous Composition** Fibrils composed of individual collagen fibres oriented parallel to each other. Fibres are assembled in layers each identical but offset by 28nm. **Mineralised Composition** Dahllite crystals are initially formed at the spaces between the fibre rows. These crystals expand in size over time eventually expanding to create continuous sheets throughout the fibre.	 **(a) Collagen Type I structure, (b) 2D section of Staggered array (c) 3D section showing showing structural arrangement of fibres. Crystals of Dahllite initially are found at the ends of each fibril (not shown) (Weiner *et al.* 1992).**
3	**Fibril array** Individual collagen fibres arrayed parallel to their neighbouring fibres. Fibril layers can be parallel or non-parallel These can have a variety of forms. They do not necessarily have to be aligned to each other.	 **Illustration of a transverse section through 4 collagen fibrils . Note the orientation of the crystal layers (Weiner *et al.* 1992).**

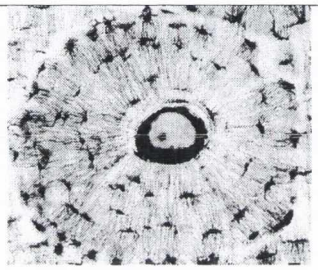
<table>
<tr><td>4</td><td><u>Fibril Array Patterns</u>

There are 4 possible patterns possible:

• Arrays of Parallel fibrils
• Woven Fibre structure
• Plywood like structures
• Radial Fibril arrays</td><td> 

An example of one of the possible fibril array patterns (Weiner et al. 1999).</td></tr>
<tr><td>5</td><td><u>Osteons.</u>

Primary osteons are found in compact bone

New (Secondary) osteons created by the action of osteoclasts removing old material. Osteoblast cells follow to lay down new material. New osteons lined with cement layer</td><td> 

A completed secondary osteon (Human bone) (Ardizzoni 2001).</td></tr>
<tr><td>6</td><td><u>Cancellous / Compact Bone</u>

Cancellous bone:

Highly Porous

High concentrations of blood vessels and cell to bone ratio

Low density

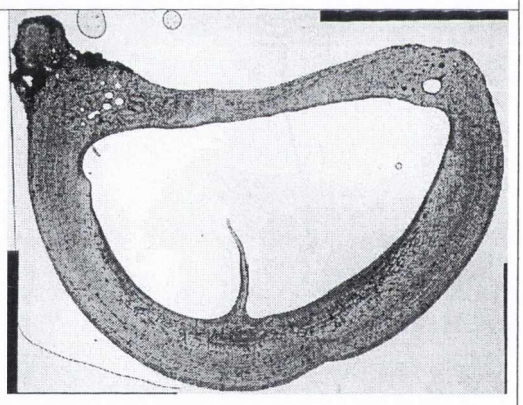
Low mechanical properties

Compact bone:

Low porosity

Few blood vessels and low cell to bone ratio

High density

High mechanical properties</td><td> 

SAM image of Ovine compact Bone section (Authors own).</td></tr>
<tr><td>7</td><td colspan="2"><u>Whole Bone:</u>

Each bone will have a unique combination of features at each hierarchical level. This includes the amount and location of compact and cancellous bone and features which occur at lower hierarchies. Most specialisation occurs in levels 4 to 7. Bone also serves other functions other than structural, for example the store of calcium and bone marrow for the creation of new blood cells.</td></tr>
</table>

Table 2 Levels of hierarchy found in bone, adapted from (Dulgar 2007).

The journey towards a full understanding of bone structure is far from complete. A detailed knowledge of the structure lays the foundation for the understanding of the mechanisms of mineralisation and mechanical properties. For example, understanding the effects of changes in parameters such as fibril array patterns has on the ultimate strength of bone and its fracture toughness. DEXA scans in a clinical setting measure the degree of mineralisation in bone tissue. This is measuring the extent of crystal growth in mineralised collagen fibril at level 2 in the hierarchy. How can insight be gained at the other levels of organisation in bone? One way is to study normal and pathological bone tissue and compare features at each level in the hierarchy. This type of study, while very complex, will lead to a better understanding of the effect of hierarchical changes due to disease on bone. Ultrasound offers compelling advantages over X-ray methods in gaining insight into bone structure. This is principally due to the fact that ultrasound is a mechanical wave and it can directly measure quantities such as Young's modulus and density.

Investigators are attempting to create a hierarchical model which relates micro-structural properties to whole bone properties. Hierarchical multiscale modelling methods are very suitable to the problems of determining the micro/macro interactions. Hierarchical multiscale modelling methods are based on the definition of two or more interconnected problems with a formulation appropriate to the scale under consideration. For example, in two-scale modelling, a macro scale problem is defined in order to study the global behaviour of the material and a microscale problem is formulated to reflect the microstructure of the material. These are complex multiscale models and are vital to understanding the dimension of hierarchy and its effect on bone mechanical properties (Ghanbari *et al.* 2009).

Mechanical properties were measured by nano-indentation and compared to bone mineral content found by back scatter electron imaging. Local elastic modulus was plotted against mineral fraction and compared with predictions of engineering bounds for a two-phase composite material (Oyen *et al.* 2008). Variations in composition and structure at the microstructural level are known to exist in bone. These add functionality at the bone tissue level including local signalling of strain to osteocytes and contribute to a toughening mechanism in bone. Simple composite models were not found to be adequate, see Figure 6. There is no simple one to one relationship between Young's modulus of bone and the volume fraction. This means a range of local structural

arrangements of mineral and organic phases must exist at fixed composition to give rise to different modulus values. The widest dispersion occurs at 50% volume fraction, the approximate composition of normal bone. This can be interpreted as being the maximum number of possible arrangements existing at this volume fraction.

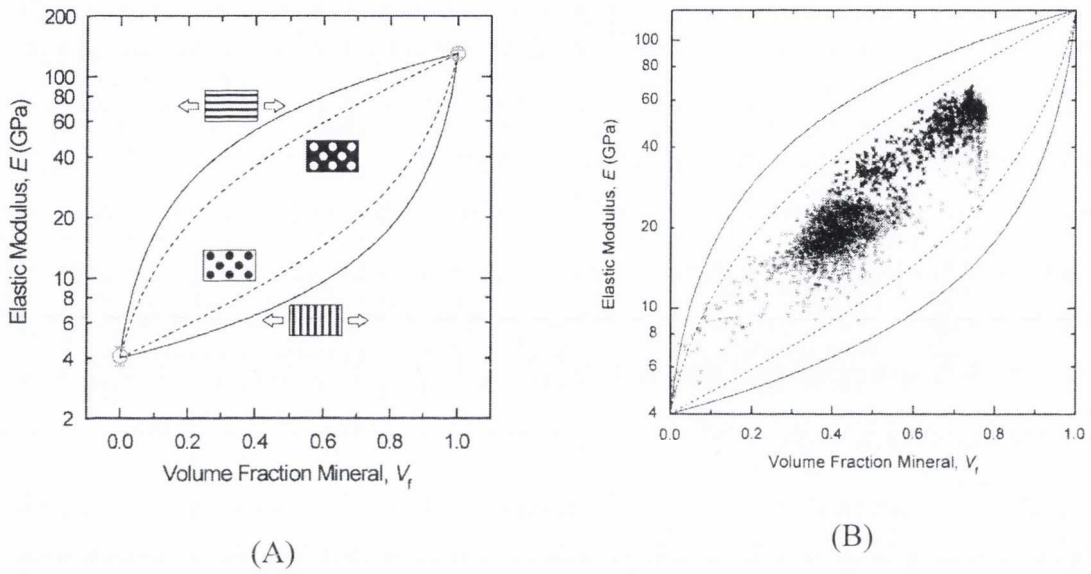


Figure 6(A) Composite elastic modulus bounds for stiff fibre reinforcement (solid line) and particle composite (dashed line), expressed in terms of the volume fraction of the stiff phase, together with illustrations of the corresponding physical structures (black represents the stiff phase). (B) Experimental data for the elastic modulus (E) versus mineral concentration (volume fraction, V_f) of PMMA-embedded bone samples (Oyen et al. 2008).

Advanced models are needed, based on statistical processes, to predict distributions of modulus values from composition. Advances in diagnosis and treatment of some bone disorders can be made by understanding the linkages between bone mineral content and mechanical function. (Oyen *et al.* 2008)

A more sophisticated model to relate micro-structural properties of bone to its mechanical properties, involved the use of a 2 level self consistent method, see Figure 7.

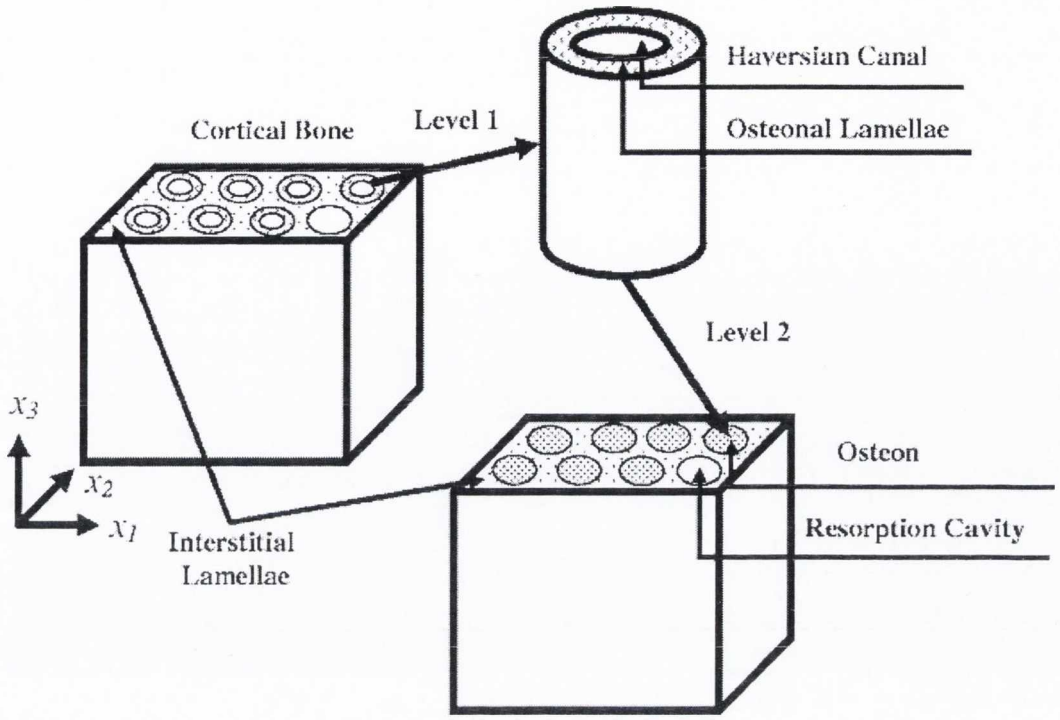


Figure 7 A two-level micromechanical model of osteonal cortical bone (Dong et al. 2006) .

The first level is of a single osteon modelled as a two phase composite. The Haversian canal is an elongated pore and the osteon is the matrix. The second level modelled osteons and resorption cavities as multiple inclusions while interstitial lamellae were regarded as matrix. This method produced results which were largely in agreement with experimental studies. This method accounted for the anisotropic behaviour of micro-structural components but it did not include the cement line. Micromechanical models were found useful in quantifying the relationship between mechanical properties and microstructural parameters. This type of model requires high quality data describing the elastic properties of each component. Methods such as nano-indentation and ultrasonic methods can provide the requisite data. (Dong *et al.* 2006)

2.1.3.3 Bone Material Models

Bone is often modelled at the macro scale (1 to 2 mm) as either transversely isotropic, orthotropic or anisotropic (Cowin *et al.* 1986) . Anisotropic materials have properties which vary in every direction. Cortical bone can also be modelled as a cylindrically orthotropic material. What follows is an explanation of each of these material models:

Hooke's law can be described in tensor notation as follows:

$$T_{ij}=C_{ijkn}\,E_{kn},\quad \textit{Equation 2-1}$$

This constitutive equation of Hooke's law can be rewritten in an alternative matrix notation as:

$$\sigma_i=c_{ij}\,\varepsilon_j\quad \textit{Equation 2-2}$$

2.1.3.3.1 Transversely Isotropic

Bone can be been modelled as a transversely isotropic material. This type of material can be characterised by five independent elastic constants. The matrix of stiffness coefficients is as follows:

$$\left[c_{ij}\right]=\begin{bmatrix} c_{11} & c_{12} & c_{13} & 0 & 0 & 0 \\ c_{12} & c_{11} & c_{13} & 0 & 0 & 0 \\ c_{13} & c_{13} & c_{33} & 0 & 0 & 0 \\ 0 & 0 & 0 & c_{44} & 0 & 0 \\ 0 & 0 & 0 & 0 & c_{55} & 0 \\ 0 & 0 & 0 & 0 & 0 & c_{66} \end{bmatrix}\qquad \textit{Equation 2-3}$$

Simplifications can be made to this matrix, as only five independent coefficients are required. Therefore:

$$E_1=E_2 \qquad \nu_{12}=\nu_{21} \qquad \nu_{31}=\nu_{32}=\nu_{13}=\nu_{23} \qquad \textit{Equation 2-4}$$

$$G_{23}=G_{31} \qquad \frac{1}{G_{12}}=\frac{E_1}{2(1+\nu_{12})} \qquad \textit{Equation 2-5}$$

2.1.3.3.2 Orthotropic

The matrix c_{ij} is known as the stiffness matrix and is in the form of a 6x6 matrix. For an orthotropic material there are 9 independent components and 3 dependent ones. The matrix is symmetric.

$$[c_{ij}] = \begin{bmatrix} c_{11} & c_{12} & c_{13} & 0 & 0 & 0 \\ c_{12} & c_{22} & c_{23} & 0 & 0 & 0 \\ c_{13} & c_{23} & c_{33} & 0 & 0 & 0 \\ 0 & 0 & 0 & c_{44} & 0 & 0 \\ 0 & 0 & 0 & 0 & c_{55} & 0 \\ 0 & 0 & 0 & 0 & 0 & c_{66} \end{bmatrix} \qquad \textit{Equation 2-6}$$

Eq. 2.6 above can be rewritten in compliance form as matrix, s_{ij}.

$$\varepsilon_j = s_{ij}\sigma_l \quad \textit{Equation 2-7}$$

Shown below is the relationship between the stiffness coefficient form and the compliance form for an orthotropic material:

$$[c_{ij}]^{-1} = [s_{ij}] = \begin{bmatrix} \frac{1}{E_1} & -\frac{v_{21}}{E_2} & -\frac{v_{31}}{E_3} & 0 & 0 & 0 \\ -\frac{v_{12}}{E_1} & \frac{1}{E_2} & -\frac{v_{32}}{E_3} & 0 & 0 & 0 \\ -\frac{v_{13}}{E_1} & -\frac{v_{23}}{E_2} & \frac{1}{E_3} & 0 & 0 & 0 \\ 0 & 0 & 0 & \frac{1}{G_{23}} & 0 & 0 \\ 0 & 0 & 0 & 0 & \frac{1}{G_{31}} & 0 \\ 0 & 0 & 0 & 0 & 0 & \frac{1}{G_{12}} \end{bmatrix} \qquad \textit{Equation 2-8}$$

The material co-ordinate system is assumed as follows; the x_1 axis is in the radial direction, the x_2 axis is in the circumferential direction and x_3 is in the longitudinal direction.

This matrix above is symmetric and this can be expressed as:

$$\frac{v_{ij}}{E_i} = \frac{v_{ji}}{E_j} \qquad \textit{Equation 2-9}$$

2.1.3.3.3 Anisotropic

Bone can also be modelled as an anisotropic material. The equations are shown below:

$$[E_{ij}]^{-1} = [S_{ij}] = \begin{bmatrix} s_{11} & s_{12} & s_{13} & s_{14} & s_{15} & s_{16} \\ - & s_{22} & s_{23} & s_{24} & s_{25} & s_{26} \\ - & - & s_{33} & s_{34} & s_{35} & s_{36} \\ - & - & - & s_{44} & s_{45} & s_{46} \\ - & - & - & - & s_{55} & s_{56} \\ - & - & - & - & - & s_{66} \end{bmatrix} \qquad \textit{Equation 2-10}$$

Materials whose properties vary in every direction are known as anisotropic. Every term of the above matrix has a value i.e. no zero terms. Therefore the diagonal condition still holds.

2.1.3.3.4 Viscoelastic properties of cortical bone

Compact bone displays visco-elastic material properties (Fung 1993);(Garner *et al.* 2000). Viscoelasticity is caused by a variety of mechanisms. Due to the hierarchical nature of bone these mechanisms have a variety of causes and occur over a wide range of scales. An example of one cause of viscoelastcity is the viscous fluid flow in the porous media of bone.

Viscoelastic damping in bone is quantified by the loss tangent (tan δ). The loss tangent is the ratio of energy dissipated to energy stored in a cycle of deformation. Impact injuries typically involve strain rates of 10 sec^{-1}. At these high strain rates bone has a higher ultimate strength but fractures at a lower strain (Garner *et al.* 2000). Human cortical bone exhibits a greater loss tangent (tan δ) when wet than when dry. The results all display a relative minimum in tan δ is found over a frequency range, 1 to 100 Hz. These are the frequencies bone is most exposed to during normal activities, see Figure 8.

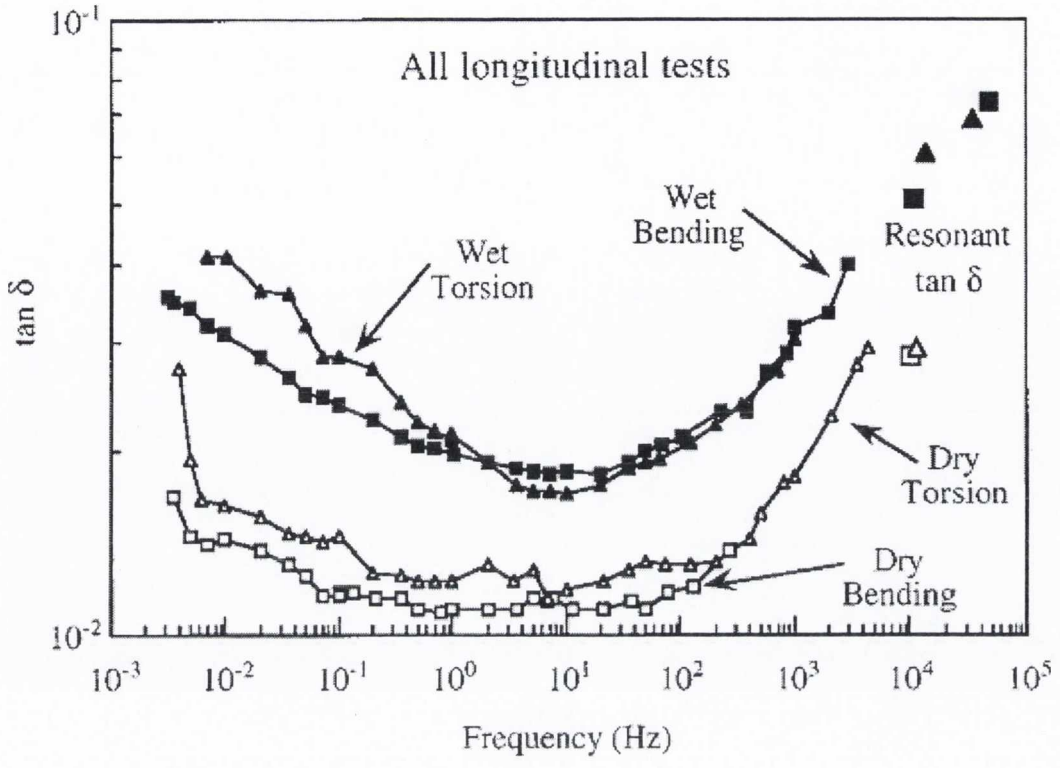


Figure 8 Comparison of measured tan δ (loss tangent) for longitudinal cut bone (Garner et al. 2000) .

The observed minimum in damping is inconsistent with a shock-absorbing role for bone based on its viscoelastic response. The damping peak, as found by finite element analysis using flow in porous media theory, occurs above 100 kHz. Therefore fluid flows freely in response to physiological mechanical stresses in bone and no pressure build-up occurs in the Haversian systems. Fluid flow in bone is of particular interest since it is a hypothetical stimulus for bone remodelling. Loss tangent can be calculated from ultrasonic measurements (Lakes *et al.* 1986).

2.1.4 Osteoporosis

The term osteoporosis was first coined by Lobstein, a French pathologist, in 1820. Osteoporosis can be defined as: "A disease characterized by low bone mass and micro architectural deterioration of bone tissue, leading to enhanced bone fragility and a consequent increase in fracture risk." Common fracture points are the hip, wrist and vertebral fracture (Anonymous 1993).

Bone mass reaches a peak at age thirty in both men and women but the way in which bone tissue is lost after the age of thirty differs between the sexes. Men lose bone mass

steadily from this peak. In women bone loss occurs after the menopause. Both men and women lose the same amount of bone mass (about 50%) But bone found in men appears to be able to compensate somewhat by external remodelling on the periosteal surfaces of the diaphysis of the long bones (Seeman 2004).

Osteoporosis can be characterised as either being primary or secondary depending on the absence or presence of underlying diseases known to be associated with bone loss.

The World Health Organisation has also proposed a specific definition and criteria for osteoporosis based on BMD (Bone mineral density) and BMC (Bone mineral content) at locations on the skeleton. Under this criteria, patients with a BMD or BMC value 2.5 or more standard deviations below the mean are classed as being osteoporotic. Patients diagnosed with this condition are at a higher risk of bone fracture. This can be diagnosed before the fractures occur and a medical intervention is required to treat the condition. This criterion is only an indication of risk and is usually used as just one of many diagnostic aids in identifying patients at risk from osteoporosis (WHO 1994).

The National Institutes of Health (NIH) have a more inclusive definition of osteoporosis which includes the idea of bone quality. To quote: "Osteoporosis is defined as a skeletal disorder characterized by compromised bone strength predisposing to an increased risk of fracture. Bone strength reflects the integration of two main features: bone density and bone quality. Bone density is expressed as grams of mineral per area or volume and in any given individual is determined by peak bone mass and amount of bone loss. Bone quality refers to architecture, turnover, damage accumulation (e.g., microfractures) and mineralisation (Anonymous 2000)."

Bone quality can therefore be summarised as the relationship between the organisation of the micro-structural features in bone and its strength and resistance to fracture.

2.1.4.1 Prevalence, economic and social cost of osteoporosis.

The clinical end-point of osteoporosis is fracture. The most common locations for fracture are the spine, wrist and hip. If the WHO definition of osteoporosis is used approximately 21% of the population are affected (Looker *et al.* 1997). 90% of hip fractures are associated with osteoporosis. In England and Wales the cost of osteoporotic fractures in 1990 was estimated at €742million per annum (Arden 1994). In the year 2000 there were 9 million osteoporosis related fractures worldwide. The greatest number, 34.8%, occurred in the EU (Johnell *et al.* 2006). Osteoporosis is also a

problem for men with one in five of men over fifty experiencing fractures (Seeman 2004; O'Neill 2005). The numbers of men and women with hip fractures in the UK are set to increase by a factor of more than two during the next 50 years.

BMD and BMC only provide part of the picture about bone quality. There is an overlap between osteoporosis and fracture risk. That is, many of the individuals who are technically osteoporotic will never suffer fracture and many people without osteoporosis suffer fractures (Njeh 1999b). This suggests that what is being measured by the WHO criteria is not the complete picture, there are other factors involved. Hence, other non-invasive methods of quantifying bone quality are required to better quantify fracture risk. Ultrasonic methods offer a way of addressing this issue. In a critique of DEXA, seen as the 'gold standard' of diagnosis of osteoporosis, Bolotin (Bolotin 2007) describes DEXA as a "mis-leading gauge of bone status." One of his arguments is that the actual BMD value is contaminated by surrounding soft tissue. BMD, as a measure of fracture risk measured by DEXA, complicates clinical trials of anti-resorpitive drugs because BMD is not sensitive and specific enough to predict fracture risk efficiently. For example 70-96% of differences in vertebral fracture risk reduction remain unaccounted for by differences in BMD. Therefore a drug treatment outcome which increases BMD is not an assurance of greater anti-fracture efficacy (Seeman 2007).

2.1.4.2 Treatment of Osteoporosis

There are many treatments available on the market today for osteoporosis. Zoledronic Acid (Novartis Pharma AG, Basel, Switzerland) represents one of the latest generation of drug treatments. This treatment is estimated to be 4 orders of magnitude more effective than previous generations of bisphosponate drugs. The action of the drug is to reduce bone turnover and this results in hyper-mineralistion of the bone tissue. This could alter the interface between the mineral and collagen component of bone and hence alter the mechanical properties of bone (Lee *et al.* 2004).

Bisphosphonates are effective agents for the management of osteoporosis. Reid *et al.* (Reid *et al.* 2002) describe a comprehensive study exploring the question of what is a clinically effective treatment regimen of Zoledronic acid (ZOL). ZOL is currently the most potent bisphosphonate to date. 351 post menopausal women were involved in the study. It was found that once-yearly dose of 4mg was equally as effective as a dose administered every 3 months over a year. The mechanism by which ZOL suppresses

bone turnover for so long is not fully understood. It is certainly not due to the persistence of the drug in the patient's system as at 1 day only 1% of original dose remains. The balance of the dose must be bound to bone. It was thought that the initial dose wiped out the current generation of BMUs but this would mean that the effect of ZOL would wear off after 3 months and this is not so. It seems that the drug is deposited on the osteoblastic and resting surfaces of bone tissue and remains there for the long term. The deposits could interfere with the future development of BMUs at these surfaces.

The effect of anti-resorptive agents is to perturb the steady state remodelling process by suppressing the birth rate of new BMUs. The change in remodelling balance is to reduce fragility from being due to bone turnover to a longer term fragility due to the accumulation of micro-damage (Seeman 2007) .

Lyles et al. (Lyles *et al.* 2007) addresses the issue of increased mortality after hip fracture. In this study a yearly dose of 5mg was administered to 1065 patients (1062 placebos) within 90 days of hip fracture repair. 8.6% of ZOL group suffered new fractures compared to 13.9% of the placebo group. An annual infusion of ZOL within 90 days post fracture healing is associated with a reduction in the rate of new clinical fractures and improved survival.

Frost (Frost 1997a) considers a number of other factors neglected by other workers in this area such as muscle strength. Muscle strength by 80 years of age can reduce by as much as 60% of a young adult's value. Deteriorating balance could also explain most falls and fractures that occur in elderly people? These could be due to neuro-muscular problems causing an increase in falls in the elderly. Health providers are now providing training to patients who have suffered falls with the aim of teaching them simple techniques to avoid falls in the future. These points can also be considered in the context of the efficacy of osteoporosis treatments. Fracture is often seen as the endpoint of a bisphosphonate study. i.e. a reduction in fractures of the bisphosphonate group when compared to the control group. This may not be the best indicator of treatment success. Drug treatments need to be evaluated using ultrasonic methods to assess bone quality

2.1.5 Mechanobiology

2.1.5.1 Introduction

Mechano-biology can be defined as "The application or analysis of the role of mechanical forces in eliciting a molecular response leading to a change in form and/or function that can be quantified" (Merryman *et al.* 2010). Mechano-biology is uniquely positioned to lead to multiple innovations that will revolutionise medicine and healthcare. It is fast becoming a mature field of study in its own right. This field is an interdisciplinary one and has great potential. It is a fundamental part of the development of engineered organs and tissues and the understanding of the mechanisms of osteoporosis.

The central question in mechano-biology is how weight bearing tissues are produced maintained and adapted by cells as an active response to biophysical stimuli in their environment. It is the idea that form follows function (van der Meulen *et al.* 2002).

Some other questions arise such as: How are mechanical loads transferred to tissues and how can cells sense these loads; How are signals translated into a cascade of biochemical reactions to produce cell expressions or differentiation? The ultimate goal is to predict growth and differentiation in quantitative terms based on a given force exerted on a given tissue matrix.

Possible sensory vehicles include:

- Osteoclasts are attracted to microcracks because of apoptosis of osteocytes and damage to the network of cell processes between osteocytes (Burger *et al.* 1999b; Hazenberg *et al.* 2006; Taylor *et al.* 2007).
- Fluid flow induced shear of bone cells has been observed to produce signalling chemicals responsible for bone remodelling (Jacobs *et al.* 1998; Cowin 2002).

To fully understand how mechanical stimulus produces biological signals for cells to adapt or differentiate we need to understand the signal transduction pathways. The first approach is to carry out experiments. The best approach involves studies where mechanical loads can be applied in a controlled environment *in-vivo*. The changes can be assessed by the use of sophisticated scanning techniques such as ultrasound or microCT.

The second approach is to investigate with computational and theoretical studies, these can provide a framework in which experimental results can be interpreted. One of the first modern analytical theories developed to explain bone remodelling was adaptive elasticity (Cowin *et al.* 1976). These early studies were phenomenological in nature and dealt with changes in density and stiffness. Later models were mechanistic such as the mechano-stat where the strain at the tissue level of bone drove the process of remodelling (Frost 1997b; McNamara *et al.* 2007; Mulvihill *et al.* 2008). A fundamental requirement of these models is that they have to be related to actual measurable parameters determined by experiment or from extrapolation of experimental data (Prendergast 2001).

2.1.5.2 Types of cells found in cortical bone

There are four main types of bone cells found in bone: bone lining cells, osteocytes, osteoblasts and osteclasts. Bone lining cells (BLCs) cover inactive (non-remodelling) bone surfaces such as the periosteum and endosteum of cortical bone (Miller *et al.* 1989). Osteocytes (See Figure 9) are embedded in the lacunae of osteonal bone. Osteoblasts are involved in the laying down of new bone and osteoclasts are involved in the removal of old bone. Approximately 15% of osteoblasts become entrapped in their own matrix and in time become osteocytes.

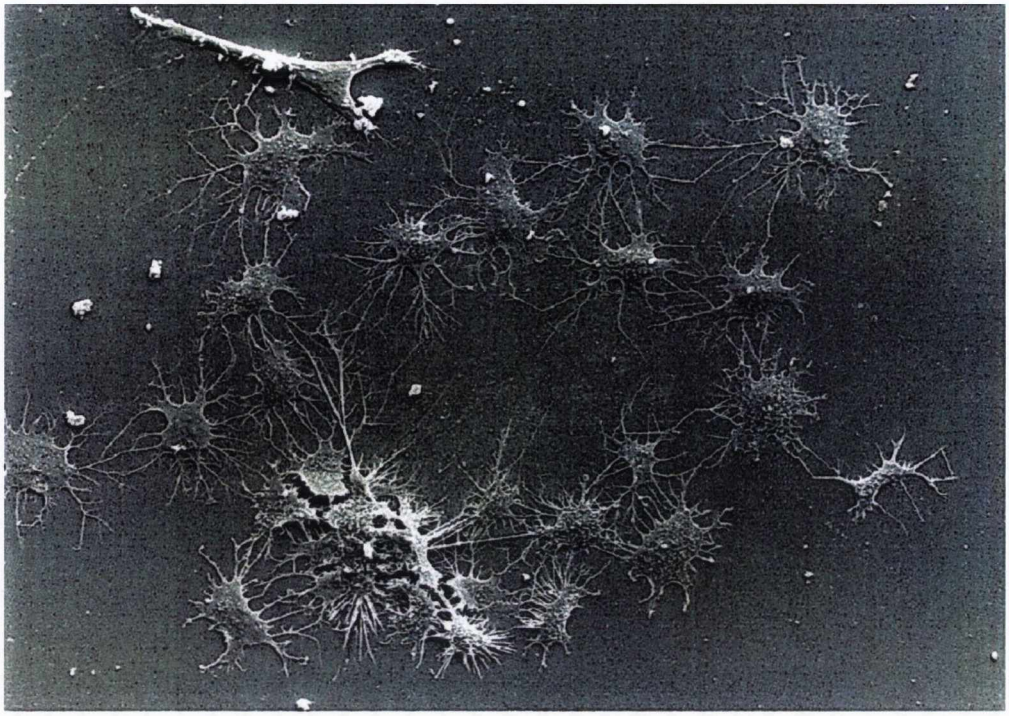


Figure 9. Scanning electron micrograph of a group of osteocytes, isolated from embryonic chicken calvariae, after 3 days of culture as monolayer. The cells have re-established a cellular network by moving away from each other and making thin, branching cell processes that connect with those of neighbouring cells. The cell in the upper left corner is an osteoblast (Burger et al. 1999b).

These osteocytes have a vast 3D network of cell processes (Gap junctions). Osteoclasts are large multi-nucleated cells that resorb bone from an acidic cavity which dissolves underlying bone. These cells work in concert in a structure known as the Basic Multicellular Unit (BMU) (van der Meulen *et al.* 2000).

2.1.5.3 Possible mechano-sensory mechanisms in bone

Cowin et al. (Cowin *et al.* 1991) describe the possible candidates for mechano-sensors in bone to sense mechanical loads. The adaptation response must be studied at two levels; tissue and cellular.

Tissue level strain initiate a response in bone but what are the magnitudes of these strain? Resorption occurs at <0.001 strain and deposition occurs > 0.003 strain. If bone cells are sensors of mechanical strain in bone then they must be extremely sensitive. These strain at the level of the cell are of the order of 10nm to 30nm. However there may be strain concentration locations in bone due to microstructural features such as lacunae etc. These amplify the tissue level strain by a factor of 10. Connected cellular

networks of cell processes are a prime candidate for a communication system by which bone remodelling and modelling signals are transmitted. The mechano-sensory system in bone has not been definitively identified, but several interactive processes by which cells receive a strain signal have been identified. Examples include stretch sensitive membrane receptors on cells and electrical charges produced by streaming potentials (Cowin *et al.* 1991).

2.1.5.4 Osteocytes as a sensing network

Strain of 0.15% in vivo have been observed to initiate recruitment of cells at the bone surface. Cells exposed to direct strain require 1-3% strain in order to obtain a response. Local forces act on cells due to fluid flow and not direct strain. This local force is due to the displacement of liquid in canaliculi (Cowin *et al.* 1991). These generate fluid shear in cell processes of the order of 0.8 to 3 Pa. This is sufficient to activate cells. Another function of fluid flow is to transmit nutrients to cells deep in bone (McGarry *et al.* 2005). This study is a interesting as it allows us to explain the way in which bone cells are more sensitive to flow induced shear strain than direct strain. This involved a computational cell model using FEA to calculate the deformation due to direct strain and shear flow strain.

Osteocytes respond to small fluid shear stresses acting on membranes of osteocytic processes and respond to strain by increasing production of nitric oxide, an inhibitor of osteoclastic resorption. This points towards a normally functioning osteocytic cell network being an inhibitor. When it is switched off or damaged, resorption of bone commences (Basso *et al.* 2002).

The capacity of bone tissue to alter mass and structure in response to mechanical demands is well known but the cellular mechanisms remain poorly understood. Osteocytes are the most plentiful cell found in bone (95%). These cells are ideal candidates for the role of mechano-sensors. The lacuno-canicular porosity structure mediates mechano-sensing. Strain derived flow appears to activate the osteocytes and transport cell signals, molecules, nutrients and waste products. It is conjectured that fatigue micro-damage leads to interference with the integrity of osteocyte and canalicular network by disrupting canaliculi and severing osteocyte processes (Taylor *et al.* 1997; Hazenberg *et al.* 2006). This fatigue damage may cause a situation resembling disuse; as fluid shear is reduced, bone resorption will occur (Burger *et al.* 1999b).

Osteocytes guard the functional integrity of bone by recruiting osteoblasts and osteoclasts as needed. Osteocytes also have hormonal receptors and act as controllers of bone metabolism (Burger *et al.* 1999a). This is a compelling explanation as it connects the damage-fatigue theory to the fluid flow shear theory.

A decline in osteocyte lacunar density in human cortical bone with age was observed and this was associated with accumulation of micro-cracks. This supports the sensory role of osteocyte which reside in lacunae. Bone porosity and micro crack density increased exponentially with the decline in osteocyte lacunar density (Vashishth *et al.* 2000).

As well as fluid flow being present in the porosity of bone during dynamic activities a hydrostatic load is also present. This load is present, for example, if an individual were on their feet all day. The leg bones would be exposed to this hydrostatic pressure. Osteocytes are also capable of responding to hydrostatic pressure in their local mechanical environment (Chen *et al.* 2010). The absence of this loading may explain resorption due to disuse observed in sedentary humans.

The cell transducing mechanism for bone damage detection is based on ruptured osteocyte processes. Relative crack displacements are capable of rupturing cell processes, see Figure 10 . This is a feasible mechanism by which bone can detect and estimate the size of a microcrack. Ruptured cell processes may directly secrete passive and active components in the extracellular matrix triggering a repair response. Fatigue damage in the form of micro-cracks appears to target and signal the initiation of the bone adaptation and repair process. Osteocyte cell process rupture is suggested as a mechanism for damage signalling. If the cell process spans a crack face this will lead to cell death. Osteocytes continuously send out an inhibitory signal which under normal conditions would lead to osteoclasts resorbing that area once it became damaged (Martin 2000b; Hazenberg *et al.* 2006).

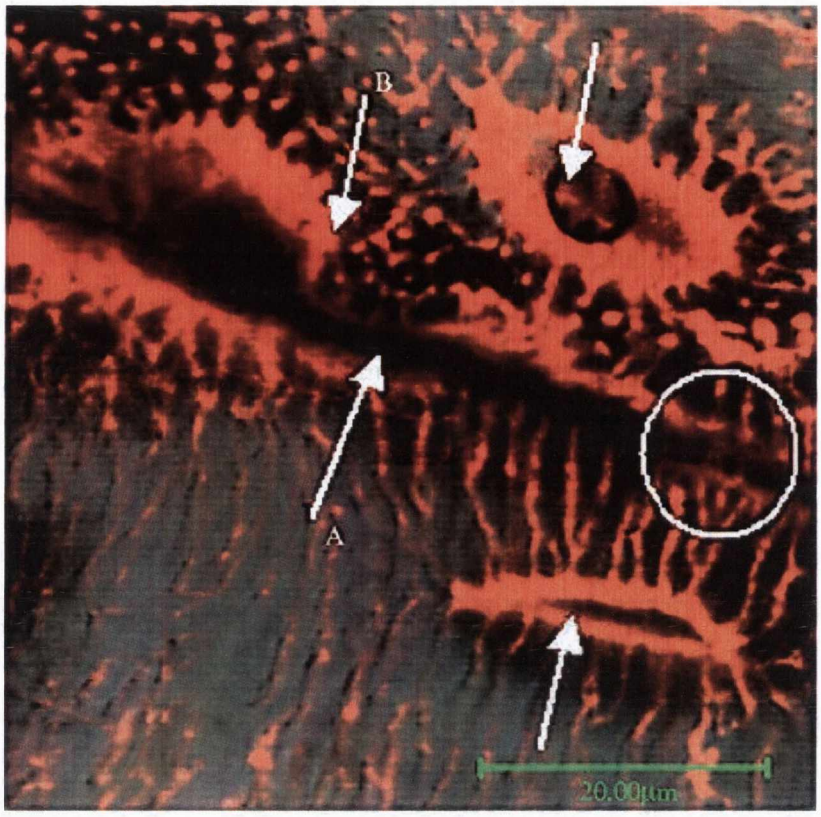


Figure 10 A confocal microscopy image of a crack and three osteocytes (solid arrows). The crack (A) has travelled through the lacuna of one osteocyte (B), which appears to have remained intact. The majority of the cell processes are broken by the crack, but some processes seem to cross the crack faces (circle) (Hazenberg et al. 2006).

BMUs appear to be activated by damage to cell processes. Large cracks tend to rupture several thousand cell processes. In normal bone cracks are normally not that long, rupture of osteocyte processes and subsequent remodelling activation could be why (Hazenberg *et al.* 2007).

Biochemical signalling processes are important in the maintenance of integrity and function in bone. One of the principal mediators of bone cell function and activation of bone remodelling is the RANKL-RANK-OPG cytokine system. In an experiment where a network of osteocytes on a plane surface were exposed to crack like features of varying thickness, it was found that injury to the cells from this source was sufficient to initiate changes in the cytokine concentrations. This experimental situation attempts to mimic the effects of microdamage induced cracks on osteocytes and their processes (Mulcahy *et al.* 2011).

Osteocytes and their network of processes are the most compelling candidates for mechano-sensing in bone. There are two possibilities by which osteocytes initiate the process of bone remodelling; by sensing of fluid flow in the micro-porosities due to strain of the structure of bone and/or by damaging cell processes by microcracks. There is compelling evidence for both. The two mechanisms may operate in concert to regulate remodelling of bone due to mechanical loading.

2.1.5.5 Fatigue properties of compact bone

Taylor et al. developed a phenomenological model of fatigue in bone. This was developed specifically to address fatigue in bone applied to stress fractures. Initiation of adaptation process (signal) is caused by passage of a crack through a barrier. Bone is operating well above its fatigue limit, and it must be continuously repaired. It appears to be relying on crack detection and repair to prevent failure (Taylor *et al.* 1997).

Microcracks were observed to initiate frequently at osteocyte lacunae. These act as stress concentration features in bone and act as a potential mechanism for detection of strain and/or damage by ostecytes in bone (Reilly 2000).

Microdamage contributes to formation of stress fractures and acts as a stimulus for bone remodelling. Results support the concept of a microstructural barrier effect existing in bone. Cracks initiate easily but slow down or stop at barriers such as cement lines. Most cracks are observed in the interstitial matrix between osteons (O'Brien *et al.* 2003).

Bone, when viewed as a composite material, has barriers to the growth of fatigue cracks. These barriers are the osteons themselves. Secondary bone can be compared to a composite material where the micro structure features within the material provide sites for crack initiation but also serve as barriers to crack growth. The cement line is a weak structure. It reduces the shear strength of osteonal bone. But it also slows crack propagation due to a reduction of strain energy. The majority of cracks observed in this study were located in interstitial bone and did not penetrate cement lines surrounding secondary osteons. The microstructural barrier concept governs fatigue behaviour of bone. There may be many cracks in bone but they are small and do not propagate to critical lengths. Failure only occurs when a very few cracks propagate to critical lengths (O'Brien *et al.* 2007).

2.1.5.6 Bone modelling and remodelling

Bone modelling is the process of internal and external modelling of bone surfaces by drift (Frost 1997a). Bone modelling is very active in young children but is not so active in adults. Larger strain are required to activate bone modelling, of the order of 2000 to 3000 microstrain. Bone remodelling is a process of internal remodelling in cortical bone involving BMUs, it is mainly involved with preserving the bone present. Bone remodelling is not capable of adding any extra bone to a cortical cross section.

Bone remodelling in cortical bone is carried out by two specialised groups of cells: osteoclasts which resorb bone by releasing powerful acid and an enzyme and osteoblasts which lay down new bone. These cells combine to make a BMU. This is a cavity about 200 microns in diameter which moves along the length of the bone at 40 microns per day (See Figure 11). The result is a new portion of bone of circular cross section known as an osteon (Taylor *et al.* 2007).

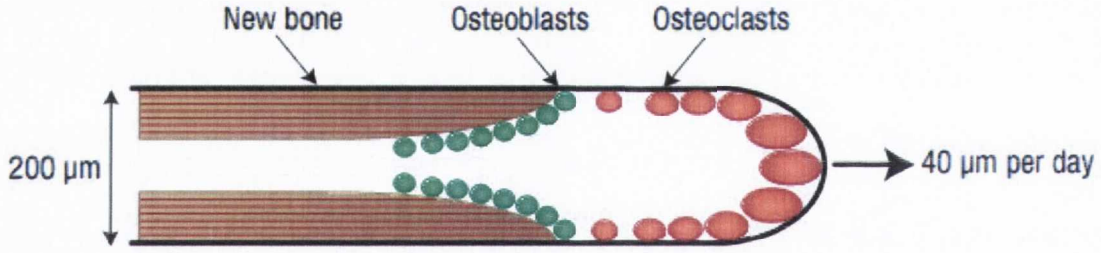


Figure 11 Schematic representation of a Basic Multicellular Unit. This collection of specialised cells removes old bone and lays down new bone (Taylor et al. 2007).

Turner summarised three 'rules' of bone adaptation to mechanical stimuli. These were:

(1) Adaptation and remodelling is driven by dynamic rather than static loads.

(2) Short duration loads are all that is necessary to initiate an adaptive response, the bone response tends to saturate.

(3) Bone cells accommodate to a customary mechanical loading environment making them less sensitive to routine loading signals.

He also goes onto say : "Bone cells begin with a genetic blueprint and sculpt until the skeletal design meets the loading requirements". Bone adaptation requires bone cells to detect mechanical signals *in situ* and integrate those signals into appropriate changes in bone architecture. Loading frequency and strain rate are important determinants of bone adaptation. This process appears to be an error driven process. The error being the difference in S -F where S is the daily loading stimulus and F is the normal loading pattern. When the error tends to zero the remodelling activity tends to zero (Turner 1998).

Martin aims to resolve the inconsistencies between observations and concepts about bone remodelling, specifically that bone remodels when mechanical loading is excessively low and when loading is very high and substantial damage occurs. This theory assumes that bone lining cells are inclined to activate remodelling unless restrained by an inhibitory signal and the mechanically provoked osteocytic signal serves this inhibitory function. However remodelling is elevated at low loads with no inhibitory signal or the signal is interrupted by damage to cell processes due to excessive loading. Otherwise remodelling is relatively low. This leads to the conclusion that one mechanically derived signal is responsible. Estrogen withdrawal can lead to bone cell apoptosis. Increased apoptosis of bone cells is observed in women with estrogen withdrawal. This would reduce the strength of the inhibitory signals generated. This leads to a situation where at every level of loading on the osteocytic network a decreased inhibitory signal is generated and an increased activation of the remodelling process is initiated, in spite of normal mechanical loads. Frost's (Frost 1997a) mechano-stat hypothesis states that lower estrogen levels shift the mechanostat set point upwards at menopause (Martin 2000a).

2.1.5.7 Is bone remodelling targeted?

The turnover rate of bone greatly exceeds that required to maintain mechanical competence. This could obviate the need for targeted remodelling although such a need may exist if turnover is at the low end of a wide-normal range. BMU origination is close to blood vessels. Targeting and directional control are due to osteocytic network. In normal circumstances the actual rate of turnover is much higher than the necessary minimum rate to ensure skeletal health. This provides a wide margin of safety for any therapeutic reduction of bone turnover in order to reduce bone loss. Some remodelling is targeted for the replacement of fatigue microdamaged bone, a substantial amount of

total skeletal remodelling is not needed for that purpose (Parfitt 2002). Many resorption spaces are not spatially associated with microcracks, but this could be due to the fact that BMUs tunnel for some distance through the cortex. Bone resorption spaces originate some distance from where BMUs originate. The traditional view was that remodelling was initiated for reasons of calcium homeostasis (Martin 2002).

Osteocyte apoptosis is spatially and temporally linked to bone fatigue induced micro damage and subsequent intracortical remodelling. Specifically regions undergo apoptosis co-localise exactly with areas subsequently resorbed by osteoclasts. It seems reasonable to conclude that the removal of apoptotic debris is the reason for targeted remodelling of damaged bone (Cardoso *et al.* 2009).

2.1.5.8 Frost's Mechano-Stat Hypothesis a framework for understanding the effect of osteoporosis on cortical bone.

Frost's Mechano-Stat hypothesis provides a framework in which to understand the process of modelling and remodelling of bone, see Figure 12.

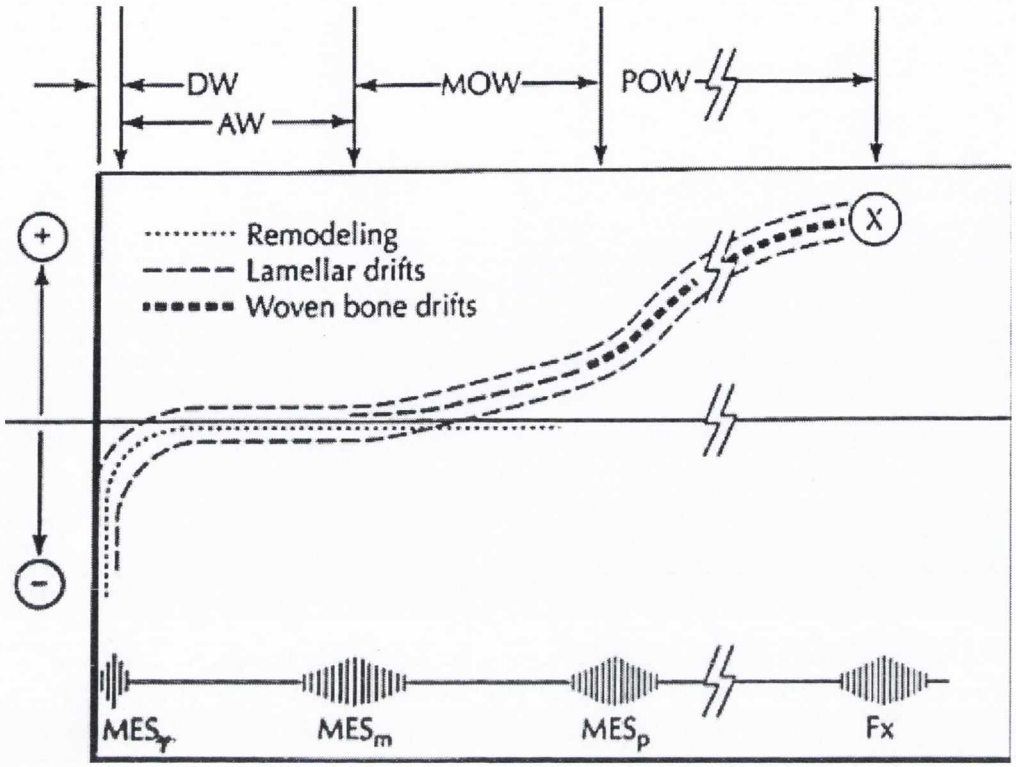


Figure 12 DW, AW, MOW and POW refer to the disuse adaptive, mild overload and pathologic overload windows respectively. MES stands for minimally effective strain, which are the setpoints separating the various windows: MESr is disuse remodelling threshold, MESm is the bone modelling threshold and MESp is the microdamage threshold. Fx is the bone's fracture strength. Note that the setpoints are not given precise values in the Mechanostat to account for individual variability as the setpoints are hypothesised to be genetically determined (Mulvihill et al. 2008) .

External modelling occurs through a process of drift of the inner and outer surfaces of cortical long bones. Bone modelling determines and increases bone mass but seldom reduces it. Modelling is not BMU based. A higher strain environment is required for activation of this process. The modelling threshold is 800 to 4000 microstrain. This threshold seems to be constant but not necessarily identical between individuals. Vigorous exercise in children can increase bone mass and strength but in aging adults this minimizes bone loss and doesn't increase bone mass. The largest mechanical loads on bone are from muscle contractions (Frost 1997a).

BMUs are responsible for bone remodelling. They go through an Activation Resorption Formation (ARF) cycle which takes about 4 months. Bone is turned over in small packets. Bone remodelling can maintain or decrease bone mass and strength but not increase it. Remodelling spaces occupy 4% to 10% of volume in bone. Bone

remodelling is active at greater than 100 microstrain. Disuse is activated at between 50 and 100 microstrain.

Rapidly growing bone is strained in the region of 2000 to 4000 microstrain as that found in children. In adult bone, modelling is less active and the peak strain caused by voluntary effort is between 800 and 1200 microstrain. The modelling threshold is roughly equal to 1000 microstrain.

Bone can have an infinite fatigue life because of action of BMUs. Bone appears to have a microdamage threshold of 3000 microstrain. Less than this and bone has an infinite fatigue life because bone repair can cope.

To confirm this theory it has been proven that weight lifters have larger muscles therefore large bone load therefore larger bone mass and strength. Long distance runners have weaker muscles but extreme endurance therefore microdamage repair is adequate and thin bones suffice (Frost 1997b).

Bone strength depends on both its architecture and amount of bone mass. The largest loads on bone are from the muscles due to an adverse lever ratio and gravity. It takes on average two kilograms of muscle force to move one kilogram of body weight. Therefore this must influence bone mass and strength. Any diseases which affects muscle strength will also affect bone (Frost 1997a).

The Mechano-stat theory of Frost hypothesises that with age or disease set points change such as: Minimum strain below which resorption is triggered. Maximum strain where by desposition occurs. Maintaining bone cell mechano-sensitivity could therefore be a therapeutic target for the prevention of osteoporosis. Changes due to drugs or diseases may lead to sensor cells that are either deaf or over reactive to their mechanical environment. In post menopausal osteoporosis there is a setpoint shift up in mechano-sensitivity. The effect would be similar to disuse and would lead to resorption (Mulvihill *et al.* 2008).

Both mechano-sensitivity changes and a change in elastic modulus of bone would change the remodelling process. Increased stiffness would change bone loss. Current treatments of osteoporosis focus on preventing over active bone resorbing osteoclasts from fully functioning (Mulvihill *et al.* 2010).

There is an integrated function between osteoblast and osteoclast for bone repair and remodelling. Disruption of this coupling between bone resorption and formation leads

to osteoporosis and osteopetrosis. The osteoblast is a relatively rare cell in bone, < 1% of bone surface in young adults. Describing the molecular phenotype of the osteoblast will lead to drug treatments that will switch on or off cell activity at will (Horne 1995).

Osteoporosis appears to attenuate the sensitivity of the osteocyte network to transduce tissue level strain and activate the remodelling process below a strain threshold above than that found in normal bone. The consequences of this set point change may not be apparent straight away on the micro-structure of cortical bone but when coupled with increased remodelling observed in osteoporotic bone due to estrogen withdrawal, could lead to less mineralised bone and overall bone stiffness being reduced. A higher resorption strain threshold equates to stiffer bone structures being resorped and being replaced with bone of lower stiffness. This process is further confounded by the increase in turnover due to osteoporosis.

2.1.6 Conclusion

Cortical bone is a complex hierarchical material. In order to fully understand the links between its structure and mechanical competence it is necessary to study bone at a variety of length scales. Disease processes such as osteoporosis can be understood in terms of the effects on bone structures at different length scale. An example would be within collagen fibril bundles or within the lamellae of osteonal bone. Contrasting the definitions of osteoporosis as given by WHO and NIH one thing is clear that measuring bone quality is a key factor in successfully diagnosing and understanding osteoporosis.

Drug treatments with bisphosphonates offer a way of halting the degradation of the bone matrix due to osteoporosis. One of these drugs is Zoledronic acid. The effect of anti-resorptive agents is to perturb the steady state remodelling process by suppressing the birth rate of new BMUs. The change in remodelling balance is to reduce fragility from being due to bone turnover to a longer term fragility due to the accumulation of micro-damage.

Mechano-biology is the study of the how mechanical forces applied to living tissue leads to a molecular response and subsequent change in its form and function.

In order for changes within the tissues to occur there must be a sensory mechanism. There are two main candidates for this :

Fatigue loading induced microcracks (Burger *et al.*, 1999b, Hazenburg *et al.*, 2006, Taylor *et al.*, 2007)

Fluid flow shear (Cowin *et al.*, 1991, Jacobs *et al.*, 1998)

The principle candidate for this is the osteocyte cell. This is the most common cell found within the bone matrix (Burger *et al.*, 1999). These cells establish branching cell processes that connect them to neighbouring cells thus producing a cellular network which extends throughout the bone to the inner and outer surfaces. This network of cell processes is a prime candidate by which bone modelling and remodelling signals can be transmitted (Cowin *et al.*, 1991).

Osteocytes have been found to be more sensitive to fluid induced shear strain than direct strain (Cowin *et al.*, 1991, McGarry *et al.*, 2005) At appropriate levels of fluid shear osteocytes respond by producing nitric acid. This points towards a normally functioning osteocytic cell network being an inhibitor. When it is switched off or damaged resorption commences. (Basso *et al.*, 2002)

Taylor et al. (1997) developed a phenomenological model of fatigue in bone. Initiation of adaptation process is caused by a crack passing through a barrier such as a cement line in bone. These cracks have been observed to sever osteocyte processes (Hazenberg *et al.*, 2006, 2007)

An experiment where a network of osteocytes on a plane surface were exposed to crack like features was sufficient to initiate changes in the cytokine concentrations. This shows that damage to cell processes due to microcracks is sufficient to initiate changes in key mediators of bone remodelling such as Rank/Rank L and nitric acid. This indicates that the hypothesis that bone remodelling is initiated by damage to cell processes is supported by this experiment. (Mulcahy *et al.*, 2011)

There is compelling evidence for both hypotheses and the mechanisms may operate in concert to regulate remodelling of bone to mechanical loading.

Bone remodelling was initially viewed as untargeted but modern research indicates that there are two mechanisms present, that which regulates calcium homeostasis (untargeted) and targeted remodelling initiated by osteocytic network. (Parfitt *et al.*, 2002, Martin *et al.*, 2002) In general the rate of bone turnover greatly exceeds that required to maintain mechanical competence. But the rate of bone turnover varies

greatly from one individual to the next. Some remodelling is targeted but a substantial amount is not needed for that purpose. (Parfitt *et al.*, 2002)

Thus we can conclude that one mechanically derived signal is responsible for activating remodelling. (Martin *et al,* 2000a)

For small or non-existant loading the inhibitory signal (Nitric acid) is not present thus initiating remodelling. Fluid shear is probably responsible for activating the inhibitory signal at low to medium strains. At high loads the inhibitory signal is also not present thus leading to remodelling. At these high loads the loss of inhibitory signal is due to the osteocyte apoptosis iniated by bone cell processes being severed by cracks. (Hazenberg *et al.* 2006, Cardoso *et al.*, 2009) Frost's mechanostat hypothesis provides a framework in which to understand the processes of bone modelling and remodelling (Frost, 1997a).

2.2 Review of "Bone For Life" study.

2.2.1 Aims of study

"Bone for life" is a multi-disciplinary project involving a number of teams of researchers from Trinity College Dublin, University College Dublin, and the Royal College of Surgeons in Ireland. The main goal is to better understand the pathogensis of osteoporosis. An animal model of post-menopausal osteoporosis can be used to understand disease pathogensesis and also investigate and evaluate new therapies. Sheep are a suitable animal model as the hormone profiles of ewes and women are similar. The most important similarity is in the bone remodelling cycles which are both between two and three months. In 1994 the food and drug administration (FDA) produced draft guidelines on the treatment and prevention of osteoporosis in which sheep were identified and accepted as an animal model (Lee *et al.* 2004).

2.2.2 Description of methods applied

71 sheep were involved in the study. Ovariectomy was performed on 34 animals. Subsequently, the first in a sequence of fluorochrome bone markers were administered to all animals. These bone markers bind to exposed calcium in bone and have been found to be an excellent method of labelling new bone formation.

The animals were divided into two studies (See Table 3). The first study ran for one year and included both control and ovariectomised animals which had recieved the fluorochrome bone markers every three months. The second study ran for two years and contained control ovariectomised and drug treated ovariectomised animals. Fluorochrome bone markers were also administered to this group at regular intervals.

Year 1 Groups	**Year 2 Groups**
Control (n=17)	Control (n=17)
OVX (n=17)	OVX (n=10)
	OVX + 5 times the clinical dose of bisphosphonate (n=10).

Table 3 "Bone for Life" animal group, initial animal numbers (Lee et al. 2004).

2.2.3 Discussion of main findings

The analyses carried out on "Bone for life" specimens included the effects of estrogen depletion and zoledronic acid therapy on cortical bone. The main effects studied were osteocyte apoptosis and microdamage. Ovariectomy (OVX) was performed on 14 skeletally mature female ewes. 10 sheep were maintained as controls (CON). 18 months post-OVX, four OVX animals were randomly selected to receive a supra-clinical dose of the bisphosphonate, Zoledronic acid (ZOL)(25mg). 31 months post OVX all animals were sacrificed. The mid diaphysis of the left meta-carpal of each sheep was used to test for microdamage and apoptotic osteocytes. Following OVX, the percentage of apoptotic osteocytes rose significantly from 0.5% to 15%. ZOL treatment resulted in a significant reduction in the percentage of apoptotic cells from 15 to 3%. There was no significant difference in crack density between CON and OVX. Crack density was significantly higher in the ZOL group than the OVX group but these cracks were much shorter than the control or OVX group. A conclusion of this study is that there is a link between estrogen withdrawl and osteocyte apoptosis. ZOL appears to significantly reduce the apoptosis of bone cells (Brennan *et al.* 2008).

Two groups of bone samples (Ovariectomised & Controls) were subject to tests to evaluate intracortical porosity, mechanical stiffness and yield strength (See Figure 13).

Year 1 bone samples were used, each group contained 19 samples. Intracortical porosity was measured in the cross sections of left metatarsals of each sheep using microCT at a resolution of eigth microns. Mechanical stiffness and yield strength were measured in compression in a tensile testing machine.

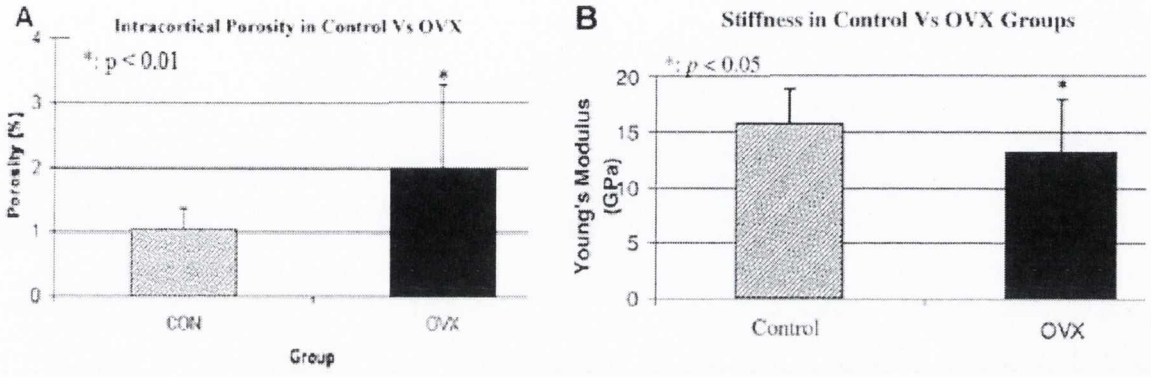


Figure 13 (a)Intracortical porosity as measured by MicroCT at a resolution of 8 microns. (b) Stiffness from compact bone samples as measured by tensile testing (Kennedy et al. 2009).

By the use of fluorochrome dyes administered to sheep at three month intervals it is possible to track which osteons form before and after ovectomy. In the first year samples, bone turnover in OVX samples was increased at 6, 9 and 12 months. Porosity was also increased for OVX versus CON. Ultimate strength and work to fracture did not change. High bone turnover can increase remodelling spaces, accelerate bone loss, increase stress concentrations and increase porosity. Bone quality is made up of a number of factors including: bone turnover, micro architecture, mineralisation, microdamage and collagen content. Increased turnover can reduces the material's local stiffness and an increased number resorption cavities creates stress concentrations which can initiate microdamage. In the OVX group when compared to controls, the stiffness and yield strength was reduced due to porosity (Kennedy *et al.* 2009) .

Beams of metatarsal cortical bone (2x2x36mm) were fatigue tested in a material testing machine. 19 samples of each type were tested, ovariectomised (OVX) and control (CON). High bone turnover resulted in reduced stiffness in the OVX group as measured at a macro scale.

Lower mineralisation can lead to higher localised strain within the osteon causing newer osteons to behave more like pores in matrix rather than functional load bearing volumes

of material. The OVX group has a lower elastic modulus and would be expected to have a shorter fatigue life but this is not the case. OVX could decrease the lifespan of an osteon because it is more likely to be resorbed away before reaching a state of complete mineralisation. Reduced mineralised osteons had the ability to impede the growth of relatively long cracks. The material's integrity has been jeopardised as evidenced by its reduced elastic modulus and slight increase in the number of fatigue cracks initiated. This has been compensated for by the toughening effect of the new osteons. It is observed in engineering composite materials that fatigue resistance can be increased by voids and weak inclusions. This is a difficult balancing act. If there are too many voids and weak inclusions the negative effects will dominate. In contrast, anti-resorptive agents cause a reduction in the number of remodelling events which can allow a more complete secondary mineralisation.

To conclude early indicators of osteoporosis may be observed a considerable time before mechanical integrity declines (Kennedy *et al.* 2008). The ovariectomised cortical bone samples from the "Bone for Life" study show the characteristics found in osteoporotic bone such as increased turnover, increased porosity and osteocyte cell apoptosis due to estrogen withdrawal.

2.3 Basic Ultrasonic principles applied to cortical bone

Introduction

Sound waves are mechanical oscillations in both space and time (Kuttruff 1991).

The equation shown below is a 1 dimensional wave equation in a fluid.

$$\frac{\partial^2 p}{\partial x^2} = \frac{1}{c^2}\frac{\partial^2 p}{\partial t^2} \qquad \textit{Equation 2-11}$$

Pressure $\boldsymbol{p}$ is a function of position and time.

$p(x,t)=F(x-ct)+G(x+ct)$ *Equation 2-12*

F and G are arbitrary functions. These could be harmonic functions such as sine and cosine. The ratio of sound pressure to particle velocity in plane wave is called the characteristic impedance.

$$\frac{p}{v_x} = \rho_0 c = Z_0 \quad \textit{Equation 2-13}$$

For a harmonic wave $\boldsymbol{p(x,t)} = \hat{p}\sin(\omega t - kr)$

$\boldsymbol{k}$= wave number

$$\boldsymbol{\omega = kc = 2\pi f} \quad \textit{Equation 2-14}$$

$\boldsymbol{p}$= sound pressure.

For a spherical wave:

$$p(r,t) = \frac{-\rho_0 \omega \hat{Q}}{4\pi r}\sin(\omega t - kr) \quad \textit{Equation 2-15}$$

Where $\hat{Q}$ = volume velocity

$\boldsymbol{\rho_0}$= static values of density

Sound propagation in solids is substantially more complex than that in fluids. This is due to the fact that a solid body tries to maintain not only volume but shape. This results in an increased variety of possible wave types in the unbounded and even more so in the bounded solid body. In solids, there are both longitudinal and transverse waves. Added complexity is observed in anisotropic solids where elastic constants as well as many other physical properties depend on direction or orientation.

For an isotropic homogenous solid there are three simultaneous partial differential equations that can be derived. These are then substituted into the wave equation above.

In Cartesian coordinates:

$$\mu\Delta\xi + (\mu+\lambda)\frac{\partial\theta}{\partial x} = \rho_0\frac{\partial^2\xi}{\partial t^2}$$
$$\mu\Delta\eta + (\mu+\lambda)\frac{\partial\theta}{\partial y} = \rho_0\frac{\partial^2\eta}{\partial t^2} \qquad \textit{Equation 2-16}$$
$$\mu\Delta\zeta + (\mu+\lambda)\frac{\partial\theta}{\partial z} = \rho_0\frac{\partial^2\zeta}{\partial t^2}$$

Here ξ, η and ζ are the components of the displacement vectors and θ is an abbreviation for the expression:

$$\theta = \frac{d\xi}{dx} + \frac{\partial\eta}{dy} + \frac{\partial\varsigma}{dz} \qquad \textit{Equation 2-17}$$

Δ denotes the Laplace operator. μ and λ are elastic constants known as Lamé constants. Assuming plane waves in the x direction, it is possible to remove the partial derivatives with respect to y and z. The resulting wave equations for the three displacement components read as follows:

$$(2\mu+\lambda)\frac{\partial^2\xi}{\partial x^2} = \rho_0\frac{\partial^2\xi}{\partial t^2}$$
$$\mu\frac{\partial\eta}{\partial y} = \rho_0\frac{\partial^2\eta}{\partial t^2} \qquad \textit{Equation 2-18}$$
$$\mu\frac{\partial\zeta}{\partial z} = \rho_0\frac{\partial^2\zeta}{\partial t^2}$$

The first of the above equations describes the longitudinal wave. The longitudinal velocity can be described as:

$$c_L = \sqrt{\frac{2\mu+\lambda}{\rho_0}} \qquad \textit{Equation 2-19}$$

The shear wave velocity can be described as:

$$c_T = \sqrt{\frac{\mu}{\rho_0}} \qquad \textit{Equation 2-20}$$

This is the velocity of the wave perpendicular to the longitudinal wave.

The shear wave velocity is always smaller than longitudinal wave.

The Lamé constants can be related to physical quantities such as Young's Modulus (***E***) and Poisson's Ratio (***v***) as below:

$$\mu = \frac{1}{2}\frac{E}{1+v} \qquad \textit{Equation 2-21}$$

$$\lambda = \frac{E}{(1+v)(1-2v)} \qquad \textit{Equation 2-22}$$

The ratio of the velocities in both the longitudinal and transverse directions can be used to write the following relation:

$$\frac{c_L}{c_T} = \sqrt{\frac{2((1-v)}{1-2v}} \qquad \textit{Equation 2-23}$$

This depends only on the Poisson's ratio, where it is in the range of 0 to 0.5.

A form of surface wave called a Rayleigh wave, which is a summation of the longitudinal and transverse components, occurs at a material interface. This is very important in the characterisation of material properties using ultrasound.

A further discussion of ultrasound theory applied to transducers can be found in Appendix 7.6.

2.3.1 Reflection and refraction

When a wave hits a boundary some of it will be reflected and the rest of it will be refracted (Kuttruff 1991). When ultrasound strikes a cortical bone interface at normal incidence, approximately 25-50% of energy of the incident beam will be transferred to reflected wave and 75% -50% to the refracted longitudinal wave. This occurs between the boundaries of two different media with different characteristic impedances (Laugier 1999). See Figure 14.

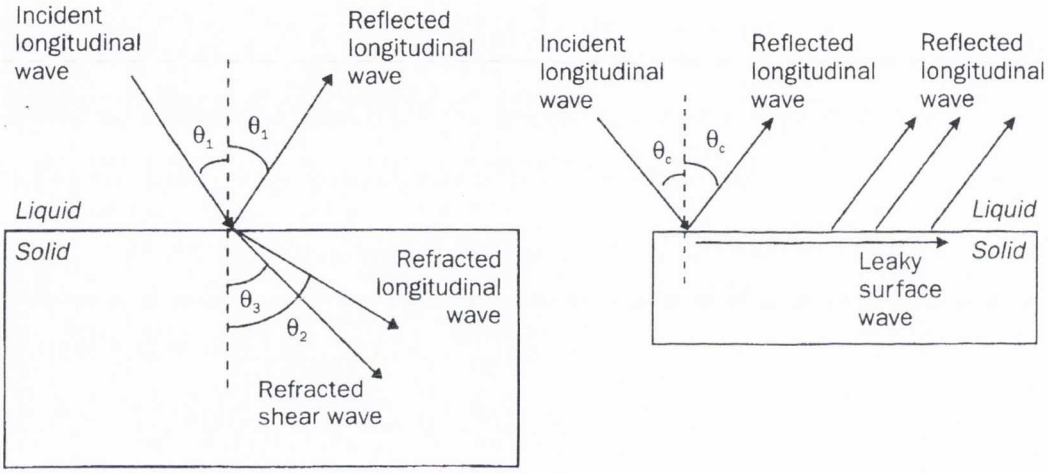


Figure 14 Diagram of types of refraction and reflection perpendicular, oblique and oblique beyond critical angle present at liquid solid interface (Laugier 1999).

For oblique incidence the longitudinal wave is partially converted into a shear wave in a solid therefore this gives rise to two refracted beams. At higher angles of incidence the longitudinal wave is no longer transmitted into the solid (total internal reflection). Instead an evanescent wave occurs which travels parallel to interface between solid and liquid. Measurement of the 1st critical angle can be used to characterise bone material. It is possible to use Snell's law to work out the velocity of sound in the bone material. This method is known as Ultrasonic critical reflectomy.

$$\frac{\sin\theta_1}{c_1} = \frac{\sin\theta_2}{c_2} = \frac{\sin\theta_3}{c_3} \qquad \textit{Equation 2-24}$$

There can be several critical angles depending on the complexity of the material. Also the surface waves excited in a solid continuously radiate energy into the fluid in the form of a longitudinal wave re-emitted at the angle θ_c . This wave is known as a leaky surface skimming compression wave (LSSC waves). This can be used to study the elasticity of cortical bone *in-vivo* and *in-vitro* (Briggs 1992; Laugier 1999).

2.3.2 Dispersion

A medium is said to be dispersive if the velocity of sound in the material is dependent on the frequency of the sound signal. This effect is non-linear. An example of this would be where a sinusoidal wave is propagated into a medium, after travelling through the medium the original sinusoidal wave increasingly steepens in the course of propagation. Sound phases with high instantaneous pressure travel faster than those of low instantaneous pressure (Kuttruff 1991). An example of this effect in bone is at 5 MHz. The axial sound velocity is 4290 m/s, at 100 MHz this velocity is 4410m/s (Lees 1992). This effect is not so substantial at lower frequencies between 1 and 16 MHz. Air infiltration into the sample will greatly change this value, therefore great care has to be taken to ensure samples are wetted through (Lakes *et al.* 1986).

2.3.3 Kramers-Kronig Relations.

Attenuation and dispersion are manifestations of the same underlying process dissipating the energy of the wave. K-K relations can be used to describe this inter-relationship. For example if one is known as a function of frequency then the other may be determined. An example of this would be an increase of phase velocity with frequency. This implies an increase in the attenuation with frequency.

This technique can be used to calculate ultrasonic properties of a material which is hard to measure. It can be difficult to measure dispersion in a soft tissue but this can be estimated from an easier to measure parameter such as attenuation. This relationship is independent of the specific mechanism responsible for attenuation (O'Donnell *et al.* 1981).

2.3.4 Attenuation and absorption

As a wave propagates some the energy lost is referred to as attenuation. A comprehensive model of the wave propagation in bone has not yet been developed. There are many mechanisms of attenuation in bone which include: absorption, refraction scattering and mode conversion (Njeh 1999a). Sound wave propagation in a

medium is mainly determined by the inertial restoring and loss parameters of the medium. In practice, parameters such as bulk variations of speed, impedance, absorption and scattering are some of the mechanisms responsible for attenuation (Bamber 1986).

The plane wave intensity can be described as:

$$I_X = I_0 e^{-\mu(f)x} \qquad \textit{Equation 2-25}$$

Where:

I_X intensity at x distance from source.

I_0 Initial intensity of wave

μ attenuation of intensity $dBcm^{-1}$

The plane wave pressure can be described as:

$$Q_X = Q_0 e^{-\alpha(f)x} \qquad \textit{Equation 2-26}$$

Where:

Q_X : intensity at x distance from source.

Q_0 :Initial intensity of wave

α : attenuation of pressure $dBcm^{-1}$

To relate α to μ the following relation can be used (Njeh 1999a) :

$$\mu(f) = 2\alpha(f) \qquad \textit{Equation 2-27}$$

Often the attenuation is broken up into two elements α_s and α_a which are amplitude scattering coefficient in the absence of attenuation and amplitude attenuation coefficient

in the absence of scattering respectively. This could be carried out by using a phantom with very little scattering and comparing it to the sample to be measured (Bamber 1986).

$$\alpha = \alpha_s + \alpha_a \qquad \textit{Equation 2-28}$$

Absorption is the result of wave energy being degraded to heat. This can be due to density fluctuations where out of phase waves attenuating the propagation of the waves through the medium. In homogenous media this is due to relaxation mechanisms (Bamber 1986).

In cortical bone there is a strong non-linear increase of attenuation with frequency (Lakes *et al.* 1986). This behaviour reflects increased scattering interactions with structural elements in bone as wavelength decreases towards typical dimensions of those elements (Njeh 1999a).

2.3.4.1 Broadband Ultrasonic Attenuation

The definition of Broadband Ultrasonic Attenuation is the measure of attenuation at 0.2 and 0.6 MHz and finding the slope between these points. The units are: attenuation per MHz. BUA has been found as good determinant of bone quality and has been used in commercial devices for the assessment of osteoporosis in bone in vivo. See Figure 15.

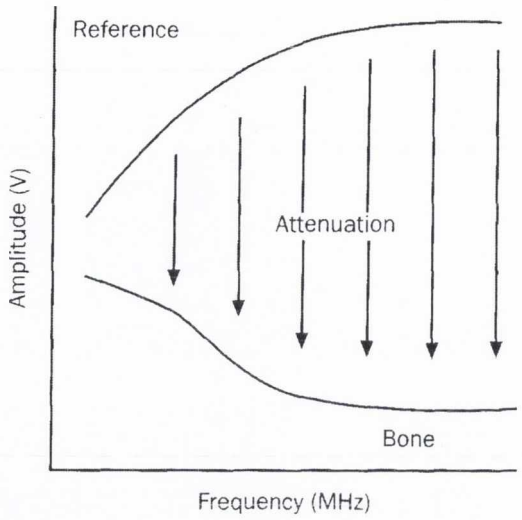


Figure 15 BUA can be found by using a phantom with a known attenuation mechanism an comparing it to an unknown such as a piece of bone (Njeh 1999a).

2.3.4.2 Attenuation in cortical bone:

Attenuation mechanisms in bone may be considered in relation to its micro-structure. However definitive identification of the mechanisms is rendered difficult by the complexity of its microstructure. Bone may be regarded as a composite with particulate porous and fibrous structural elements at different length scales. The nature and typical size of these structural elements are shown in the table below:

Structural feature	Role in Composite structure	Size μm	Frequency (MHz) for size=λ/2
Osteons (human)	Fibre		
Laminae(bovine)	Lamina	250	8
Haversian Canals	Pore or Fluid Channel	50-150	40-120
Osteocyte Lacunae	Pore	10-25	80-200
Lamella	Lamina	5	400
Collagen Fibre	Fibre	1-2	2000-1000
Apatite Crystal	Particulate inclusion	0.005-0.05	$400x10^3$-$40x10^3$

Table 4 Ultrasonic frequency required to image various constituent parts of cortical bone. Adapted from (Lakes et al. 1986).

Scattering of waves from in-homogeneities has been identified as an attenuation mechanism in various synthetic composites. In composites with a regular structure, a sharp maximum in the attenuation is expected when the ultrasonic wavelength equals twice the size of the unit cell in the propagation direction. A cut-off frequency is observed at which the wave-speed drops to zero. In composites with a random micro-structure this effect is not observed.

No evidence is found of this cut-off in bone due to the a-periodic microstructure of bone. An additional wave attenuation mechanism may be encountered in materials with interconnected fluid filled channels. Biot (Biot 1956) postulated a theory which explained the propagation of ultrasound in a porous medium. This type of attenuation is dependent on the geometry and the volume fraction of the pores. The pores present in cortical bone are more complex than the Biot theory envisages (Lakes *et al.* 1986).

2.3.5 Tissue penetration

Within practical limits of signal to noise ratio effective penetration of US in tissues is 100 wave lengths (Soft tissue). The table below provides some examples of the penetration of ultrasound into various tissues. As the depth of penetration is dependent on the frequency of the ultrasound, the units $dBcm^{-1}$ MHz^{-1} are used. Most ultrasonic systems have a maximum signal to noise level of 60dB. Therefore this limits the depth to which signals can be returned to the ultrasonic lens. Generally the higher the frequency the greater the attenuation and lower the depth of penetration (Bamber 1986).

	US Vel. c, m/s	**Z Impedance $Ns^{-1}m^{-3}$**	**Attenuation $dBcm^{-1}$ MHz^{-1}**
Water	1480	1.48e6	0.002
Air	340	440	
Cancellous Bone	1450-1800		10-40
Cortical Bone	3000-4000	4e6-8e6	5
Fat	1460	1.38e6	0.8
Liver	1560	1.65e6	0.6-0.9
Muscle	1550-1630	1.65-1.74e6	0.5-1.5

Table 5 Attenuations for various biological materials (Laugier 1999).

The maximum depth of penetration of ultrasound beam is set by tissue attenuation. Normally attenuation of -60dB is considered to be the maximum which the an ultrasonic imaging system can deal with. This equation is an approximation of that maximum attenuation.

$$\textit{Max attenuation} = -1.4 f D_{max}; \qquad \textit{Equation 2-29}$$

$$D_{max} = -60 / -1.4 f\,(cm) = 43 / f\ cm \qquad \textit{Equation 2-30}$$

Typical values at the frequencies dealt with in this report are:

Frequency (MHz)	Maximum Depth (-60dB) (mm)
150	2.2
200	2.8

Table 6 Typical depth achievable at various frequencies for cortical bone

2.3.6 Scattering

When a wave of a particular wavelength interacts with a solid medium, some of the wave undergoes scattering. This is another loss mechanism associated with attenuation. Scattering is dependent on the internal structure of the medium.

At low ultrasonic frequencies, less than 5 MHz, bone appears as a homogenous material. For example at 1 MHz, the wavelength is 4mm. The minimum size of feature an ultrasonic wave will "see" is half a wavelength or 2mm. An osteon is about 250μm. Therefore these structures will not be visible by the ultrasonic signal (Nicholson 1999).

Scattering can be classified as a function of the relationship between the size of the feature or scattering cross section (a) and the wave number (k). The wave-number k is the inverse of the wave length of the ultrasonic wave.

Scattering where $a<<k$ is called Rayleigh scattering. The intensity of the scattered wave is proportional to the 4^{th} power of the frequency transmitted wave. The intensity of the transmitted wave after scattering is proportional to the 6^{th} power of size of the scatters (a) (Dickinson 1986); (Feynman 2006)

The case where $a \approx k$ is difficult to solve and especially so in a material which is inhomogeneous and anisotropic (Morse P. M. 1987). One possible solution to this is a numerical solution to the scattering problem (Moilanen 2007). In this study the propagation of the sound wave through a microCT model of a long bone was used. This allowed experimental ultrasound test to be compared to a computer model. Scattering due to factors such as porosity could be modelled well with this method but only at low frequencies, 250kHz to 1 MHz. At higher frequencies the computational overhead becomes enormous.

To summarise if the object or scattering cross section is small compared to wavelength the sound shadow will be small. If the object is large compared to the wave-number then there will be shadow behind and brightening at front of the object.

Cortical bone is a multiscale material. At different ultrasonic frequencies different parts of the material respond in different ways. Collagen is often suggested as a major contribution to scattering (Dickinson 1986).

Biot (Biot 1956) proposed a phenomenological model of wave propagation in fluid saturated porous media. It assumes macroscopically isotropic and homogenous materials. It predicts two compressive waves and one shear wave (Williams 1992). When this is applied to cortical bone a slow wave is indeed observed (Lakes 1983). Biot theory provides an insight into the propagation of a sound wave in a porous media. In order to understand fully how ultrasound interacts with bone Biot theory must be included in any method which seeks to image bone in three dimensions. Biot theory is particularly relevant to the propagation of ultrasound in cancellous bone where scattering is the primary mode of attenuation.

2.3.7 Speed of sound.

There are two main definitions of the sound velocity in a material. The first is known as the phase velocity. This is the velocity measured in the material from a continuous wave such as a sinusoid. Where a pulsed signal is used, which is composed of a group of sinusoids packed into a short space of time, the velocity of the sound in a material is known as the group velocity. In the case of water the group and phase velocity are the same. Where the group and phase velocity diverge, in say bone, it is indicative of a dispersive medium (Bamber 1986; Kuttruff 1991). Physical properties of the material dictate the velocity of sound in the material, namely density and compressibility. In bone there are many parameters which affect the velocity of sound these are: water content, mineral content, orientation of the sample and porosity (Lees *et al.* 1983).

Acoustic velocity in osteoporotic bone, from the human iliac crest, was found to be 6.2% lower than that in age matched normal bone but 3.4% higher than that of bone from premenopausal women. This implies that osteoporosis involves altered tissue elasticity. The lowest values were measured in premenopausal normal subjects. It was concluded because of premenopausal normal bone having a lower velocity than

osteoporotic bone, that elastic material properties of bone are not as important a factor as bone mass (Hasegawa *et al.* 1995).

Good correlation was observed between longitudinal velocity and elastic constant and its density. Velocity is also more sensitive to bone fragility from diseases such as osteoporosis, than either BUA or attenuation. This study was carried out at frequencies between 0.2 to 0.8 MHz, which implies a relatively low resolution (Evans *et al.* 1990; Tavakoli *et al.* 1991).

There does not seem to be a consensus in the literature about what causes these changes in acoustic velocity between osteoporotic cortical bone and normal cortical bone. However acoustic velocity appears to be sensitive to changes in bone microstructure due to bone disease.

2.3.8 Assessment of mechanical and physical properties

Quantitative Ultrasound, in principle, should allow advanced assessment of bone strength since ultrasound propagation characteristics are principally determined by mechanical properties (Bossy 2007). In order to evaluate the mechanical properties, both density and Young's modulus, of a sample C-scanned by SAM at a location, it is necessary to know the speed of sound and impedance at every point. When a sound wave is directed on to a large interface, the reflected portion contains information about the material's mechanical properties (Raum *et al.* 2006b). A SAM resolution of at least 20 microns is required for reliable parameter estimation in cortical bone.

Acoustic reflectance can be related to impedance by:

$$R=(Z_1 - Z_2)/(Z_1+Z_2) \quad \textit{Equation 2-31}$$

Where Z_1 is the coupling media and the Z_2 is the impedance of the medium of interest.

Acoustic impedance is the product of density and acoustic velocity in the material:

$$Z=\rho v \quad \textit{Equation 2-32}$$

Therefore there exists a direct proportionality between acoustic impedance and the mechanical properties of the material.

The stiffness coefficient can be related to velocity by:

$$C_{ij}=\rho v_{ij}^2 \qquad \textit{Equation 2-33}$$

$$C_{ij}=Z^2\rho^{-1} \qquad \textit{Equation 2-34}$$

An empirical relation can be derived from experiment and is used to relate acoustic properties Z to mechanical properties C_{ij}. The experiment involves measuring both the sonic velocity and impedance at the same points this procedure is repeated at many points in the sample Equation 2-34 and Equation 2-32 can be used to find C_{ij} directly from these two independent measures.

In a paper by Shieh et al., (Shieh *et al.* 1995) SAM was used as a way of investigating the remodelling of bone around a defect in a sheep metatarsal. The specimens were scanned using a 50 MHz piezoelectric transducer. This gave a lateral resolution of 75 μm. Cross-sectional pieces of the cortical bone specimens were prepared and imaged on their surface. A map of acoustic reflectance was built up over the surface of the sample. A method was also developed to relate the acoustic reflectance (***R***) parameter to mechanical stiffness $\boldsymbol{C_{33}}$. This was performed by using a 2nd order polynomial empirical curve to relate $\boldsymbol{C_{33}}$ to ***R***. This curve was generated from experimental data and statistically processed to create a best fit polynomial (Meunier 1991).

Figure 16 shows a comparison of two methods for assessing the stiffness coefficient C_{33}. Shieh et al., (Shieh *et al.* 1995) used the curve above which was imaged at 30 MHz for ovine bone. Raum et al., (Raum *et al.* 2006a) used an ultrasonic frequency of 200 MHz with human cortical bone. A difference is observed in the relationship between acoustic reflectance R and C_{33} at different frequencies. This is of course due to the multi-scale nature of bone and differences between ovine bone and human bone.

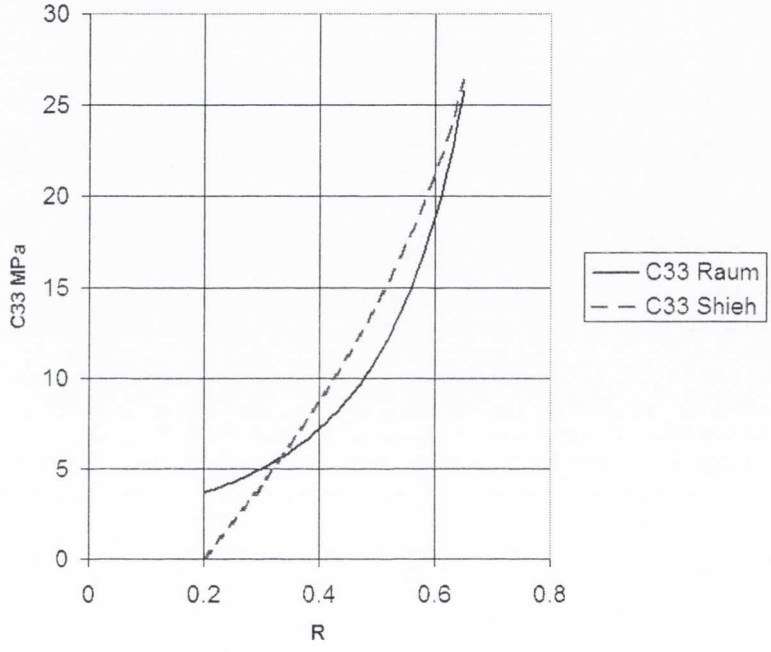


Figure 16 Comparison of empirical equations for relating Acoustic Reflectance R and Elastic Stiffness C_{33} (Shieh et al. 1995; Raum et al. 2006a).

It is possible to recover the stiffness coefficients C_{ii} from the independent estimation of mass density (by the Archimedes Principle or independent measurement of the Velocity of sound.) and the acoustic impedance Z_i. To obtain other elastic coefficients (i.e. in other directions) it is necessary to know additional parameters. For example, cortical bone tissue in the peripheral skeleton is usually assumed to have transverse isotropic material properties with equal Young's moduli in the radial plane (1 and 2 axes) and a higher Young's modulus in the longitudinal direction (3 axis), that is, $E_1 = E_2 < E_3$. With this assumption the Young's modulus in the x_3-direction is shown by:

$$E_3 = \frac{(1+\nu_{12})(1-\nu_{12}-2\nu_{13}\nu_{31})}{1-\nu_{12}^2} \cdot c_{33} \qquad \textit{Equation 2-35}$$

Where ν_{12} is the Poisson's ratio in the cross-sectional plane (x_1x_2–plane) and $\boldsymbol{\nu_{13}} = \boldsymbol{\nu_{23}}$ and $\boldsymbol{\nu_{31}} = \boldsymbol{\nu_{32}}$ are the Poisson ratios in the longitudinal section (i.e., x_1x_3- and x_1x_2-) planes. Determining the Poisson ratios requires further independent measurements. However, at these length scales tissue level quantities have not yet been ascertained. Therefore, an isotropic Poisson ratio $\boldsymbol{\nu_{iso}} = 0.3$ is usually assumed for the derivation of the Young's modulus in bone.

With this assumption the above equation becomes

$$E_3 = 0.7429C_{33}. \qquad \textit{Equation 2-36}$$

It has also been demonstrated that reliable estimates of C_{33} in cortical bone can be derived from acoustic impedance Z_3 alone (Raum 2008). This is justified by examining the figure above, Acoustic impedance Z verses C_{33} is plotted for a wide variety of materials, from plastics to metals. It can be seen that Z is generally a better predictor of the elastic properties of a material than the mass density.

The elastic stiffness coefficient is highly correlated with acoustic impedance for homogeneous materials (See Figure 17). The validity of this assumption for deriving the elastic stiffness coefficient from acoustic impedance in bone has to be verified at each hierarchical level of organisation. At frequencies up to 2 GHz, none of the basic constituents of bone (mineral, collagen, and water) or the individual mineralised collagen fibrils can be resolved.

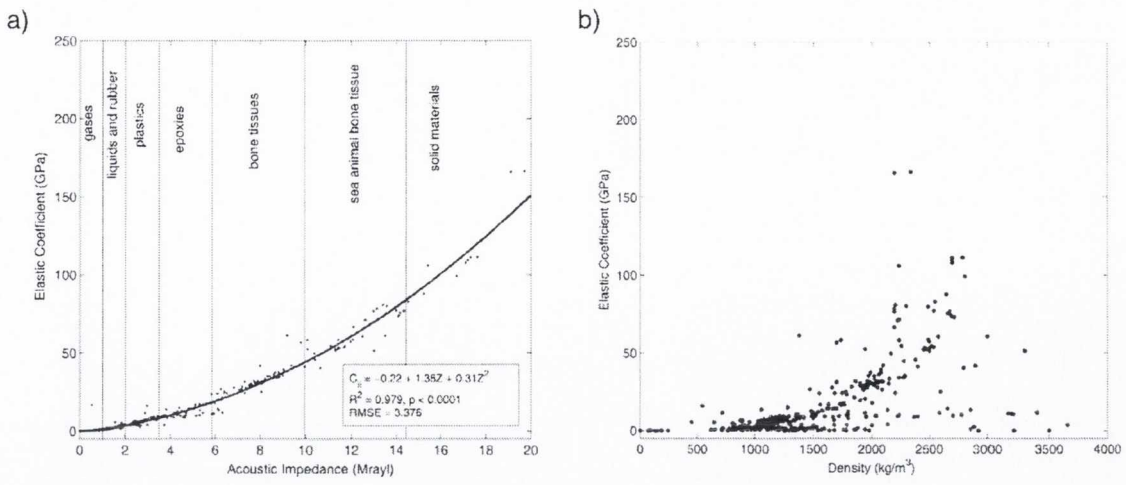


Figure 17 Relationship between acoustic impedance, mass density, and elastic stiffness for different materials (Raum 2008).

At frequencies between 50 MHz and 200 MHz, the acoustic wavelength is much larger than the individual layers of a lamellar unit. This lamellar unit can be considered to be periodic over a certain distance within the osteon. The effective compound material properties "are seen" by the wave. The tissue matrix properties are affected by the layer arrangement and by the material properties of the fibrils. Features such as osteocyte lacunae, canaliculi, and microcracks, contribute to the effective compound properties (Raum 2008).

2.3.9 Conclusion

Ultrasound by its nature is a mechanical wave. Therefore properties of that wave are effected by the medium it travels through. Sound propagation in solids is complex and is influenced by the material's degree of anisotropy. In an isotropic material there are both longitudinal and transverse waves. In an anisotropic solid greater complexity is observed where elastic constants as well as other physical properties depend on either direction or orientation. These complex interactions between the ultrasound wave and the solid can be used to characterise biological materials in a non-destructive manner at high resolutions.

There are a variety of phenomena observed in how ultrasound waves interact with bone. These include reflection and refraction, dispersion, attenuation and absorption, scattering and speed of sound. Each of these phenomena has an important role in characterising cortical bone and assessing bone quality. For the research presented in

this thesis the phenomena of reflection and refraction are used in the imaging of the bone samples. When ultrasound strikes a cortical bone interface at normal incidence, approximately 25-50% of energy of the incident beam will be transferred to reflected wave and 75% -50% to the refracted longitudinal wave. This occurs between the boundaries of two different media with different characteristic impedances. If one of the impedances is known (i.e. the coupling media, water) then the impedance of the solid at that location can be found.

When a sound wave is directed on to a large interface, the reflected portion contains information about the material's mechanical properties (Raum et al. 2006b). A SAM resolution of at least 20 microns is required for reliable parameter estimation in cortical bone. This is due to the larger porosities in bone, such as Haversian canals, effecting the accurate impedance estimation. In order to evaluate the mechanical properties, both density and Young's modulus, of a sample C-scanned by SAM at a location, it is necessary to know the speed of sound and impedance at every point. An empirical relation can be derived from experiment and is used to relate acoustic properties Z to mechanical properties Cij. The experiment involves measuring both the sonic velocity and impedance at the same points this procedure is repeated at many points. The empirical relationship generated from this experiment has to be at the same resolution as the imaging of the bone samples. This is of course due to the multi-scale nature of bone. In the research presented in this thesis an empirical relationship developed by Raum et al. (2006a) was used. This was developed from human cortical bone at an ultrasonic frequency of 200MHz. It has also been demonstrated that reliable estimates of C_{33} in cortical bone can be derived from acoustic impedance Z_3 alone (Raum 2008). This finding is crucial to the research presented here as acoustic impedance is the sole parameter being measured by SAM.

The elastic stiffness coefficient is highly correlated with acoustic impedance for homogeneous materials. The validity of this assumption for deriving the elastic stiffness coefficient from acoustic impedance in bone has to be verified at each hierarchical level of organisation. None of the basic constituents of bone (mineral, collagen, and water) or the individual mineralised collagen fibrils can be resolved at ultrasonic frequencies up to 2GHz. At frequencies between 50 MHz and 200 MHz, the acoustic wavelength is much larger than the individual layers of a lamellar unit. The effective features such as osteocyte lacunae, canaliculi, and microcracks, contribute to the effective compound

properties (Raum 2008). In essence the compound material properties "are seen" by the wave averaged over the resolution of the acoustic lens. In the case of the research presented in this thesis the resolution is 20μm. The power of acoustic methods of investigation of bone is the ability to estimate mechanical parameters at a wide range of length scales. This ability can be adjusted by the choice of ultrasonic lens and frequency used.

2.4 Scanning Acoustic Microscopy

Acoustic microscopy is akin to optical microscopy. In the case of ultrasound the contrast can be related to the mechanical properties of the material being imaged. See Figure 18. Acoustic impedance is a product of density and velocity of ultrasound in material. To optimise imaging a coupling agent is used (water).

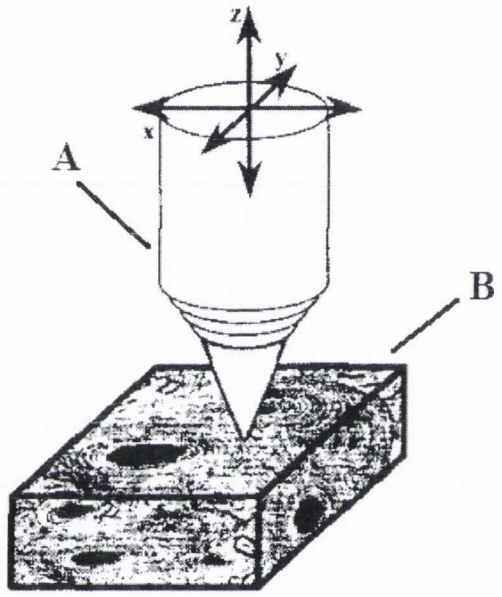


Figure 18 Scanning acoustic microscope. The acoustic lens (A) scans over the sample (B) in a raster fashion building up an acoustic image of the samples (Raum 2003).

There is a direct proportionality between acoustic impedance and mechanical properties. The technique has been used in the semi-conductor industry for over 30 years.

The advantages of acoustic microscopy can be summarised as follows:

Images can be quickly and easily generated in which contrast is based solely on differing elastic properties taking into account both material structure and density. The only preparation required is embedding and sectioning. Samples can also be studied fresh. Acoustic microscopy has better resolution than microCT or DEXA (Zimmerman 2001).

The concept of acoustic microscopy was put forward in 1949 by Sokolov (Yu *et al.* 1995). SAM was originally developed by Lemons et al. (Lemons *et al.* 1974). It

involves the raster scan of the surface of a sample in a water bath using a focused ultrasonic transducer. The same transducer is used to both send and receive ultrasonic signals. With the transducer focused on the surface of the sample, the magnitude of the returned signal from that point can be stored for each scan point. This allows an image to be built up where each pixel in the image represents acoustic reflectance. From this, the acoustic impedance of the point can also be computed, as acoustic reflectance is a ratio of impedances. As the impedance of water is known, the impedance of the sample can be found. The images produced are a representation of the material properties of the sample. The spatial resolution is dependent on the ultrasonic frequency being used (Briggs 1992). The higher the frequency the better the resolution but the lower the depth to which the ultrasonic beam penetrates.

There are two main modes of operation; Pulse echo mode and burst mode. Pulse echo is used at frequencies below 100 MHz and burst mode is used at frequencies greater than 100 MHz. Burst involves the excitation of the transducer with a train of several sinusoidal waves.

2.4.1 A scan imaging

Figure 19 shows an A-scan plot, this is the raw ultrasonic data. It is the RF signal received from a single point. On the SAM it appears on the screen as an oscilloscope trace. The y axis is signal amplitude and the x axis is time. This type of scan is useful for determining the time of flight of the ultrasonic pulse through the sample. If the thickness of the sample is known then it is possible to calculate out the speed of sound in the material.

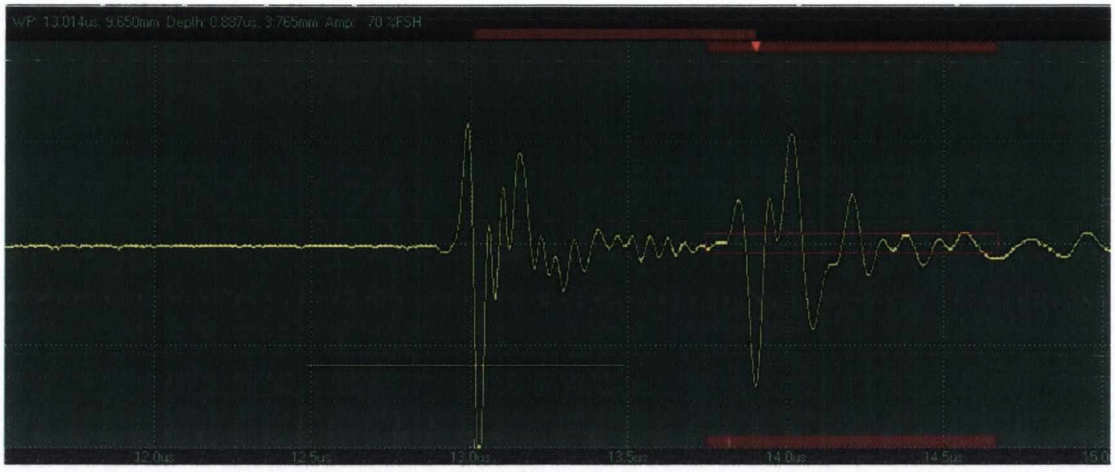


Figure 19 A-scan plot with amplitude on Y axis and time on X axis. (From Sonix (2005))

2.4.2 C scan Imaging

A C-Scan is an image from a specified depth over the entire scan area (See Figure 20). (Horizontal cross-section.) This is the most common type of scan. When the ultrasonic transducer is focussed on the surface then impedance dominates and it is possible to create an impedance map of the surface of the sample (Briggs 1992).

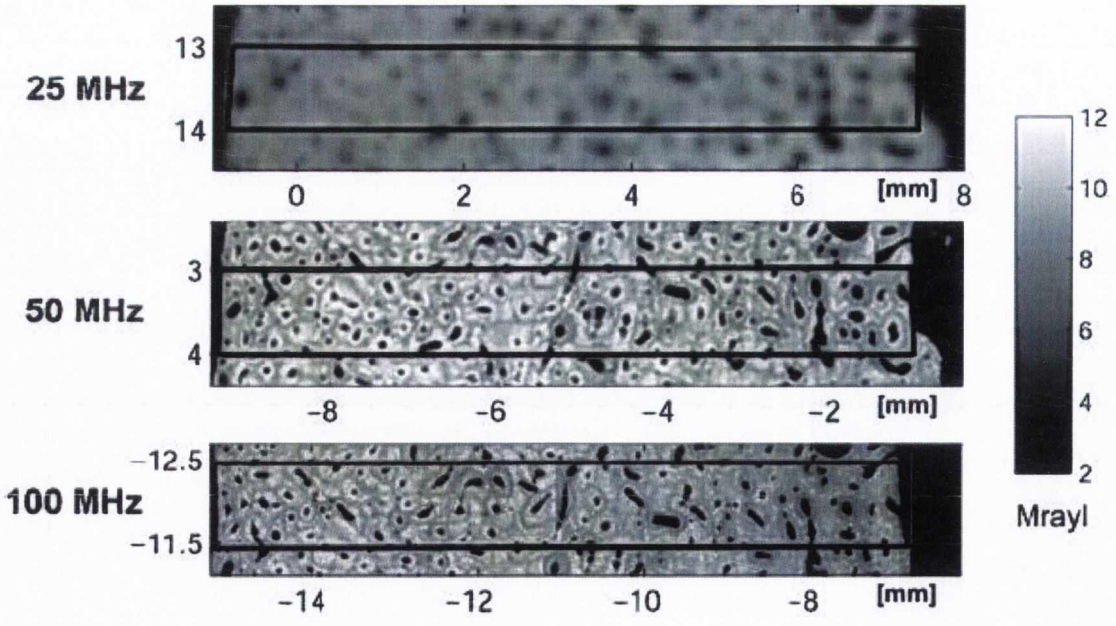


Figure 20 C-Scan Image of cortical bone at various resolutions. From (Raum et al. 2004).

2.4.3 Time of Flight measurement

Time of flight is the time taken for an ultrasonic pulse to travel from an ultrasonic lens to an interface and its reflected signal return to the lens. It is also possible to create a map of the time of flight using a C-scan image. This allows an assessment of the speed of sound at every point across a sample. This requires the sample thickness to be known. If the sample is not properly prepared and not entirely flat then errors will result.

2.4.4 Scanning Acoustic Microscopy applied to cortical bone

In this section a short survey is made of scanning acoustic microscopy studies applied to cortical bone. This survey extends from 1991 to the present and is focused on research that aims to evaluate material properties from SAM data. A number of research questions are explored such as comparison of osteoporotic bone with normal bone, comparison of elastic properties with other methods such as nano-indentation and, as the field is seen to mature, image fusion of SAM data with other methods such as high resolution CT imaging. A representative selection of papers are shown in Table 7.

Study	Frequency	Resolution µm	Comments
Katz & Meunier, (1993)	30-100 MHz	30	Human & Canine femoral cortical bone.
Shieh et al., (1995)	50 MHz	75	Low resolution study on sheep metatarsal.
Eckardt et al., (2001)	400 MHz	2.5	Imaged at angular increments to primary axis of human femoral bone.
Raum et al., (2002)	0.8-1.3 GHz	1	Can see individual lamellae but poor depth of penetration, human cortical bone.
Raum et al., (2004)	25-100 MHz	150-20	Haversian structure just visible at 100 MHz. Human cortical femoral bone
Hofmann et al., (2005)	911 MHz	3-1	Combined with Raman spectroscopy lamellae visible.
Raum et al., (2006)	200 MHz	4	Combined imaging with SR-microCT and SAM.

Table 7 Summary of representative studies on cortical bone using SAM, showing the increasing sophistication of the techniques (Increased resolution) and technologies applied to imaging cortical bone both quantitatively and qualitatively.

"Bone is a complex hierarchical structure that requires multi modality and multi scale technologies to reliably assess its mechanical competencies. Ultrasound is a versatile

technology that allows the measurement of a variety of material and structural properties at several descriptive levels of bone from tissue to organ level" (Laugier 2008).

Interpretation of Quantitative Ultrasound (QUS) data is hampered by the structural complexity of bone and also down to the fact that the interaction mechanisms between US and bone are poorly understood. The elucidation of this problem will rely on coupling of multilevel ultrasound with structural and mechanical information.

Katz & Meunier (Katz *et al.* 1993) using an Olympus UH3 SAM to study human compact bone, both in pulse mode, at 30 to 100 MHz with a 30μm resolution, and in burst mode for high resolutions at 200-600 MHz. This resulted in a resolution of 1.7μm. The samples studied were of human and canine femoral compact cortical bone. This provided detailed images of both the human and canine single osteons and osteonic lamellae at resolutions down to approximately 1.7 microns. This is certainly within the thickness of a lamella as viewed in a specimen cut transverse to the femoral axis. A lens with an angle greater than a critical angle was used to generate surface waves in the sample. When the transducer is defocused into the sample , interference occurs between the longitudinal waves and the surface waves. This can be used to evaluate the speed of these surface waves and gain additional material properties, for example, stiffness in the transverse direction. However their attempts to evaluate this v(z) curve proved unsuccessful. At 400 MHz and 600 MHz transducer frequency it was observed that the outer one or two lamellae had a lower reflectivity than the inner lamellae. It also appeared there was blending of properties between one Haversian system and its neighbour. New growth areas appeared with a lower reflectance than older areas due to higher degree of mineralisation in older bone versus newer bone. This effect was also observed by other researchers (Bumrerraj *et al.* 2001). This study used frequencies of 400 to 600 MHz. It was observed that the outermost lamellae of osteons were always dark gray i.e. less stiff/mineralised and the outermost lamellae of adjacent abutting osteons had essentially the same dark gray levels to the point of not being able to separate them.

SAM was used to evaluate bone remodelling around a cylindrical unicortical defect in a metatarsal of Suffolk sheep (n=12, 2 controls, 10 bilateral operations). 6 months post implantation of the inclusions new bone formation was observed on the inner and outer part of the sheep metatarsal. It was seen that little internal remodelling occurred in the

intracortical region. The primary mechanism of strain induced bone remodelling observed in this study was surface remodelling. The evaluation of bone remodelling by SAM was achieved at a level of detail not attainable with conventional mechanical testing. Bone remodelling could be assessed indirectly by measuring the acoustic impedance. Newly formed regions were visible by change in contrast in the SAM image, average acoustic impedance Z=8.58±0.7MRayl and newer bone had a value of 7.03±0.5MRayl. Combined with histological analysis, SAM provided an insight into bone adaptation mechanisms responding to altered strain distributions. This study used a relatively low frequency transducer (50 MHz) with a lateral resolution of 75 microns. It can be seen even with low frequency transducers it is possible to achieve good results and achieve a good assessment of bone stiffness (Shieh *et al.* 1995).

Osteoporotic properties of human bone were measured using SAM at an ultrasonic frequency of 400 MHz (Hasegawa *et al.* 1995). The ultrasonic parameter being measured was acoustic velocity. The samples were from biopsied human iliac bones. Three groups were available for the study; pre-menopausal (n=10). osteoporotic (n=20) and post-menopausal (n=10) Samples were between 1 and 0.5mm thick. 5 points on each sample were measured. Reproducibility of acoustic measurements was of the order 0.13% to 0.51 %. Acoustic velocity was: 3318 ±319m/s (premenopausal), 3663 ±63m/s (normal) and 3436±209m/s (osteoporotic). Acoustic Velocity was 6.2% lower in osteoporotic bone compared to aged matched bone but 3.4% higher than in pre-menopausal normal women. This is counter intuitive and may indicate that a complex relationship exists between tissue level properties and fragility in bone. Mean activation frequency of osteoporotic bone was about 40% higher and mean activation rate 25% lower than aged matched controls. It is possible that greater mean activation frequency and slower mineral apposition rate in osteoporotic bone decreased both the mean tissue age and mineralisation, and subsequently the acoustic velocity. However this does not explain the lower velocity in pre-menopausal samples. Therefore one could conclude that elastic material properties are not as important a factor in fracture as bone mass.

The organic content of bone was deliberately reduced in samples to study the effects on mechanical properties measured both by ultrasound and by mechanical tests (Mehta *et al.* 1998). To study directional dependency in the bone samples, Ultrasonic Critical angle Reflectometry (UCR) was used. The samples studied were of bovine cortical bone. Agents used were bleach and urea. Mechanical testing was also carried out and

this correlated well with the values calculated by ultrasound. The organic matrix exerts a powerful influence on the elasticity of bone and indicates that measurements of elastic properties are required at multiple directions to assess bone mechanical competence. UCR has the ability to measure all parts of a fully anisotropic stiffness matrix.

Human femoral bone was imaged using a Sonix SAM at 150 MHz. The lateral resolution achieved was 10 microns. In this study nano-indentation was used to assess whether there was a correlation between the Elastic stiffness coefficients measured by the two methods. A reasonable correlation was found ($p=0.001$, $r^2=0.581$). It was discovered that only 34% of the variation in elastic modulus could be explained by the C_{33}. This could be explained by heterogeneity and anisotropy in the sample and the method used to carry out the nano-indentation study. In order to understand the mechanisms of mechano-transduction an understanding of the physical environment at the level of the cell is required, as mechanical signals are perceived at this level. The SAM technique offers a glimpse at the physical structure and properties at this level. (Hoffler 1999)

Nano-indentation and SAM were used to evaluate elastic properties of cortical and cancellous bone and answer the question about whether they both measure the same quantity (Turner *et al.* 1999). A further aim was to compare properties between cortical and cancellous samples. The resolution of SAM was 30-60 microns (50 MHz lens, pulse echo mode) and the resolution of the nano-indentation was 1-5 microns. The samples used were of human bone (1 donor). Trabecular bone was from the distal femur and cortical bone from the femoral mid-shaft. The ultrasonic parameter measured was acoustic velocity. The Young's modulus of cortical bone in its principal axis is 40% greater than intransverse direction. Young's modulus of trabecular bone was slightly higher than transverse modulus of cortical bone but substantially lower than the longitudinal modulus of cortical bone. Nanoindentation estimated Young's modulus 4-14% higher than SAM but the anisotropy ratio was similar. Elastic constant for trabecular bone tissue falls between elastic constants for cortical bone tissue. Therefore moduli of trabecular bone is similar to cortical bone especially in transverse direction.

In a study using a KSI SAM 2000 machine, human femora samples were imaged at a frequency of 900 MHz (Smitmans 2000). This equates to a lateral resolution of 1.5 microns with a 4 micron depth of focus and a lens aperture angle of 100 degrees. Human femora (17 females, 9 male) were cut at various angles of orientation and

analysed with SAM to produce impedance maps. Specimens were dehydrated and embedded in PMMA. At these high frequencies surface artefacts are of the order of the depth of focus. Raum and his group developed a technique where by this effect can be compensated for. It is called the Multi Layer Technique. The surface of the bone sample can be likened to peaks and valleys. Softer material has been worn away to create a valley and harder material is left at the peaks. This technique is only required at very high frequencies. It was noted that the impedances observed at these frequencies were lower than that observed at lower frequencies. The aim of this study was to look at the anisotropy of impedance of bone at different orientations. Significant angular dependence was found. It was a maximum at 10 degrees. However female samples exhibited a remarkable decrease of impedance at an angle of 15 degrees. Samples from women over 70 years of age were found to have higher impedance in comparison with the male group. At these frequencies it is possible to image individual lamellae, however the ability to look far below the surface is limited.

A SAM study investigated if there was any dependence of micro-mechanical properties in human femoral cortical bone on the orientation of the cutting plane relative to the primary axis of the bone (Eckardt *et al.* 2001). To do this acoustic impedance was measured as a function of cutting angle. Samples were cut at angles from 0° to 90° in increments of 15°. The samples were embedded, cut and polished. The samples were imaged at 400 MHz at a resolution of 2.5 microns. It was found that older interstitial lamellas displayed higher acoustic impedance compared to younger regions. The lowest Z values were measured for outer lamellas of younger osteons. Interestingly it was found that there is no indicator for an angular dependence for acousto-mechanical properties of bone at this length scale. The distortion of the 75° and 15° cutting angle is due to the preferential removal of softer regions in the polishing process. It was noted that this technique can complete the knowledge about the elasto-mechanical properties of bone anisotropy due to macroscopic factors. It is also interesting to note that these findings are at odds with the work of Smitmans et al. (2000) where it was concluded that acoustical properties peaked between 0° and 30°. The conclusions of Eckardt et al. (2001) seems to point towards the fact that at the lamellae level and at the length scale of 1 to 3 microns, the material model which works best is an isotropic one.

For very high resolution studies (0.8 to 1.2 GHz) of cortical bone a method was developed in order to compensate for surface irregularities (Raum *2002a*). The samples

studied were of human cortical bone from the femur. This technique allows observation of the surface topology and irregularities of a sample surface. This setup is capable of lateral resolutions of 1 μm; however depth of focus is limited (7 μm). This is one of the many limitations of using very high frequencies. It was observed that the inner most lamellae had a higher impedance and that secondary osteons had a higher impedance than primary osteons. This effect is also observed in later studies, see Table 8 (Raum *et al.* 2006a).

Using a custom built SAM, human femurs were imaged at an ultrasonic frequency of 100 MHz. The samples were cut at different orientations from 0^{o} to 90^{o}. This study achieved a maximum lateral resolution of 20 microns with a F=1 lens at 100 MHz. C-scan were taken at each orientation to build up an acoustic picture. Differences in morphology were observed; young samples had a large number of osteons with small channel diameter < 50 microns, whereas over 70s group have less osteons and greater sized channels >100 microns (Raum 2002b).

In a study by Raum and his co-workers, the simultaneous determination of Z, longitudinal and lateral wave velocities were carried out in order to characterise the elastic microstructure of cortical bone. The equipment used was a 50 MHz confocal ultrasonic microscope. This technique is able to evaluate the isotropic material properties of bone. Embedded bovine femoral samples were used. Density and longitudinal acoustic velocity didn't correlate well with Young's Modulus. Acoustic impedance appeared to be a more suitable parameter for the prediction of elastic stiffness with a good correlation value of: R^2=0.594 (Raum *2003*).

Raum et al., (Raum *et al.* 2004) examined the influence of frequency and spatial resolution on anisotropic impedance estimation of cortical bone form 25-100 MHz. The samples were also cut at a variety of angles from 0^{o} to 90^{o}. The samples of human cortical bone were imaged by SAM in C-mode. The structures such as, size and distribution of Haversian channels and resulting porosity had a significant effect at lower resolutions resulting in under evaluation of acoustic properties. For example at 25 MHz the average impedance was lower than at the 50-100 MHz. Approximately 90% of low impedance at low frequency could be explained by structural parameters, the remainder is due to dispersion.

	Interstitial	Osteonal
N (Number of samples)	257	228
Z (MRayl.)	9.3±1.0	7.2±1.1
DMB g/cm^{-3}	1.116±0.05	1.06±0.07
ρ gcm^{-3}	1.93±0.03	1.85±0.05
C_{33} GPa	45.6± 10.1	28.4±8.3
E_3 GPa	33.8±7.5	21.1±6.2

Table 8 Typical physical values of bone samples (Raum et al. 2006a).

Other techniques have been combined with SAM to achieve greater insights into the microstructure of bone. Human cortical radius bone was imaged using both synchrotron radiation, micro CT and SAM (Raum *et al.* 2006b). The samples were imaged at 200 MHz using SAM and achieved a resolution of 4 microns. The SR-microCT achieved a voxel size of 4.9 microns. The three dimensional SR-microCT models were combined with the 2D SAM images. The SR-microCT measured DMB, and SAM measured surface acoustic properties such as acoustic impedance Z. Therefore, independent measurements of density and elastic properties could be achieved at each location on the surface of the 3D model. It was shown that the derived C_{33} correlated more closely with Z (R^2=0.996) than with mass density (R^2=0.310). This suggests that estimates of C_{33} made from measurements of Z are more reliable than from density measurements. The relationship between mineral density and stiffness is not clear. It is likely that mineral density is not an accurate determinant of elasticity. There is a strong correlation between Z_3 and C_{33} and reliable estimates of elastic stiffness can be made from Z_3 alone. Hofmann and co-workers (Hofmann *et al.* 2006) carried out site matched imaging of human femoral cortical bone at an extremely high resolution both with SAM and Raman spectroscopy and nano-indentation. This technique allowed the structure, chemical composition and anisotropic elasticity of individual lamella to be investigated. It was also possible to assess orientation alignment of the fibrils inside the lamella. In addition, knowledge of material properties gained from SAM can be used in finite element or finite difference models.

2.4.5 Conclusion

Scanning Acoustic Microscopy is akin to optical microscopy but what is observed is acoustic reflectance and impedance. These parameters are directly proportional to structural and mechanical parameters such as density and elastic stiffness of the solid being imaged.

SAM is particularly useful for the imaging of biological samples as the samples can be imaged fresh or embedded. The only special requirement is that the sample surfaces are flat and free from debris.

From a technical point of view there are a wide variety of methods which can be applied to image samples. A-scans involve viewing the return signal amplitude over time. By interpreting this plot it is possible to work out the speed of sound in bone once the thickness is accurately known at that point. C scans allow the surface of the sample to be imaged in a raster fashion. This is a powerful technique as the bone sample can be probed at thousands of points and images can be built up from these scans.

Early attempts to study compact bone with SAM (Katz et al. 1993) were able to achieve a resolution of up to 1.7microns. This is within the thickness of a lamella. It was also observed that new growth areas appeared to have a lower acoustic reflectance than older areas due to the higher degree of mineralisation in older versus newer bone. Also outer lamellae of the osteons had lower reflectance than the inner ones (Katz et al. 1993) (Bumrerraj et al. 2001). This concept of being able to assess areas of recently completed remodelling were utilised by Shieh et al 1993. Combined with histological analysis, SAM provided an insight into bone adaptation mechanisms responding to altered strain distributions.

Nano-indentation was used to validate elastic stiffness measured by SAM techniques (Hoffler 1999) A reasonably good correlation was found between stiffness measured by each method ($r^2=0.58$).

SAM can be combined with other methods to achieve simultaneous assessment of properties such as elastic stiffness, degree of mineralisation and chemical content. One method involves the use of microCT and SAM (Raum et al 2006b). Other methods have used SAM combined with Raman spectroscopy and nano-indentation (Hoffmann et al. 2006).

One of the most interesting prospects is the development and validation of quantitative SAM on small animal models. This may be of interest to pharmaceutical companies interested in the effects of new drug treatments on bone.

SAM offers a unique method of obtaining image samples of prepared cortical bone non-destructively. It can image both physical and mechanical properties of samples at resolutions approaching that of optical microscopy. It can also be used with other techniques to create a clearer picture of bone microstructure. This will allow researchers to quantify the effects of drug treatments and other stimuli on the micro-structure of cortical bone.

2.5 Computational simulation of cortical bone microstructure and remodelling.

2.5.1 The Finite Element method.

Today the finite element method is a powerful computer aided engineering analysis tool. The technique in its modern form was developed to cater for a need to design and analyse complex delta aircraft wing structures in the 1950s.

To briefly define the technique; The basic concept in FEM is the sub-division of a continuum for analysis, such as a thin plate, into a number of components of simple geometry called finite elements. The response of each element is expressed in terms of a finite number of degrees of freedom characterised as the value of an unknown function, or functions, at a set of nodal points. The response of the mathematical model is then considered to be approximated by that of the discrete model obtained by connecting or assembling the collection of all elements (Felippa 2011).

For displacement/stiffness based finite element analysis, the characteristic system of equations is:

$$\{F\}=[K]\{u\} \quad \textit{Equation 2-37}$$

This equation is essentially a matrix form of Hooke's Law. The vector F represents the externally applied loads on the system. K is a square matrix known as the stiffness matrix and the vector u represents the known and unknown displacement degrees of freedom in the system. Degrees of freedom can represent quantities such as displacements, nodes can have more than one degree of freedom (Cook *et al.* 2002) . For example, in a two dimensional problem, nodes will have two degrees of freedom for displacements in the x and y directions. Solving for the unknowns in **u** involves:

$$\{u\}=[K]^{-1}\{F\} \quad \textit{Equation 2-38}$$

2.5.1.1 Element Formulation

The element used in this study is an eight node iso-parametric two dimensional quadrilateral element (Element Plane 183, ANSYS Version 8.1) .

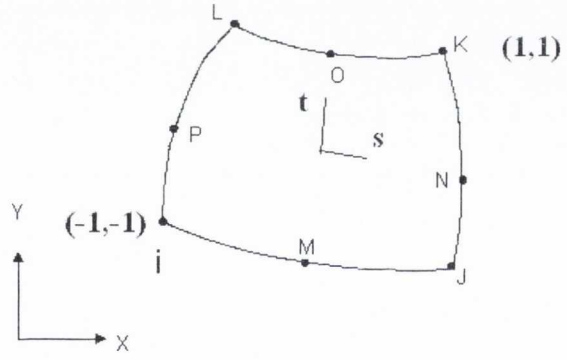


Figure 21 Eight node quadrilateral element showing the global coordinate system (x,y) and the local element coordinate system (s,t) with natural coordinates. Node i in (s,t) coordinates is (-1,-1) for example. This element has mid-side nodes m,n,o and p(Image adapted from (ANSYS 2004)) .

Figure 21 shows a detailed image of an eight node quadrilateral element. This element is iso-parametric and uses Lagrangian interpolation. The eight shape functions for this element are:

$$N_{i,j,k,l} = \frac{1}{4}(1 \pm s)(1 \pm t)(\pm s \pm t - 1)$$

$$N_{m,o} = \frac{1}{2}(1 - s^2)(1 \pm t) \qquad \textit{Equation 2-39}$$

$$N_{n,p} = \frac{1}{2}(1 \pm s)(1 - t^2)$$

$$\{u\}^{(e)} = N^{(e)}\{D\}^{(e)} \qquad \textit{Equation 2-40}$$

The shape functions can be used to derive the stiffness matrix by deriving the strain displacement matrix **B.** This matrix is the 1st derivative of the shape function matrix **N.**

$$K^{(e)} = \int_{\Omega^{(e)}} hB^T EBd\Omega \qquad \textit{Equation 2-41}$$

Where h is the thickness of the element and E a matrix which describes the mechanical properties of the material. To derive the stiffness equation $K^{(e)}$ for this element it is necessary to solve the integral above. This integral can be solved numerically using Gaussian 2x2 integration points (See Figure 22). Gaussian quadrature is the method of numerical integration used to solve integral in Equation 2-41.

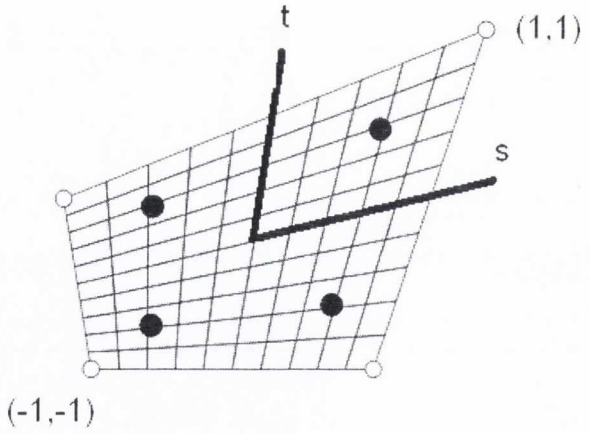


Figure 22 Illustration of 2x2 integration points. The integral is evaluated at the locations of the black dots shown on the element above for Gaussian Quadrature. The natural coordinates (s,t)are shown, adapted from (Felippa 2011) .

$$\int_{-1}^{1}\int_{-1}^{1} F(s,t)dsdt = \int_{-1}^{1}dt\int_{-1}^{1} F(s,t)ds \approx \sum_{i=1}^{2}\sum_{j=1}^{2} w_i w_j F(s_i,t_j) \quad \textit{Equation 2-42}$$

The equation above shows how the integral (Eq 2.42) is solved using Gaussian quadrature. w_i and w_j refer to the weights and s_i and t_j refer to the locations in natural coordinates on the element the integral is evaluated.

With a solution for $K^{(e)}$ it is possible to find the stiffness matrix for each element in a model and assemble the individual elements into an overall stiffness matrix. An additional step not covered here is the transformation from local coordinates of the individual elements to the global coordinates of the system. This is accomplished using a Jacobian matrix **J.** The externally applied force vector and displacement vector are also assembled. Equation 2.37 is then solved for the unknown displacements.

2.5.2 Application of Finite Element Analysis to the assessment of stresses and strain at the tissue level in bone.

The data gleaned from SAM on the mechanical properties of bone at the micro-structural scale can used to form a finite element model. In this section a number of studies using finite element based micro-mechanical models of cortical bone will be discussed.

Prendergast et al. (Prendergast *et al.* 1996) developed a 2D finite element model of an osteon and applied physiological loadings to it. Its purpose was to investigate whether damage generates strain which may stimulate bone remodelling. The study found that micro damage alters the local deformation behaviour around lacunae and that the changes increase as damage increases. It is thought that osteocytes occupy these lacunae and that the deformation of these spaces may stimulate the cells to initiate bone remodelling. Examination of the strain amplification abilities of lacunae has also been examined (Bonivtch *et al.* 2007) . This finite element model only took into account the lacunae and a limited area around it. It was also a parametric study where parameters such as canalicular diameters, perilacunar tissue material moduli and perilacunar tissue were varied and there effects evaluated. It was found that the lacunae caused strain amplifications of 3 or more over the applied strain. Models such as the one shown below combined with data from SAM studies, could be used to gain even more insight into the micro-mechanical environment of cortical bone.

Finite element models of bone microstructures can be used to drive bone remodelling algorithms (McNamara *et al.* 2007). A single trabecula was modelled in a finite elements and two bone regulation algorithms were implemented. The algorithms implemented were damage based and strain based. The hypothesis tested was that bone remodelling is regulated by both strain and microdamage mechanisms. Remodelling of trabecula is accomplished by external remodelling by BMUs. Sensors were implemented on the surface (bone lining cells) and internally in the model (osteocytes). It was proposed that the regulatory system is capable of responding to either strain or microdamge but it was found that the only situation which provided a plausible prediction of BMU behaviour was if damaged bone above a certain threshold was removed. It was concluded that this may be due to too much damage, causing osteocyte cell processes to become damaged leading to cell apoptosis and interference with normal cell signalling.

More modern studies have looked at crack propagation in realistic models of bone microstructures using finite element computer codes (Abdel-Wahab *et al.* 2011). The aim of this study was to investigate the effects of micro-structure and material properties of bone on crack propagation. A two dimensional finite element fracture model for osteonal bovine cortical bone was developed. An optical microscope image of the osteonal structure of a bone sample cross section was used to construct the model. Mechanical properties were found using nano-indentation. Three models were created, one with homogenous properties, one with representative properties but without cement lines and the final one with representative properties and cement lines. It was found that micro-structural features such as cement lines were especially important in the development of bone failure due to fracture. Cement lines were found to raise the stress and strain required to propagate a crack. Of the three models, the model with cement lines arrested crack growth in the finite element model.

In a related study, crack growth was studied around a single osteon using finite element analysis(Mischinski *et al.* 2011). The aim of this study was to analyse possible mechanisms that effect crack penetration into osteons or deflection into cement lines using fracture based finite element modelling. The simulations showed that low cement line strength facilitated crack deflection irrespective of the fracture toughness of the cement line. However low cement line fracture toughness did not guarantee crack deflection if the cement line had high strength. Changing the fracture properties of the

osteon influenced the crack propagation path but varying the elastic modulus of the osteon had little effect on crack trajectory.

2.5.3 Validation of the FE models

Nicolella and co-workers (Nicolella 2001; Nicolella *et al.* 2005; Nicolella *et al.* 2006) have developed a technique to assess the strain in a prepared sample of cortical bone. The bone is cut to a thin slice. It is then fitted into a rig which is capable of applying a controlled level of strain to the sample. The sample is subject to a small preload. A digital image is then acquired. A physiological loading is then applied, usually axially. Another image is taken. The images are then split into small squares as shown on the image below and to the right. These are in effect the strain gauges except that these strain gauges are 20 microns in length. A special algorithm assesses which parts of the image have deformed. It then is capable of displaying a picture of the strain in the sample due to the applied strain (See Figure 23).

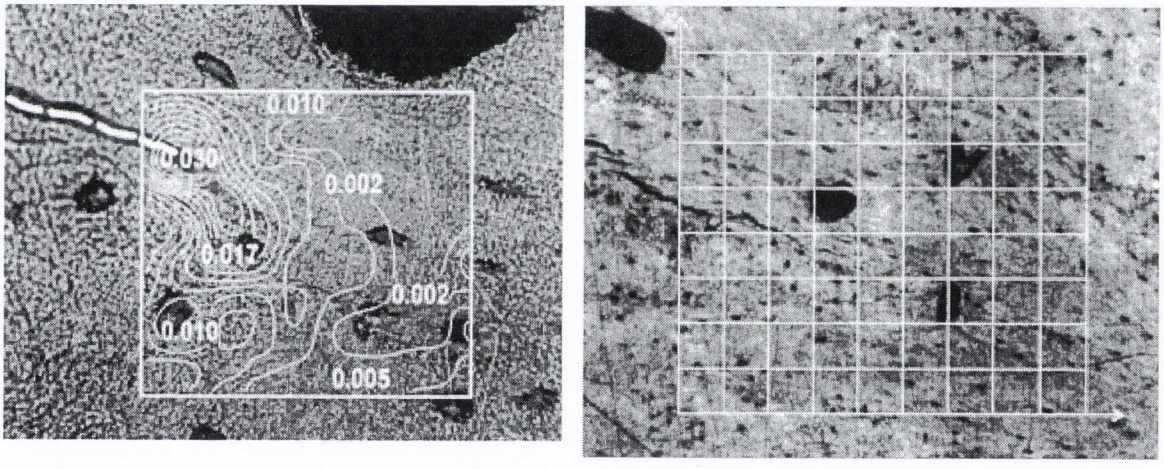


Figure 23 Images of strain in cortical bone samples taken by the stereoimaging technique (Nicolella 2001). An image is taken of sample with no load applied, this is then compared with an image taken with load applied. An algorithm is used to detect differences in displacement in sample. These are converted to strains which are shown on the image on the left hand side.

The understanding of local micro-structural deformations may lead to a better understanding of cortical bone development fracture and remodelling. Strain concentration factors are 1.1 to 3.8 times physiological loading of 2000μ strain. This technique has errors of between 39 and 564 μ strain depending on the gauge length chosen.

2.5.4 Conclusion

In order to study the research hypothesis that osteoporosis changes the mechanical stimuli of the mechano-tranduction system of bone it is necessary to convert the values of mechanical stiffness into estimates of Young's modulus at each measured location on the bone sample. This process is documented in the methods section to follow.

Finite element techniques have been used by many investigators to assess the micromechanical strain environment of bone. It has been found that features such as cement lines and lacunae act as concentrators of strain within bone. Investigators such as Raum have used a histogram to represent the distribution of mechanical properties in a bone samples. This can be taken a step further by showing the resulting stress and strain distributions calculated by FE.

3 Methods

3.1 Introduction

There are four separate strands to the methodologies used in this project. These include, in order of their usage:

1. Preparing and imaging of samples with Scanning Acoustic Microscopy (SAM).
2. Calibration, correction and image analysis of images from SAM.
3. Finite Element Analysis (FEA) applied to sections of the images from the image processing step above.
4. Statistical analysis carried out on the SAM images and FEA analysis. This was to test the hypothesis that osteoporosis causes changes to the biophysical stimuli within cortical bone.

3.2 Sourcing of Cortical Bone Samples

Bone samples used in this research were from the "Bone for Life" (BFL) project, as described in Chapter 2. This study comprised of 71 sheep in total, of these 34 were ovariectomised. At discrete increments in time each sheep was given fluorochrome bone markers to label new bone formation.

Three types of ovine cortical metacarpal bone samples from the "Bone for Life" project were tested in the research presented in this thesis: Normal (CON), ovariectomised (OVX) and drug-treated ovariectomised (Zoledronic acid, OVX+ZOL). These samples were available as year 1 and year 2 groups. The year 1 group consisted of CON and OVX samples. The year 2 group consisted of CON, OVX and OVX-ZOL.

3.3 Sample Preparation

The samples used in this study were cut perpendicular to the primary axis of the bone, using a diamond saw (Struers Minitom). The samples were then polished using successive grades of abrasive paper and finally polished with 1 μm diamond paste on a polishing wheel (Struers DAP2). The samples were subsequently cleaned ultrasonically and checked with an optical microscope. The samples were kept wet at all times. Samples were stored frozen at –18 ^{o}C.

3.4 Ovine Cortical Bone samples

3.4.1 Statement of the experimental objectives:

The basic research hypothesis is that the process of osteoporosis changes the magnitude and distribution of stress and strain in the cortical bone samples.

The numbers of samples of each type are shown in Tables 9 and 10 above. Three random areas were selected in each bone sample image. These constituted the basic experimental unit of the statistical analysis. In order to statistically infer changes in bone due to osteoporosis a set of control samples were used (CON Y1 & CON Y2).

	Year 1 (Y1)	**Year 2 (Y2)**
CON	✓	✓
OVX	✓	✓
OVX-ZOL		✓

Table 9 Sample types available in study.

Sample type	**No. of samples**	**No. of sub-images**
CON Y1	6	18
OVX Y1	6	18
CON Y2	3	9
OVX Y2	3	9
ZOL Y2	3	9

Table 10 Number of samples in statistical analysis. Each sub image has 5151 pixels.

A total of 21 bone samples were tested using SAM. See Table 11 for a complete listing. Sample numbers refer to the "Bone for Life" sample register. This allows cross referencing to other "Bone for Life" studies.

Sample No.	Sample type
6	CON Y1
2	CON Y1
5B	CON Y1
20	CON Y1
22B	CON Y1
31	CON Y1
4A	OVX Y1
4B	OVX Y1
15	OVX Y1
23	OVX Y1
23B	OVX Y1
32A	OVX Y1
40	CONY2
52	CONY2
67	CONY2
36A	OVX-ZOL Y2
36B	OVX-ZOL Y2
51	OVX-ZOL Y2
54	OVX Y2
45B	OVX Y2
58	OVX Y2

Table 11 Year 1 and year 2 Samples imaged by SAM, Y1 and Y2 indicate year 1 and year 2 samples respectively. CON refers to bone samples which come from control sheep, OVX refers to samples from ovariectomised sheep and OVX-ZOL refers to bone samples from sheep which have been ovariectomised and subsequently administered Zoledronic acid.

3.5 Ultrasonic equipment.

The SAM used for imaging bone samples was a SONIX UHR 2001 with a JSR DPR 500 Pulsar/Receiver. The samples were imaged at 150MHz using the ultrasonic lens shown in Table 12 below:

Transducer Name	Spot Size in water (mm)	Focal Zone in water (mm)	F#
V3849 150 MHz 3.2 mm	0.020169	0.308742	2

Table 12 Transducer details (From Sonix correspondence).

An ultrasonic frequency 150MHz represents a good compromise of penetration depth and resolution. For this study the evaluation of the acoustic properties was of the sample surface where impedance dominates the contrast in the images (Briggs 1992). Ultrasonic lateral resolution for lens in Table 12 is plotted for a range of frequencies in Figure 24.

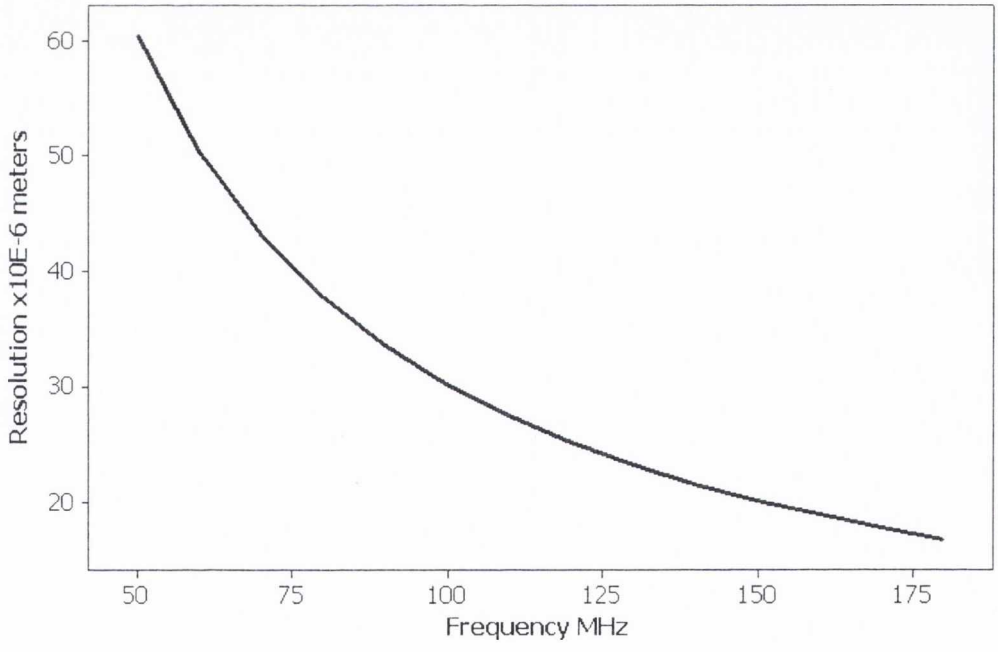


Figure 24 Ultrasonic lateral resolution for lens in Table 12 for a range of frequencies.

The maximum achievable resolution with this lens is 20μm. The focal zone is the region of peak sensitivity for the transducer and is defined as the region to the left and right of the peak focus where the amplitude falls off by 6dB from the peak, (see Figure 25 below).

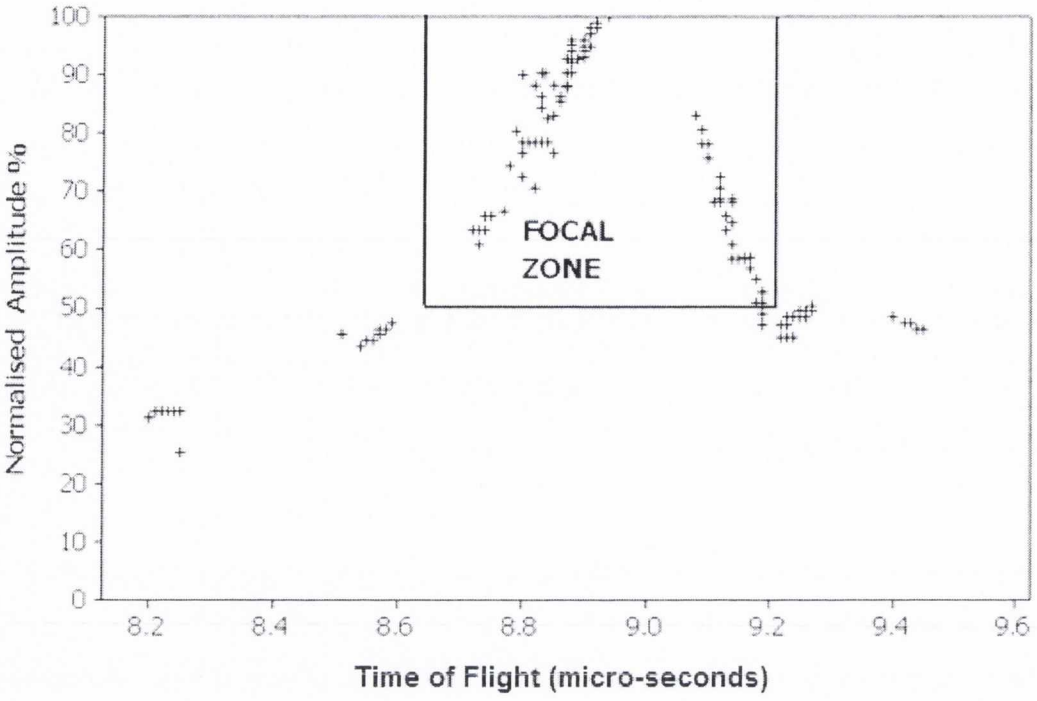


Figure 25: Normalised plot of Amplitude Vs. TOF (Time of Flight). The peak amplitude is at 8.94μsec for this lens. The Ultrasonic beam has a focal zone which is defined as the area each side of the peak where amplitude drops to 50% of maximum (-6dB). In this region a maximum lateral resolution of 20μm is achieved. The values shown are for the V3849 transducer. All measurements taken at 20dB attenuation.

3.6 Experimental procedure.

Imaging of the bone samples involved probing the surface of the samples with an ultrasonic pulse and moving the ultrasonic transducer in a raster fashion, to build up an image of the sample. This procedure is known as C-scan imaging. The samples were imaged whole using a scan/step size of 25μm and was at the limit of the machine's capabilities. This resulted in images with a pixel size of 25μm. The C-scans were acquired at an attenuation of 20dB.

The experimental steps consisted of:

1. The V3849 acoustic lens was used. The step/scan size of 25 μm was used. The images produced were saved in TIFF format.
2. The three (Poly Carbonate, PVC and Quartz) calibration samples were scanned in C-scan mode, attenuation set to 20dB.
3. Fifty random points were picked on each calibration sample; the water path and the amplitude were measured at these points.
4. The bone samples were imaged at 20dB in the C-scan mode. The focus was set to get amplitude of about 70%; this was repeated for all samples.
5. Six points were chosen around each bone sample. The location amplitude and water path time was recorded for each point. This was repeated for all samples. This was used to adjust for surface undulations in the bone samples.

Considerable testing was required to develop an experimental protocol which produced good images. Two rounds of imaging with SAM were required to perfect the protocol shown above. The SAM used was not designed for imaging of biological samples therefore procedures had to be developed to get the best out of the machine. A note of thanks to Tony Compagno at Tyndall for his contribution in achieving good SAM images. A new ultrasonic lense was also secured. This had a reduced F number (2) compared to the original one (3.3). The lower the F number the higher the resolution. The lenses are custom made. The manufacturer of the lens had many problems making the lens hence this lead to a six month delay in delivery. Shown below is an image taken using the imaging protocol discussed.

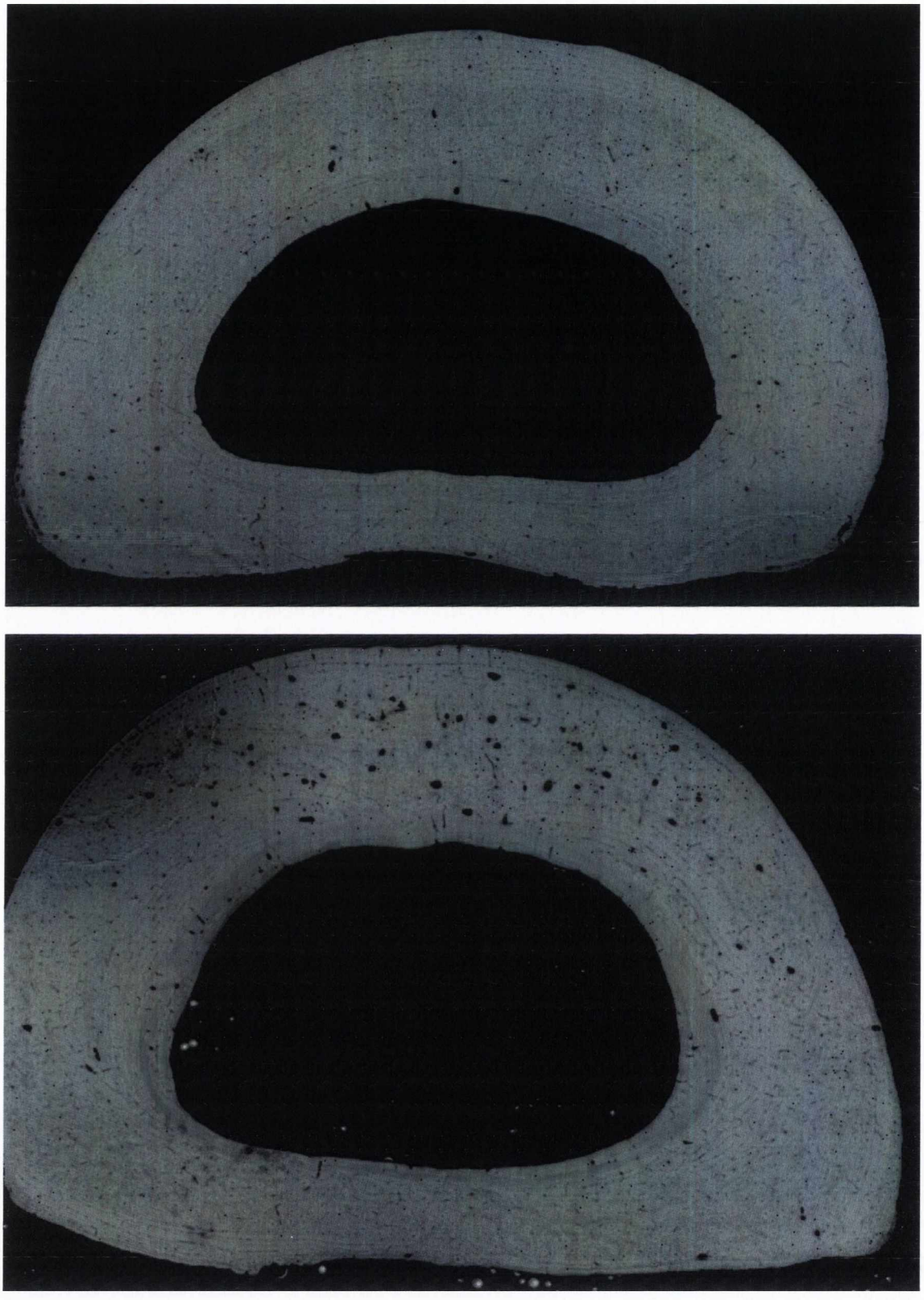


Figure 26 Sample 67 and Sample 58A unprocessed SAM images 1 pixel=25μm. Note features such as osteons, cement lines and Haversian canals can be observed.

3.6.1 Calibration

Three calibration samples were imaged with SAM, see Table 13. These acted as references for calibrating the machine for the accurate calculation of acoustic impedance (Z) and

acoustic reflectance (R) of the bone samples. Figure 27 shows the calibration curve. A line is fitted to this data and is used to relate experimental to actual reflectance.

Material Definitions	
QZ Quartz	Vitreosil 5x5x1mm
PC Polycarbonate	Thin sheet Supplier: Ensinger 1mm sheet
PVC	Thin sheet: Tecavinyl PVC 1mm sheet.

Table 13 Materials used for calibration.

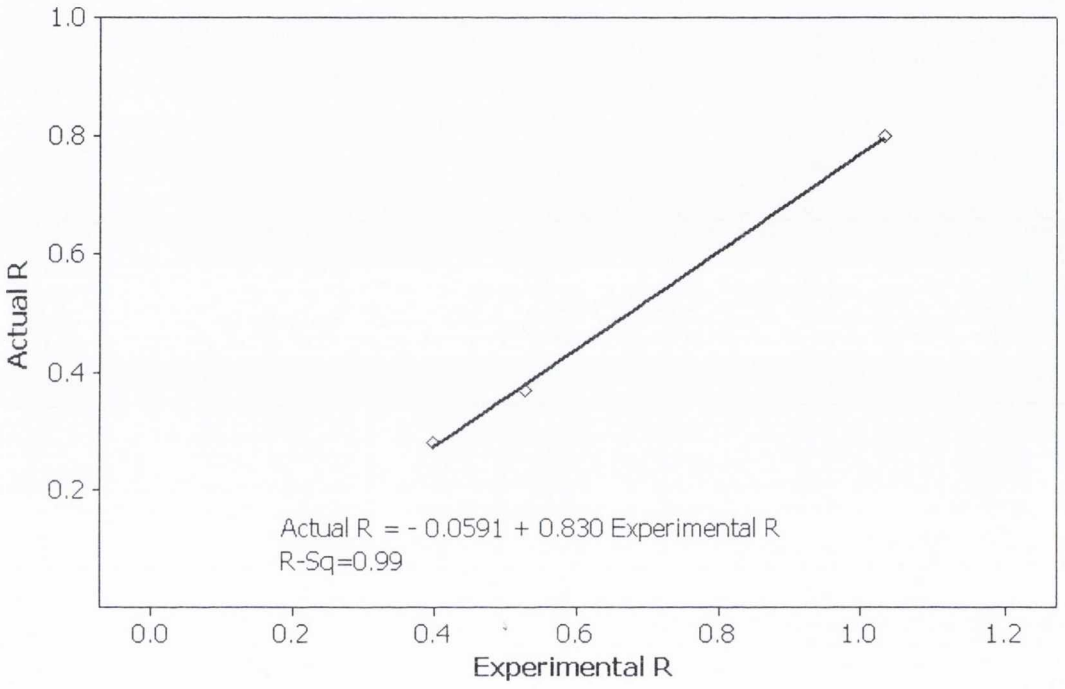


Figure 27 Calibration curve for Poly Carbonate, Poly Vinyl Chloride & Quartz. (20dB attenuation)

The calibration samples were imaged using the same settings as would be applied to the bone samples.

The bone samples were not entirely flat so a method had to be found to correct for this. The SAM can indicate the water path time of flight (TOF). This is the time taken for the ultrasonic signal to go from the transducer to sample surface and back again. With this piece of information, it is possible to find out if the lens is in focus or not. The points in Figure 28 were found by experiment. For each calibration material there is a known R value available in the literature. Random points on each calibration sample were scanned with the SAM. The parameters of TOF and amplitude were taken at each point. This was repeated 50 times for each calibration sample to build up the plots shown. The data points

were normalised by dividing the recorded amplitude by the maximum amplitude at focus for each calibration sample type. The sample points for each calibration material were collected together into one data set.

A similar procedure was followed for the bone samples. Peak experimental amplitude of 83% was found for the bone samples at focus. This value is within an acceptable range. Consulting Figure 27 a measured value of 83% amplitude equates to a value of 0.63 for acoustic reflectance (Raum 2008) .

This value of reflectance is within the normal range of 0.6 to 0.7 expected for bone. In Figures 28 and 29 it is possible to see a good correlation between the data gathered for the calibration materials and that of bone for TOF versus measured experimental amplitude.

Figure 28 shows a plot of TOF against normalised measured amplitude. The peak amplitude for each calibration sample was normalised by taking the peak value at the focus and normalising it to a value of 1. This procedure was also carried out for the bone sample points. The graph demonstrates a good correlation between the bone data and the calibration data. The variation between the two data sets is due to the slightly different values of amplitude at each point in the bone sample. However, this does demonstrate the effect that defocus has on the measured value of amplitude and it also demonstrated how such a curve could be used to correct for defocus in the images.

This approach to focus correction is similar to that used by Hofmann et al. (2006). In this study the TOF was known for every point on the image (Hofmann *et al.* 2006). In the research presented here an estimate had to be made as to the surface undulations present in the sample, using an averaging procedure. The averaging procedure found a gray value averaged over a 15 by 15 pixel area. This average value is indicative of how in or out of focus that area is. Averaging over a large area removes the effect of gray level changes due to the variation of acoustical properties of bone and allows an estimate to be made of the defocus at a particular location within an image.

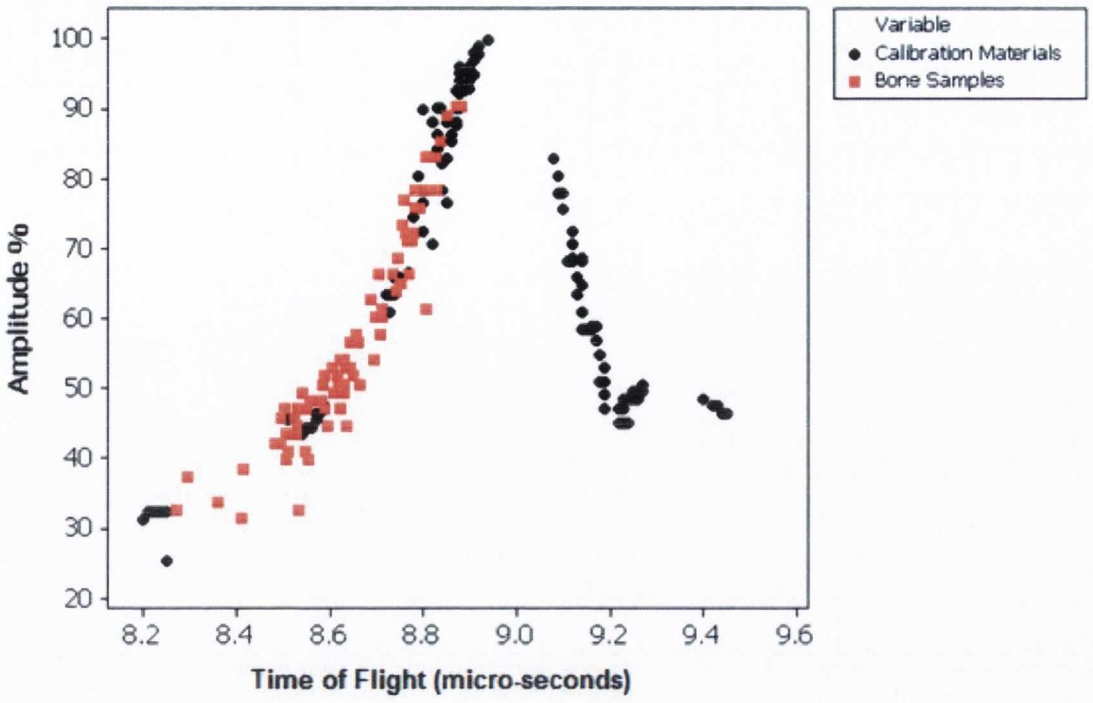


Figure 28 Plot of Normalised Measured Amplitude Vs. TOF in μsec. Both the Bone and calibration samples are shown on this graph. There is a good correlation between these two data sets. Note that the error increases to the left of the focus peak as time of flight decreases.

The area of interest in Figure 28 is left of the peak. This is the area of the lens focus which is used to image the bone samples. Figure 29 shows this area in more detail. Least squares regression polynomial curves shows good correlation between the bone and calibration material data points. This is demonstrated by the close correlation in the values of the polynomials for the two fitted curves.

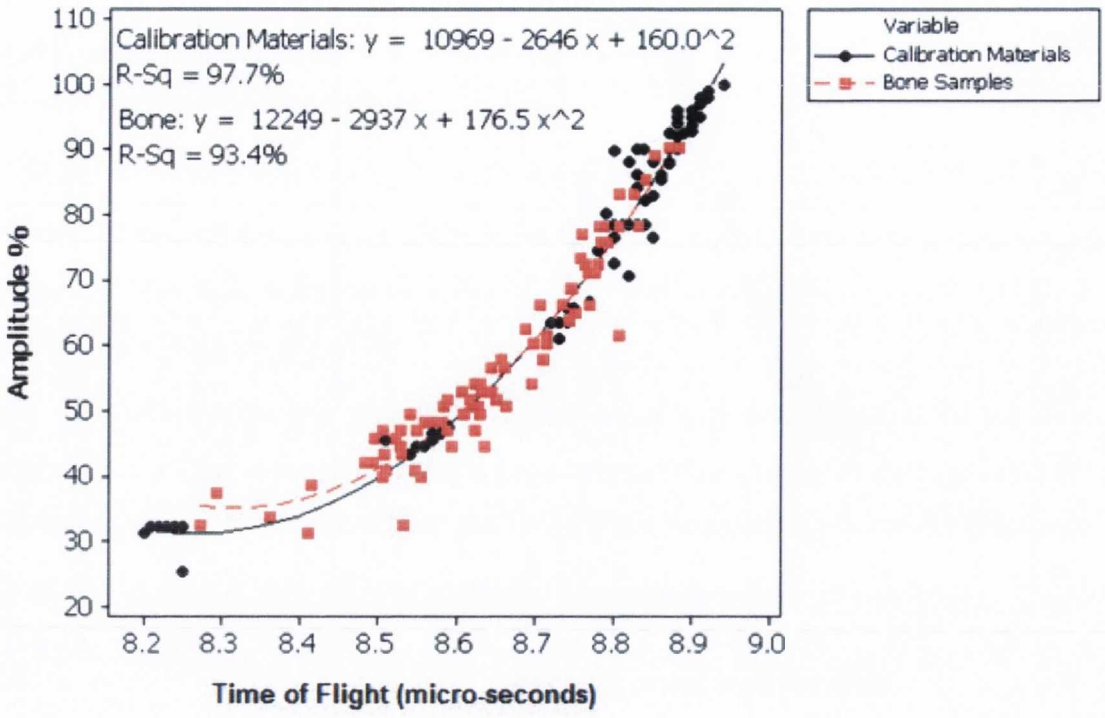


Figure 29 Plot of Normalised Measured experimental Amplitude Vs. TOF μSec. Curves are shown for both bone and calibration materials. These are normalised so they can be displayed on the same plot.

3.6.2 Data gates on Sonix SAM machine:

Gates are used to collect information at desired interfaces within the samples, see Figure 30. The absolute value of the highest amplitude signal which breaks the gated threshold within the gated region is recorded. If no signal breaks the gate, no data is recorded. The gate has to be set so it captures the TOF range due to surface undulations in the bone samples.

Gates are used to collect information at desired interfaces within the sample.

•The gate is placed over the signal or signals of interest.

•The absolute value of the highest amplitude signal which breaks the gate threshold within the gated region is recorded. (Figure 1)

•If no signal breaks the gate threshold no data is recorded. (Figure 2)

•Signal amplitude can be increased or decreased by adjusting gain.

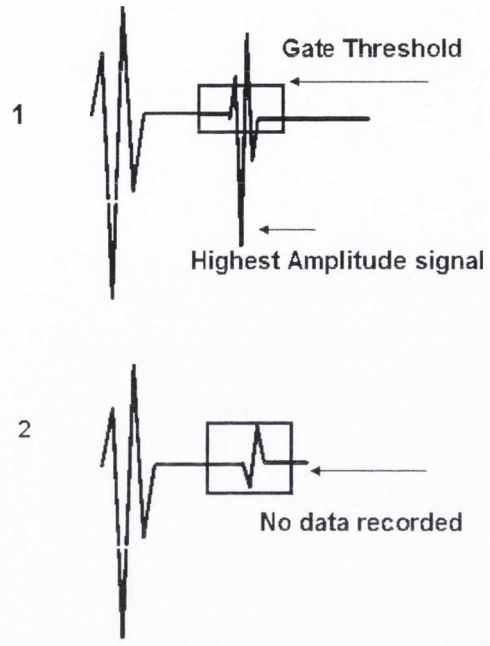


Figure 30 Sonix Machine Data gates. The horizontal axis is TOF in μsec. The vertical axis is the amplitude of the signal. From (Sonix 2005).

3.6.3 Surface roughness and surface undulation issues.

No matter how well the samples are prepared, it will not be possible to have perfectly flat and smooth samples. Every ultrasonic lens has a focus point. An experimental study is required to find the relationship between the lens distance from the sample and the amplitude of the returned signal from the surface. Using this data it is possible to work out correction factors for areas of the samples which are not in focus.

The starting and ending points of the focal zone are located where the on-axis pulse-echo signal amplitude drops to -6dB of the amplitude of the focal point. The length of the focal zone for the lens used in this study is 0.3087mm. Therefore, -6 dB is a reduction of 50% in the maximum amplitude. To calculate the focal zone in terms of the TOF the equation below can be used:

$$TOF = \frac{2L_{FZ}}{c_w} \quad \textit{Equation 3-1}$$

Where L_{FZ} is the focal zone length and c_w is the speed of sound in water. Using Equation 3-1 the focal zone corresponds to a time of flight of 0.429 micro seconds. This compares well to the graph shown in Figure 28.

3.7 Image analysis

3.7.1 Regression Analysis

Images of the samples acquired by the SAM have to be transformed into usable maps of bone mechanical properties. A number of problems were encountered doing this. First it was found that the samples were uneven. A procedure was developed using a linear regression procedure. This is possible because for each sample at least five points have a known amplitude and TOF (See Figure 31) and it is possible to estimate the undulations of the surface of the sample. These five points were fitted to a linear regression surface using a MATLAB script. A height map was produced as a result of the regression analysis. This height map was used to adjust the gray level of each pixel to take into account for focus. Figure 32 shows the differences in gray level across the image. This is due to surface undulations due to polishing etc.

Examining Figure 32, regression analysis does improve the image but substantial areas are not totally corrected. For example the upper left hand side and the lower right hand size of the image. It was decided a better defocus strategy was required.

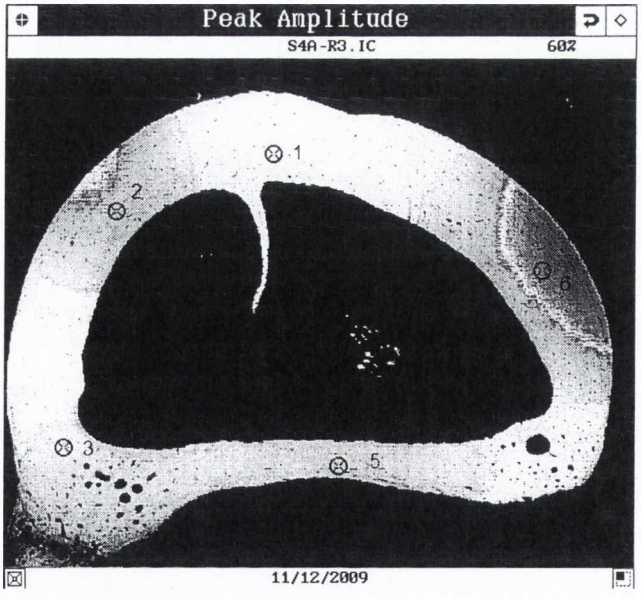


Figure 31 Points on Image with known focus. (Sample 4A)

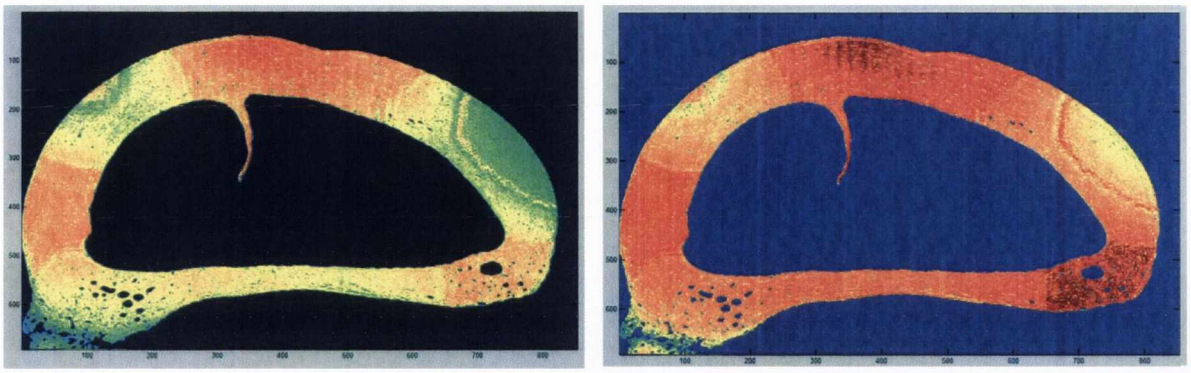


Figure 32 Sample 4A shown before (on left) and after (on right) regression analysis.

3.7.2 Focus Correction using Time of Flight estimation

The next idea to be explored was to use the relationship between TOF and amplitude. Acoustic reflection values are between 0.6 and 0.7 for bone. It is possible to develop a map of the TOF over the whole image from the relationship between measured amplitude and TOF, as shown in Figure 28.

To summarise the technique, take a 15 by 15 pixel area surrounding the pixel of interest. The aim of this procedure is to remove the variation in amplitude due to the underlying variation in the bone sample height itself and quantify on a longer period, features due to surface undulations. With this averaged image it is possible to use the relationship between amplitude and TOF in Figure 28 to create a map of TOF for the whole image.

ImageJ (Version 1.43u, NIH, USA) was used to clean up the raw SAM images. This comprised of removing black or white pixels which occurred in the images due to errors in produced by the SAM machine. This was carried out using the outlier filter. The image was then exported out as a bitmap from ImageJ.

The image was then imported into MATLAB R2007b (The Mathworks Inc., Natick, MA, USA) and each pixel was converted to an amplitude value from 0 to 1. An averaging filter was then applied to the original image. Various averaging levels were tested and 15x15 was found to be the most effective. This meant the average value was found over a 15x15 pixel area around a particular pixel. This value was then stored in a new matrix. This procedure was repeated for all pixels in the image.

The TOF matrix was then transformed back into a matrix of amplitude values. However this time it consisted of correction values for defocus of acoustic lens. The next stage was to find the inverse of these values and multiply it by the original image. This in effect corrects for defocus in the original image.

The corrected image is then calibrated using the calibration line in Figure 27. Next these corrected and calibrated images of reflectance can be converted into Z (Acoustic Impedance) and C_{33} (Elastic Modulus) using the equations below:

$$Z = \frac{R_{bone} + 1}{R_{bone} - 1} 1.48 \qquad \textit{Equation 3-2}$$

$$C_{33} = 1.31 + 0.075Z + 0.5Z^2 \qquad \textit{Equation 3-3}$$

$$E_3 = 0.865C_{33} \qquad \textit{Equation 3-4}$$

This process is explained more clearly with the help of two flowchart diagrams:

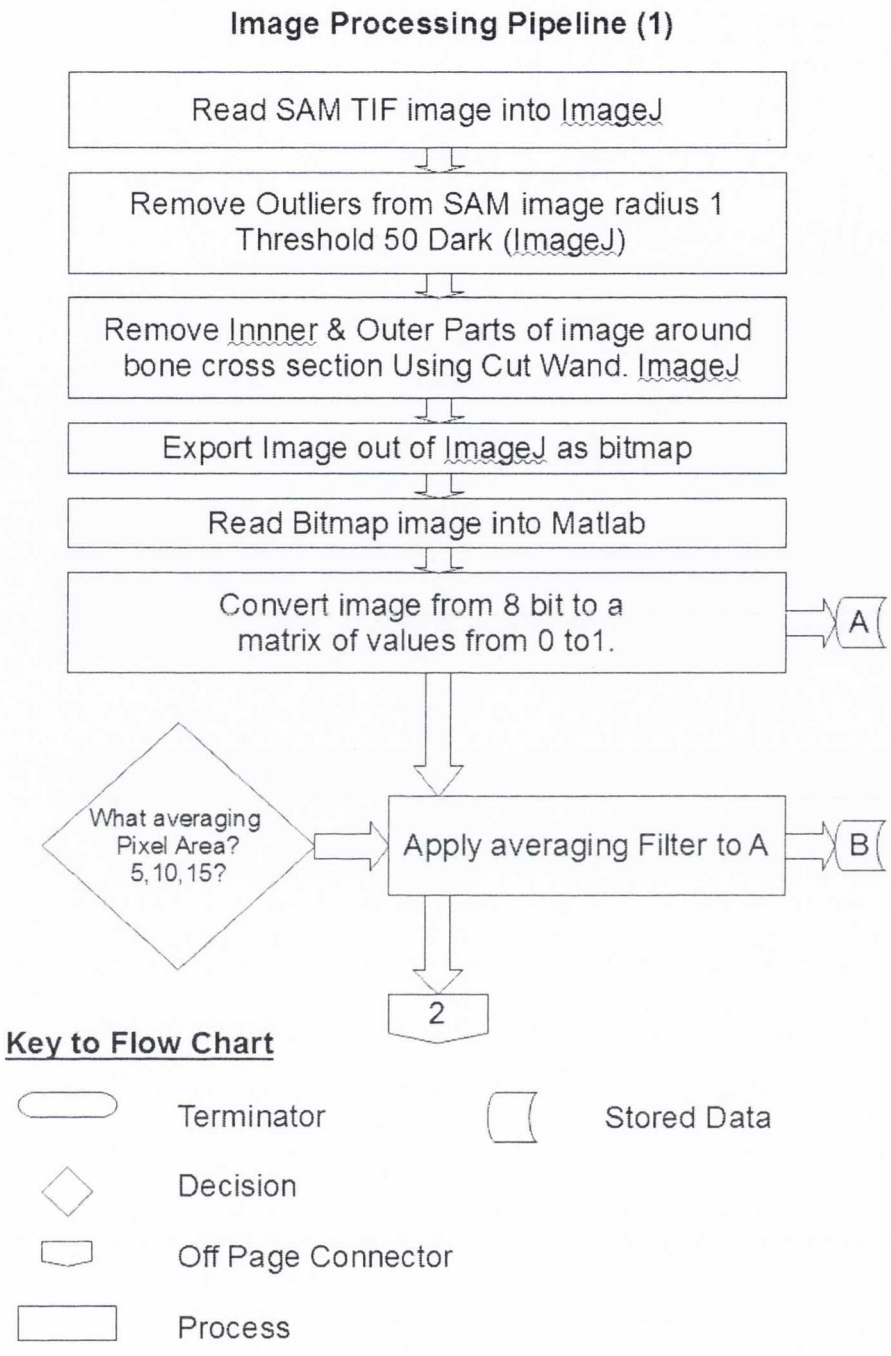


Figure 33 Flowchart 1 Image Processing Pipeline.

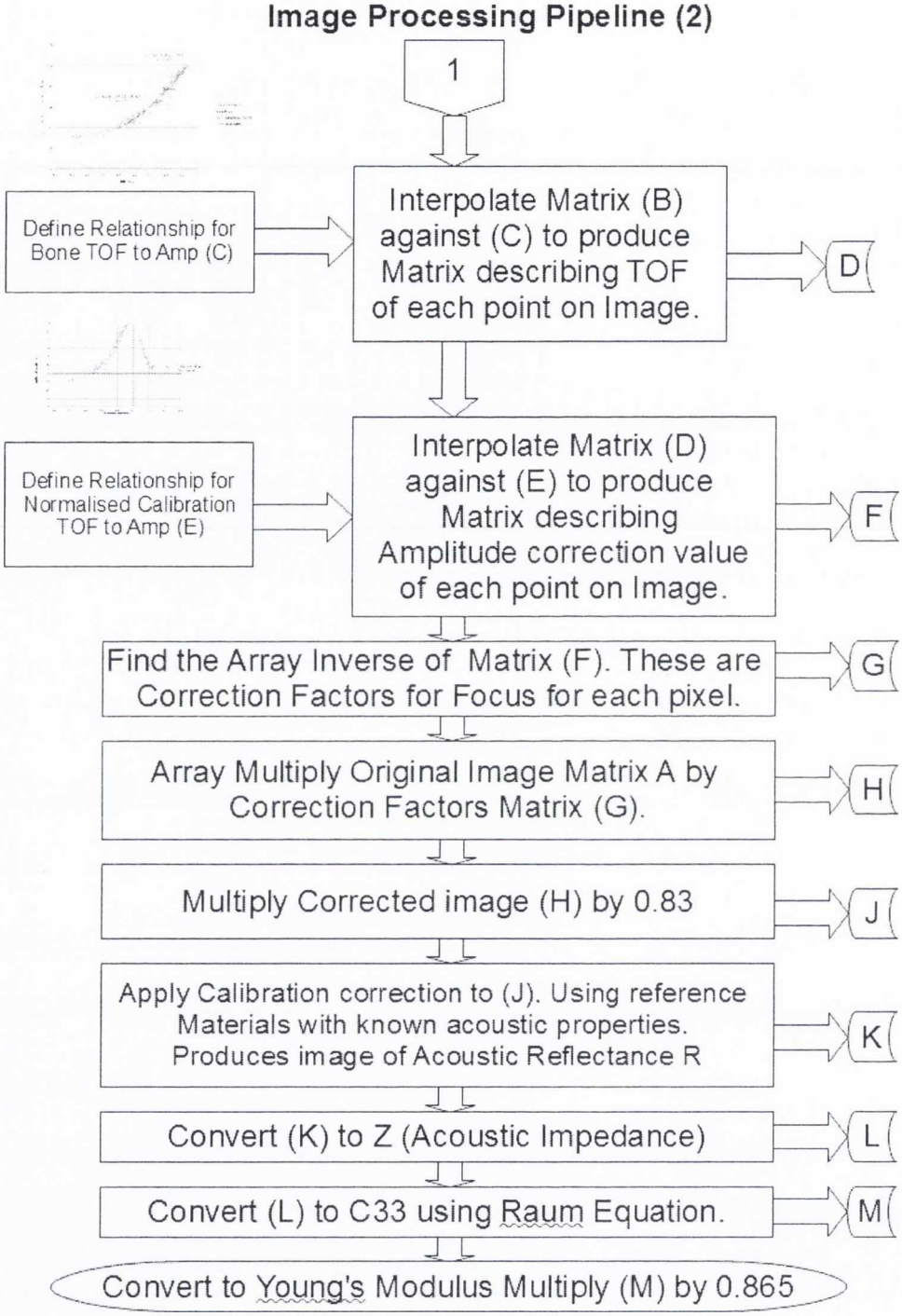
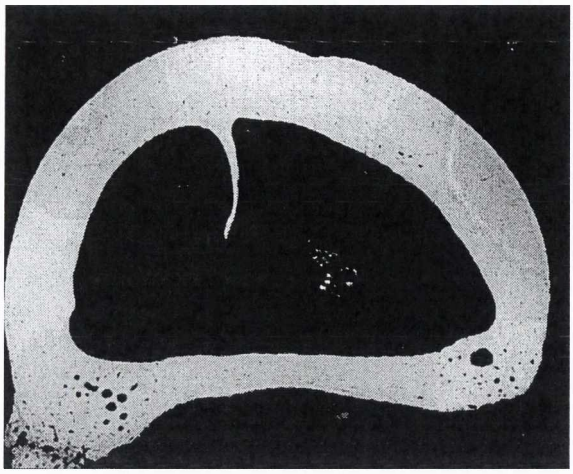


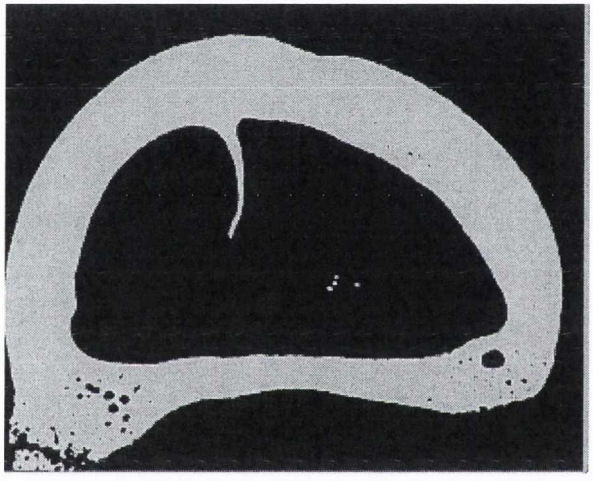
Figure 34 Flowchart 2 Image Processing Pipeline.

Figure 35 illustrates the impact of the focus correction procedure detailed in Figure 33 and 34. The original image from the SAM is shown in Figure 35(a). In Figure 35(b) five pixel by five pixel averaging is observed to remove areas out of focus as shown in Figure 34(a) as large areas darker than surrounding areas. In Figure 35 (c) fringing at the edges of the

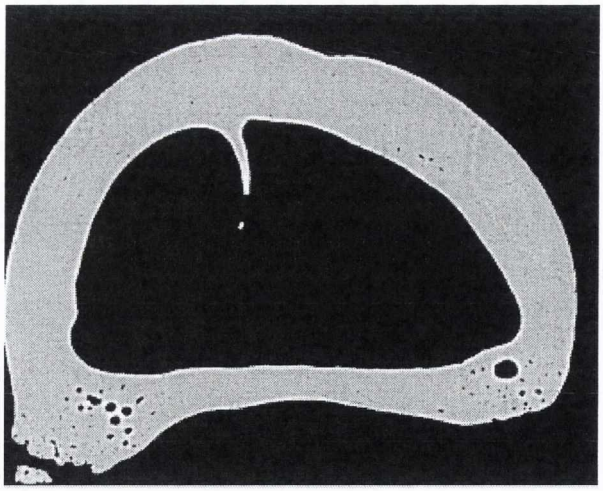
bone sample is observed. A simple solution was devised where the black background was changed to the average grey value of the bone area. This was done before the averaging algorithm was applied to the image. When the averaging procedure had been carried out the non-bone area in the image was then returned to its previous state.



(a) Original Image.



(b) 5x5 Averaging.



(c) 15x15 Averaging.

Figure 35 Averaging applied to original SAM image to account to surface undulations.

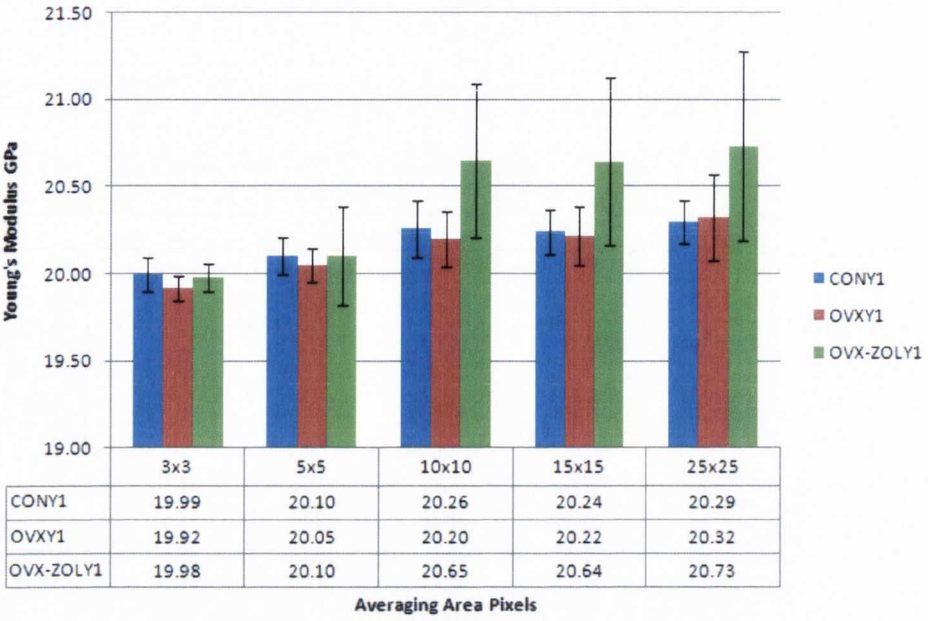
3.7.3 Selection of appropriate averaging size.

Table 14 illustrates appropriate choices of averaging area by comparing these areas to size of micro-structural features in cortical bone. The minimum sampling area, which achieved good results, was a 15x15 area. The 15x15 pixel area corresponds to an area over twice that of an average osteon of a diameter of 250 microns.

Averaging pixels	**Area mm^2**	**Cortical Bone Feature with similar Area.**
3x3	$5.625x10^{-3}$	Haversian Canal
5x5	$1.562x10^{-2}$	
10x10	$6.25x10^{-2}$	Osteon
15x15	$1.406x10^{-1}$	
20x20	$2.5x10^{-1}$	Group of Osteons
25x25	$3.906x10^{-1}$	

Table 14 Averaging in mm^2 for each increment. Note an osteon has area of about $6.25x10^{-2}mm^2$.

A study was performed on all samples to investigate the effects of averaging area size on parameters such as the mean, median and standard deviation. A summary of this analysis is shown in Figure 36. From analysis of this Figure an observation can be made that the mean and standard deviation of Young's modulus converges as the number of averaging pixels increases.



	3x3	5x5	10x10	15x15	25x25
CONY1	19.99	20.10	20.26	20.24	20.29
OVXY1	19.92	20.05	20.20	20.22	20.32
OVX-ZOLY1	19.98	20.10	20.65	20.64	20.73

Figure 36 The relationship between the Young's Modulus and averaging area for a range of averaging areas. There are 18 sub samples for CONY1, OVXY1 and 12 for OVX-ZOLY1. Each sub sample has 5151 pixels.

Another conclusion from this study shows that an increase in averaging area was observed to reduce the number of outliers. This fact leads to choosing the 15x15 averaging area.

The Fourier analysis shown in Figure 37 indicates that there is a cluster of small period features with periods of between 2 and 22 pixels. There are two others peaks at about 30 and 60 pixels. These are most likely due to surface undulations and not changes in the acoustic properties of the bone sample. By combining the findings of Figure 36 and 37 it can be seen that a suitable choice of averaging is 15x15 pixels.

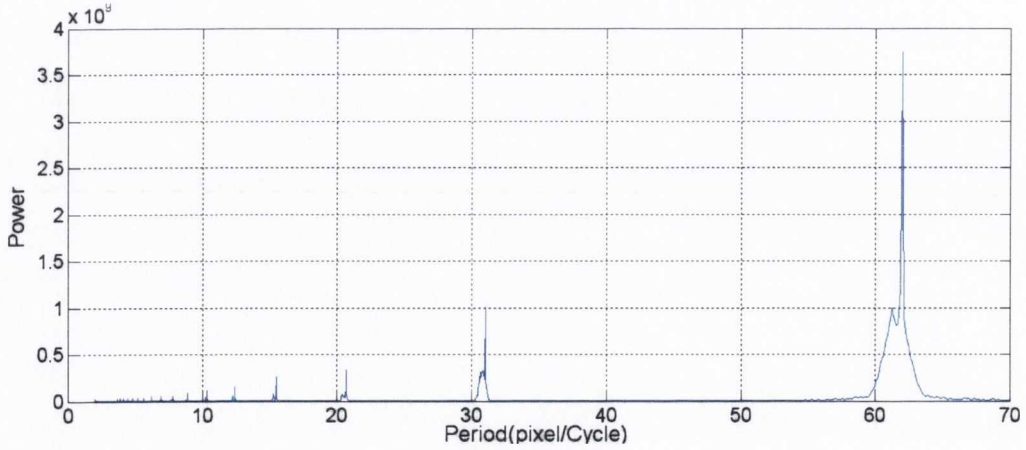


Figure 37 FFT frequency domain plot from 0 to 70 pixels. An area of a SAM Image was chosen (25110 pixels). This consisted of the raw unprocessed image data. This data was taken from sample 15.

3.7.4 Uncertainty analysis of image processing pipeline

Each step of image processing introduces errors and uncertainties into the results. Broadly speaking our input is the raw reflectance from the SAM, the output of the process is a value of elastic stiffness C_{33} for the stiffness of the underlying bone being imaged. In the table below is an estimate for the standard deviation for a sample for each image processing step. These are then summed in quadrature.. It can be seen that the largest contributor to error is in the conversion of acoustic impedance Z to elastic stiffness C_{33}. The negative impact of this can be reduced by limiting the depth to which focus correction is applied, i.e. as defocus increases error increases.

	Standard Deviation	
Error source	GPa	**Note**
Focus correction	1.78	Limiting Focus correction to 8.8μsec and above.
Calibration with known materials	3.19	Found by experiment
Conversion of Z to C_{33}	8.3	Raum *et al.* (2006)
Errors summed in quadrature	**9.06**	

Table 15 Breakdown of error sources for image processing pipeline.

3.8 FE Analysis

Three samples of each SAM image, 101 by 51 pixels, was analysed using Finite Element Analysis (FEA). A tensile load of 1500 μ strain was applied at each end of selected area. An eight node quadrilateral 2D element was used (PLANE183). This element was used in its plane stress mode. An ANSYS (ANSYS Inc., Canonsburg, PA, USA) APDL script was written to import E_3 data into the FEA model for each sample. More details can be found in Appendix 7.2.

3.8.1 Input images:

The images from the image processing stage were transformed into FE models using a customised ANSYS APDL script. A number of sections of each of the bone samples were selected from each of the sample types (OVX, CON & OVX-ZOL). There are 21 sample images and three sub-images from each of these were selected randomly giving 63 FE models in total.

3.8.2 Modelling Assumptions.

Each sub-image was 51 by 101 pixels. Each pixel was 25 microns across and was assigned with a value for stiffness. Each pixel in the image corresponded to an element. There were 5151 elements in each sub-image.

Plane stress was assumed in the element formulation. A plate loaded in its midplane is said to be in a state of plane stress, or a membrane state, if the following assumptions hold:

1. All loads applied to the plate act in the midplane direction, and are symmetric with respect to the midplane.

2. All support conditions are symmetric about the midplane.

3. In-plane displacements, strain and stresses can be taken to be uniform through the thickness.

4. The normal and shear stress components in the z direction are zero or negligible.

5. The plate is fabricated of the same material through the thickness (Felippa 2011).

In this study all these conditions can be met.

The finite element model has linear material properties but the distribution of these properties is not homogenous.

3.8.3 Material Models

The finite element model had 168 material properties from 2 GPa to 70 GPa. Between 2 and 40GPa the increment of Young's modulus property was 0.25GPa, above 40 GPa the increment was 2 GPa. There was also a null property for pixels below 2GPa. These were assigned values of 1E1N/mm^2 (1 MPa). A Poisson's ratio of 0.3 was assumed for all material models.

3.8.4 Element type

An eight node quadrilateral, two dimensional element was used. (PLANE183 ANSYS Element). This element is available with 2x2 and 3x3 integration points. 3x3 integration points were used in this analysis. Having more integration points can help with resolving the deformation better across the element, hence the stress and strain contours. It was used in its plane stress mode.

3.8.5 Loads and constraints

An applied displacement of 1500 μ strain was applied to the model. This equated to a displacement, in mm, which gives 1500 μ strain. The section was 2.525mm long.

To apply a load of 1500 μ strain a displacement of :

$$0.0015*2.525= 0.00378\text{mm}$$

is required.

The constraints consist of the line on left hand side of Figure 39 being constrained for zero displacement in the horizontal direction. The bottom left keypoint was constrained in all directions.

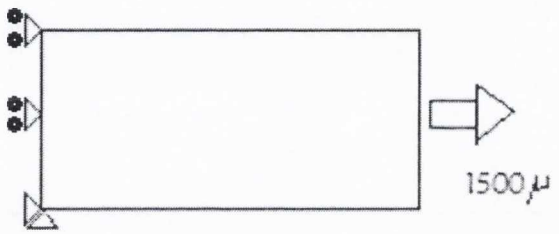


Figure 38 Loads and constraints on analysed section.

3.8.6 Results Required:

1. Plots of Equivalent stress and strain across the bone sections.

2. Plots of the material properties across the bone sections.

3. Output files containing the stress and strain results for later processing in MATLAB and MINITAB 16 (State College, PA, USA) to produce histograms.

Equivalent stress is computed as:

$$\sigma_e = \left[\frac{1}{2}((\sigma_1-\sigma_2)^2+(\sigma_2-\sigma_3)^2+(\sigma_3-\sigma_1)^2)\right]^{\frac{1}{2}} \quad \textit{Equation 3-5}$$

Equivalent strain is computed as:

$$\varepsilon_e = \frac{1}{1+\upsilon}\left[\frac{1}{2}((\varepsilon_1-\varepsilon_2)^2+(\varepsilon_2-\varepsilon_3)^2+(\varepsilon_3-\varepsilon_1)^2)\right]^{\frac{1}{2}} \quad \textit{Equation 3-6}$$

Where σ_1, σ_2 and σ_3 are principal stresses and ε_1, ε_2 and ε_3 are principal strains (ANSYS 2004).

3.9 Statistical Analysis Procedures:

Detailed in the following section is a description of the statistical procedures applied to the data.

3.9.1 Descriptive Statistics Required

These consisted of graphical plots of the distributions of Young's Modulus, stress and strain for each experimental unit and each treatment (Histograms, boxplots and empirical cumulative frequency distributions). Basic statistics for each experimental unit and treatment were also generated. These consisted of: mean, median and standard deviation.

3.9.2 Statistical inference test applied to results:

The tests for statistical significance outlined below were applied to both the Young's modulus data and the results of the FEA (Equivalent stress and Equivalent strain). If the p-values found by tests of inference are found to be less than α=0.05 then the null hypothesis will be rejected.

t-test

The null hypothesis for all tests is that there are no differences between the sample means of Young's modulus, stresses and strain for the comparisons shown in Table 13. The null hypothesis is assumed true until proven otherwise. This testing was applied using Mintab 16.

Anderson Darling Normality Test on distributions.

A test for normality was performed on all experimental units. This was done to see if the conditions for the valid use of ANOVA were met. If this condition was not met then non-parametric ANOVA like statistical test for inference was used such as Kruskal Wallis. This testing was applied using Mintab 16.

One way ANOVA

A one way ANOVA test was chosen to test if the means of the five groups were the same. The null hypothesis was that all samples from the five groups have the same means. This testing was applied using Mintab 16.

Kruskal Wallace test

The Kruskal Wallace procedure is a one way analysis of variance by ranks and is a non-parametric method for testing whether samples originate from the same distribution using the median values. The null hypothesis was that the sample medians are the same. This testing was applied using Mintab 16.

Kolmgorov-Smirnov test

A non parametric test, which compares both means and standard deviations of two bell shaped sets of data was applied to in comparisons of OVX and CON samples (Wallace *et al.* 2010). This test is known as the Kolmogorov-Smirnov test of the underyling distributions. It is sensitive to differences in both location and shape of the empirical cumulative distribution functions of the two samples. The null hypothesis was that the distributions were the same. This testing was applied using Mintab 16 macro and the R statistical software package.

Anderson-Darling k-sample test.

The Anderson-Darling K-sample test can be used to test whether several independent random samples of various sizes come from the same but unspecified continuous

distribution. This was applied to answer the question of: Do the five sample types share a common distribution or not? The test was also applied within the year 1 and year 2 sample groups. This statistical test was applied using the R statistical package using a package called ADK (Scholz *et al.* 1987).

3.10 Conclusions

In this chapter, methods have been presented which are capable of testing the hypothesis that biophysical stimuli (stress and strain) are altered fundamentally within cortical bone tissue by osteoporosis, and that treatment returns them to normative values. These methods combine scanning acoustic microscopy and finite element analysis of the "Bone for Life" bone samples.

4 Results

4.1 Experimental Results

Experimental data were collected from the Scanning Acoustic Microscope (SAM) in the form of images and tabulated data. These data were then processed for analysis. This involved image processing, statistical analysis and finite element analysis. As described in the methods section, a number of image processing methods were tested and it was found that an averaging area of 15 by 15 pixels for focus correction gave the best results. These are the results presented here. The data discussed here were collected during two sessions 11th December 2009 [Year 1 samples] and 30th September 2011 [Year 2 samples].

4.1.1 SAM images

Raw images were captured from the SAM, of bone and calibration samples, in lossless tagged image file format (TIFF). Shown below are a number of the processed images used. The samples were imaged at an attenuation of 20dB, See Figure 40 and 41 below. This was found to be the best attenuation setting after considerable amounts of testing. The choice of attenuation is dependent on the type of SAM imaging, the material being imaged and acoustic lens being used.

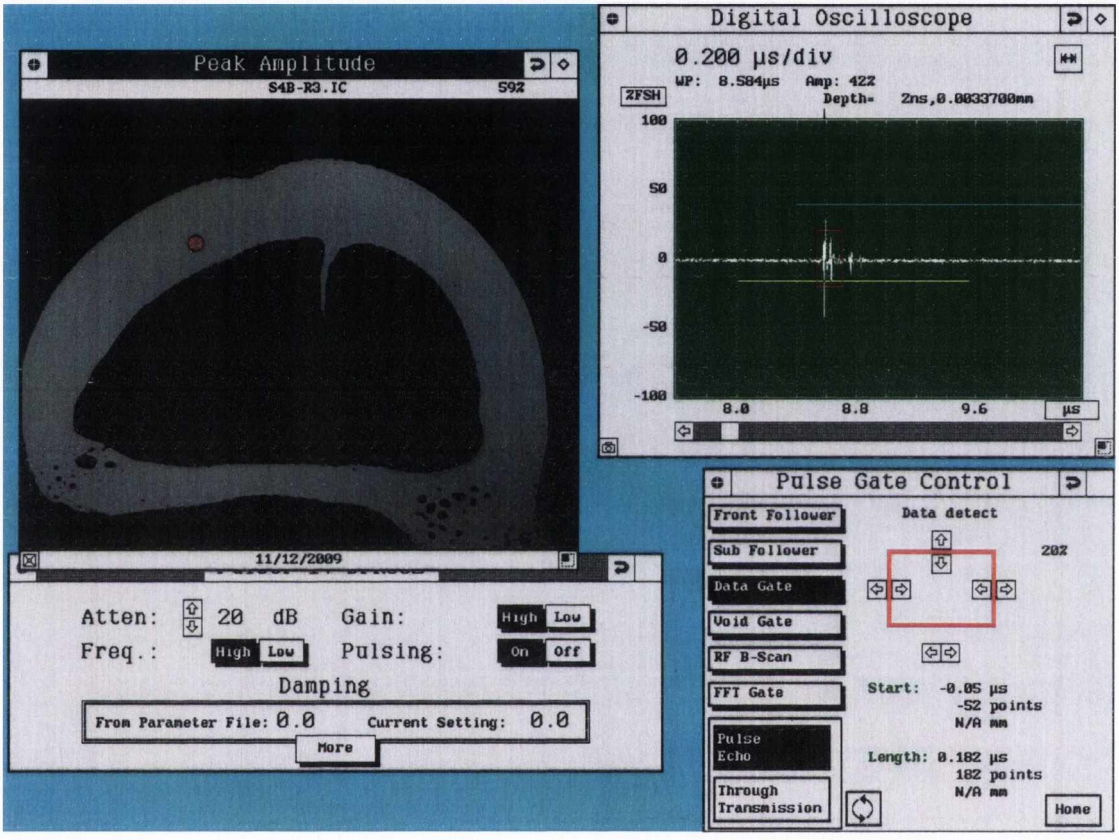


Figure 39 Screenshoot from SAM, showing image of sample 4b.Showing the acquired SAM image top left , The A-scan for the point shown with water path (WP) and amplitude is displayed in the top right.

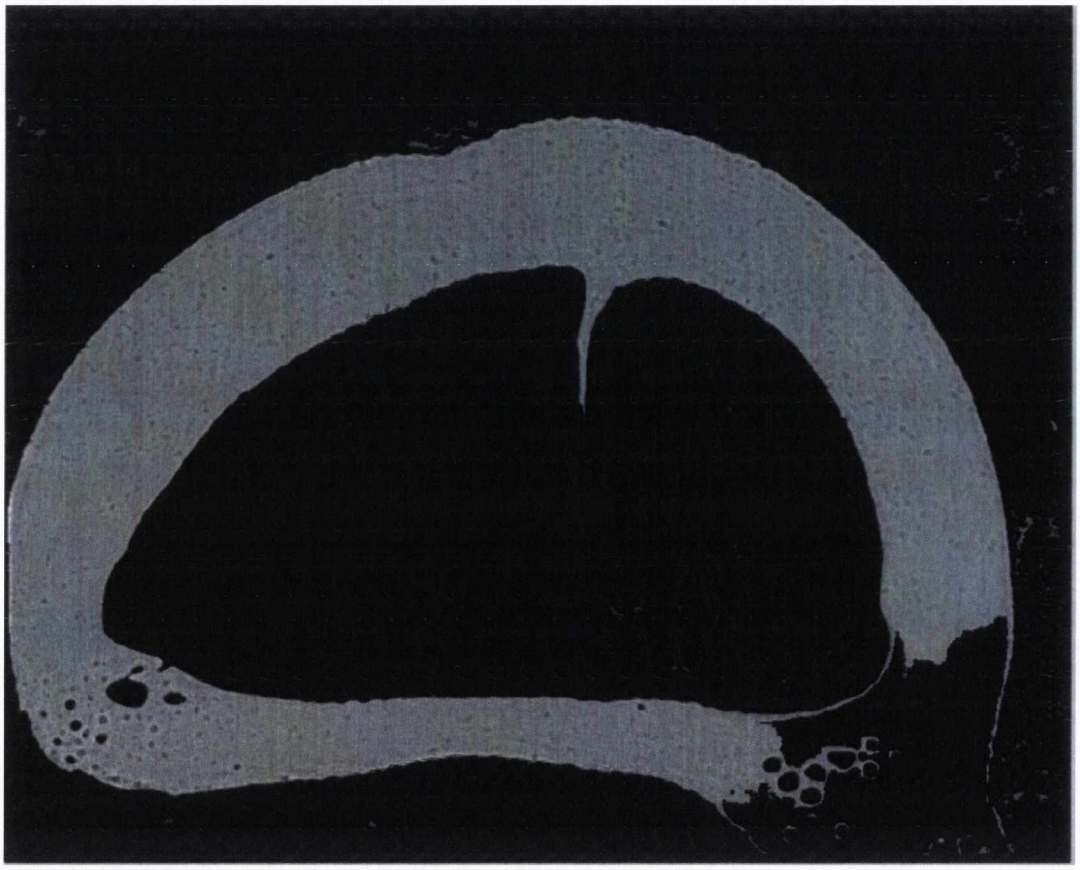


Figure 40 Input Image for Sample 4b. Acoustic Reflectance R, 15x15 averaging. Area shown in black at bottom right of image is out of focus.

4.1.2 Acoustic lens characterisation

A large number of individual points were measured on each bone sample and each of the calibration samples. This exercise served a number of functions. It allowed the creation of a characteristic curve of Time Of Flight (TOF) Versus Amplitude for each material. Data of this type could be used to correct for focus errors in each sample, due to surface irregularities, see Figure 42.

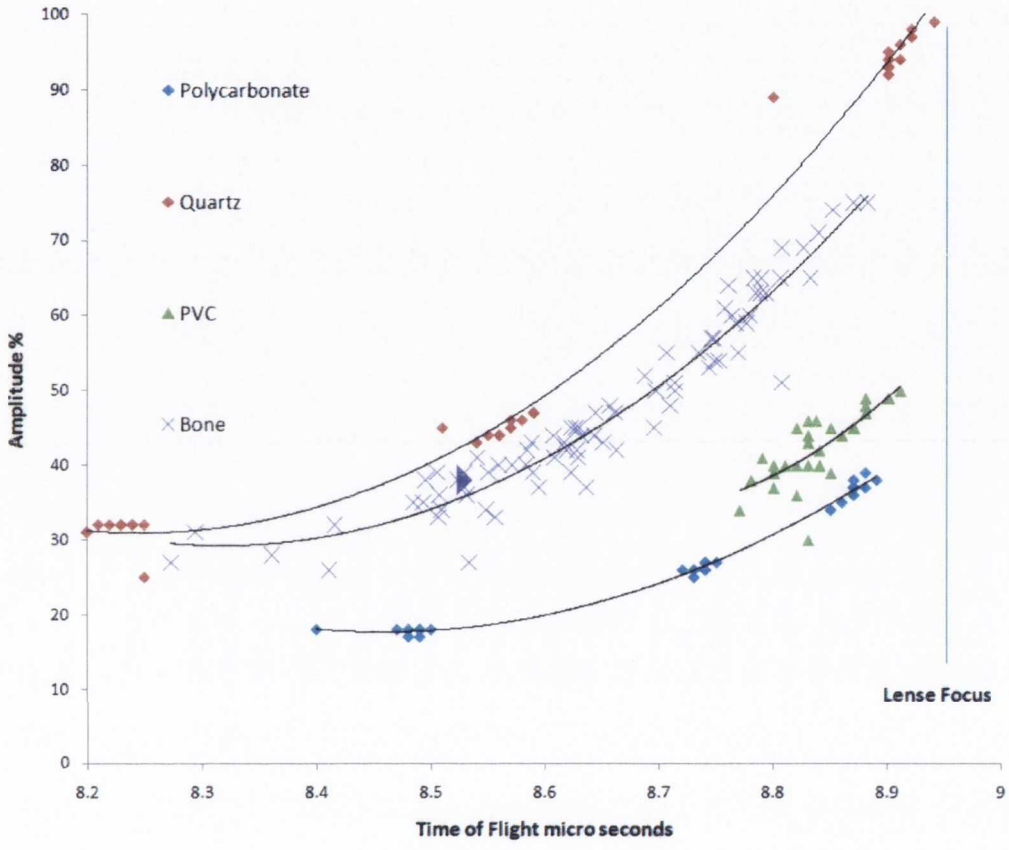


Figure 41 Lens characteristic curves for Bone, Quartz, PVC and PC. (11-12-2009)

4.1.3 Calibration

Calibration samples were imaged using SAM. This data was used to create a calibration curve of samples with known properties of acoustic Reflectance (R) and Impedance (Z). The calibration samples have a known thickness (1mm) and are flat. The samples were setup and imaged with the acoustic lens at a known focus on each sample. These samples were also imaged at the same attenuation as the bone samples. Bone samples had to be corrected for defocus. This was accomplished by applying a correction factor found from Figure 43 to give the measured amplitude at focus for each calibration material, see Table 16.

The plots below (Figure 43) show that the calibration data has a small standard deviation and can be used to accurately calibrate the SAM to measure the acoustic reflectance of the bone samples. The results shown in Figure 43 are for the SAM study carried out on the 11th of December 2009.

	Measured Mean Amplitude	Water Path µSec.	Defocus corrected mean Amplitude	Defocus corrected Standard Deviation	Count
PVC	0.47	8.87	0.53	0.025	10000
PC	0.37	8.87	0.4	0.015	10000
QZ	0.93	8.9	1.03	0.024	10000

Table 16 Measured acoustic reflectance for calibration materials. (20dB attenuation). (11-12-2009).

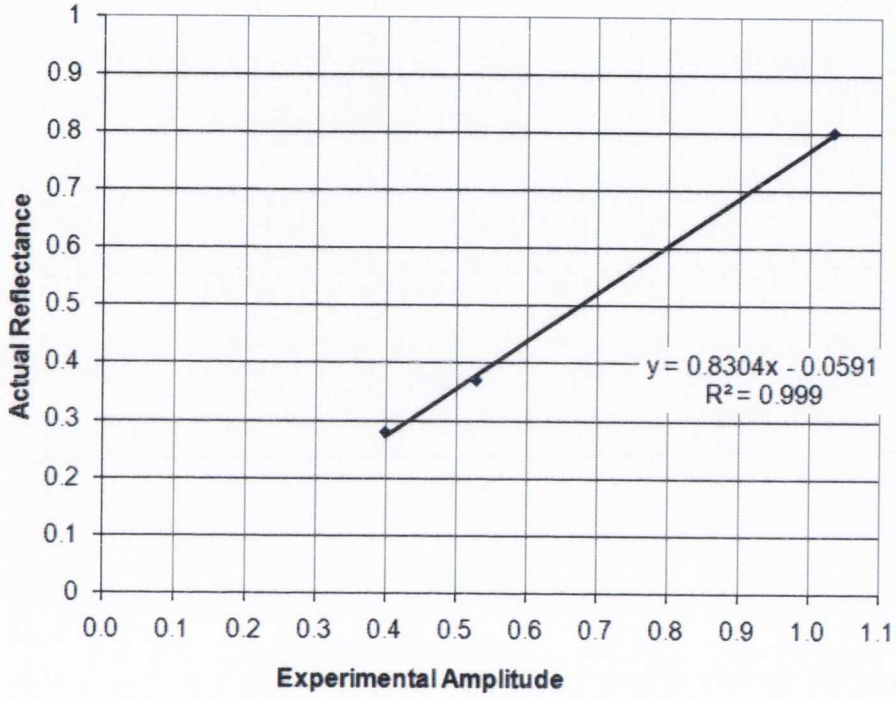


Figure 42 Calibration curve relating measured acoustic reflectance to actual acoustic reflectance. (20dB attenuation) (11-12-2009).

4.1.4 SAM Images

Displayed in the Tables 17 to 20 below are the unprocessed images taken from the SAM. These are divided into year 1 and year 2 samples.

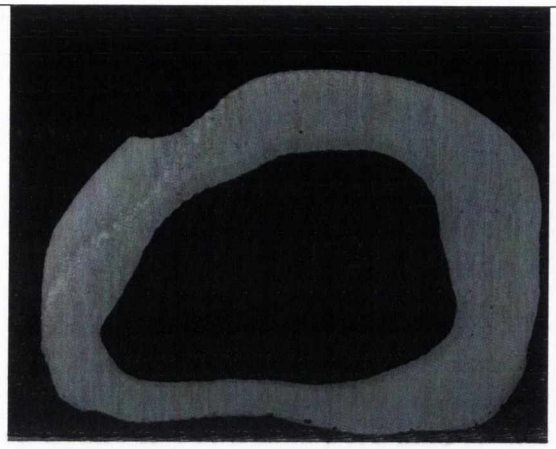
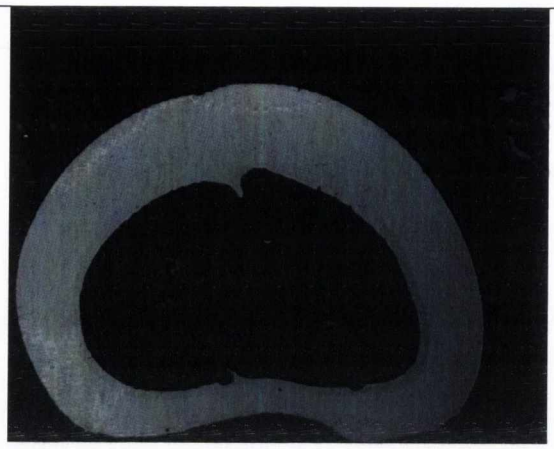
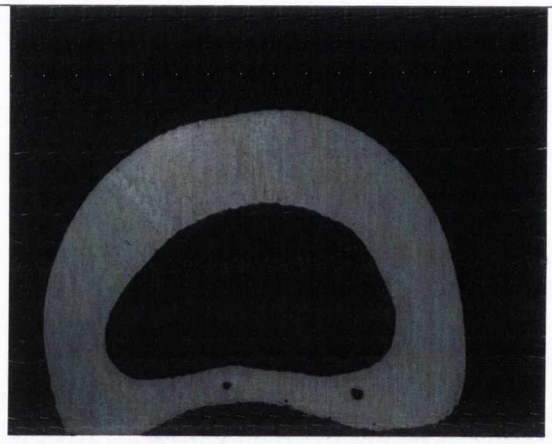
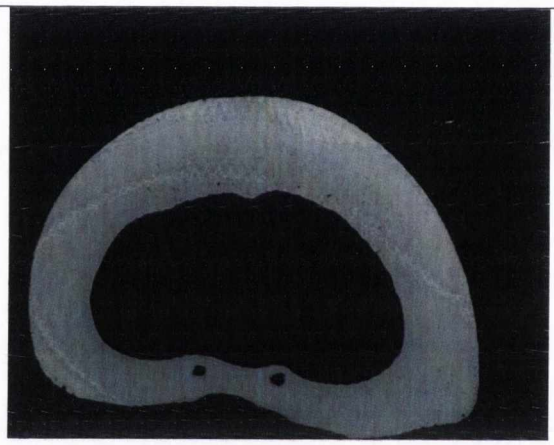
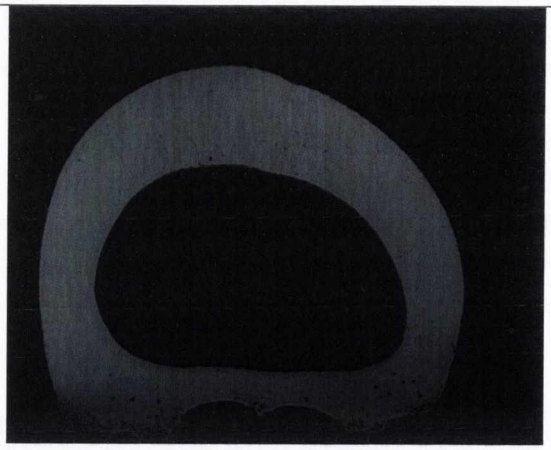
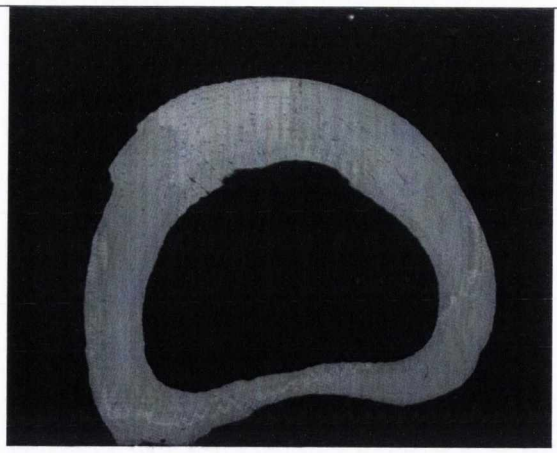
	
2	20
	
5B	22B
	
6	31

Table 17 Unprocessed SAM images, Control year 1 samples (CONY1) imaged on the 11th December 2009.

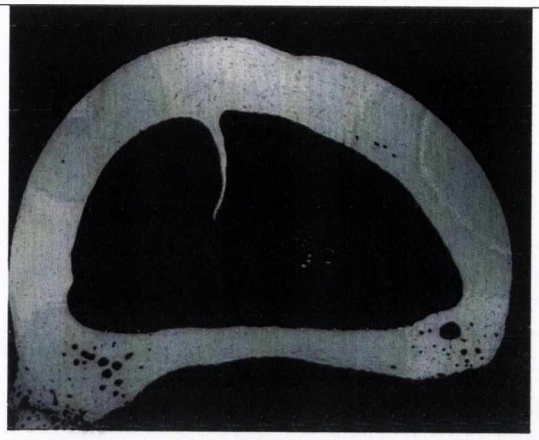
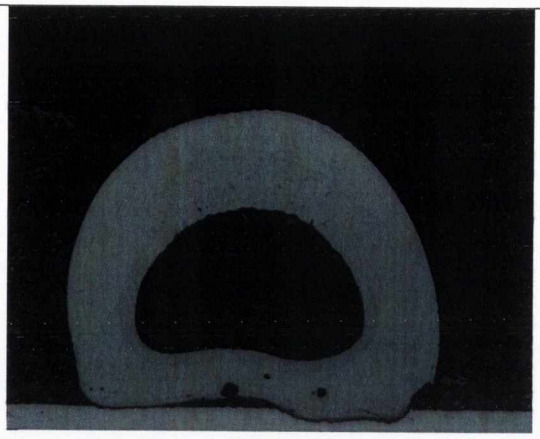
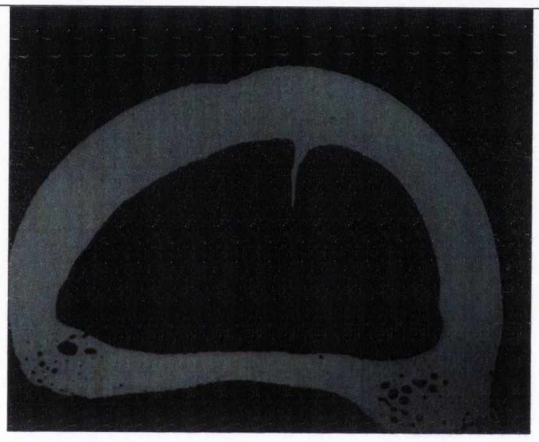
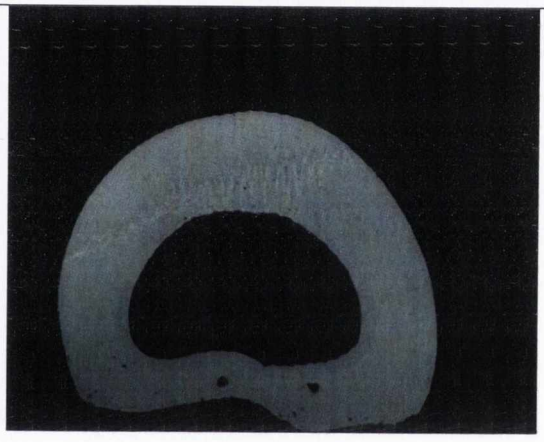
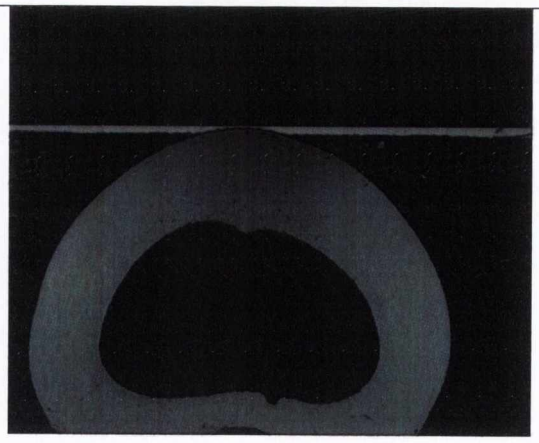
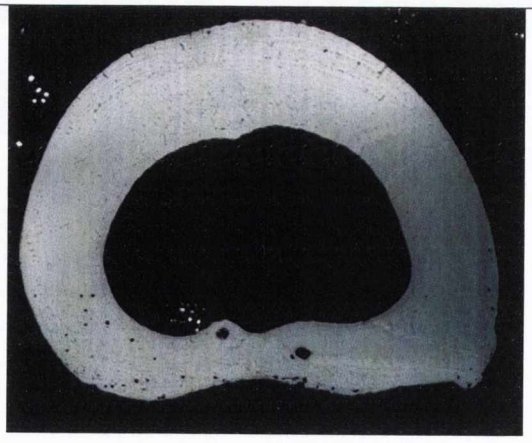
	
4A	23
	
4B	23B
	
15	32A

Table 18 Unprocessed SAM images, ovariectomised year 1 samples (OVXY1) imaged on the 11th December 2009.

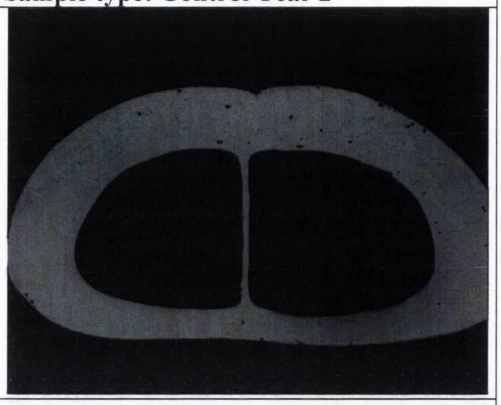
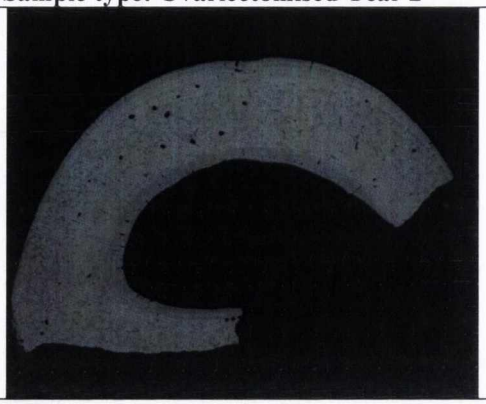
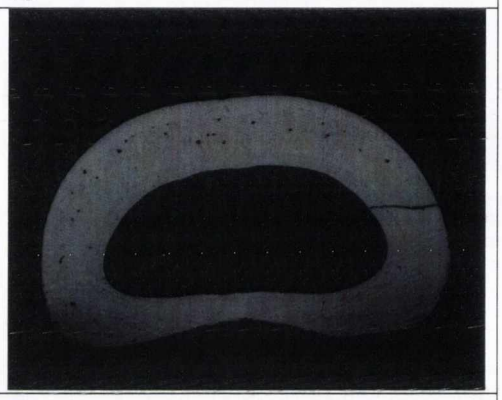
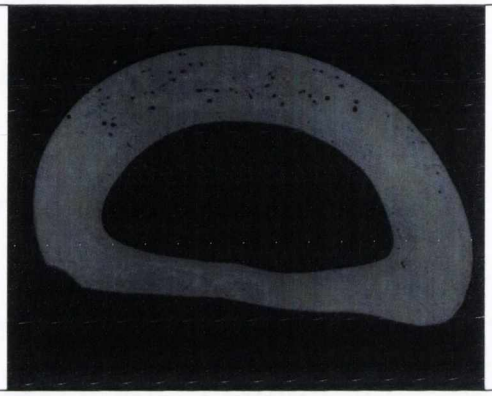
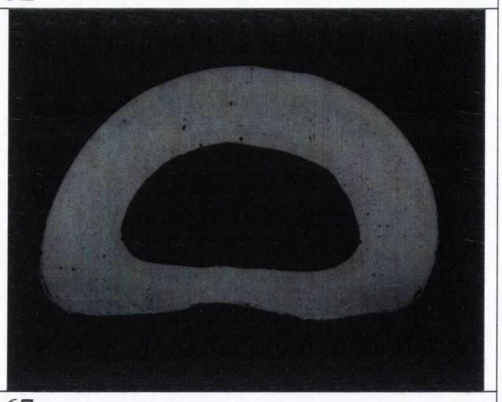
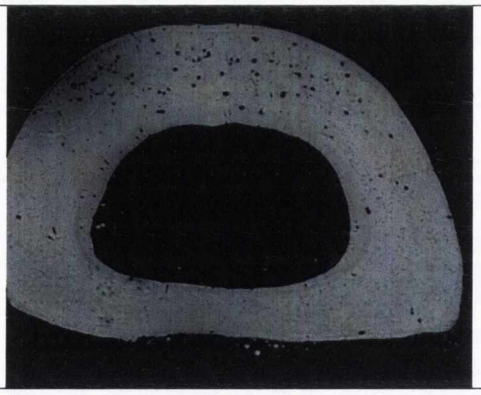
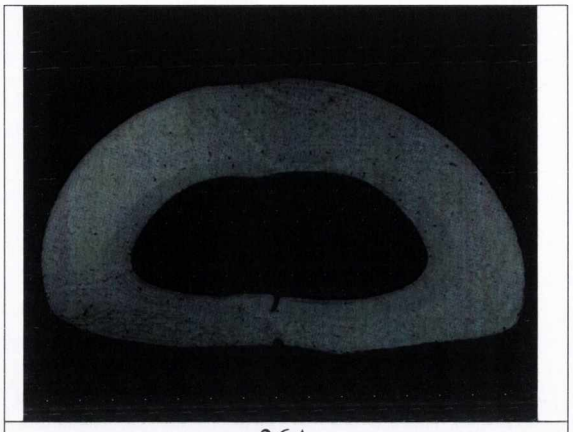
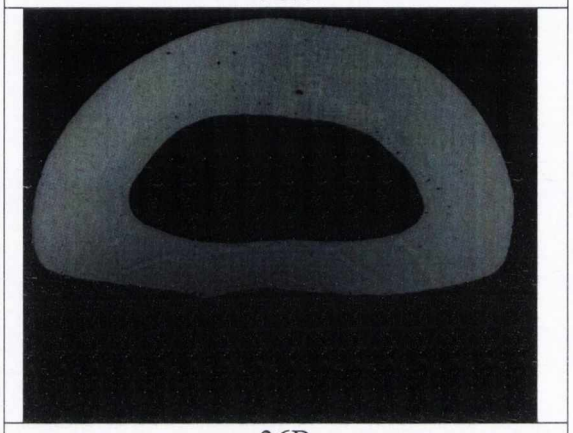
Sample type: Control Year 2	Sample type: Ovariectomised Year 2
	
40	45b
	
52	54
	
67	58

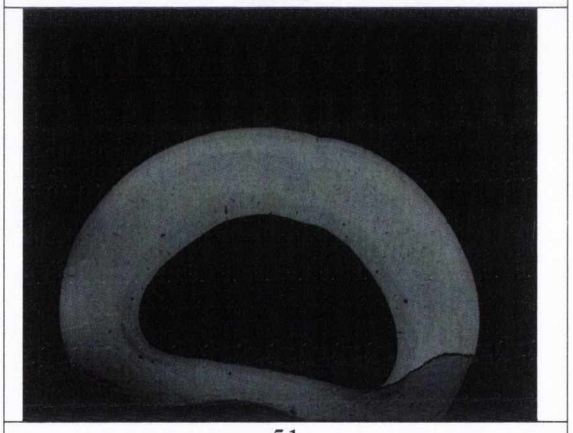
Table 19 Unprocessed SAM images. Samples in left column are control year2 (CONY2). Samples in the right column are the ovariectomised year 2 samples (OVXY2). Imaged on the 30th September 2011.



36A



36B



51

Table 20 Unprocessed SAM images, ovariectomised year 2 bone samples (OVX-ZOLY2). Imaged on the 30 9 2011.

4.2 Processed Results

4.2.1 Finite Element Analysis Results Plots

The raw SAM images were transformed into maps of Young's Modulus for each sample. Three sections of each sample were extracted (51x101 pixels) and used to create a finite element model. The locations chosen in each SAM image can be found in Appendix 7.1.

The data extracted from these finite element models was of the form of stresses and strain (Equivalent) for each element. This data is displayed in graphical form below in Figure 44 and 45.

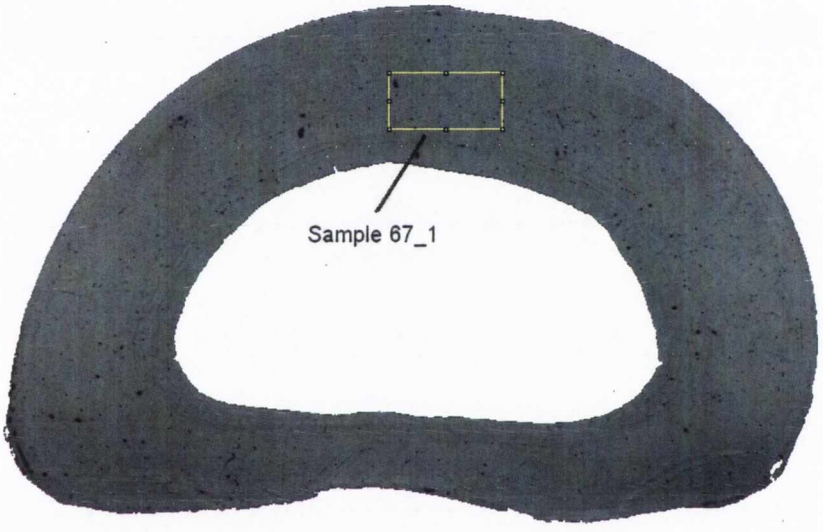


Figure 43Raw SAM image of Sample 67 showing location of sub-image 1.

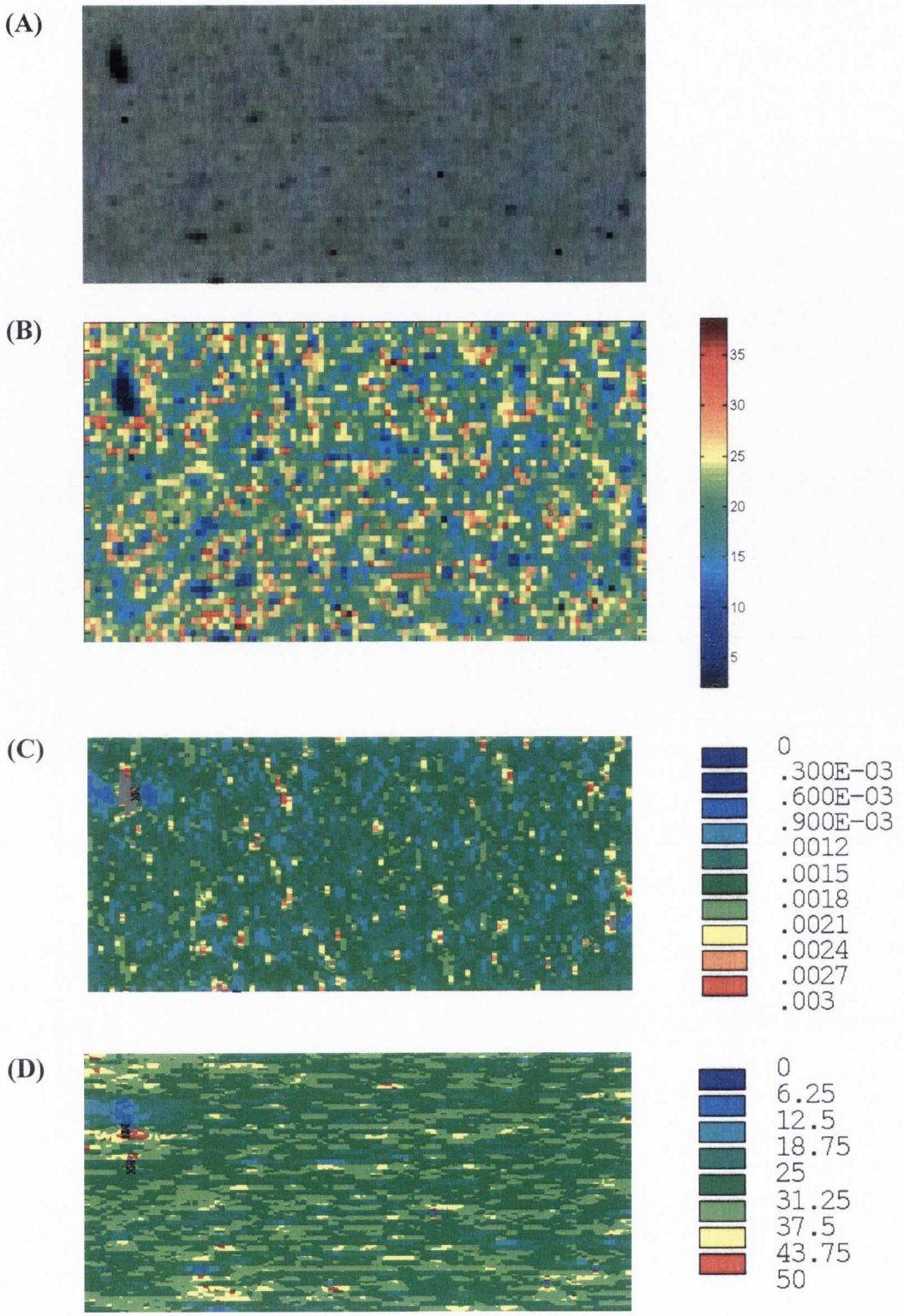


Figure 44(A) Raw unprocessed sub-image sample 67, (B) Young's Modulus (GPa) values assigned to FE model, (C) Equivalent strain, (D) Equivalent stress (MPa).

4.3 Descriptive Statistics

Descriptive statistics are provided for the Young's modulus data, which was inputted as material properties for the finite element analysis. Statistics are also provided for equivalent stress and strain which were outputs of the finite element analysis. For the purposes of statistical analysis the data derived from images shown in Tables 16, 17, 18 and 19 were prefixed with the letter "s". For example data derived from sample image 54 in Table 18 becomes "s54" in the statistical analysis data shown below.

4.3.1 Young's Modulus

Young's modulus data was produced for each sample from the image processing of the raw SAM images, See Table 21 below.

Sample type	Year 1	Mean (GPa)	StDev	Median	Year 2	Mean(GPa)	StDev	Median
Control (CON)	s2	20.386	4.448	20.337	s40	19.985	4.376	19.949
	s5B	20.092	3.395	20.159	s52	20.179	4.887	20.119
	s6	20.137	3.667	20.001	s67	20.040	4.689	20.191
	s20	20.328	4.386	20.120				
	s22b	20.181	3.613	20.145				
	s31	20.307	4.044	20.558				
Ovariectomised (OVX)	s4a	20.488	4.081	20.546	s45b	21.026	7.101	20.763
	s4b	20.277	4.142	20.153	s54	20.220	6.787	20.008
	s15	20.103	3.519	20.068	s58	20.302	6.321	20.431
	s23	20.178	3.894	19.967				
	s32a	20.169	3.417	20.213				
	s23b	20.071	3.476	20.007				
Drug treated Ovariectomised (OVX-ZOL)	No data				s36a	20.887	6.544	20.737
					s36b	19.759	3.564	19.906
					s51	20.234	4.849	20.262

Table 21 Young's Modulus (GPa) data for year 1 and year 2 samples.

The means, standard deviations and medians of the year 1 samples for Young's modulus between sample types show no significant differences. This is borne out in the empirical cumulative density function plots, boxplots and distributions, see Figures 45 to 48.

The means and medians of the year 2 samples for Young's modulus between sample types show little variation. The ovariectomised (OVX) sample types exhibit a greater standard deviation than the controls (CON). The situation with the ovariectomised drug treated (ZOLY2) samples is more complex with the standard deviations varying within individual samples when compared to the consistent standard deviations observed in the

individual samples of the control group. These observations are visible in the empirical cumulative density function plots, boxplots and distributions on the following pages, see Figures 45 to 48.

Note: In the diagrams below, OVX-ZOLY2 has been shortened to ZOLY2 referring to the ovariectomised drug treated year 2 samples.

The individual sample plots shown in Figure 45 and Figure 46 show that the year 1 samples of both sample types have very similar distributions.

In the year 2 samples it can again be observed that control and ovariectomised drug treated samples have very similar histogram distributions across individual samples, see Figure 46. The situation is very different with the ovariectomised samples with a consistently greater area in the left tail when compared with the control samples. There is also greater variability in the year 2 ovariectomised drug treated samples, this is indicated by the very different individual sample distributions found on Figure 46.

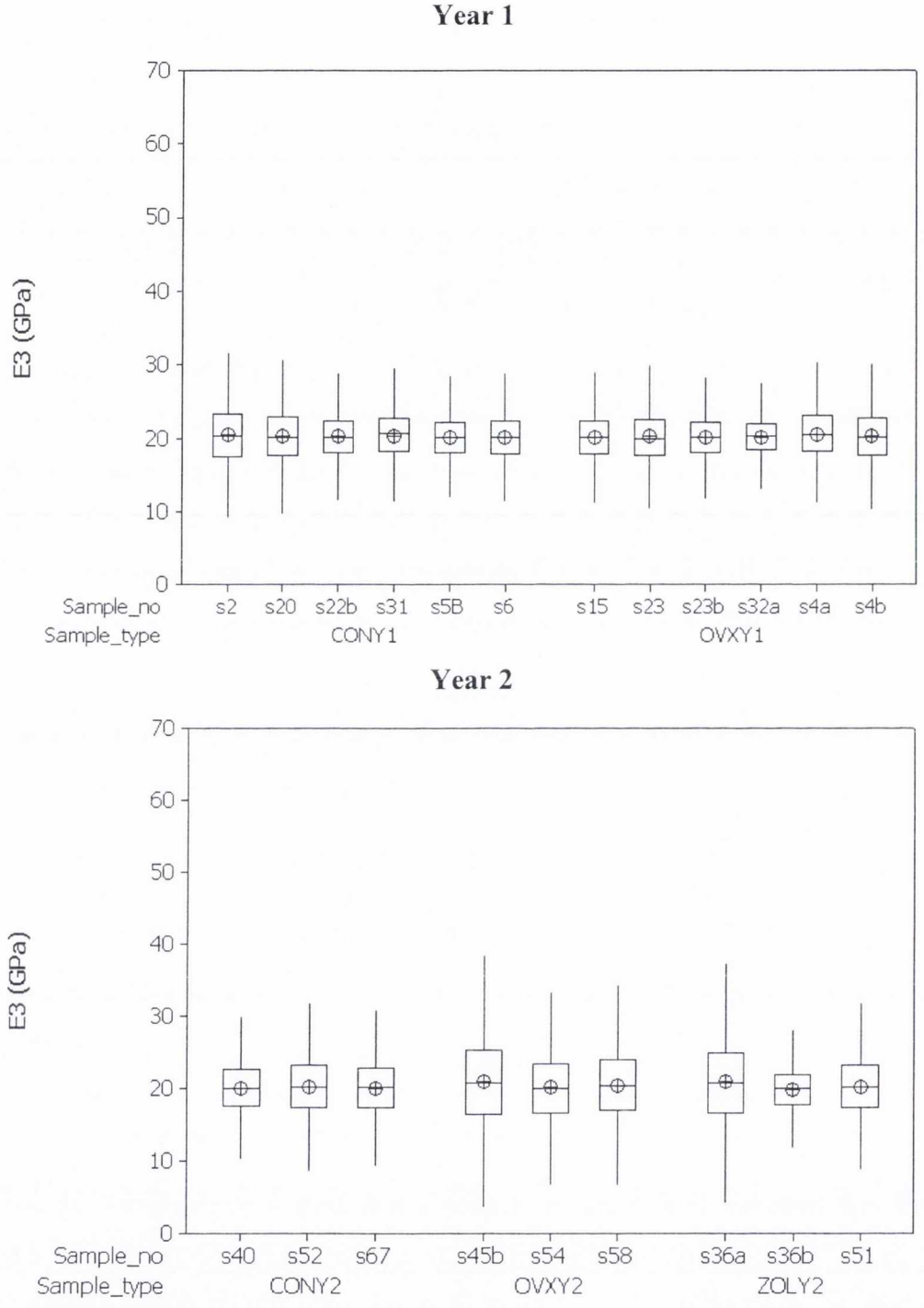


Figure 45 Boxplots of Young's modulus (GPa) for Year 1 (top) and Year 2 (bottom) Samples. Within the year 1 data there is little variation in mean and standard deviation between sample types. Within the year 2 data ovariectomised samples have a greater value of standard deviation when compared to controls.

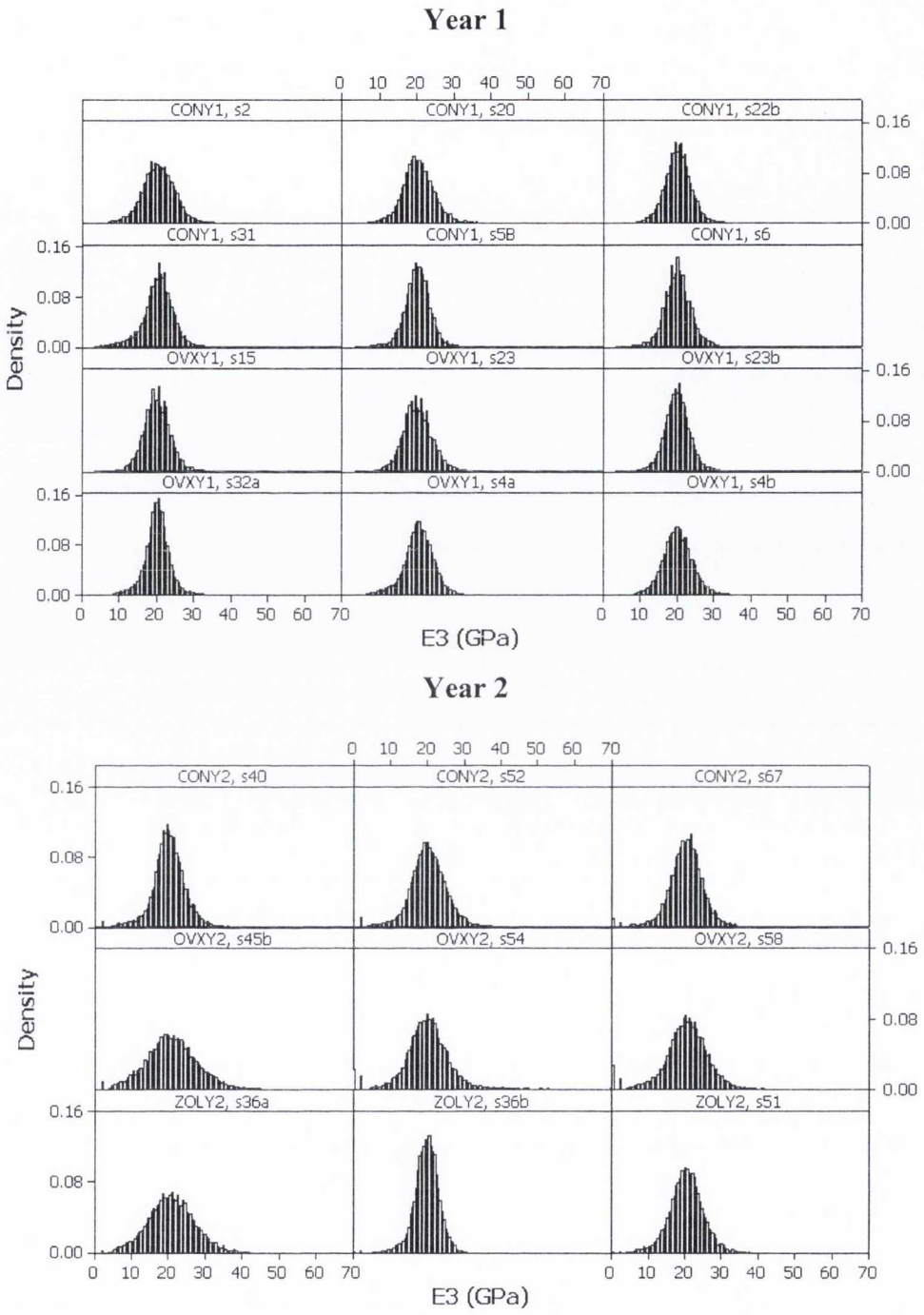


Figure 46 Year 1 and year 2 individual sample histograms. Within the year 1 histograms the distributions between and within sample types are similar. For the year 2 samples, comparing the distributions of ovariectomised sample types with control samples types, the ovariectomised samples have fatter tails to the left of the mean of the distribution.

Examining the year 1 histogram, the distribution are overlapping indicating that the measurement technique (SAM) can not find differences between the ovariectomised and control sample types see Figure 47.

The year 2 histogram show the control and ovariectomised drug treated sample types are similar. However the ovariectomised distribution differs noticeably from both the control and ovariectomised drug treated sample types. Zero values shown in the year 2 data are a result of more cavities being detected by SAM when compared to the Year 1 samples. Close inspection of the raw images shows the presence of more of these cavities in the year 2 samples when compared to the year 1 samples.

The cumulative distribution function for year 1 and year 2 also display the trends discussed above, see Figure 48.

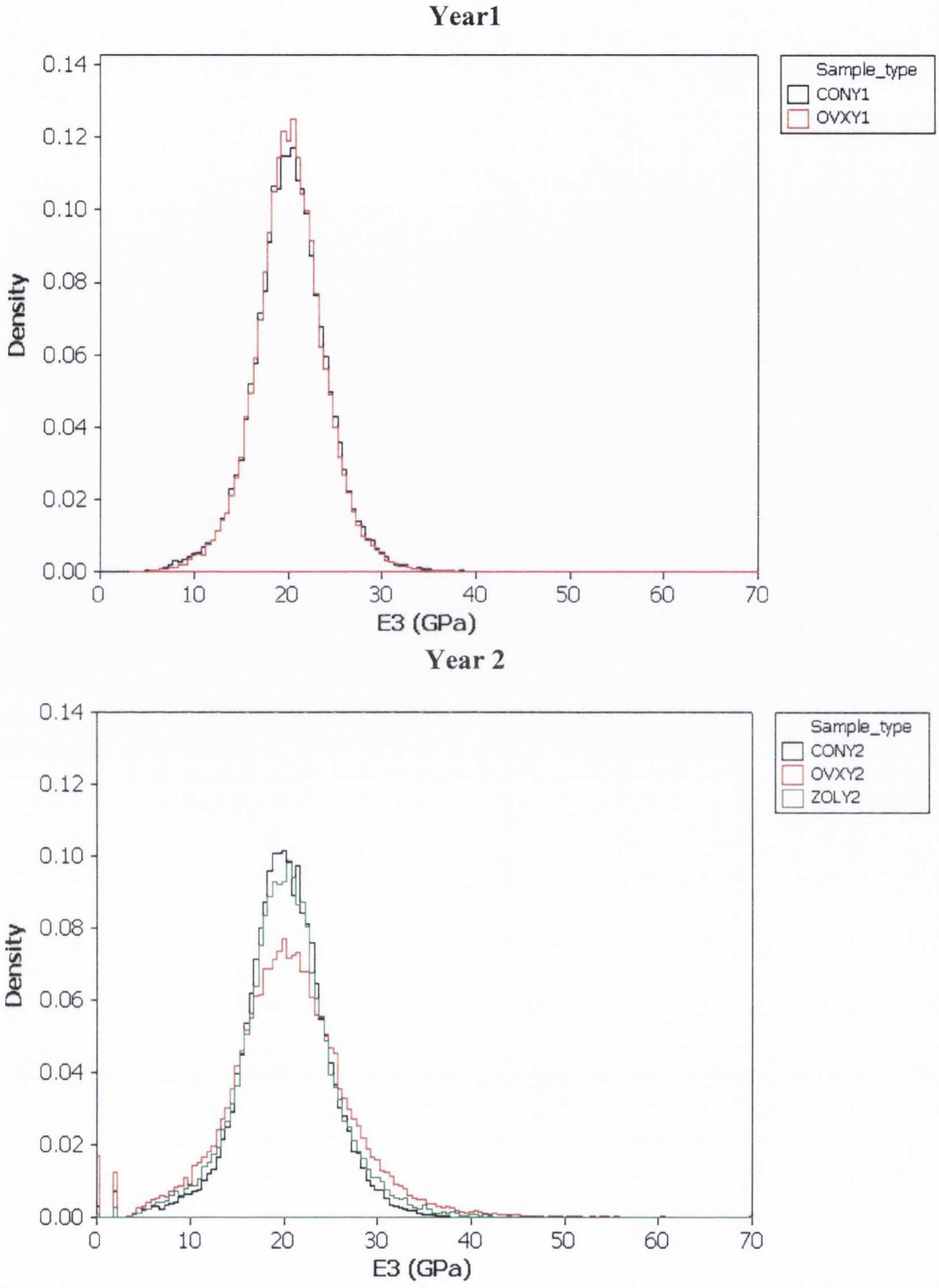


Figure 47 Year 1 and Year 2 Histograms for each sample type. Each sample type shown is made up of the pooled data from each sample. For year 1 sample types the distributions are overlapping. Within year 2 sample types control and drug treated ovariectomised samples have similar distributions, conversely the ovariectomised sample type has a different distribution, having larger tails when compared with controls.

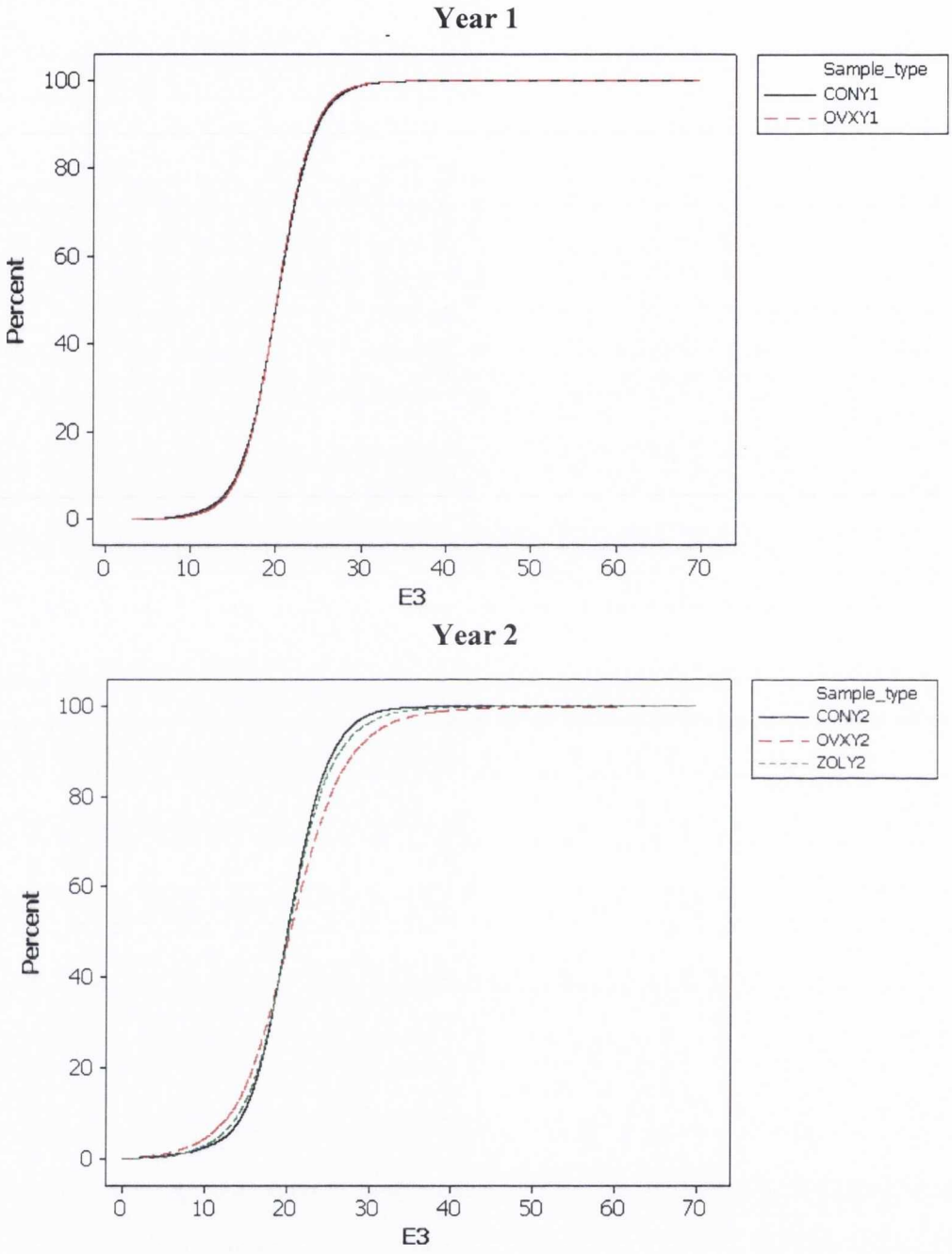


Figure 48 Year 1 and Year 2 Empirical cumulative density function. The zeros have been removed from the empirical cumulative density function plots shown above to avoid distorting the distributions observed.

4.3.2 Equivalent Stress

The results below were from the Finite Element models. The equivalent stress was evaluated at each element in the model (See Table below). The equivalent stress calculated by the finite element programme was von Mises stress.

Sample type	Year 1	Mean (MPa)	StDev	Median	Year 2	Mean (MPa)	StDev	Median
CON	s2	29.983	3.972	30.065	s40	29.117	4.047	29.242
	s5B	29.819	2.882	29.867	s52	29.315	4.649	29.401
	s6	29.795	2.884	29.776	s67	28.910	5.103	29.236
	s20	29.998	4.058	29.971				
	s22b	29.971	3.252	29.983				
	s31	29.939	3.700	30.078				
OVX	s4a	30.291	4.087	30.373	s45b	29.364	5.915	29.432
	s4b	29.876	3.406	29.832	s54	28.125	8.063	28.899
	s15	29.773	2.648	29.752	s58	27.411	8.280	28.418
	s23	29.815	3.115	29.773				
	s32a	30.008	3.312	30.081				
	s23b	29.809	2.904	29.824				
OVX-ZOL	No data				s36a	29.662	5.616	29.705
					s36b	29.198	3.379	29.359
					s51	29.395	4.218	29.602

Table 22 Equivalent stress (MPa) Data for year 1 and year 2 samples.

The means, standard deviations and medians of the year 1 samples for equivalent stress between sample types show no significant differences. This is borne out in the empirical cumulative density functions, boxplots and distributions on the following pages, see Figure 49 and 50.

Within the year 1 data there is little variation in mean and standard deviation between sample types, see Figure 49. Within the year 2 data, ovariectomised samples have a greater value of standard deviation when compared to controls.

In the year 2 samples it can again be observed that control and ovariectomised drug treated samples have very similar histogram distributions across individual samples. The situation is very different with the ovariectomised samples, with a consistently greater area in the left tail when compared with the control samples, see Figure 50. Substantial variability of the distributions is observed in ovariectomised drug treated samples within individual samples, see Figure 50.

Note: In the diagrams below, OVX-ZOL has been shortened to ZOLY2 referring to the ovariectomised drug treated year 2 samples.

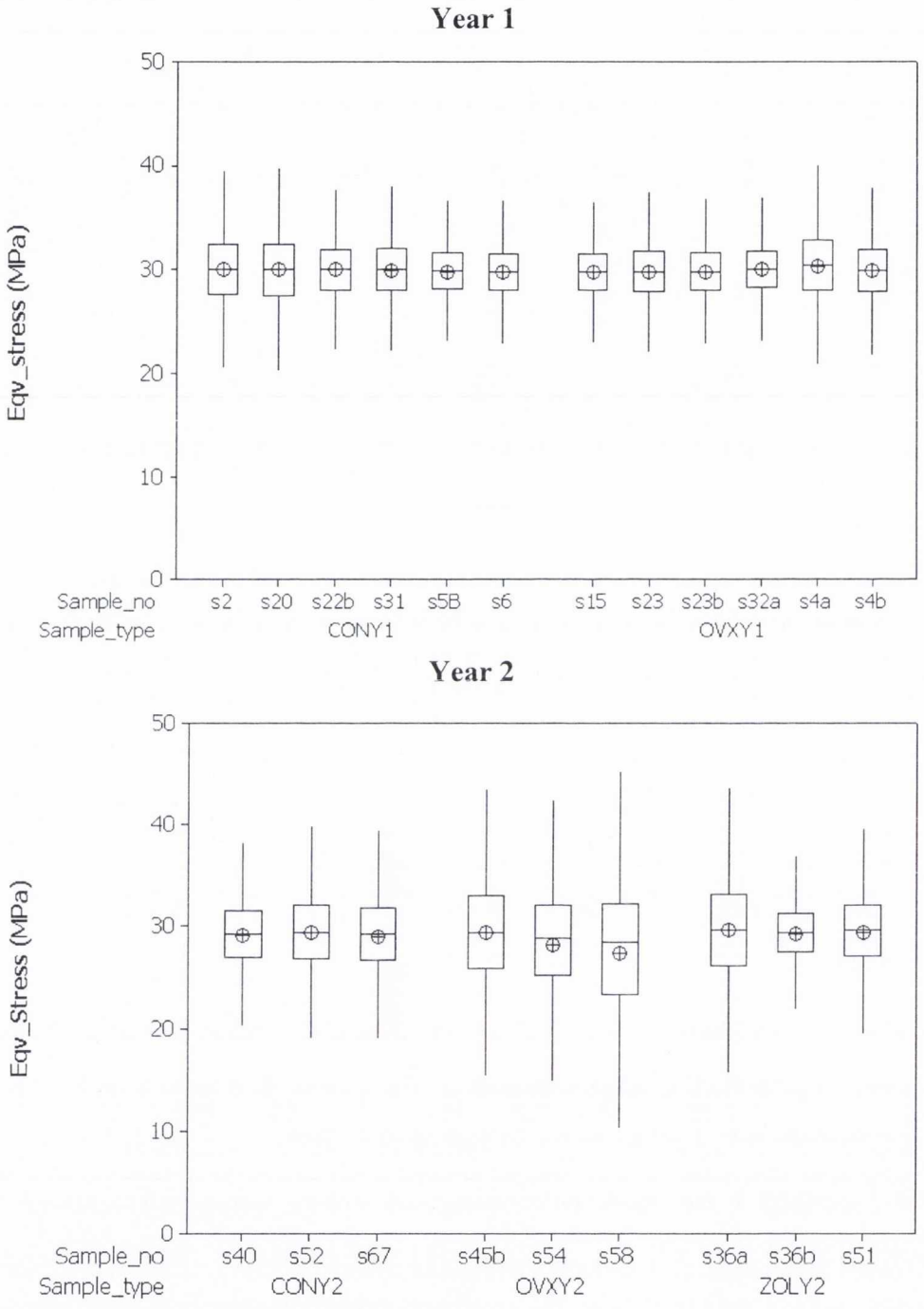


Figure 49 Boxplots of Equivalent stress (MPa) for year 1 (top) and year 2 (bottom) Samples. Within the year 1 data there is little variation in mean and standard deviation between sample types. Within the year 2 data ovariectomised samples have a greater value of standard deviation when compared to controls.

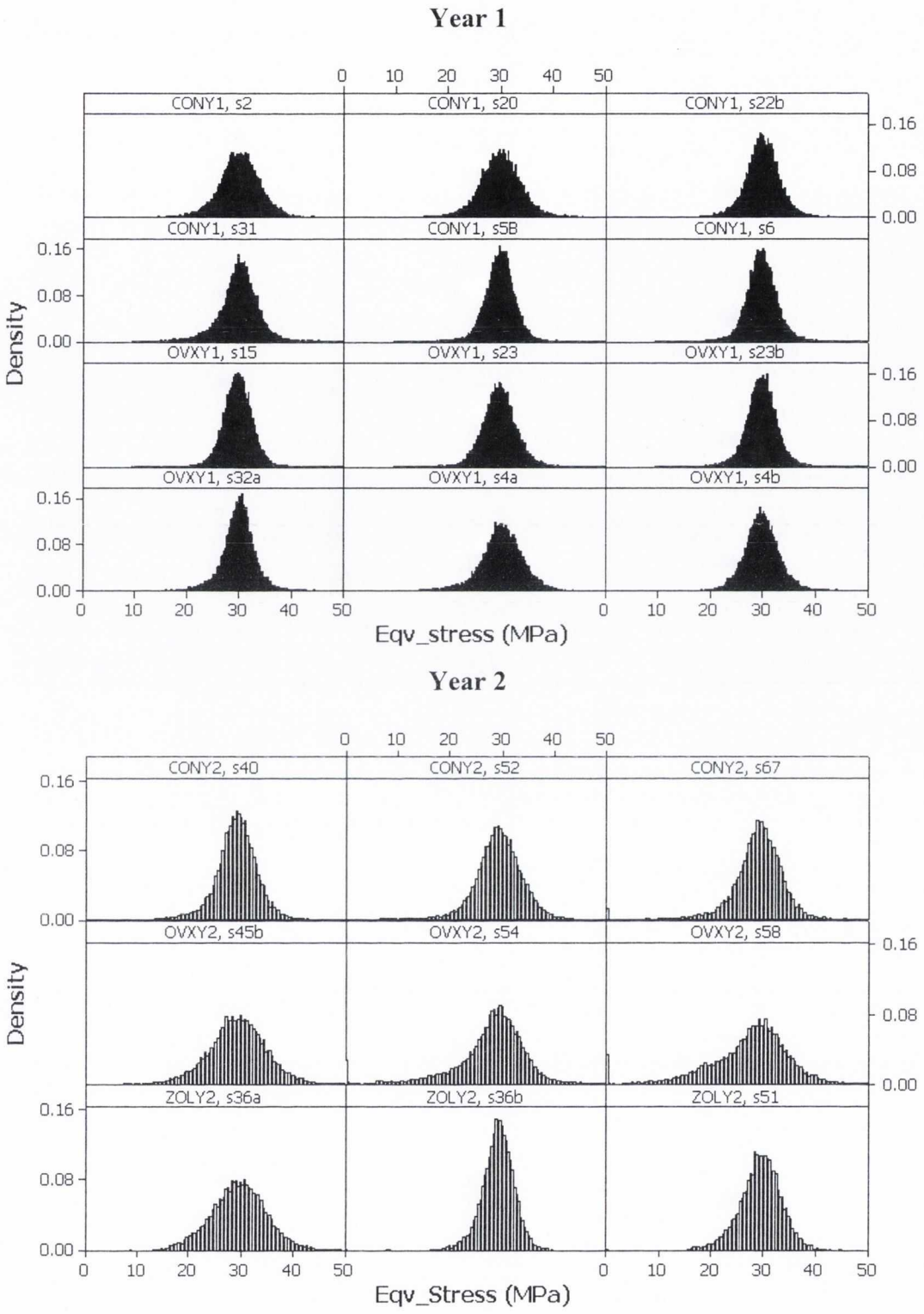


Figure 50 Year 1 and year 2 individual sample histograms. Equivalent stress (MPa). Within the year 1 histograms the distributions between and within sample types are similar. For the year 2 samples, comparing the distributions of ovariectomised sample types with control samples types, the ovariectomised samples have fatter tails to the left of the mean of the distribution.

For the year 1 histograms, see Figure 51, the distribution are overlapping indicating that the measurement technique (SAM) cannot find differences between the ovariectomised and control sample types.

The year 2 histograms show the control and drug treated ovariectomised sample types have similar stress distributions, see Figure 51. However the ovariectomised distribution differs noticeably from both the control and drug treated ovariectomised sample types. The zeros shown in the year 2 data are a result of more cavities being detected by SAM when compared to the Year 1 samples. Close inspection of the raw images shows the presence of more of these cavities in the year 2 samples when compared to the year 1 samples. The left tail of the ovariectomised distribution has a larger area than that of the control or drug treated ovariectomised distributions. This is an indication that a greater area of bone is experiencing a lower stress level for a given physiological strain (1500 μ strain) than control or drug treated ovariectomised bone sample types.

The cumulative distribution function for year 1 and year 2, also display the trends discussed above. The zero values have been removed from the empirical cumulative density function, plots shown above to avoid distortion and allow easier comparison between the sample type distributions, see Figure 52.

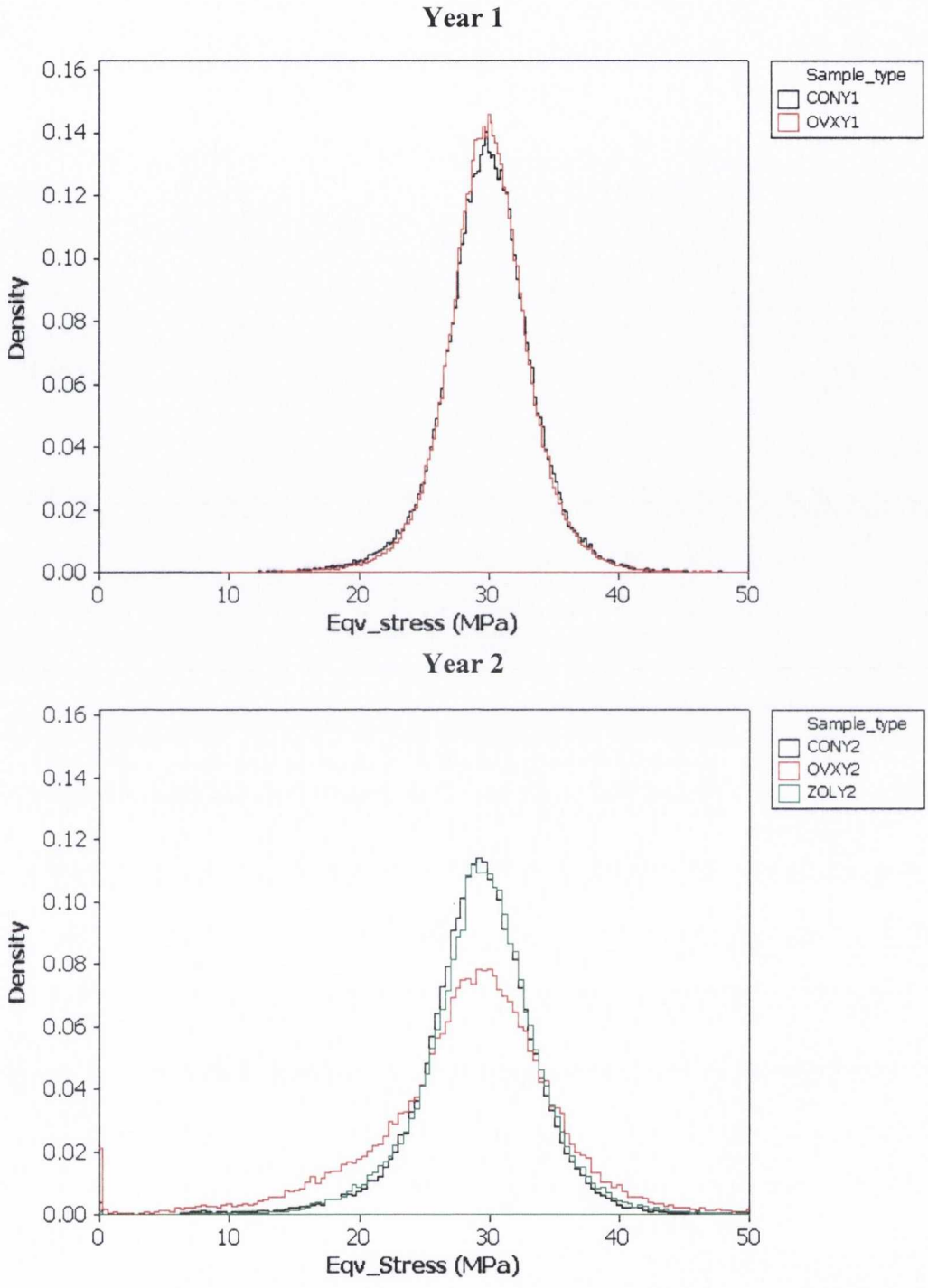


Figure 51 Year 1 and year 2 Histograms for each sample type. Equivalent stress (MPa). Each sample type shown is made up of the pooled data from each sample. For year 1 sample types the distributions are overlapping. Within year 2 sample types control and drug treated ovariectomised samples have similar distributions, conversely the ovariectomised sample type has a different distribution, having larger tails when compared with controls.

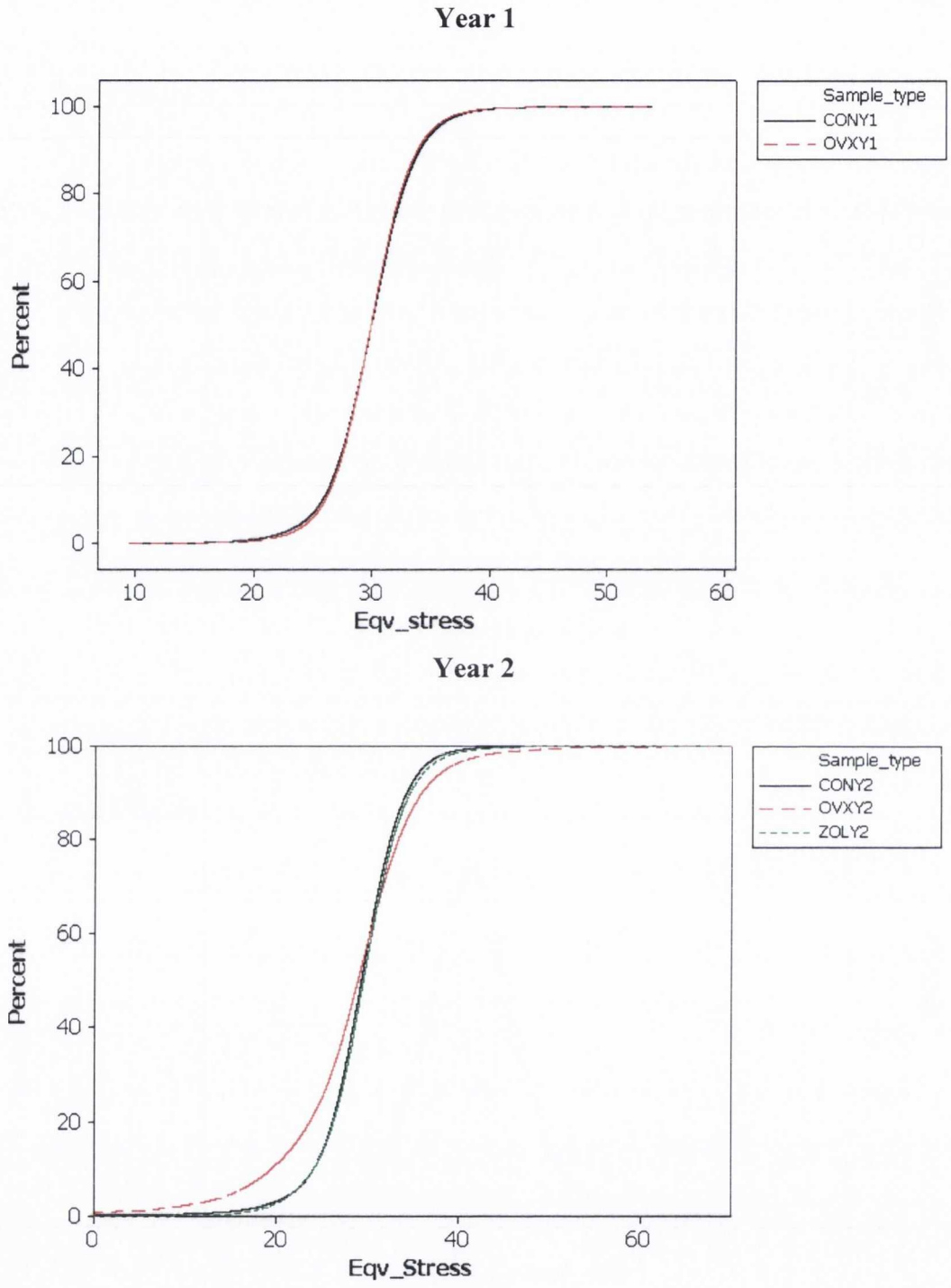


Figure 52 Year 1 and year 2 Empirical cumulative density function Equivalent stress (MPa). The zeros have been removed from the empirical cumulative density function plots shown above to avoid distorting the distributions observed.

4.3.3 Equivalent Strain

The results below were sourced from the Finite Element models. The equivalent strain was evaluated at each element in the model as shown in Table 23. The finite element programme generated equivalent strain as von Mises strain.

Sample type	Year 1	Mean	StDev	Median	Year 2	Mean	StDev	Median
(CON)	s2	0.001509	0.000239	0.001484	s40	0.001510	0.000371	0.001463
	s5B	0.001506	0.000193	0.001484	s52	0.001513	0.000343	0.001467
	s6	0.001506	0.000206	0.001489	s67	0.001523	0.000574	0.001456
	s20	0.001509	0.000220	0.001489				
	s22b	0.001506	0.000181	0.001492				
	s31	0.001510	0.000244	0.001475				
(OVX)	s4a	0.001509	0.000226	0.001479	s45b	0.001521	0.000496	0.001435
	s4b	0.001507	0.000228	0.001484	s54	0.001554	0.001084	0.001442
	s15	0.001505	0.000196	0.001488	s58	0.001562	0.001316	0.001401
	s23	0.001506	0.000208	0.001489				
	s32a	0.001505	0.000178	0.001486				
	s23b	0.001505	0.000182	0.001490				
(OVX-ZOL)	No data				s36a	0.001517	0.000400	0.001449
					s36b	0.001509	0.000264	0.001474
					s51	0.001512	0.000322	0.001465

Table 23 Equivalent strain data for year 1 and year 2 samples.

The means, standard deviations and medians of the year 1 samples for equivalent strain between sample types show no significant differences. This is borne out in the empirical cumulative density functions, boxplots and distributions on the following pages. The means and medians for year 1 samples should be the same because a physiological loading was applied to the finite element model of 1500 μ strain.

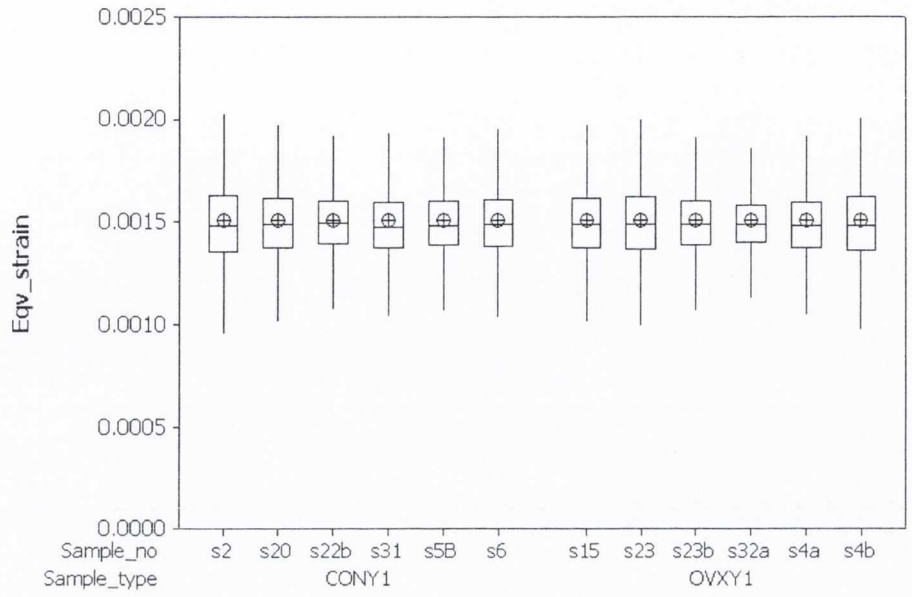
For the year 2 sample types the ovariectomised (OVX) sample types exhibit a greater standard deviation than the controls. The situation with the drug treated ovariectomised (OVX-ZOL) samples is more complex with the standard deviations varying within individual samples when compared to the more consistent standard deviations observed in the individual samples of the control (CON) group. These observations are visible in the empirical cumulative density function plots, boxplots and distributions on the following pages, see Figures 54 to 57.

Note: In the diagrams below, OVX-ZOL has been shortened to ZOLY2 referring to the ovariectomised drug treated year 2 samples.

The individual sample plots shown in Figure 53 and 54 show that the year 1 samples of both sample types have very similar distributions.

For the year 2 samples it can again be observed that control and drug treated ovariectomised samples have very similar histogram distributions across individual samples. The situation is very different with the ovariectomised samples with a consistently greater area in the left tail when compared with the control samples, see Figure 54.

Year 1



Year 2

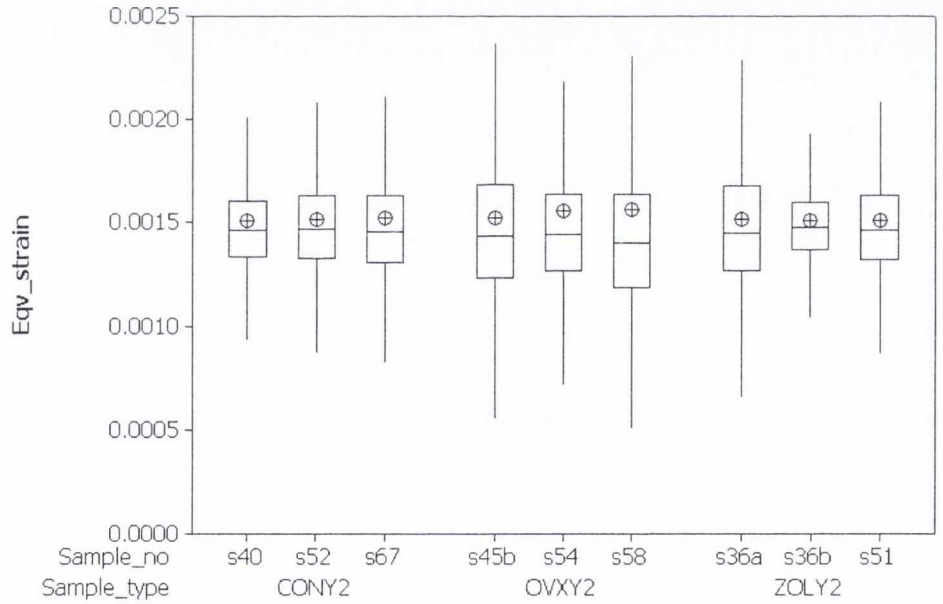


Figure 53 Boxplots of Equivalent strain for year 1 and year 2 Samples. .Within the year 1 data there is little variation in the standard deviation between sample types. Within the year 2 data ovariectomised samples have a greater value of standard deviation when compared to controls.

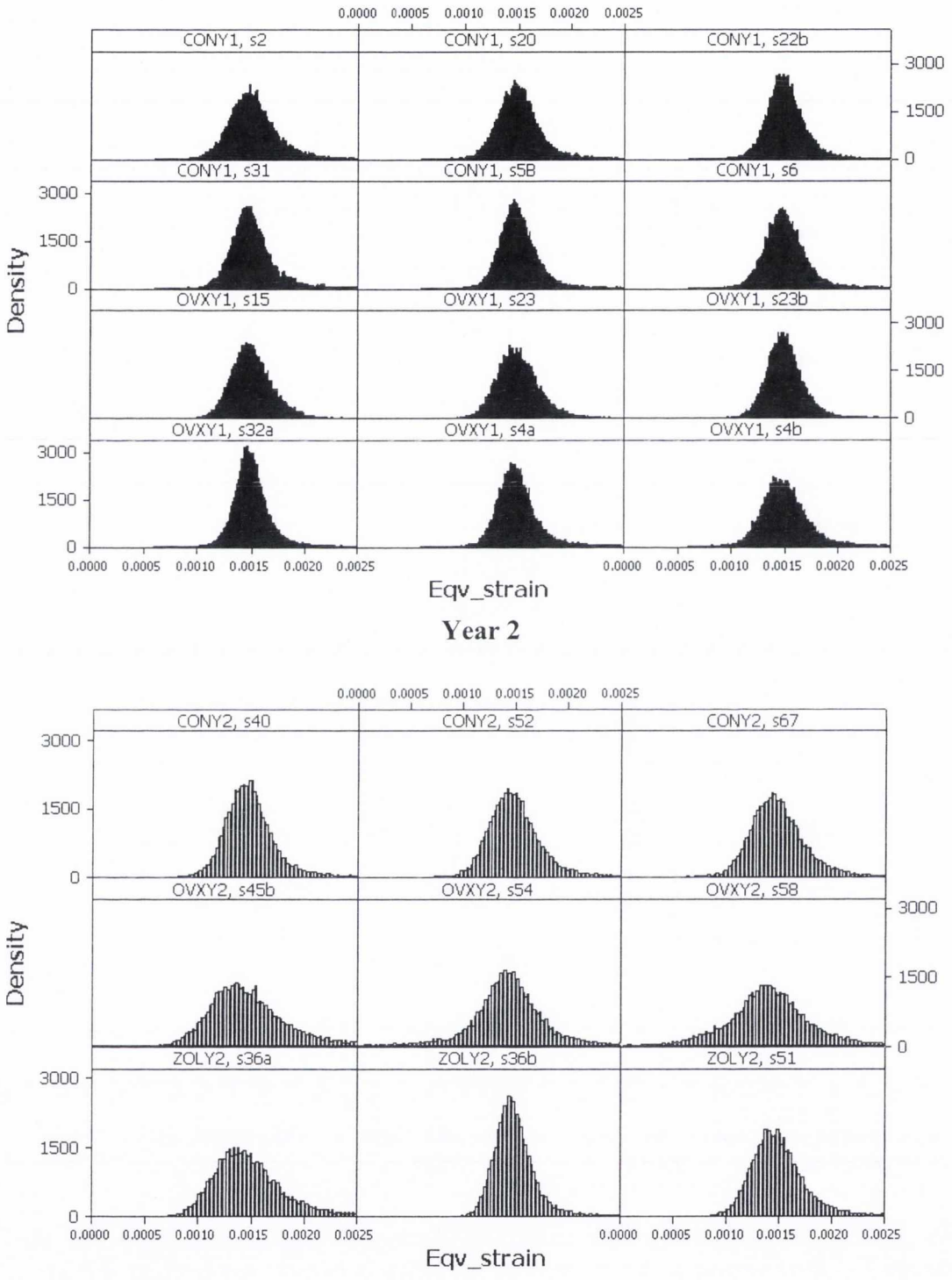


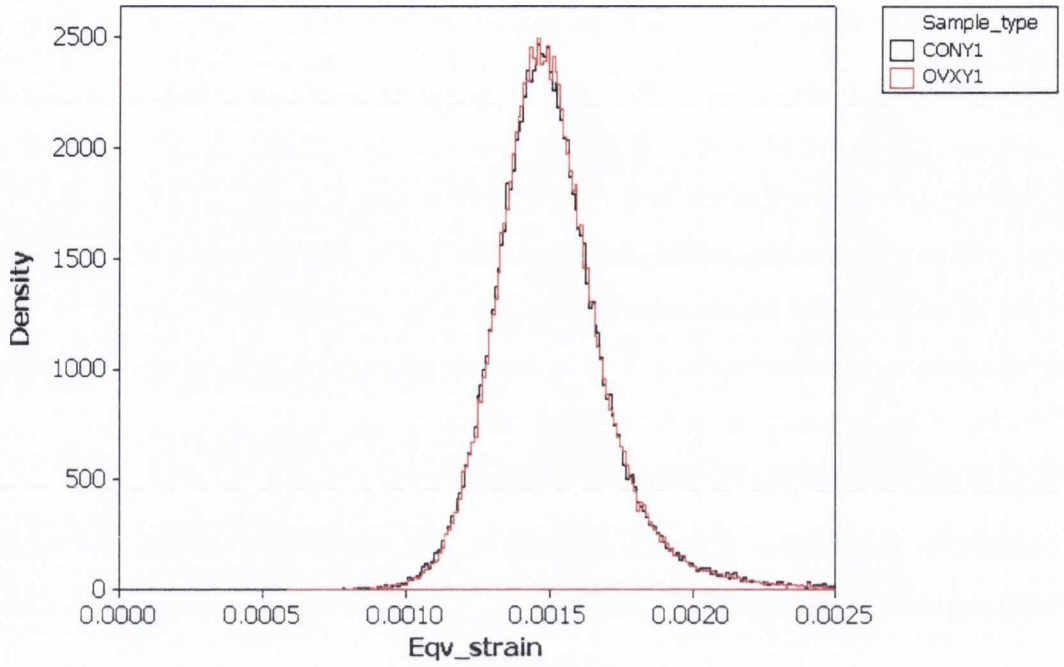
Figure 54 Year 1 and year 2 individual sample histograms. Equivalent strain. Within the year 1 histograms the distributions between and within sample types are similar. For the year 2 samples, comparing the distributions of ovariectomised sample types with control samples types, the ovariectomised samples have fatter tails to the left of the mean of the distribution.

In the year 1 histogram the distribution are overlapping indicating that the measurement technique (SAM) can not find differences between the ovariectomised and control sample types, see Figure 55.

The year 2 histogram shows the control and drug treated ovariectomised sample types have similar strain distributions. However the ovariectomised distribution differs noticeably from both the control and drug treated ovariectomised sample types. The cumulative distribution function for year 1 and year 2 also display these trends. The left tail of the ovariectomised distribution has a larger area than that of the control or drug treated ovariectomised distributions. This is an indication that a greater area of bone is experiencing a lower strain level for a given physiological strain (1500 μ strain) than control or drug treated ovariectomised bone sample types.

The cumulative distribution function for year 1 and year 2 also display the trends discussed above, see Figure 56.

Year 1



Year 2

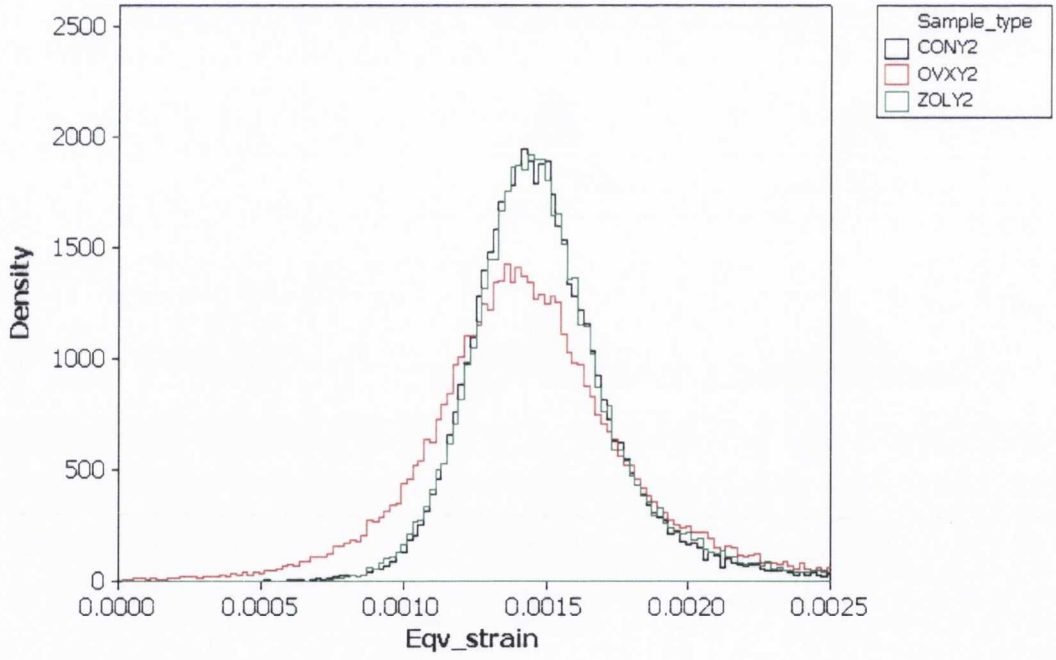
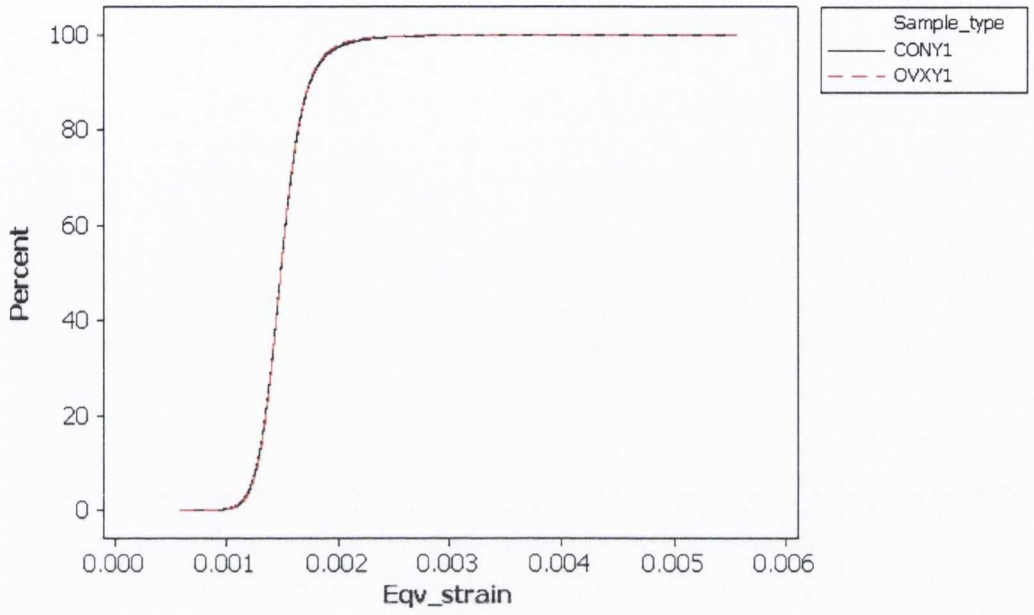


Figure 55 Year 1 and year 2 Histograms for each sample type. Equivalent strain. Each sample type shown is made up of the pooled data from each sample. For year 1 sample types the distributions are overlapping. Within year 2 sample types control and drug treated ovariectomised samples have similar distributions, conversely the ovariectomised sample type has a different distribution, having larger tails when compared with controls.

Year 1



Year 2

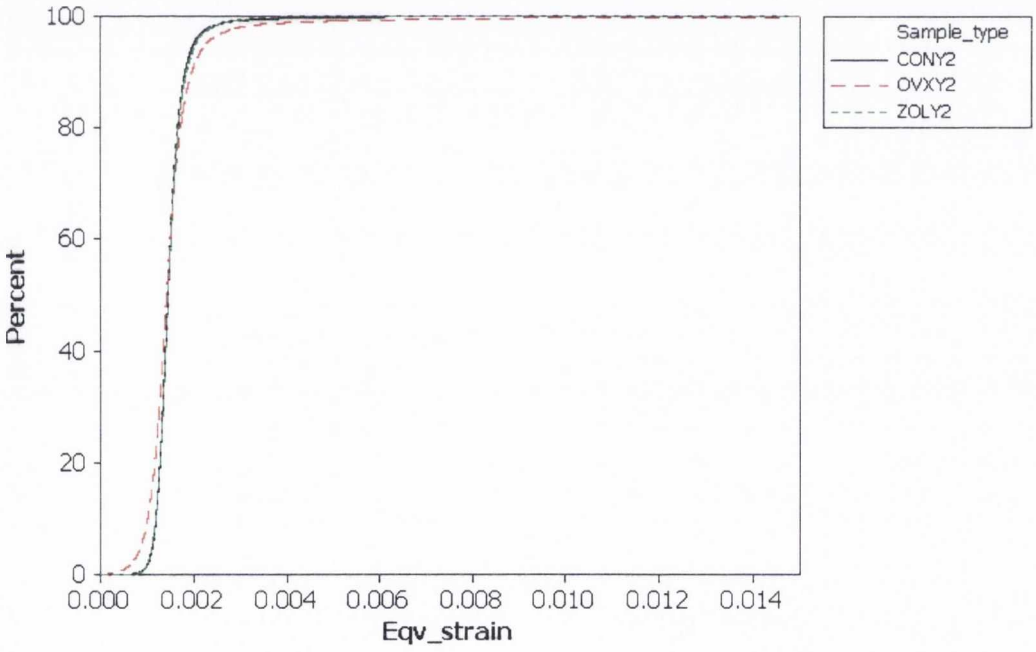


Figure 56 Year 1 and year 2 empirical cumulative density function. Equivalent strain. The zero values have been removed to avoid distortion and allow easier comparison between the sample type distributions

4.4 Inferential Statistics

A number of statistical tests were performed these include:

- t-test to compare year 1 and year 2 sample types.
- A one way ANOVA test to analyse for differences between the means of the 5 sample types.
- A Kruskal Wallis non parametric test of the medians of the 5 sample types.
- A two sided non-parametric Kolmgorov Smirnov test was used to test if the distributions between sample types in the year 1 and year 2 data were the same. This was applied by comparing two sample type distributions at a time. This was implemented using the "ks.boot" routine in R . This routine can cope with ties in the input data (Sekhon 2011).
- An Anderson-Darling k-sample test was applied to the 5 sample type distributions. This test can be used to test whether several independent random samples of various sizes come from the same but unspecified continuous distribution (Scholz *et al.* 1987).

From examination of the descriptive statistics data it can be inferred that there are no differences between principal stress and equivalent stress distributions, this is also true of the principal strain and equivalent strain. Therefore, only equivalent stress and strain distributions will be analysed using inferential statistical methods.

4.4.1 Young's Modulus

There are not enough samples to definitively say there are differences in the means and standard deviations between the control year 2 groups and the ovariectomised year 2 group for Young's modulus, see Table 24. A one way ANOVA test was applied to all 5 sample types and no significant differences were found between means (p=0.353). A non-parametric Kruskal Wallace test for all 5 sample types found no significant differences between medians (p=0.674).

A Kolmgorov Smirnov (KS) test was applied to carry out comparisons between sample types as shown in Table 27. The null hypothesis for this test is that the two distributions being tested are the same. For the year 1 comparison between control and ovariectomised samples the two sample types share a common distribution. For Year 2 the K-S test found that that control and drug treated ovariectomised sample types shared a common distribution, see Table 25.

A two sided Anderson Darling K (ADK) test was applied to see if the sample types shared a common distribution, see Table 26. It was found that for Year 1 the sample types shared a common distribution. For year 2 comparisons control and ovareictomised sample types do not share a common distribution. It was found that control year2 and drug treated ovariectomised sample types shared a common distribution. It was also found that ovariectomised year 2 and drug treated ovariectomised sample types did not share a common distribution according to the ADK test, see Table 26. These conclusions were also found in the combined ADK test, see Table 27.

Comparison	**Are means different? (2 sample t test) P value**
CONY1 Vs. OVXY1	0.769
CONY2 Vs. OVXY2	0.230
CONY2 Vs. ZOLY2	0.567
OVXY2 Vs. ZOLY2	0.629

Table 24 Two sample t test: Young's modulus for year 1 and year 2 comparison.

Year 1 Comparison	P Value	Year 2 Comparison	P Value
CONY1 Vs OVX Y1	0.3136	CONY2 Vs. OVXY2	2.27e-06
		CONY2 Vs. ZOLY2	0.6476
		OVXY2 Vs. ZOLY2	6.062e-05

Table 25 Two sided K-S test for Young's modulus. No removal of zeros (1000 points sample)

Year 1 Comparison	P Value	Year 2 Comparison	P Value
CONY1 Vs OVX Y1	0.28463	CONY2 Vs. OVXY2	0
		CONY2 Vs. ZOLY2	0.49155
		OVXY2 Vs. ZOLY2	0

Table 26 Two sided ADK test for Young's modulus. No removal of zeros (1000 random points from each sample type)

Test	P Value
Within Year 1	0.28463
Within Year 2	0

Table 27 Combined ADK test for Young's modulus. No removal of zeros (1000 random points from each sample type) Null hypothesis at least one sample type shares a common distribution.

To conclude there are no statistically significant differences in the means or medians between year 1 sample types they were also found to share a common distribution as calculated using the K-S and ADK tests. Within year 2 sample types the results of the K-S and ADK tests agree; Control year 2 and drug treated ovariectomised sample types share a common distribution.

4.4.2 Equivalent Stress

A two sample t test showed no statistically significant differences between means for comparisons among the five sample types (See Table 28). A one way ANOVA analysis was performed on the means of the samples of the five sample types. It was found that there was a statistically significant difference between the ZOLY2 and OVXY2 using the Tukey method at the 95% confidence level. A Kruskal Wallace test found that a statistically significant differences of at least one of the medians among the 5 sample types (p=0.004).

A Kolmgorov Smirnov (K-S) test was applied to carry out comparisons between sample types as shown in Table 31. The null hypothesis for this test is that the two distributions being tested are the same. For the year 1 comparison between control and ovariectomised samples it was found that they share a common distribution. For Year 2 sample types the K-S test found that the control year 2 and drug treated ovariectomised sample types shared a common distribution See Table 29.

A two sided Anderson Darling K (ADK) test was applied to see if the sample types shared a common distribution, see Table 30. It was found that for Year 1 the sample types shared a common distribution. For year 2 comparisons control year 2 and drug treated ovariectomised sample types shared a common distribution. These conclusions were also found in the combined ADK test (See Table 31).

Comparison	**Are means different? (2 sample t test) P value**
CONY1 Vs. OVXY1	0.904
CONY2 Vs. OVXY2	0.297
CONY2 Vs. ZOLY2	0.186
OVXY2 Vs. ZOLY2	0.197

Table 28 Two sample t test: Equivalent stress for year 1 and year 2 comparison.

Year 1 Comparison	P Value	Year 2 Comparison	P Value
CONY1 Vs OVX Y1	0.6099	CONY2 Vs. OVXY2	1.106e-09
		CONY2 Vs. ZOLY2	0.5727
		OVXY2 Vs. ZOLY2	1.533e-07

Table 29 2 sided K-S test Equivalent Stress. No removal of zeros 1000 point sample

Year 1 Comparison	P Value	Year 2 Comparison	P Value
CONY1 Vs OVX Y1	0.46188	CONY2 Vs. OVXY2	0.01856
		CONY2 Vs. ZOLY2	0.37758
		OVXY2 Vs. ZOLY2	0

Table 30 Two sided ADK test for Equivalent Stress. No removal of zeros (1000 random points from each sample type)

Test	P Value
Within Year 1	0.46188
Within Year 2	0

Table 31 Combined ADK test for Equivalent stress. No removal of zeros (1000 random points from each sample type)

The results of the tests examining the hypothesis of common distributions for year 2 sample types are clear. Examination of the results of the K S test and ADK test with respect to the empirical cumulative density functions in Figure 52 show that control year 2 and drug treated ovariectomised sample types share a common distribution for equivalent stress.

4.4.3 Equivalent Strain

A Kolmgorov Smirnov (K-S) test was applied to carry out comparisons between sample types as shown in Table 32. The null hypothesis for this test is that the two distributions being tested are the same. For the year 1 comparison between control and ovariectomised samples it was found that they share a common distribution. For year 2 sample types the K-S test found that control year 2 and ovariectomised drug treated year 2 shared a common distribution See Table 32.

A two sided Anderson Darling K (ADK) test was applied to see if the sample types shared a common distribution, see Table 33. It was found that for year 1 the sample types shared a common distribution. For year 2 comparison of control year 2 and drug treated ovariectomised showed they shared a common distribution. These conclusions were also found in the combined ADK test, see Table 34.

Year 1 Comparison	P Value	Year 2 Comparison	P Value
CONY1 Vs OVX Y1	0.3136	CONY2 Vs. OVXY2	2.27e-06
		CONY2 Vs. ZOLY2	0.6476
		OVXY2 Vs. ZOLY2	6.062e-05

Table 32 2 sided K-S test Equivalent Strain. No removal of zeros, 1000 point sample.

Year 1 Comparison	P Value	Year 2 Comparison	P Value
CONY1 Vs OVX Y1	0.28463	CONY2 Vs. OVXY2	0
		CONY2 Vs. ZOLY2	0.49155
		OVXY2 Vs. ZOLY2	0

Table 33 Two sided ADK test for Equivalent Strain. No removal of zeros, 1000 point sample.

Test	P Value
Within Year 1	0.50412
Within Year 2	0

Table 34 Combined ADK test for Young's modulus. No removal of zeros, 1000 point sample.

To conclude there are no statistically significant differences in the means or medians between year 1 sample types. The results of the tests examining the hypothesis of common distributions for year 2 sample types are clear. Examination of the results of the K S test and ADK test with respect to the empirical cumulative density functions in Figure 56 show that the control year 2 and drug treated ovariectomised year 2 sample types share a common distribution for equivalent strain.

4.5 Concluding Statement on results.

From analysis of the descriptive statistics tables above for Young's modulus stress and strain it can be concluded that there are no statistically significant differences between the year 1 sample types. Year 1 ovariectomised and control samples share a common distribution and have essentially the same distributions of Young's modulus, equivalent stress and equivalent strain.

Applying a non parametric test, which compares the distributions between the sample types, a statistically significant result was found that the distributions of control year 2 and drug treated ovariectomised sample types for Young's modulus, equivalent stress and equivalent strain share a common distribution. Therefore it is possible to conclude that the effect of the Zoledronic Acid drug treatment on ovariectomised ovine cortical bone is to restore the distribution of mechanical properties stresses and strain to that of disease free control samples.

Ovariectomised samples for year 2 do not share a common distribution of Young's modulus, equivalent stress or equivalent strain with disease free control samples

5 Discussion

5.1 Discussion of research outcomes

5.1.1 Research Objectives

The hypotheses to be accepted or rejected in this thesis is whether the process of osteoporosis changes the magnitude and distribution of stress and strain in cortical bone tissue and that this drives the pathology through altered cell responses. One way that this could happen is if ovariectomy, leading to osteoporosis, triggers a change in the bone remodelling strain set point threshold for resorption. This in turn has a structural consequence for bone, which further alters future cell responses to load. If the hypothesis is found to be true, it will be possible to quantify this response and understand how the process proceeds over time. This insight will be invaluable to further understanding and developing treatments for osteoporosis. Applying computational simulation techniques (Finite Element Analysis) allows study of the strain field in bone microstructure which is difficult if not impossible to undertake using histological methods. If it is true that biophysical stimuli are pathological in osteoporotic bone then cells may be responding normally to the abnormal stimulus from the bone matrix and may not be at fault in the disease process of osteoporosis. Thus the degradation of bone matrix is responsible for the clinical consequences of osteoporosis.

5.1.2 Research Background

5.1.2.1 Mechano-biology applied to Cortical Bone.

Mechano-biology can be defined as "The application or analysis of the role of mechanical forces in eliciting a molecular response leading to a change in form and/or function that can be quantified (Merryman *et al.* 2010)." Mechano-biology is uniquely positioned to lead to multiple innovations that will revolutionise medicine and healthcare.

To apply this concept to bone, one must answer the question how does cortical bone sense mechanical forces and what signals are generated to initiate a response? The goal is to predict growth and differentiation in quantitative terms based on a force exerted on a given bone matrix (van der Meulen *et al.* 2002).

Bone is capable of self repair, therefore there must be a mechanism for sensing and detecting locations in bone which require it. This is known as targeted remodelling. The most likely candidates for this role are osteocytes. These are the most abundant cell type

in cortical bone, making up 95% of the cells found in the bone matrix. These cells have a vast 3D network of cell processes (Gap junctions) which connect each osteocyte with its nearest neighbour and with the periosteum and endosteum (van der Meulen *et al.* 2000).

The mechanism by which need to repair is determined can be addressed in two ways:

There is experimental evidence that osteocytes are able to respond to strain induced fluid shear (Basso *et al.* 2002). This response is in the form of chemical signal release.

Fatigue damage due to microcracks is thought to be the second mechanism. The cell transducing mechanism for bone damage detection is based on ruptured osteocyte processes. Relative crack displacements are capable of rupturing cell processes (Hazenberg *et al.* 2006).

Osteocytes respond to small fluid shear stresses acting on membranes of osteocytic processes and respond to strain by increasing production of nitric oxide, an inhibitor of osteoclastic resorption. This points towards a normally functioning osteocytic cell network being an inhibitor. When it is switched off or damaged, resorption of bone starts (Basso *et al.* 2002). It is conjectured that fatigue micro-damage leads to interference with the integrity of osteocyte and canalicular network by disrupting canaliculi and severing osteocyte processes leading to apoptosis (Taylor *et al.* 1997; Hazenberg *et al.* 2006). Fatigue damage may cause a situation resembling disuse, as when fluid shear is reduced, bone resorption will occur (Burger *et al.* 1999b). This is a compelling explanation for targeted bone remodelling as it connects the damage-fatigue theory to the fluid flow shear theory of mechano-transduction. Cortical bone appears to have over-lapping mechanisms for the detection and initiation of repair due to fatigue and mechanical loading.

Bone remodelling in cortical bone is carried out by two specialised groups of cells: osteoclasts which resorb bone by releasing powerful acid and an enzyme and osteoblasts which lay down new bone. These cells combine to make a BMU. This is a cavity about 200 microns in diameter which moves along the length of the bone at 40 microns per day (Taylor *et al.* 2007).

Martin (Martin 2000b) aims to resolve the inconsistencies between observations and concepts about bone remodelling, specifically that bone remodels when mechanical loading is excessively low and when loading is very high and substantial damage

occurs. This theory assumes bone lining cells are inclined to activate remodelling unless restrained by an inhibitory signal and the mechanically provoked osteocytic signal serves this inhibitory function. However remodelling is elevated at low loads with no inhibitory signal or the signal is interrupted by damage to cell processes due to excessive loading, otherwise remodelling is relatively low. This leads to the conclusion that one mechanically derived signal is responsible for both. Osteocyte survival exhibits a U shaped relationship with bone tissue level strain. At low strain, osteocytes die by apoptosis. Loadings to produce strain within the physiological range appear to reduce apoptosis in osteocytes, however loading at high levels of strain increases apoptosis (Brennan 2008).

Frost's Mechano-Stat hypothesis provides a framework by which to understand the process of modelling and remodelling of bone (Frost 1997a). He postulates that below 100 microstrain resorption occurs in normal bone. The set point changes with age or disease. e.g. the minimum strain below which resorption is triggered or the maximum strain where by desposition occurs. Changes due to drugs or diseases may lead to sensor cells that are either deaf or are over reactive to their mechanical environment. In post menopausal osteoporosis there is a setpoint shift up in mechano-sensitivity increasing the minimum strain below which resorption of bone is triggered. The effect would be similar to disuse and lead to resorption (Mulvihill *et al.* 2008).

5.1.2.2 Osteoporosis

Osteoporosis is a disease of bone tissue which leads to a reduction in bone mass and a deterioration in bone quality. In a clinical setting, osteoporosis presents as increased risk of fracture. Common fracture points are the hip, wrist and vertebral fracture (Anonymous 1993); (Anonymous 2000).

At the micro-structural level of cortical bone, osteoporosis, due to estrogen withdrawal, appears to attenuate the sensitivity of the osteocyte network to transduce tissue level strain. A consequence of this is a higher tissue strain threshold under which bone is resorbed. In Frost's Mechano-Stat paradigm, there is an increase in the strain threshold for resorption due to disuse. This is due to an increase in osteocyte apoptosis as observed in human bone. It is speculated that this leads to bone fragility and impairment of adaptive responses to loading. Increased remodelling is also associated with an increased proportion of apoptotic osteocytes (Tomkinson *et al.* 1997). The

consequences of this impairment in the adaptive response may not be immediately apparent on the micro-structure of cortical bone but coupled with increased remodelling this could lead to less mineralised bone and overall bone stiffness being reduced . A higher resorption strain threshold equates to stiffer bone structures being resorbed and being replaced with bone with lower stiffness. This process is further compounded by the increase in turnover due to osteoporosis

Drug treatments are available to limit, and in some cases reverse the effects of osteoporosis by limiting resorption of bone. Zoledronic Acid is one of the latest generation of bisphosphonates and is the most potent to date. It is a nitrogen containing bisphosphonate and it works by inhibiting osteoclast adhesion to the mineralised bone matrix and thus reducing resorption of old bone. It also acts to increase osteoclast apoptosis (Benford *et al.* 2001). An anti-apoptotic effect on osteocytes has also been observed (Plotkin *et al.* 1999) . This has two effects on bone; it maintains the sensitivity of the osteocyte network to mechanical strain and it reduces bone turnover due to osteocyte apoptosis.

5.1.2.3 Ultrasonic Methods applied to investigate bone microstructure.

This section will discuss where other researchers have used SAM to image bone report some of their findings relevant to this study. The use of SAM to evaluate the mechanical stiffness of bone material at high resolution will be discussed.

SAM has been used to assess the mechanical properties of bone through surface imaging of bone cross sections. When the ultrasonic transducer is focused on the surface of a sample, impedance dominates. From this it is possible to create images of the acoustic impedance Z of the bone sample (Briggs 1992). Quantitative ultrasound in principle should allow advanced assessment of the mechanical properties of bone, as the ultrasound propagation characteristics are principally determined by the mechanical properties (Bossy 2007).

It can be demonstrated that reliable estimates of C_{33} in cortical bone can be made from acoustic impedance Z alone (Raum 2008). This assumption is valid for homogeneous materials. The validity of this assumption has to be verified at each hierarchical level of organisation in bone. At the frequencies used in the research presented in this study, (150 MHz) the acoustic wavelength is much greater than the individual layers of the lamellar unit. Therefore, the effective compound material properties are seen by the

acoustic wave. Porous features such as osteocyte lacunae, canaliculi and microcracks contribute to the effective compound properties.

There is compelling evidence that Z (acoustic impedance) measured by SAM at the surface of a bone sample cross section is strongly correlated to the stiffness C_{33}. Independent estimates of Z and density were found in human cortical bone for 257 points in osteonal and 228 points in interstitial bone (R^2=0.99 $p<0.001$). Density was found using μCT. The strong correlation of Z_3 and C_{33} implies that Z_3 may be a good proxy for C_{33} and reliable estimates of C_{33} can be made from measurements of Z_3 alone (Raum *et al.* 2006a).

5.1.2.4 Use of FE to estimate stress and strain in bone micro-environment.

In order to utilise two dimensional maps of mechanical stiffness generated by SAM, to estimate stresses and strain in the micro-structure of cortical bone, the finite element analysis technique can be utilised. Each pixel in an image can be represented by a finite element with appropriate stiffness. Appropriate boundary conditions and physiological loading are applied and the strain environment evaluated. Many researchers have estimated the strain around representative models of cortical bone micro-structure but they lacked exact values for stiffness in their finite element models (Prendergast *et al.* 1996; Bonivtch *et al.* 2007; Abdel-Wahab *et al.* 2011; Mischinski *et al.* 2011).With more realistic finite element models it is possible to assess the strain environments of actual bone samples. This allows comparison of bone types, for example bone from ovariectomised sheep compared to control samples. This also allows direct comparison of the strain environments between sample types. It also allows better assessment of crack propagation in actual bone samples using finite element analysis.

5.1.3 Research outcomes

The hypotheses to be accepted or rejected in this thesis is whether the process of osteoporosis changes the magnitude and distribution of stress and strain in cortical bone tissue and whether this drives the pathology through altered cell responses. The stresses and strain were calculated using material properties evaluated by acoustic methods. Evaluation of stresses and strain was by use of a computational simulation technique finite element analysis.

5.1.3.1 Year 1 samples

The year 1 samples were divided into two types: The first were from ovariectomised (OVX) sheep and the second were control (CON) animals. Six bone samples of each type were tested.

There were no differences detected in the means and standard deviations of the Young's modulus values between the bone sample types. SAM was unable to discriminate between OVX and CON samples. This is at odds with the Young's modulus values calculated for OVX whole bone by compression load test on metatarsal bone (Kennedy *et al.* 2009). An explanation is that increased porosity in the year 1 OVX samples when compared to CON leads to less bone area being available for loading.

A similar situation was observed with the stress and strain results. For equivalent strain and principal strain there were no detectible differences in the standard deviations of strain or in the distributions of strain for each sample type (OVX and CON). For equivalent stress and principal stress there were no detectible differences between the means and standard deviations of stress or in the distribution of stress for each sample type.

Evidently from the results, the base bone material itself is unchanged at length scales being examined by SAM. This indicates that for year 1 samples, porosity is the largest contributor to whole bone Young's modulus reduction (Kennedy 2007) . This is mainly due to porosity which is doubled from 1% to 2% in OVX versus Control for Year 1 samples. The porosity is due to the number of resorption cavities per unit area being significantly greater in OVX samples than the control group. There may be local variability between bone types which could also explain the discrepancy. The samples used in the whole bone compression tests were metatarsals. The samples used as part of the research presented in this thesis came from the metacarpal bone.

5.1.3.2 Year 2 samples

The year 2 samples were divided into three types: The first were from ovariectomised sheep (OVX), the second were control animals (CON). The third type was from ovariectomised drug treated animals (OVX-ZOL). Three bone samples of each type were tested.

Comparing the means and standard deviations of Young's modulus of the three sample types, there is no statistically significant difference between them. Comparing the

distributions of the CON and OVX-ZOL samples it is evident that overall they have very similar distributions (ADK test p=0.49). When the individual distributions are examined, it is clear that the individual response in each sample is different for the OVX-ZOL year 2 samples. This may indicate an animal specific response to the Zoledronic acid treatment.

In comparing the equivalent stress distributions for year 2 OVX and CON sample groups, it is clear that the OVX distribution is skewed to the left. It could be interpreted that a greater proportion of the OVX sample is at lower stress when compared to controls. This effect is observed in each of the samples making up the OVX year 2 group. There does not seem to be a difference in the results between principal stress (mainly tensile stress) and equivalent stress for the year 2 samples. The OVX-ZOL and CON samples appear to have the same overall distribution (ADK test p=0.377), however in the individual OVX-ZOL samples, significant differences are observed in the distributions.

For equivalent strain & principal strain in the year 2 samples, CON and OVX-ZOL sample types have similar distributions of strain (ADK test p=0.491) and standard deviations. This indicates the restorative effects of Zoledronic acid on the mechanical competence of bone. Again, a varying animal response to the drug treatment is observed as varying distributions between samples in the OVX-ZOL group. Comparison of year 2 OVX and CON sample types shows strain distributions of which a significant area of the bone sample is experiencing a lower strain than the mean when compared to controls.

Interpreting the significance of the distributions of mechanical properties, when comparing OVX versus CON samples for year 2: Initially endocrine factors accelerate untargeted bone turnover (withdrawal of estrogen). The redistribution of strain in bone due to new partially mineralised bone, results in targeted remodelling with a disuse threshold set higher due to the loss of sensitivity of the remaining osteocyte network. This leads to further acceleration of bone loss and an accelerated remodelling rate.

In comparing year 2 sample types with each other, overall the CON and OVX-ZOL samples have similar distributions of mechanical properties. On examination of the individual distributions it is clear that the response in each sample is different for the

OVX-ZOL year 2 samples. This may indicate an animal specific response to the Zoledronic acid treatment.

This pharmacological action of Zoledronic acid is in two parts;

(i) The impaired function of the osteoclast cell to resorb bone and

(ii) The suppression of the effect of estrogen withdrawal on osteocyte apoptosis (Plotkin *et al.* 1999; Benford *et al.* 2001). For the "Bone for life" samples it was also found that Zoledronic acid slowed down bone turnover when compared to controls (Brennan 2008). Overall the results indicate that the Zoledronic acid treatment is restoring the mechanical competence of bone and that this is represented in the data collected in this study.

5.2 Discussion of experimental techniques and results processing.

5.2.1 Bone for Life Samples

The sheep animal model used in the "Bone for Life" study has a hormone profile and bone remodelling cycle similar to women. Sheep metabolic rate is similar to that of humans per gram of body weight. In 1994 the Food and Drug Administration (FDA) produced draft guidelines on the treatment and prevention of osteoporosis in which sheep were identified and accepted as an animal model (Lee *et al.* 2004).

The "Bone for Life" study provides an opportunity to examine bone response to reduced hormone levels only (Kennedy 2007). OVX "Bone for Life" samples have exhibited significant changes in osteocyte apoptosis, material changes and structural strength. All of these changes have been observed in osteoporotic human patients proving the animal model was functionally successful (Brennan 2008).

A seasonal variation may exist between year 1 and year 2 samples. This may distort comparisons between year 1 and year 2 samples. Year 1 animals were killed in November and the year 2 animals (31 months) were killed in June.

5.2.2 Limitations of methods used

5.2.2.1 Focus correction algorithm

A comprehensive image analysis process was developed to take the raw SAM images and convert them into images of Young's modulus properties across a bone sample surface.

The cortical bone samples were not completely flat and a method was required to compensate for this. The method developed is similar to Raum et al. (Raum *et al.* 2004), the main difference being that an estimate of the de-focus of the lens is made by averaging over a 15x15 pixel area . This makes it possible to remove the changes in the acoustic reflectance due to de-focus without modifying the underlying acoustical reflectance due to the bone material.

A comprehensive analysis was carried out to evaluate whether the focus correction algorithm was working as intended, see Table 35 and Figure 57 below. This was accomplished using an orthogonal regression. During the experimental phase, 5 points per sample were recorded, where both the time of flight (TOF) and the amplitude were collected. This allowed comparison of actual TOF with calculated TOF using the focus correction algorithm. A linear relationship is clearly visible. An orthogonal regression can determine whether the two measurement systems are equivalent. The results of this regression showed that the relationship was indeed linear but they were not equivalent. This introduces bias into the process however this step is consistently applied across all samples.

Averaging	Orthogonal Regression equation	95 % Confidence Interval Constant, SAM_TOF	Standard Error Constant, SAM_TOF	P (Level of Significance)
15x15 pixels	15x15AVG = - 0.707 + 1.078 SAM_TOF	(-1.13365, -0.27970) (1.02909, 1.12761)	0.217850 0.025133	0.001 0.000

Table 35 Results of Orthogonal Regression for a 15x15 averaging areas for focus correction algorithm. If the measuring methods are equivalent then the confidence intervals for the slope should include 1 and the intercept should include 0.

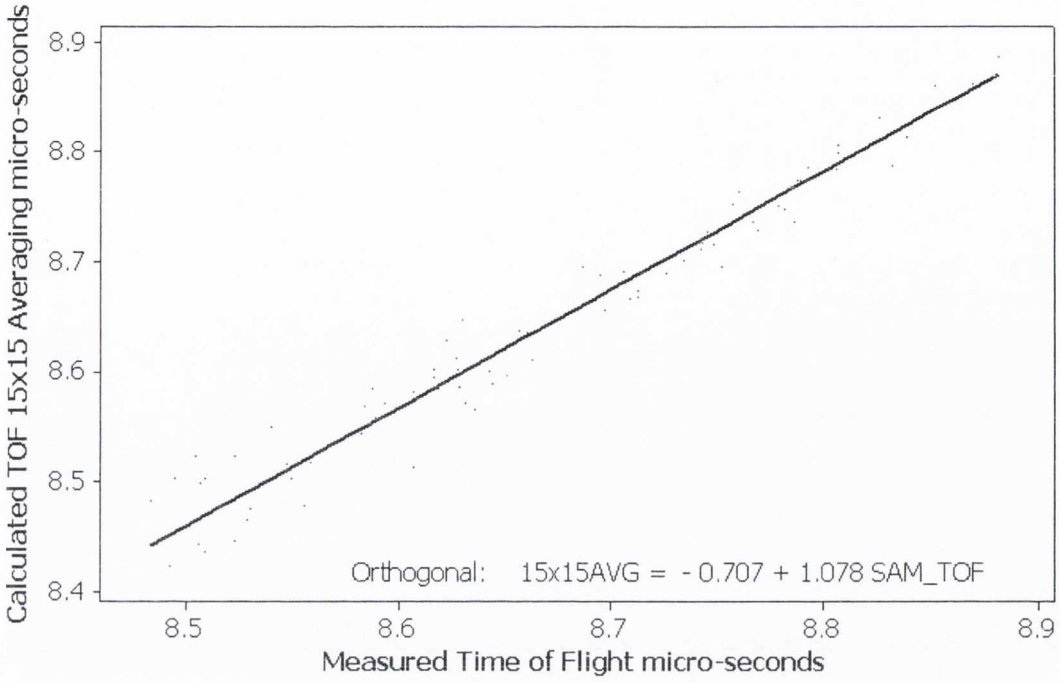


Figure 57 Calculated TOF Vs. Actual TOF orthogonal regression analysis. We can see there is a strong correlation between the measured TOF and the calculated TOF. Note a steady increase in the scatter of points from focus (right hand side of graph) to out of focus (left hand side).

5.2.2.2 Variation in Acoustic Impedance due to temperature

The coupling medium used in the SAM is water. Its acoustic properties are dependent on temperature , see Table 36. Therefore, during a test, this parameter must be recorded accurately to ensure accurate estimation of the acoustic impedance of the underlying material being scanned.

Temperature	Acoustic Impedance *Z* MRayl.
0°C	1.4
37°C	1.51
60°C	1.53

Table 36 Variation of acoustic Impedance of water with temperature.

5.2.2.3 Data Cleaning

Data cleaning was applied to the sub-images of Young's Modulus. This involved setting all the values that were NaN (Not a number) to zero. The NaN values indicated regions which were too out of focus to be corrected for. All values above 70GPa were set to 70GPa.

5.2.2.4 SAM machine

The assumption has been made that the Young's Modulus material properties are the same in all directions (isotropic material properties). This is a limitation of the SAM technique used. It is only capable of measuring the mechanical properties on a plane perpendicular to the ultrasonic beam. In this case measurement is being made of the Young's modulus in the axial plane of the sample.

The resolution of the SAM is limited and cannot fully resolve the osteonal structure of bone. This is due to the ultrasonic frequency used. 150 MHz represents a good balance between adequate resolution of microstructural features in bone and reasonable depth of focus of the ultrasonic lens. At higher frequencies, sample preparation is more difficult and compensation for unevenness in samples becomes more critical.

5.2.2.5 Errors introduced in Image Processing Pipeline:

Table 37 illustrates all the errors introduced by image processing required to convert raw SAM images to FE models. The largest error is that due to the focus correction algorithm. Raum et al. (Raum 2008) suggests using focus corrections within a margin where the RMS error is less than 1%. Examining Figure 57 it is clear that the error increases as the lens moves away from focus.

Error	Root mean square error GPa	Root mean square error Acoustic Amplitude
Least squares regression of TOF Vs. Amplitude. (Focus Correction)	7.5	3.79% (Note majority of this error is when lens is most out of focus.)
Averaging Algorithm (15x15)	3	1.71%
Fundamental precision of measurement of SAM, 8 bit images, 192 grey levels. Max Young's Modulus 45GPa	0.23	0.52%
FEA discretisation of material properties	0.25	
Calibration with known materials	3	2%
Empirical Equation relating measured acoustic impedance **Z** with $\mathbf{C_{33}}$	0.76	

Table 37 An estimate of the errors in the image processing of samples from raw SAM images to finite element models.

5.2.2.6 Use of Calibration samples

It is essential to image calibration materials periodically throughout the test. In this study samples of Quartz, Polycarbonate and PVC with known acoustic properties and dimensional properties were used. It is recommended to image these samples at least 10 times in order to estimate the reproducibility of acoustic parameters from the SAM images. Hasegawa et al. found a variation of about 0.13-0.51% in the acoustic parameters measured. (Hasegawa *et al.* 1995)

5.2.2.7 Conversion of C_{33} to Young's modulus.

The value used in this study to convert the $\mathbf{C_{33}}$ data to $\mathbf{E_3}$ relies on Poisson's ratios from other experimental studies (Rho 1996). It would be of more benefit to the study if the actual Poisson's ratios for the samples themselves could be determined. However, at the length scales of 25 microns, characterising Poisson's ratio has not yet been carried out (Raum *et al.* 2006a) . To deal with this uncertainty, it is necessary to look at the absolute maximum and minimum values of the factor needed to convert from $\mathbf{C_{33}}$ to $\mathbf{E_3}$. The estimated maximum and minimum values of this factor are 0.865 and 0.606. This equates to an error of ±18%.

5.2.2.8 Number of Samples

The number of samples available per sample type is not sufficient to discern differences in the means between Young's modulus values. However, with the large number of data points available for each sample and sample type, it is possible to investigate whether the underlying distributions of each sample type are different.

5.2.2.9 Comparisons between Year 1 and Year 2 samples

Year 1 and year 2 samples were imaged using SAM almost two years apart and thus comparison across years may not give accurate results. Year 1 samples were imaged using SAM in December 2009 and the year 2 samples were imaged in September 2011. Between December 2009 and September 2011, components of the SAM were serviced.

A calibration study was carried out at each imaging session. The results of this showed, that the servicing had indeed changed the sensitivity of the machine. This became apparent during the SAM imaging of the calibration samples. The imaging of the calibration sample with highest acoustic impedance, quartz, gave some unexpected results. It was decided for the September 2011 session to only use two out of the three calibration materials in the production of the calibration curve to relate measured values of acoustic reflectance with actual values of acoustic reflectance R.

The consequences of this is are, comparison between year 1 and year 2 samples may not be reliable.

5.2.2.10 FEA technique

An eight node quadrilateral element is used. Each element was assigned a Young's modulus value from the corresponding location in the Young's modulus sub-image. Hence, the finite element model has a linear Young's modulus property per element but the distribution of these properties leads to a model with a spatial inhomogeneous distribution of Young's modulus values. The element is used in its plane stress state. Due to the element formulation, only linear variations of stress and strain are permitted between overlapping elements.

Building of three dimensional finite element models of cortical bone from ultrasound data would allow the assessment of stress and strain in the whole bone. Realistic loading and boundary conditions could be applied to these models to estimate the micromechanical stress and strain stimuli. Comparisons could be made between bones for example between healthy and osteoporotic bone. These models by their very nature

would contain a great deal of elements. These models would be ideal for use with bone remodelling algorithms.

5.3 Consequences of Research Findings

5.3.1 Clinical Consequences

The most compelling finding of this research is the proof that Zoledronic Acid is able to maintain osteoporotic cortical bone's distribution of Young's modulus back to that of normal healthy bone.

The methods and techniques could be viewed as another powerful tool in evaluating the efficacy of drug treatments for osteoporosis, and as a method for characterising bone quality. Methods such as DEXA and MicroCT are good at measuring bone density but are poor at assessing bone stiffness and bone architecture.

This is the first such use of this technique for evaluating the effectiveness of these drug treatments. The year 2 OVX-ZOL samples clearly show maintenance of bone mechanical competence as a result of Zoledronic acid treatment. This is a result of reduced osteocyte apoptosis and reduced turnover when compared to OVX year 2 samples (Brennan 2008; Brennan *et al.* 2011).

5.3.2 Biomechanical consequences

This research provides a way in which to view the distribution of stresses, strain and Young's modulus in bone samples. These distributions are in effect a representation of the load induced stimuli which load sensing osteocytes, embedded in bone, are exposed to. When applied to diseased or drug treated samples a comparison can be made as to the changes in load induced stimuli sensed by osteocytes. Following on from this, the effect of anti-resorptive drug treatments on the micro-mechanical environment of cortical bone can be characterised.

In Figure 58(a) normal bone is characterised by a tail region to the left, which is a candidate for targeted resorption under normal physiological loads. The tail region to the right is bone, which will be subject to targeted remodelling or bone modelling if the strain is high enough. Figure 58(b) is a representation of the situation occurring in osteoporotic bone as found by this study in the year 2 ovariectomised samples. There is a larger area of bone in the left tail when compared to normal bone. The bone in this region is a candidate for targeted resorption due to disuse. This is further complicated

by the shifting of the adaptive window to the right, due to osteoporosis, that leads to more bone area being at risk of resorption. In Figure 58(c) the combined strain-adaptive remodelling and damage simulated resorption algorithm is shown (Mulvihill *et al.* 2010) . Using this algorithm it is can be seen that bone is adapted so long as the vast majority of the bone area is within the strain adaptive window. If for example, the disuse threshold increases, more bone is at risk of resportion.

This enhances our knowledge of osteoporosis in cortical bone due to estrogen withdrawal and builds on ideas and paradigms developed by Frost (Frost 1997a).

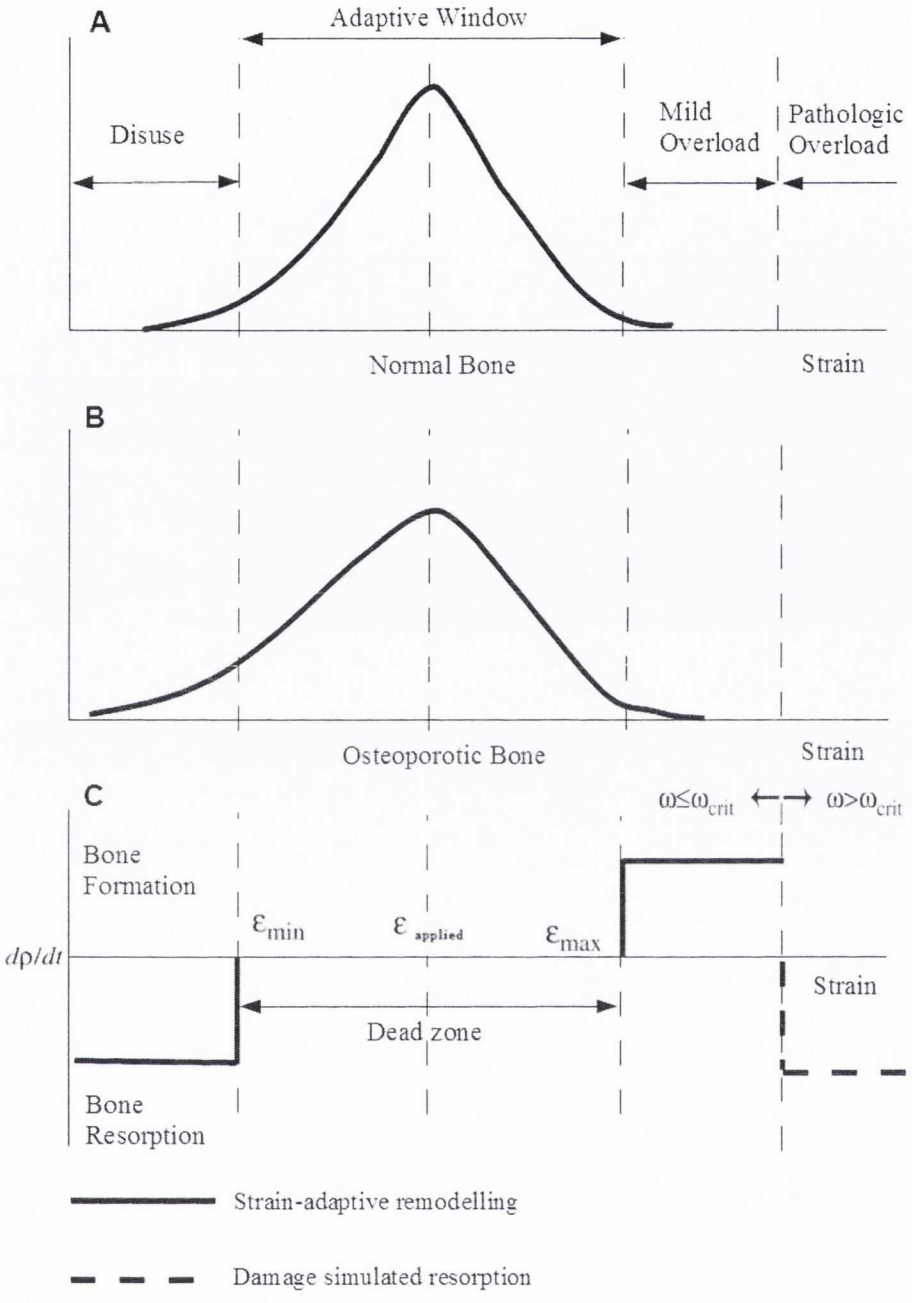


Figure 58 An interpretation of the altered distribution of strains, when compared to controls, due to osteoporosis. Diagram (A) above shows normal bone exposed to a physiological strain $\varepsilon_{applied}$. The distribution can be divided into a disuse window where bone can be resorbed, an adaptive window where no targeted remodelling takes place and a mild overload window where bone formation will occur. The most extreme situation to the right is where bone is resorbed due to it being damaged. Diagram (B) shows the strain distribution in osteoporotic bone. Comparing it with normal bone it has a fatter tail region to the left of the distribution. This can be interpreted that for a given disuse window and physiological strain load more area of bone in osteoporotic bone is at risk of resorption than in normal bone. Diagram (C) is the combined strain-adaptive remodelling and damage simulated resorption algorithm using the ON/OFF remodelling concept (Mulvihill et al. 2010).

Data on Young's modulus of a bone sample measured by SAM could be used as input material properties for bone remodelling simulations. This is a marked improvement over nano-indentation methods of evaluating bone stiffness.

The imaging of samples is non destructive. Fresh samples can be used. No special preparation is required other than the samples must be flat and polished. Subsequently, other tests can be performed on the samples.

Modelling of crack propagation in cortical bone can be performed using material properties found by SAM. Further understanding can be gained about the crack arresting properties of bone features such as osteons and cement line, and how disease effects these properties.

Young's modulus data from processed SAM images can be used to build better theoretical hierarchical models of bone microstructure. Using a range of SAM resolutions it is possible to collect the material property data at the different length scales required to build these models. Therefore the stresses and strains found in this study are only valid at the resolution of the SAM (25 μm) they are not those that bone cells such as osteocytes are exposed to.

The SAM method used here has the ability to quantify the effect of increasing the remodelling rate in cortical bone due to the estrogen withdrawal in an ovine animal model. The effects resulting from estrogen withdrawal such as osteocyte apoptosis and increased remodelling can be readily assessed and visualised. The effect of drug treatments on osteoporotic bone can also be visualised in the distributions of stress and strain. This allows comparison of new drug therapies for osteoporosis with normal bone to quantify how effective they are at restoring diseased bone to a more healthy state.

"Bone for Life" samples have undergone many types of testing. The techniques developed and the conclusion found by this research further complement and extends understanding of the changes which occur in bone undergoing estrogen withdrawal.

5.4 Future Work.

Utilising the data collected as part of this study, a number of other research questions could be addressed:

- What is the elastic stiffness of the cement lines and do they vary between samples and sample types? For example between Control and ovariectomised bone samples. Careful study of the SAM images shows that the cement lines are visible around the secondary osteons.
- Would it be possible, using image registration techniques developed by Raum *et al.* and others (Raum *et al.* 2006b; Basillais *et al.* 2007), to find the bone mineral density and mechanical stiffness of every point in sample? MicroCT and epi-fluorescent imaging was carried out on all the samples used in this study. The microCT imaging was carried out by Peter Mauer from the RCSI. This could lead to a rich vein of future work. This would allow a fuller picture of the effect of estrogen withdrawal osteoporosis on cortical bone.
- Are the flourochrome labelled osteons different in terms of mechanical stiffness across sample types? Using image registration techniques it is possible to locate osteons on SAM images which are marked with flourochrome dyes. Compare the dye marked osteons across bone sample types.
- What are the effects of changes to the mechano-stat thresholds on the mechanical properties of bone? Using a finite element analysis computer package such as ANSYS it would be possible to write a macro to simulate bone remodelling. The SAM based images of Young's modulus could be used as input to the model. Algorithms developed by McNamara (McNamara *et al.* 2007) and Mulvihill (Mulvihill *et al.* 2008) could be implemented. This could be investigated with data taken from actual samples of normal, ovariectomised and drug treated ovariectomised bone.

Using a modern SAM, a more accurate assessment of bone mechanical stiffness could be accomplished. With programmable access to a SAM it would be possible to capture the time of flight and the A scan waveform for each point in a SAM image. This would allow better focus compensation. It would also be possible to measure the speed of sound at every point in the sample. Thus both bone density and stiffness would be

available at every point. Using a sophisticated technique such as the v(z) technique, measurement of elastic stiffness in directions other than the axial direction could be accomplished.

Three dimensional cortical bone models could be constructed. A bone sample could be cut into many thin slices and SAM images taken of each slice. These slices could then be assembled in a FE model. SAM is limited in its resolution, therefore the stresses and strains evaluated from these SAM images is limited to that resolution. Sub-structured finite element models could be used to extend the resolution down to the level of the osteocyte lacuna. The boundary conditions and loadings for these sub-structured models would come from the lower resolution SAM based FE models.

By validating the methods and techniques used to assess the Young's modulus in bone samples imaged using SAM, this could become a recognised method for assessing the effectiveness of anti-resorptive drug effectiveness assessment during the pre-clinical phase of drug evaluation.

Part of this validation would be to assess if the finite element models were accurately measuring the micro-structural strain field in bone samples. This could be accomplished using techniques of assessing strain *in-vitro* developed by Nicolella and co-workers. (Nicolella *et al.* 2005).

6 Conclusions

1. A novel technique was successfully developed to evaluate the microstructural stress and strain environment that load sensing elements within cortical bone would experience. This was accomplished by a three step process. The first stage involved imaging cortical bone samples using scanning acoustic microscopy (SAM). A considerable number of attempts were required to get good images. Success involved developing good sample preparation and imaging protocols. The second step involved converting images into calibrated high resolution maps of acoustic impedance. Using relationships between acoustic impedance Z and elastic stiffness C_{33} developed by Raum et al. these images were then converted to Young's modulus values. The third stage involved developing a customised ANSYS script to build a computational finite element models which evaluated stresses and strain due to physiological strain loadings (1500 μ strain).
2. This technique was applied to ovine bone samples from the "Bone for Life" project. These samples were available in three types (ovariectomised, normal and drug treated ovariectomised) and at two time periods (12 months and 31 months).
3. It was found that the bisphosponate, Zoledronic acid maintained the mechanical competence of the year 2 drug treated ovariectomised bone samples. This is in agreement with the findings of other investigators working in the "Bone for Life" project. The distributions of Young's modulus, stress and strain for the ovariectomised drug treated samples are almost overlapping with the year 2 control bone samples.

4. The fruits of this research give a new ability to view the distribution of stresses, strain and Young's modulus in bone samples. These distributions are in effect a representation of the load induced stimuli to which load sensing osteocytes, embedded in bone, are exposed. When applied to diseased or drug treated samples, comparison can be made as to the changes in load induced stimuli sensed by osteocytes.

5. The methods and techniques developed as a result of this research could be used as a powerful tool in evaluating the efficacy of drug treatments for osteoporosis and as a method for characterising bone quality.

   This research can be used to develop and extend existing paradigms about bone remodelling and resorption in cortical bone due to estrogen withdrawal. The findings of this research appear to confirm the idea that osteoporosis causes a shift up in the disuse threshold thus leading to accelerated bone resorption. From the data collected in this research it appears that osteoporosis causes the distributions of strain to become skewed where more bone is at a lower strain when compared to controls. This points to a situation where for a given load on bone a larger volume of bone is at a lower strain value. This in turn has a structural consequence for bone which further alters future cell responses to load.

7 Appendices

7.1 Matlab Code for Image Processing

7.1.1 Year 1 samples

7.1.1.1 Image Processing

This matlab script was used to take images generated by SAM and turn them into plots Young's modulus plots for each sample. These samples were imaged on the 11th of December 2011.

sample_processing_v5_15x15.m

```
%Image processing scheme using idea of moving average. For SAM bone
imaging
%Ver 4. Confirmed
%Written by PW 5 July 2010. Updated 14 July 2010. Updated 16 July
2010
%Edited 20/9/2010 added gaussian filter. Edited 5/12/10
%Edited 5/1/2011.
%Edited 12/1/2011 Add 15x15 averaging
%Next job is to turn this into a function how do we use names in
output
%files? sort this out. this will reduce size of this file.


s15r3mod2=double(s15r3mod1); % conversion from unit8 to double
precesion
%if required
s15r3mod3=s15r3mod2/255;     %Conversion from value from 0 to 1
%
vector_s15r3mod3=s15r3mod3(:); %create vector from r3mod3 image
zero_locations_vector_s15r3mod3 = find(vector_s15r3mod3<0.001); %find
the zero locations in image
avg_s15r3mod3=sum(vector_s15r3mod3)/(max(size(vector_s15r3mod3)-
max(size(zero_locations_vector_s15r3mod3)))); % Find average.
%
zero_locations_s15r3mod3 = find(s15r3mod3<0.001); %Replace values
less than 0.001 with average value.
s15r3mod3(zero_locations_s15r3mod3) = avg_s15r3mod3;% Set as average
for bone sample
%
h=fspecial('average',15); % Average filter convolution trying 3 5 10
15 20 decided on 5.
s15r3mod3avg=imfilter(s15r3mod3,h); % use filter to produce average
value matrix
p=[1.465 -24.37 101.66]; % polynomial for Bone TOF to Amp curve. See
timevamp228_6_10.xlsx updated 12 July 2010
time_mu_sec=linspace(8.35,8.91,100); % Linear space between 8.35 and
8.91 micro seconds 100 points
amp_bone=polyval(p,time_mu_sec); % Evaluate Polynomial p
TOF_s15r3mod3=interp1(amp_bone,time_mu_sec,s15r3mod3avg); %
interpolate for Bone TOF to Amp curve.
%
```

```
amp_factor_s15r3mod3=interp1(time_mu_sec,amp_correction_bone,TOF_s15r
3mod3); % interpolate for bone amp Vs TOF See timevamp228_6_10.xlsx
updated 12 July 2010
%
s15r3mod4a=amp_factor_s15r3mod3.*s15r3mod3; %peak value on bone tof
to amp. See timevamp228_6_10.xlsx updated 12 July 2010
s15r3mod4a(zero_locations_s15r3mod3) = 0;%replace average with zeros.
%
s15r3mod6a=0.8304.*s15r3mod4a-0.0591; % R adjust to calibration curve
for materials see 'copy of calbration_worksheet_5_7_10.xls updated:
12 july 2010
s15zs=-(((s15r3mod6a+1)./(s15r3mod6a-1)).*1.48); % Z value of bone
should be 6.28+ or -0.54 MRayl.
s15r3c33=1.31+0.075.*s15zs+0.5.*s15zs.^2; % C33 Raum equation value
s15r3E3=s15r3c33*0.865; %r3E3 Conversion from C33 to r3E3 factor can
be 0.606 to 0.865
```

7.1.1.2 Selection of sub images from SAM source images

In this script three areas are selected from each SAM image. These are stored in a vector format.

Selections.m

```
%Selection of areas
%FOR FEA work for all images
% updated to select 3 areas per SAM image.
% mod 4 20/12/2010
%Script to automate selection of area of image for FE analysis and
stat
%analysis in Minitab
%sample 15

selection_s15r3mod6a_1=s15r3mod6a(495:(495+50),617:(617+100));
selection_s15zs_1=s15zs(495:(495+50),617:(617+100));
selection_s15r3E3_1=s15r3E3(495:(495+50),617:(617+100));
vector_selection_s15r3mod6a_1=selection_s15r3mod6a_1(:);
vector_selection_s15zs_1=selection_s15zs_1(:);
vector_selection_s15r3E3_1=selection_s15r3E3_1(:);

selection_s15r3mod6a_2=s15r3mod6a(382:(382+50),567:(567+100));
selection_s15zs_2=s15zs(382:(382+50),567:(567+100));
selection_s15r3E3_2=s15r3E3(382:(382+50),567:(567+100));
vector_selection_s15r3mod6a_2=selection_s15r3mod6a_2(:);
vector_selection_s15zs_2=selection_s15zs_2(:);
vector_selection_s15r3E3_2=selection_s15r3E3_2(:);

selection_s15r3mod6a_3=s15r3mod6a(558:(558+50),615:(615+100));
selection_s15zs_3=s15zs(558:(558+50),615:(615+100));
selection_s15r3E3_3=s15r3E3(558:(558+50),615:(615+100));
vector_selection_s15r3mod6a_3=selection_s15r3mod6a_3(:);
vector_selection_s15zs_3=selection_s15zs_3(:);
vector_selection_s15r3E3_3=selection_s15r3E3_3(:);


%Script to automate selection of area of image for FE analysis and
stat
%analysis in Minitab

%sample 20
selection_s20r3mod6a_1=s20r3mod6a(200:(200+50),400:(400+100));
selection_s20zs_1=s20zs(200:(200+50),400:(400+100));
selection_s20r3E3_1=s20r3E3(200:(200+50),400:(400+100));
vector_selection_s20r3mod6a_1=selection_s20r3mod6a_1(:);
vector_selection_s20zs_1=selection_s20zs_1(:);
vector_selection_s20r3E3_1=selection_s20r3E3_1(:);

selection_s20r3mod6a_2=s20r3mod6a(187:(187+50),443:(443+100));
selection_s20zs_2=s20zs(187:(187+50),443:(443+100));
selection_s20r3E3_2=s20r3E3(187:(187+50),443:(443+100));
vector_selection_s20r3mod6a_2=selection_s20r3mod6a_2(:);
vector_selection_s20zs_2=selection_s20zs_2(:);
vector_selection_s20r3E3_2=selection_s20r3E3_2(:);
```

```
selection_s20r3mod6a_3=s20r3mod6a(210:(210+50),239:(239+100));
selection_s20zs_3=s20zs(210:(210+50),239:(239+100));
selection_s20r3E3_3=s20r3E3(210:(210+50),239:(239+100));
vector_selection_s20r3mod6a_3=selection_s20r3mod6a_3(:);
vector_selection_s20zs_3=selection_s20zs_3(:);
vector_selection_s20r3E3_3=selection_s20r3E3_3(:);

%Script to automate selection of area of image for FE analysis and
stat
%analysis in Minitab
%sample 22b
selection_s22br3mod6a_1=s22br3mod6a(592:(592+50),623:(623+100));
selection_s22bzs_1=s22bzs(592:(592+50),623:(623+100));
selection_s22br3E3_1=s22br3E3(592:(592+50),623:(623+100));
vector_selection_s22br3mod6a_1=selection_s22br3mod6a_1(:);
vector_selection_s22bzs_1=selection_s22bzs_1(:);
vector_selection_s22br3E3_1=selection_s22br3E3_1(:);

selection_s22br3mod6a_2=s22br3mod6a(186:(186+50),314:(314+100));
selection_s22bzs_2=s22bzs(186:(186+50),314:(314+100));
selection_s22br3E3_2=s22br3E3(186:(186+50),314:(314+100));
vector_selection_s22br3mod6a_2=selection_s22br3mod6a_2(:);
vector_selection_s22bzs_2=selection_s22bzs_2(:);
vector_selection_s22br3E3_2=selection_s22br3E3_2(:);

selection_s22br3mod6a_3=s22br3mod6a(613:(613+50),495:(495+100));
selection_s22bzs_3=s22bzs(613:(613+50),495:(495+100));
selection_s22br3E3_3=s22br3E3(613:(613+50),495:(495+100));
vector_selection_s22br3mod6a_3=selection_s22br3mod6a_3(:);
vector_selection_s22bzs_3=selection_s22bzs_3(:);
vector_selection_s22br3E3_3=selection_s22br3E3_3(:);



%Script to automate selection of area of image for FE analysis and
stat
%analysis in Minitab
%sample 2

selection_s2zs_1=s2zs(208:(208+50),645:(645+100));
selection_s2r3mod6a_1=s2r3mod6a(208:(208+50),645:(645+100));
selection_s2r3E3_1=s2r3E3(208:(208+50),645:(645+100));
vector_selection_s2zs_1=selection_s2zs_1(:);
vector_selection_s2r3mod6a_1=selection_s2r3mod6a_1(:);
vector_selection_s2r3E3_1=selection_s2r3E3_1(:);

selection_s2zs_2=s2zs(150:(150+50),397:(397+100));
selection_s2r3mod6a_2=s2r3mod6a(150:(150+50),397:(397+100));
selection_s2r3E3_2=s2r3E3(150:(150+50),397:(397+100));
vector_selection_s2zs_2=selection_s2zs_2(:);
vector_selection_s2r3mod6a_2=selection_s2r3mod6a_2(:);
vector_selection_s2r3E3_2=selection_s2r3E3_2(:);

selection_s2zs_3=s2zs(155:(155+50),571:(571+100));
selection_s2r3mod6a_3=s2r3mod6a(155:(155+50),571:(571+100));
selection_s2r3E3_3=s2r3E3(155:(155+50),571:(571+100));
vector_selection_s2zs_3=selection_s2zs_3(:);
vector_selection_s2r3mod6a_3=selection_s2r3mod6a_3(:);
vector_selection_s2r3E3_3=selection_s2r3E3_3(:);
```

```
%Script to automate selection of area of image for FE analysis and
stat
%analysis in Minitab
%sample 31
selection_s31r3mod6a_1=s31r3mod6a(183:(183+50),522:(522+100));
selection_s31zs_1=s31zs(183:(183+50),522:(522+100));
selection_s31r3E3_1=s31r3E3(183:(183+50),522:(522+100));
vector_selection_s31r3mod6a_1=selection_s31r3mod6a_1(:);
vector_selection_s31zs_1=selection_s31zs_1(:);
vector_selection_s31r3E3_1=selection_s31r3E3_1(:);

selection_s31r3mod6a_2=s31r3mod6a(192:(192+50),530:(530+100));
selection_s31zs_2=s31zs(192:(192+50),530:(530+100));
selection_s31r3E3_2=s31r3E3(192:(192+50),530:(530+100));
vector_selection_s31r3mod6a_2=selection_s31r3mod6a_2(:);
vector_selection_s31zs_2=selection_s31zs_2(:);
vector_selection_s31r3E3_2=selection_s31r3E3_2(:);

selection_s31r3mod6a_3=s31r3mod6a(196:(196+50),284:(284+100));
selection_s31zs_3=s31zs(196:(196+50),284:(284+100));
selection_s31r3E3_3=s31r3E3(196:(196+50),284:(284+100));
vector_selection_s31r3mod6a_3=selection_s31r3mod6a_3(:);
vector_selection_s31zs_3=selection_s31zs_3(:);
vector_selection_s31r3E3_3=selection_s31r3E3_3(:);

%Script to automate selection of area of image for FE analysis and
stat
%analysis in Minitab
%sample 32a

selection_s32ar3mod6a_1=s32ar3mod6a(457:(457+50),434:(434+100));
selection_s32azs_1=s32azs(457:(457+50),434:(434+100));
selection_s32ar3E3_1=s32ar3E3(457:(457+50),434:(434+100));
vector_selection_s32ar3mod6a_1=selection_s32ar3mod6a_1(:);
vector_selection_s32azs_1=selection_s32azs_1(:);
vector_selection_s32ar3E3_1=selection_s32ar3E3_1(:);

selection_s32ar3mod6a_2=s32ar3mod6a(199:(199+50),58:(58+100));
selection_s32azs_2=s32azs(199:(199+50),58:(58+100));
selection_s32ar3E3_2=s32ar3E3(199:(199+50),58:(58+100));
vector_selection_s32ar3mod6a_2=selection_s32ar3mod6a_2(:);
vector_selection_s32azs_2=selection_s32azs_2(:);
vector_selection_s32ar3E3_2=selection_s32ar3E3_2(:);

selection_s32ar3mod6a_3=s32ar3mod6a(338:(338+50),28:(28+100));
selection_s32azs_3=s32azs(338:(338+50),28:(28+100));
selection_s32ar3E3_3=s32ar3E3(338:(338+50),28:(28+100));
vector_selection_s32ar3mod6a_3=selection_s32ar3mod6a_3(:);
vector_selection_s32azs_3=selection_s32azs_3(:);
vector_selection_s32ar3E3_3=selection_s32ar3E3_3(:);



%Script to automate selection of area of image for FE analysis and
stat
```

```
%analysis in Minitab
%sample 4a
selection_s4ar3mod6a_1=s4ar3mod6a(116:(116+50),387:(387+100));
selection_s4azs_1=s4azs(116:(116+50),387:(387+100));
selection_s4ar3E3_1=s4ar3E3(116:(116+50),387:(387+100));
vector_selection_s4ar3mod6a_1=selection_s4ar3mod6a_1(:);
vector_selection_s4azs_1=selection_s4azs_1(:);
vector_selection_s4ar3E3_1=selection_s4ar3E3_1(:);

selection_s4ar3mod6a_2=s4ar3mod6a(101:(101+50),424:(424+100));
selection_s4azs_2=s4azs(101:(101+50),424:(424+100));
selection_s4ar3E3_2=s4ar3E3(101:(101+50),424:(424+100));
vector_selection_s4ar3mod6a_2=selection_s4ar3mod6a_2(:);
vector_selection_s4azs_2=selection_s4azs_2(:);
vector_selection_s4ar3E3_2=selection_s4ar3E3_2(:);

selection_s4ar3mod6a_3=s4ar3mod6a(529:(529+50),536:(536+100));
selection_s4azs_3=s4azs(529:(529+50),536:(536+100));
selection_s4ar3E3_3=s4ar3E3(529:(529+50),536:(536+100));
vector_selection_s4ar3mod6a_3=selection_s4ar3mod6a_3(:);
vector_selection_s4azs_3=selection_s4azs_3(:);
vector_selection_s4ar3E3_3=selection_s4ar3E3_3(:);

%Script to automate selection of area of image for FE analysis and
stat
%analysis in Minitab
%sample 4b

selection_s4br3mod6a_1=s4br3mod6a(170:(170+50),552:(552+100));
selection_s4bzs_1=s4bzs(170:(170+50),552:(552+100));
selection_s4br3E3_1=s4br3E3(170:(170+50),552:(552+100));
vector_selection_s4br3mod6a_1=selection_s4br3mod6a_1(:);
vector_selection_s4bzs_1=selection_s4bzs_1(:);
vector_selection_s4br3E3_1=selection_s4br3E3_1(:);

selection_s4br3mod6a_2=s4br3mod6a(197:(197+50),175:(175+100));
selection_s4bzs_2=s4bzs(197:(197+50),175:(175+100));
selection_s4br3E3_2=s4br3E3(197:(197+50),175:(175+100));
vector_selection_s4br3mod6a_2=selection_s4br3mod6a_2(:);
vector_selection_s4bzs_2=selection_s4bzs_2(:);
vector_selection_s4br3E3_2=selection_s4br3E3_2(:);

selection_s4br3mod6a_3=s4br3mod6a(154:(154+50),402:(402+100));
selection_s4bzs_3=s4bzs(154:(154+50),402:(402+100));
selection_s4br3E3_3=s4br3E3(154:(154+50),402:(402+100));
vector_selection_s4br3mod6a_3=selection_s4br3mod6a_3(:);
vector_selection_s4bzs_3=selection_s4bzs_3(:);
vector_selection_s4br3E3_3=selection_s4br3E3_3(:);


%Script to automate selection of area of image for FE analysis and
stat
%analysis in Minitab
%sample5b

selection_s5br3mod6a_1=s5br3mod6a(263:(263+50),504:(504+100));
selection_s5bzs_1=s5bzs(263:(263+50),504:(504+100));
selection_s5br3E3_1=s5br3E3(263:(263+50),504:(504+100));
vector_selection_s5br3mod6a_1=selection_s5br3mod6a_1(:);
```

```
vector_selection_s5bzs_1=selection_s5bzs_1(:);
vector_selection_s5br3E3_1=selection_s5br3E3_1(:);

selection_s5br3mod6a_2=s5br3mod6a(229:(229+50),464:(464+100));
selection_s5bzs_2=s5bzs(229:(229+50),464:(464+100));
selection_s5br3E3_2=s5br3E3(229:(229+50),464:(464+100));
vector_selection_s5br3mod6a_2=selection_s5br3mod6a_2(:);
vector_selection_s5bzs_2=selection_s5bzs_2(:);
vector_selection_s5br3E3_2=selection_s5br3E3_2(:);

selection_s5br3mod6a_3=s5br3mod6a(530:(530+50),617:(617+100));
selection_s5bzs_3=s5bzs(530:(530+50),617:(617+100));
selection_s5br3E3_3=s5br3E3(530:(530+50),617:(617+100));
vector_selection_s5br3mod6a_3=selection_s5br3mod6a_3(:);
vector_selection_s5bzs_3=selection_s5bzs_3(:);
vector_selection_s5br3E3_3=selection_s5br3E3_3(:);

%Script to automate selection of area of image for FE analysis and
stat
%analysis in Minitab
%sample6

selection_s6r3mod6a_1=s6r3mod6a(263:(263+50),554:(554+100));
selection_s6zs_1=s6zs(263:(263+50),554:(554+100));
selection_s6r3E3_1=s6r3E3(263:(263+50),554:(554+100));
vector_selection_s6r3mod6a_1=selection_s6r3mod6a_1(:);
vector_selection_s6zs_1=selection_s6zs_1(:);
vector_selection_s6r3E3_1=selection_s6r3E3_1(:);

selection_s6r3mod6a_2=s6r3mod6a(166:(166+50),245:(245+100));
selection_s6zs_2=s6zs(166:(166+50),245:(245+100));
selection_s6r3E3_2=s6r3E3(166:(166+50),245:(245+100));
vector_selection_s6r3mod6a_2=selection_s6r3mod6a_2(:);
vector_selection_s6zs_2=selection_s6zs_2(:);
vector_selection_s6r3E3_2=selection_s6r3E3_2(:);

selection_s6r3mod6a_3=s6r3mod6a(265:(265+50),88:(88+100));
selection_s6zs_3=s6zs(265:(265+50),88:(88+100));
selection_s6r3E3_3=s6r3E3(265:(265+50),88:(88+100));
vector_selection_s6r3mod6a_3=selection_s6r3mod6a_3(:);
vector_selection_s6zs_3=selection_s6zs_3(:);
vector_selection_s6r3E3_3=selection_s6r3E3_3(:);
```

7.1.1.3 Dataprocessing

This script is used to process the three selected areas per SAM image and remove any NaN (Not a Number) entries and remove any Young's Modulus values above 70 and set them to 70. These vectors are then wrote out as text files for each sub-image.

Dataprocessing.m

```
%Dataprocessing.m mod 2, mod 3
%Modified for 3 sub images per sample.
%20/12/2010
%Modified changed sample names to less than 8 characters
%5 Jan. 2011.


%Get rid of NaN in data
vector_selection_s15r3E3_1(isnan(vector_selection_s15r3E3_1))=0;
vector_selection_s20r3E3_1(isnan(vector_selection_s20r3E3_1))=0;
vector_selection_s22br3E3_1(isnan(vector_selection_s22br3E3_1))=0;
vector_selection_s23br3E3_1(isnan(vector_selection_s23br3E3_1))=0;
vector_selection_s23r3E3_1(isnan(vector_selection_s23r3E3_1))=0;
vector_selection_s2r3E3_1(isnan(vector_selection_s2r3E3_1))=0;
vector_selection_s31r3E3_1(isnan(vector_selection_s31r3E3_1))=0;
vector_selection_s32ar3E3_1(isnan(vector_selection_s32ar3E3_1))=0;
vector_selection_s4ar3E3_1(isnan(vector_selection_s4ar3E3_1))=0;
vector_selection_s4br3E3_1(isnan(vector_selection_s4br3E3_1))=0;
vector_selection_s5br3E3_1(isnan(vector_selection_s5br3E3_1))=0;
vector_selection_s6r3E3_1(isnan(vector_selection_s6r3E3_1))=0;

vector_selection_s15r3E3_2(isnan(vector_selection_s15r3E3_2))=0;
vector_selection_s20r3E3_2(isnan(vector_selection_s20r3E3_2))=0;
vector_selection_s22br3E3_2(isnan(vector_selection_s22br3E3_2))=0;
vector_selection_s23br3E3_2(isnan(vector_selection_s23br3E3_2))=0;
vector_selection_s23r3E3_2(isnan(vector_selection_s23r3E3_2))=0;
vector_selection_s2r3E3_2(isnan(vector_selection_s2r3E3_2))=0;
vector_selection_s31r3E3_2(isnan(vector_selection_s31r3E3_2))=0;
vector_selection_s32ar3E3_2(isnan(vector_selection_s32ar3E3_2))=0;
vector_selection_s4ar3E3_2(isnan(vector_selection_s4ar3E3_2))=0;
vector_selection_s4br3E3_2(isnan(vector_selection_s4br3E3_2))=0;
vector_selection_s5br3E3_2(isnan(vector_selection_s5br3E3_2))=0;
vector_selection_s6r3E3_2(isnan(vector_selection_s6r3E3_2))=0;

vector_selection_s15r3E3_3(isnan(vector_selection_s15r3E3_3))=0;
vector_selection_s20r3E3_3(isnan(vector_selection_s20r3E3_3))=0;
vector_selection_s22br3E3_3(isnan(vector_selection_s22br3E3_3))=0;
vector_selection_s23br3E3_3(isnan(vector_selection_s23br3E3_3))=0;
vector_selection_s23r3E3_3(isnan(vector_selection_s23r3E3_3))=0;
vector_selection_s2r3E3_3(isnan(vector_selection_s2r3E3_3))=0;
vector_selection_s31r3E3_3(isnan(vector_selection_s31r3E3_3))=0;
vector_selection_s32ar3E3_3(isnan(vector_selection_s32ar3E3_3))=0;
vector_selection_s4ar3E3_3(isnan(vector_selection_s4ar3E3_3))=0;
vector_selection_s4br3E3_3(isnan(vector_selection_s4br3E3_3))=0;
vector_selection_s5br3E3_3(isnan(vector_selection_s5br3E3_3))=0;
vector_selection_s6r3E3_3(isnan(vector_selection_s6r3E3_3))=0;


%Remove values above 70GPa
```

```
gt70loc=find(vector_selection_s15r3E3_1>70);
vector_selection_s15r3E3_1(gt70loc)=70;

gt70loc=find(vector_selection_s20r3E3_1>70);
vector_selection_s20r3E3_1(gt70loc)=70;

gt70loc=find(vector_selection_s22br3E3_1>70);
vector_selection_s22br3E3_1(gt70loc)=70;

gt70loc=find(vector_selection_s23br3E3_1>70);
vector_selection_s23br3E3_1(gt70loc)=70;

gt70loc=find(vector_selection_s23r3E3_1>70);
vector_selection_s23r3E3_1(gt70loc)=70;

gt70loc=find(vector_selection_s31r3E3_1>70);
vector_selection_s31r3E3_1(gt70loc)=70;

gt70loc=find(vector_selection_s32ar3E3_1>70);
vector_selection_s32ar3E3_1(gt70loc)=70;

gt70loc=find(vector_selection_s4ar3E3_1>70);
vector_selection_s4ar3E3_1(gt70loc)=70;

gt70loc=find(vector_selection_s4br3E3_1>70);
vector_selection_s4br3E3_1(gt70loc)=70;


gt70loc=find(vector_selection_s5br3E3_1>70);
vector_selection_s5br3E3_1(gt70loc)=70;

gt70loc=find(vector_selection_s6r3E3_1>70);
vector_selection_s6r3E3_1(gt70loc)=70;



gt70loc=find(vector_selection_s15r3E3_2>70);
vector_selection_s15r3E3_2(gt70loc)=70;

gt70loc=find(vector_selection_s20r3E3_2>70);
vector_selection_s20r3E3_2(gt70loc)=70;

gt70loc=find(vector_selection_s22br3E3_2>70);
vector_selection_s22br3E3_2(gt70loc)=70;

gt70loc=find(vector_selection_s23br3E3_2>70);
vector_selection_s23br3E3_2(gt70loc)=70;

gt70loc=find(vector_selection_s23r3E3_2>70);
vector_selection_s23r3E3_2(gt70loc)=70;

gt70loc=find(vector_selection_s31r3E3_2>70);
vector_selection_s31r3E3_2(gt70loc)=70;

gt70loc=find(vector_selection_s32ar3E3_2>70);
vector_selection_s32ar3E3_2(gt70loc)=70;
```

```
gt70loc=find(vector_selection_s4ar3E3_2>70);
vector_selection_s4ar3E3_2(gt70loc)=70;

gt70loc=find(vector_selection_s4br3E3_2>70);
vector_selection_s4br3E3_2(gt70loc)=70;


gt70loc=find(vector_selection_s5br3E3_2>70);
vector_selection_s5br3E3_2(gt70loc)=70;

gt70loc=find(vector_selection_s6r3E3_2>70);
vector_selection_s6r3E3_2(gt70loc)=70;




gt70loc=find(vector_selection_s15r3E3_3>70);
vector_selection_s15r3E3_3(gt70loc)=70;

gt70loc=find(vector_selection_s20r3E3_3>70);
vector_selection_s20r3E3_3(gt70loc)=70;

gt70loc=find(vector_selection_s22br3E3_3>70);
vector_selection_s22br3E3_3(gt70loc)=70;

gt70loc=find(vector_selection_s23br3E3_3>70);
vector_selection_s23br3E3_3(gt70loc)=70;

gt70loc=find(vector_selection_s23r3E3_3>70);
vector_selection_s23r3E3_3(gt70loc)=70;

gt70loc=find(vector_selection_s31r3E3_3>70);
vector_selection_s31r3E3_3(gt70loc)=70;

gt70loc=find(vector_selection_s32ar3E3_3>70);
vector_selection_s32ar3E3_3(gt70loc)=70;

gt70loc=find(vector_selection_s4ar3E3_3>70);
vector_selection_s4ar3E3_3(gt70loc)=70;

gt70loc=find(vector_selection_s4br3E3_3>70);
vector_selection_s4br3E3_3(gt70loc)=70;

gt70loc=find(vector_selection_s5br3E3_3>70);
vector_selection_s5br3E3_3(gt70loc)=70;

gt70loc=find(vector_selection_s6r3E3_3>70);
vector_selection_s6r3E3_3(gt70loc)=70;




%Write out files for FEA work
dlmwrite('s15E3_1.txt',vector_selection_s15r3E3_1);
```

```
dlmwrite('s20E3_1.txt',vector_selection_s20r3E3_1);
dlmwrite('s22BE3_1.txt',vector_selection_s22br3E3_1);
dlmwrite('s23bE3_1.txt',vector_selection_s23br3E3_1);
dlmwrite('s23E3_1.txt',vector_selection_s23r3E3_1);
dlmwrite('s2E3_1.txt',vector_selection_s2r3E3_1);
dlmwrite('s31E3_1.txt',vector_selection_s31r3E3_1);
dlmwrite('s32aE3_1.txt',vector_selection_s32ar3E3_1);
dlmwrite('s4AE3_1.txt',vector_selection_s4ar3E3_1);
dlmwrite('s4bE3_1.txt',vector_selection_s4br3E3_1);
dlmwrite('s5BE3_1.txt',vector_selection_s5br3E3_1);
dlmwrite('s6E3_1.txt',vector_selection_s6r3E3_1);

%Write out files for FEA work
dlmwrite('s15E3_2.txt',vector_selection_s15r3E3_2);
dlmwrite('s20E3_2.txt',vector_selection_s20r3E3_2);
dlmwrite('s22BE3_2.txt',vector_selection_s22br3E3_2);
dlmwrite('s23bE3_2.txt',vector_selection_s23br3E3_2);
dlmwrite('s23E3_2.txt',vector_selection_s23r3E3_2);
dlmwrite('s2E3_2.txt',vector_selection_s2r3E3_2);
dlmwrite('s31E3_2.txt',vector_selection_s31r3E3_2);
dlmwrite('s32aE3_2.txt',vector_selection_s32ar3E3_2);
dlmwrite('s4AE3_2.txt',vector_selection_s4ar3E3_2);
dlmwrite('s4bE3_2.txt',vector_selection_s4br3E3_2);
dlmwrite('s5BE3_2.txt',vector_selection_s5br3E3_2);
dlmwrite('s6E3_2.txt',vector_selection_s6r3E3_2);

%Write out files for FEA work
dlmwrite('s15E3_3.txt',vector_selection_s15r3E3_3);
dlmwrite('s20E3_3.txt',vector_selection_s20r3E3_3);
dlmwrite('s22BE3_3.txt',vector_selection_s22br3E3_3);
dlmwrite('s23bE3_3.txt',vector_selection_s23br3E3_3);
dlmwrite('s23E3_3.txt',vector_selection_s23r3E3_3);
dlmwrite('s2E3_3.txt',vector_selection_s2r3E3_3);
dlmwrite('s31E3_3.txt',vector_selection_s31r3E3_3);
dlmwrite('s32aE3_3.txt',vector_selection_s32ar3E3_3);
dlmwrite('s4AE3_3.txt',vector_selection_s4ar3E3_3);
dlmwrite('s4bE3_3.txt',vector_selection_s4br3E3_3);
dlmwrite('s5BE3_3.txt',vector_selection_s5br3E3_3);
dlmwrite('s6E3_3.txt',vector_selection_s6r3E3_3);
```

7.1.2 Year 2 samples

7.1.2.1 Image Processing

Below is a set of scripts used to transform SAM source images of each sample into plots of Young's modulus. These samples were imaged on the 30th of September 2011.

```
%Year 2 Samples Imaged on the 30th September 2011
%
% Based on image processing from 30/11/09 samples.
% Sample s36a
%step1
s36amod2=double(s36a); % conversion from unit8 to double precesion
%
%step2
s36amod3=s36amod2/255;    %Conversion from value from 0 to 1
%
%step3
vector_s36amod3=s36amod3(:); %create vector from r3mod3 image
zero_locations_vector_s36amod3 = find(vector_s36amod3<0.001); %find
the zero locations in image
avg_s36amod3=sum(vector_s36amod3)/(max(size(vector_s36amod3)-
max(size(zero_locations_vector_s36amod3)))); % Find average.
%
zero_locations_s36amod3 = find(s36amod3<0.001); %Replace values less
than 0.001 with average value.
s36amod3(zero_locations_s36amod3) = avg_s36amod3;% Set as average for
bone sample
%End Threshold section
%Averaging filter
h=fspecial('average',15); % Average filter convolution
s36amod3avg=imfilter(s36amod3,h); % use filter to produce average
value matrix
%p=[-1.333 24.73 -144.0]; % polynomial for Bone TOF to Amp curve.
%time_mu_sec=linspace(8.35,8.98,100); % Linear space between 8.35 and
8.91 micro seconds 100 points
%amp_bone=polyval(p,time_mu_sec); % Evaluate Polynomial p
TOF_s36amod3=interp1(amp_bone,time_mu_sec,s36amod3avg); % interpolate
for Bone TOF to Amp curve.
%
amp_factor_s36amod3=interp1(time_mu_sec,amp_correct_bone,TOF_s36amod3
); % interpolate for bone amp Vs TOF
%
s36amod4a=amp_factor_s36amod3.*s36amod3; %peak value on bone tof to
amp.
s36amod4a(zero_locations_s36amod3) = 0;%replace average with zeros.
%
%Step4
s36amod6a=1.125.*s36amod4a-0.0237; % R adjust to calibration curve
for materials
%Step5
s36azs=-(((s36amod6a+1)./(s36amod6a-1)).*1.48); % Z=1.48 @22 degrees?
Z value of bone should be 6.28+ or -0.54 MRayl.
%Step6
s36ac33=1.31+0.075.*s36azs+0.5.*s36azs.^2; % C33 Raum equation value
```

```
%Step7
s36aE3=s36ac33*0.865; %r3E3 Conversion from C33 to r3E3 factor can be
0.606 to 0.865
```

7.1.2.2 Selection of sub images from SAM source images

In this set of matlab scripts, three areas are selected from each SAM image. These are stored in a vector format.

```
%sample 36a

selection_s36amod6a_1=s36amod6a(190:(190+50),205:(205+100));
selection_s36azs_1=s36azs(190:(190+50),205:(205+100));
selection_s36aE3_1=s36aE3(190:(190+50),205:(205+100));
vector_selection_s36amod6a_1=selection_s36amod6a_1(:);
vector_selection_s36azs_1=selection_s36azs_1(:);
vector_selection_s36aE3_1=selection_s36aE3_1(:);

selection_s36amod6a_2=s36amod6a(385:(385+50),708:(708+100));
selection_s36azs_2=s36azs(385:(385+50),708:(708+100));
selection_s36aE3_2=s36aE3(385:(385+50),708:(708+100));
vector_selection_s36amod6a_2=selection_s36amod6a_2(:);
vector_selection_s36azs_2=selection_s36azs_2(:);
vector_selection_s36aE3_2=selection_s36aE3_2(:);

selection_s36amod6a_3=s36amod6a(232:(232+50),138:(138+100));
selection_s36azs_3=s36azs(232:(232+50),138:(138+100));
selection_s36aE3_3=s36aE3(232:(232+50),138:(138+100));
vector_selection_s36amod6a_3=selection_s36amod6a_3(:);
vector_selection_s36azs_3=selection_s36azs_3(:);
vector_selection_s36aE3_3=selection_s36aE3_3(:);

%sample 36b

selection_s36bmod6a_1=s36bmod6a(322:(322+50),685:(685+100));
selection_s36bzs_1=s36bzs(322:(322+50),685:(685+100));
selection_s36bE3_1=s36bE3(322:(322+50),685:(685+100));
vector_selection_s36bmod6a_1=selection_s36bmod6a_1(:);
vector_selection_s36bzs_1=selection_s36bzs_1(:);
vector_selection_s36bE3_1=selection_s36bE3_1(:);

selection_s36bmod6a_2=s36bmod6a(165:(165+50),640:(640+100));
selection_s36bzs_2=s36bzs(165:(165+50),640:(640+100));
selection_s36bE3_2=s36bE3(165:(165+50),640:(640+100));
vector_selection_s36bmod6a_2=selection_s36bmod6a_2(:);
vector_selection_s36bzs_2=selection_s36bzs_2(:);
vector_selection_s36bE3_2=selection_s36bE3_2(:);

selection_s36bmod6a_3=s36bmod6a(139:(139+50),138:(138+100));
selection_s36bzs_3=s36bzs(139:(139+50),138:(138+100));
selection_s36bE3_3=s36bE3(139:(139+50),138:(138+100));
vector_selection_s36bmod6a_3=selection_s36bmod6a_3(:);
vector_selection_s36bzs_3=selection_s36bzs_3(:);
vector_selection_s36bE3_3=selection_s36bE3_3(:);

%sample 40
```

```
selection_s40mod6a_1=s40mod6a(357:(357+50),16:(16+100));
selection_s40zs_1=s40zs(357:(357+50),16:(16+100));
selection_s40E3_1=s40E3(357:(357+50),16:(16+100));
vector_selection_s40mod6a_1=selection_s40mod6a_1(:);
vector_selection_s40zs_1=selection_s40zs_1(:);
vector_selection_s40E3_1=selection_s40E3_1(:);

selection_s40mod6a_2=s40mod6a(180:(180+50),373:(373+100));
selection_s40zs_2=s40zs(180:(180+50),373:(373+100));
selection_s40E3_2=s40E3(180:(180+50),373:(373+100));
vector_selection_s40mod6a_2=selection_s40mod6a_2(:);
vector_selection_s40zs_2=selection_s40zs_2(:);
vector_selection_s40E3_2=selection_s40E3_2(:);

selection_s40mod6a_3=s40mod6a(340:(340+50),745:(745+100));
selection_s40zs_3=s40zs(340:(340+50),745:(745+100));
selection_s40E3_3=s40E3(340:(340+50),745:(745+100));
vector_selection_s40mod6a_3=selection_s40mod6a_3(:);
vector_selection_s40zs_3=selection_s40zs_3(:);
vector_selection_s40E3_3=selection_s40E3_3(:);

%sample 45b

selection_s45bmod6a_1=s45bmod6a(201:(201+50),521:(521+100));
selection_s45bzs_1=s45bzs(201:(201+50),521:(521+100));
selection_s45bE3_1=s45bE3(201:(201+50),521:(521+100));
vector_selection_s45bmod6a_1=selection_s45bmod6a_1(:);
vector_selection_s45bzs_1=selection_s45bzs_1(:);
vector_selection_s45bE3_1=selection_s45bE3_1(:);

selection_s45bmod6a_2=s45bmod6a(129:(129+50),332:(332+100));
selection_s45bzs_2=s45bzs(129:(129+50),332:(332+100));
selection_s45bE3_2=s45bE3(129:(129+50),332:(332+100));
vector_selection_s45bmod6a_2=selection_s45bmod6a_2(:);
vector_selection_s45bzs_2=selection_s45bzs_2(:);
vector_selection_s45bE3_2=selection_s45bE3_2(:);

selection_s45bmod6a_3=s45bmod6a(282:(282+50),78:(78+100));
selection_s45bzs_3=s45bzs(282:(282+50),78:(78+100));
selection_s45bE3_3=s45bE3(282:(282+50),78:(78+100));
vector_selection_s45bmod6a_3=selection_s45bmod6a_3(:);
vector_selection_s45bzs_3=selection_s45bzs_3(:);
vector_selection_s45bE3_3=selection_s45bE3_3(:);

%sample 51

selection_s51mod6a_1=s51mod6a(307:(307+50),155:(155+100));
selection_s51zs_1=s51zs(307:(307+50),155:(155+100));
selection_s51E3_1=s51E3(307:(307+50),155:(155+100));
vector_selection_s51mod6a_1=selection_s51mod6a_1(:);
vector_selection_s51zs_1=selection_s51zs_1(:);
vector_selection_s51E3_1=selection_s51E3_1(:);

selection_s51mod6a_2=s51mod6a(217:(217+50),299:(299+100));
selection_s51zs_2=s51zs(217:(217+50),299:(299+100));
selection_s51E3_2=s51E3(217:(217+50),299:(299+100));
vector_selection_s51mod6a_2=selection_s51mod6a_2(:);
vector_selection_s51zs_2=selection_s51zs_2(:);
```

```
vector_selection_s51E3_2=selection_s51E3_2(:);

selection_s51mod6a_3=s51mod6a(371:(371+50),593:(593+100));
selection_s51zs_3=s51zs(371:(371+50),593:(593+100));
selection_s51E3_3=s51E3(371:(371+50),593:(593+100));
vector_selection_s51mod6a_3=selection_s51mod6a_3(:);
vector_selection_s51zs_3=selection_s51zs_3(:);
vector_selection_s51E3_3=selection_s51E3_3(:);

%sample 52

selection_s52mod6a_1=s52mod6a(297:(297+50),114:(114+100));
selection_s52zs_1=s52zs(297:(297+50),114:(114+100));
selection_s52E3_1=s52E3(297:(297+50),114:(114+100));
vector_selection_s52mod6a_1=selection_s52mod6a_1(:);
vector_selection_s52zs_1=selection_s52zs_1(:);
vector_selection_s52E3_1=selection_s52E3_1(:);

selection_s52mod6a_2=s52mod6a(196:(196+50),350:(350+100));
selection_s52zs_2=s52zs(196:(196+50),350:(350+100));
selection_s52E3_2=s52E3(196:(196+50),350:(350+100));
vector_selection_s52mod6a_2=selection_s52mod6a_2(:);
vector_selection_s52zs_2=selection_s52zs_2(:);
vector_selection_s52E3_2=selection_s52E3_2(:);

selection_s52mod6a_3=s52mod6a(282:(282+50),626:(626+100));
selection_s52zs_3=s52zs(282:(282+50),626:(626+100));
selection_s52E3_3=s52E3(282:(282+50),626:(626+100));
vector_selection_s52mod6a_3=selection_s52mod6a_3(:);
vector_selection_s52zs_3=selection_s52zs_3(:);
vector_selection_s52E3_3=selection_s52E3_3(:);

%sample 54

selection_s54mod6a_1=s54mod6a(275:(275+50),74:(74+100));
selection_s54zs_1=s54zs(275:(275+50),74:(74+100));
selection_s54E3_1=s54E3(275:(275+50),74:(74+100));
vector_selection_s54mod6a_1=selection_s54mod6a_1(:);
vector_selection_s54zs_1=selection_s54zs_1(:);
vector_selection_s54E3_1=selection_s54E3_1(:);

selection_s54mod6a_2=s54mod6a(131:(131+50),352:(352+100));
selection_s54zs_2=s54zs(131:(131+50),352:(352+100));
selection_s54E3_2=s54E3(131:(131+50),352:(352+100));
vector_selection_s54mod6a_2=selection_s54mod6a_2(:);
vector_selection_s54zs_2=selection_s54zs_2(:);
vector_selection_s54E3_2=selection_s54E3_2(:);

selection_s54mod6a_3=s54mod6a(316:(316+50),686:(686+100));
selection_s54zs_3=s54zs(316:(316+50),686:(686+100));
selection_s54E3_3=s54E3(316:(316+50),686:(686+100));
vector_selection_s54mod6a_3=selection_s54mod6a_3(:);
vector_selection_s54zs_3=selection_s54zs_3(:);
vector_selection_s54E3_3=selection_s54E3_3(:);

%sample 58

selection_s58mod6a_1=s58mod6a(309:(309+50),540:(540+100));
selection_s58zs_1=s58zs(309:(309+50),540:(540+100));
```

```
selection_s58E3_1=s58E3(309:(309+50),540:(540+100));
vector_selection_s58mod6a_1=selection_s58mod6a_1(:);
vector_selection_s58zs_1=selection_s58zs_1(:);
vector_selection_s58E3_1=selection_s58E3_1(:);

selection_s58mod6a_2=s58mod6a(317:(317+50),6:(6+100));
selection_s58zs_2=s58zs(317:(317+50),6:(6+100));
selection_s58E3_2=s58E3(317:(317+50),6:(6+100));
vector_selection_s58mod6a_2=selection_s58mod6a_2(:);
vector_selection_s58zs_2=selection_s58zs_2(:);
vector_selection_s58E3_2=selection_s58E3_2(:);

selection_s58mod6a_3=s58mod6a(449:(449+50),276:(276+100));
selection_s58zs_3=s58zs(449:(449+50),276:(276+100));
selection_s58E3_3=s58E3(449:(449+50),276:(276+100));
vector_selection_s58mod6a_3=selection_s58mod6a_3(:);
vector_selection_s58zs_3=selection_s58zs_3(:);
vector_selection_s58E3_3=selection_s58E3_3(:);

%sample 67

selection_s67mod6a_1=s67mod6a(160:(160+50),391:(391+100));
selection_s67zs_1=s67zs(160:(160+50),391:(391+100));
selection_s67E3_1=s67E3(160:(160+50),391:(391+100));
vector_selection_s67mod6a_1=selection_s67mod6a_1(:);
vector_selection_s67zs_1=selection_s67zs_1(:);
vector_selection_s67E3_1=selection_s67E3_1(:);

selection_s67mod6a_2=s67mod6a(305:(305+50),106:(106+100));
selection_s67zs_2=s67zs(305:(305+50),106:(106+100));
selection_s67E3_2=s67E3(305:(305+50),106:(106+100));
vector_selection_s67mod6a_2=selection_s67mod6a_2(:);
vector_selection_s67zs_2=selection_s67zs_2(:);
vector_selection_s67E3_2=selection_s67E3_2(:);

selection_s67mod6a_3=s67mod6a(326:(326+50),629:(629+100));
selection_s67zs_3=s67zs(326:(326+50),629:(629+100));
selection_s67E3_3=s67E3(326:(326+50),629:(629+100));
vector_selection_s67mod6a_3=selection_s67mod6a_3(:);
vector_selection_s67zs_3=selection_s67zs_3(:);
vector_selection_s67E3_3=selection_s67E3_3(:);
```

7.1.2.3 Dataprocessing

This script is used to process the three selected areas per SAM image and remove any NaN (Not a Number) entries and remove any Young's Modulus values above 70 and set them to 70. These vectors are then wrote out as text files for each sub-image.

```
%Dataprocessing.m mod 2, mod 3 mod 4
%Modified for 3 sub images per sample.
%20/12/2010
%Modified changed sample names to less than 8 characters
%5 Jan. 2011.
%modified for Year 2 samples 30 Septemebr 2011 8th October 2011


%Get rid of NaN in data
vector_selection_s40E3_1(isnan(vector_selection_s40E3_1))=0;
vector_selection_s52E3_1(isnan(vector_selection_s52E3_1))=0;
vector_selection_s67E3_1(isnan(vector_selection_s67E3_1))=0;

vector_selection_s54E3_1(isnan(vector_selection_s54E3_1))=0;
vector_selection_s45bE3_1(isnan(vector_selection_s45bE3_1))=0;
vector_selection_s58E3_1(isnan(vector_selection_s58E3_1))=0;

vector_selection_s36aE3_1(isnan(vector_selection_s36aE3_1))=0;
vector_selection_s36bE3_1(isnan(vector_selection_s36bE3_1))=0;
vector_selection_s51E3_1(isnan(vector_selection_s51E3_1))=0;

vector_selection_s40E3_2(isnan(vector_selection_s40E3_2))=0;
vector_selection_s52E3_2(isnan(vector_selection_s52E3_2))=0;
vector_selection_s67E3_2(isnan(vector_selection_s67E3_2))=0;

vector_selection_s54E3_2(isnan(vector_selection_s54E3_2))=0;
vector_selection_s45bE3_2(isnan(vector_selection_s45bE3_2))=0;
vector_selection_s58E3_2(isnan(vector_selection_s58E3_2))=0;

vector_selection_s36aE3_2(isnan(vector_selection_s36aE3_2))=0;
vector_selection_s36bE3_2(isnan(vector_selection_s36bE3_2))=0;
vector_selection_s51E3_2(isnan(vector_selection_s51E3_2))=0;

vector_selection_s40E3_3(isnan(vector_selection_s40E3_3))=0;
vector_selection_s52E3_3(isnan(vector_selection_s52E3_3))=0;
vector_selection_s67E3_3(isnan(vector_selection_s67E3_3))=0;

vector_selection_s54E3_3(isnan(vector_selection_s54E3_3))=0;
vector_selection_s45bE3_3(isnan(vector_selection_s45bE3_3))=0;
vector_selection_s58E3_3(isnan(vector_selection_s58E3_3))=0;

vector_selection_s36aE3_3(isnan(vector_selection_s36aE3_3))=0;
vector_selection_s36bE3_3(isnan(vector_selection_s36bE3_3))=0;
vector_selection_s51E3_3(isnan(vector_selection_s51E3_3))=0;


%Remove values above 70GPa
gt70loc=find(vector_selection_s40E3_1>70);
```

```
vector_selection_s40E3_1(gt70loc)=70;

gt70loc=find(vector_selection_s52E3_1>70);
vector_selection_s52E3_1(gt70loc)=70;

gt70loc=find(vector_selection_s67E3_1>70);
vector_selection_s67E3_1(gt70loc)=70;

gt70loc=find(vector_selection_s54E3_1>70);
vector_selection_s54E3_1(gt70loc)=70;

gt70loc=find(vector_selection_s45bE3_1>70);
vector_selection_s45bE3_1(gt70loc)=70;

gt70loc=find(vector_selection_s58E3_1>70);
vector_selection_s58E3_1(gt70loc)=70;

gt70loc=find(vector_selection_s36aE3_1>70);
vector_selection_s36aE3_1(gt70loc)=70;

gt70loc=find(vector_selection_s36bE3_1>70);
vector_selection_s36bE3_1(gt70loc)=70;

gt70loc=find(vector_selection_s51E3_1>70);
vector_selection_s51E3_1(gt70loc)=70;




gt70loc=find(vector_selection_s40E3_2>70);
vector_selection_s40E3_2(gt70loc)=70;

gt70loc=find(vector_selection_s52E3_2>70);
vector_selection_s52E3_2(gt70loc)=70;

gt70loc=find(vector_selection_s67E3_2>70);
vector_selection_s67E3_2(gt70loc)=70;

gt70loc=find(vector_selection_s54E3_2>70);
vector_selection_s54E3_2(gt70loc)=70;

gt70loc=find(vector_selection_s45bE3_2>70);
vector_selection_s45bE3_2(gt70loc)=70;

gt70loc=find(vector_selection_s58E3_2>70);
vector_selection_s58E3_2(gt70loc)=70;

gt70loc=find(vector_selection_s36aE3_2>70);
vector_selection_s36aE3_2(gt70loc)=70;

gt70loc=find(vector_selection_s36bE3_2>70);
vector_selection_s36bE3_2(gt70loc)=70;

gt70loc=find(vector_selection_s51E3_2>70);
vector_selection_s51E3_2(gt70loc)=70;
```

```
gt70loc=find(vector_selection_s40E3_3>70);
vector_selection_s40E3_3(gt70loc)=70;

gt70loc=find(vector_selection_s52E3_3>70);
vector_selection_s52E3_3(gt70loc)=70;

gt70loc=find(vector_selection_s67E3_3>70);
vector_selection_s67E3_3(gt70loc)=70;

gt70loc=find(vector_selection_s54E3_3>70);
vector_selection_s54E3_3(gt70loc)=70;

gt70loc=find(vector_selection_s45bE3_3>70);
vector_selection_s45bE3_3(gt70loc)=70;

gt70loc=find(vector_selection_s58E3_3>70);
vector_selection_s58E3_3(gt70loc)=70;

gt70loc=find(vector_selection_s36aE3_3>70);
vector_selection_s36aE3_3(gt70loc)=70;

gt70loc=find(vector_selection_s36bE3_3>70);
vector_selection_s36bE3_3(gt70loc)=70;

gt70loc=find(vector_selection_s51E3_3>70);
vector_selection_s51E3_3(gt70loc)=70;
```

```
%Write out files for FEA work
dlmwrite('s40E3_1.txt',vector_selection_s40E3_1);
dlmwrite('s52E3_1.txt',vector_selection_s52E3_1);
dlmwrite('s67E3_1.txt',vector_selection_s67E3_1);
dlmwrite('s54E3_1.txt',vector_selection_s54E3_1);
dlmwrite('s45bE3_1.txt',vector_selection_s45bE3_1);
dlmwrite('s58E3_1.txt',vector_selection_s58E3_1);
dlmwrite('s36aE3_1.txt',vector_selection_s36aE3_1);
dlmwrite('s36bE3_1.txt',vector_selection_s36bE3_1);
dlmwrite('s51E3_1.txt',vector_selection_s51E3_1);

dlmwrite('s40E3_2.txt',vector_selection_s40E3_2);
dlmwrite('s52E3_2.txt',vector_selection_s52E3_2);
dlmwrite('s67E3_2.txt',vector_selection_s67E3_2);
dlmwrite('s54E3_2.txt',vector_selection_s54E3_2);
dlmwrite('s45bE3_2.txt',vector_selection_s45bE3_2);
dlmwrite('s58E3_2.txt',vector_selection_s58E3_2);
dlmwrite('s36aE3_2.txt',vector_selection_s36aE3_2);
dlmwrite('s36bE3_2.txt',vector_selection_s36bE3_2);
dlmwrite('s51E3_2.txt',vector_selection_s51E3_2);

dlmwrite('s40E3_3.txt',vector_selection_s40E3_3);
dlmwrite('s52E3_3.txt',vector_selection_s52E3_3);
dlmwrite('s67E3_3.txt',vector_selection_s67E3_3);
```

```
dlmwrite('s54E3_3.txt',vector_selection_s54E3_3);
dlmwrite('s45bE3_3.txt',vector_selection_s45bE3_3);
dlmwrite('s58E3_3.txt',vector_selection_s58E3_3);
dlmwrite('s36aE3_3.txt',vector_selection_s36aE3_3);
dlmwrite('s36bE3_3.txt',vector_selection_s36bE3_3);
dlmwrite('s51E3_3.txt',vector_selection_s51E3_3);
```

7.2 ANSYS Macro for generating FE models

An ANSYS macro was written in the APDL command language. This was used to take the output from image processing of a sub-image of Young's Modulus properties of each bone sample and calculate the stress and strain at each point in the sub image.

```
! SAMFEAV5.mac
!ver 5 5th Jan. 2010.
!Arguments:
!arg1 name of input file assumes a .txt extension less
than 8 character in single quotes
!arg2
!arg3

finish
/clear
/FILNAME,arg1,1
/title, arg1

! SCRIPT TO AUTOMATE THE PRODUCTION OF FEA MODELS FROM
SAM IMAGES
/PREP7
ET,1,plane183  ! 8 node 2D Higher order Quad Element
!*
KEYOPT,1,3,3
KEYOPT,1,6,0
KEYOPT,1,10,0
!*
!*
R,1,0.25,
!*
BLC4,0,0,1.275,2.525
! APLOT
! Line size edge 0.025
LESIZE,ALL,0.025, , , ,1, , ,1,
! LPLOT
! Mesh The Rectangle
MSHAPE,0,2D
MSHKEY,1
!*
CM,_Y,AREA
ASEL, , , ,       1
CM,_Y1,AREA
CHKMSH,'AREA'
CMSEL,S,_Y
!*
```

```
AMESH,_Y1
!*
CMDELE,_Y
CMDELE,_Y1
CMDELE,_Y2

! APPLY BOUNDARY CONDITIONS 1500 MICRO STRAIN
FLST,2,1,4,ORDE,1
FITEM,2,1
!*
/GO
DL,P51X, ,UY,0
FLST,2,1,4,ORDE,1
FITEM,2,3
!*
/GO
DL,P51X, ,UY,0.0037875

FLST,2,1,3,ORDE,1
FITEM,2,1
!*
/GO
DK,P51X, ,0, ,0,UX,UY, , , , ,

!DECLARE MATERIAL PROPERTIES. WE CAN ADD AS MANY AS WE
WANT TO
! HERE BUT WE MUST HAVE MORE IF THEN ELSE STATEMENTS
LATER IN
! MACRO VERSION 2 UPDATED 16TH JULY 2010
! UPDATED VERSION 3 UPDATED 18TH SEPTEMBER 2010
! Updated Version 4 4th Jan 2011

!Null Property.
MP,EX,169,1E1
MP,NUXY,169,0.3

! Additional materials using the repeat command
!From 2GPa to 40 GPa in Steps of 0.25GPa
MP,EX,1,2E3
*REPEAT,153,0,1,0.25E3

!From 40 to 70 GPa in steps of 2 GPa
MP,EX,154,42E3
*REPEAT,15,0,1,2E3

!All Poisson Ratio values are the same
MP,NUXY,1,0.3
*REPEAT,168,0,1,0

!Read data in from text file in vector format
```

```
!Each location in vector refers to individual numbered
element

*DIM,EXAMPLE,,5151
! Declare parameter vector EXAMPLE 5151 rows long
! IMPORT.TXT MUST BE PLACED IN WORKING DIRECTORY

*VREAD,EXAMPLE(1,1),arg1,txt ,,,JIK,1,5151
(F9.0)


!Fortran Real format 6 spaces left of decimal point to
start of line
! zero to the right

!Next place each value from matlab into each element.
! USE A DO LOOP TO DO THIS

*DO,N,1,5151      ! For N = 1 to 5151: 5151 ENTRIES IN
VECTOR EXAMPLE

!IF THEN ELSE CONSTRUCT TO ASSIGN MATERIAL PROPERTIES TO
MODEL
! ACCORDING TO INPUT VECTOR EXAMPLE


  *IF,EXAMPLE(N,1),LT,1,THEN ! Null property
     EMODIF,N,MAT,169


    *ELSEIF,EXAMPLE(N,1),LT,2
      EMODIF,N,MAT,1

      *ELSEIF,EXAMPLE(N,1),LT,2.25
        EMODIF,N,MAT,2

          *ELSEIF,EXAMPLE(N,1),LT,2.5
               EMODIF,N,MAT,3

               *ELSEIF,EXAMPLE(N,1),LT,2.75
                    EMODIF,N,MAT,4

                    *ELSEIF,EXAMPLE(N,1),LT,3
                         EMODIF,N,MAT,5

                         *ELSEIF,EXAMPLE(N,1),LT,3.25
                              EMODIF,N,MAT,6

                              *ELSEIF,EXAMPLE(N,1),LT,3.5
                                   EMODIF,N,MAT,7
```

```
*ELSEIF,EXAMPLE(N,1),LT,3.75
                                        EMODIF,N,MAT,8

*ELSEIF,EXAMPLE(N,1),LT,4

EMODIF,N,MAT,9

*ELSEIF,EXAMPLE(N,1),LT,4.25

EMODIF,N,MAT,10

            *ELSEIF,EXAMPLE(N,1),LT,4.5
                    EMODIF,N,MAT,11

                *ELSEIF,EXAMPLE(N,1),LT,4.75
                 EMODIF,N,MAT,12

                  *ELSEIF,EXAMPLE(N,1),LT,5
                    EMODIF,N,MAT,13

                     *ELSEIF,EXAMPLE(N,1),LT,5.25
                          EMODIF,N,MAT,14

                          *ELSEIF,EXAMPLE(N,1),LT,5.5
                               EMODIF,N,MAT,15

*ELSEIF,EXAMPLE(N,1),LT,5.75
                                        EMODIF,N,MAT,16

*ELSEIF,EXAMPLE(N,1),LT,6

EMODIF,N,MAT,17

*ELSEIF,EXAMPLE(N,1),LT,6.25

EMODIF,N,MAT,18

*ELSEIF,EXAMPLE(N,1),LT,6.5

EMODIF,N,MAT,19


*ELSEIF,EXAMPLE(N,1),LT,6.75
```

```
   EMODIF,N,MAT,20

*ELSEIF,EXAMPLE(N,1),LT,7
    EMODIF,N,MAT,21

    *ELSEIF,EXAMPLE(N,1),LT,7.25
      EMODIF,N,MAT,22

        *ELSEIF,EXAMPLE(N,1),LT,7.5
             EMODIF,N,MAT,23

             *ELSEIF,EXAMPLE(N,1),LT,7.75
                  EMODIF,N,MAT,24

                  *ELSEIF,EXAMPLE(N,1),LT,8
                       EMODIF,N,MAT,25

                       *ELSEIF,EXAMPLE(N,1),LT,8.25
                            EMODIF,N,MAT,26

                            *ELSEIF,EXAMPLE(N,1),LT,8.5
                                 EMODIF,N,MAT,27


   *ELSEIF,EXAMPLE(N,1),LT,8.75
                                          EMODIF,N,MAT,28


   *ELSEIF,EXAMPLE(N,1),LT,9

   EMODIF,N,MAT,29


   *ELSEIF,EXAMPLE(N,1),LT,9.25

   EMODIF,N,MAT,30

               *ELSEIF,EXAMPLE(N,1),LT,9.5
                    EMODIF,N,MAT,31

                   *ELSEIF,EXAMPLE(N,1),LT,9.75
                    EMODIF,N,MAT,32

                     *ELSEIF,EXAMPLE(N,1),LT,10
                      EMODIF,N,MAT,33

                       *ELSEIF,EXAMPLE(N,1),LT,10.25
                            EMODIF,N,MAT,34
```

```
      *ELSEIF,EXAMPLE(N,1),LT,10.5
                                        EMODIF,N,MAT,35

      *ELSEIF,EXAMPLE(N,1),LT,10.75
                                              EMODIF,N,MAT,36

      *ELSEIF,EXAMPLE(N,1),LT,11

      EMODIF,N,MAT,37

      *ELSEIF,EXAMPLE(N,1),LT,11.25

      EMODIF,N,MAT,38

      *ELSEIF,EXAMPLE(N,1),LT,11.5

      EMODIF,N,MAT,39


      *ELSEIF,EXAMPLE(N,1),LT,11.75

      EMODIF,N,MAT,40


*ELSEIF,EXAMPLE(N,1),LT,12
      EMODIF,N,MAT,41

           *ELSEIF,EXAMPLE(N,1),LT,12.25
                EMODIF,N,MAT,42

                *ELSEIF,EXAMPLE(N,1),LT,12.5
                     EMODIF,N,MAT,43

                     *ELSEIF,EXAMPLE(N,1),LT,12.75
                          EMODIF,N,MAT,44

                          *ELSEIF,EXAMPLE(N,1),LT,13
                               EMODIF,N,MAT,45


      *ELSEIF,EXAMPLE(N,1),LT,13.25
                                        EMODIF,N,MAT,46


      *ELSEIF,EXAMPLE(N,1),LT,13.5
```

```
                                                    EMODIF,N,MAT,47

*ELSEIF,EXAMPLE(N,1),LT,13.75

EMODIF,N,MAT,48

*ELSEIF,EXAMPLE(N,1),LT,14

EMODIF,N,MAT,49

*ELSEIF,EXAMPLE(N,1),LT,14.25

EMODIF,N,MAT,50

            *ELSEIF,EXAMPLE(N,1),LT,14.5
                    EMODIF,N,MAT,51

                *ELSEIF,EXAMPLE(N,1),LT,14.75
                 EMODIF,N,MAT,52

                  *ELSEIF,EXAMPLE(N,1),LT,15
                    EMODIF,N,MAT,53

                    *ELSEIF,EXAMPLE(N,1),LT,15.25
                         EMODIF,N,MAT,54

*ELSEIF,EXAMPLE(N,1),LT,15.5
                                    EMODIF,N,MAT,55

*ELSEIF,EXAMPLE(N,1),LT,15.75
                                            EMODIF,N,MAT,56

*ELSEIF,EXAMPLE(N,1),LT,16

EMODIF,N,MAT,57

*ELSEIF,EXAMPLE(N,1),LT,16.25

EMODIF,N,MAT,58

*ELSEIF,EXAMPLE(N,1),LT,16.5
```

```
EMODIF,N,MAT,59


*ELSEIF,EXAMPLE(N,1),LT,16.75

EMODIF,N,MAT,60



 *ELSEIF,EXAMPLE(N,1),LT,17
   EMODIF,N,MAT,61

     *ELSEIF,EXAMPLE(N,1),LT,17.25
          EMODIF,N,MAT,62

          *ELSEIF,EXAMPLE(N,1),LT,17.5
               EMODIF,N,MAT,63

               *ELSEIF,EXAMPLE(N,1),LT,17.75
                    EMODIF,N,MAT,64

                    *ELSEIF,EXAMPLE(N,1),LT,18
                         EMODIF,N,MAT,65


*ELSEIF,EXAMPLE(N,1),LT,18.25
                              EMODIF,N,MAT,66


*ELSEIF,EXAMPLE(N,1),LT,18.5
                                   EMODIF,N,MAT,67


*ELSEIF,EXAMPLE(N,1),LT,18.75

EMODIF,N,MAT,68


*ELSEIF,EXAMPLE(N,1),LT,19

EMODIF,N,MAT,69


*ELSEIF,EXAMPLE(N,1),LT,19.25

EMODIF,N,MAT,70

          *ELSEIF,EXAMPLE(N,1),LT,19.5
```

```
                    EMODIF,N,MAT,71

                  *ELSEIF,EXAMPLE(N,1),LT,19.75
                   EMODIF,N,MAT,72

                    *ELSEIF,EXAMPLE(N,1),LT,20
                     EMODIF,N,MAT,73

                      *ELSEIF,EXAMPLE(N,1),LT,20.25
                          EMODIF,N,MAT,74


*ELSEIF,EXAMPLE(N,1),LT,20.5
                                  EMODIF,N,MAT,75


*ELSEIF,EXAMPLE(N,1),LT,20.75
                                       EMODIF,N,MAT,76


*ELSEIF,EXAMPLE(N,1),LT,21

EMODIF,N,MAT,77


*ELSEIF,EXAMPLE(N,1),LT,21.25

EMODIF,N,MAT,78


*ELSEIF,EXAMPLE(N,1),LT,21.5

EMODIF,N,MAT,79



*ELSEIF,EXAMPLE(N,1),LT,21.75

EMODIF,N,MAT,80

 *ELSEIF,EXAMPLE(N,1),LT,22
   EMODIF,N,MAT,81

     *ELSEIF,EXAMPLE(N,1),LT,22.25
          EMODIF,N,MAT,82

           *ELSEIF,EXAMPLE(N,1),LT,22.5
                EMODIF,N,MAT,83

                 *ELSEIF,EXAMPLE(N,1),LT,22.75
                      EMODIF,N,MAT,84
```

```
                    *ELSEIF,EXAMPLE(N,1),LT,23
                        EMODIF,N,MAT,85

*ELSEIF,EXAMPLE(N,1),LT,23.25
                                EMODIF,N,MAT,86

*ELSEIF,EXAMPLE(N,1),LT,23.5
                                        EMODIF,N,MAT,87

*ELSEIF,EXAMPLE(N,1),LT,23.75

EMODIF,N,MAT,88

*ELSEIF,EXAMPLE(N,1),LT,24

EMODIF,N,MAT,89

*ELSEIF,EXAMPLE(N,1),LT,24.25

EMODIF,N,MAT,90

            *ELSEIF,EXAMPLE(N,1),LT,24.5
                    EMODIF,N,MAT,91

                *ELSEIF,EXAMPLE(N,1),LT,24.75
                 EMODIF,N,MAT,92

                  *ELSEIF,EXAMPLE(N,1),LT,25
                    EMODIF,N,MAT,93

                    *ELSEIF,EXAMPLE(N,1),LT,25.25
                        EMODIF,N,MAT,94

*ELSEIF,EXAMPLE(N,1),LT,25.5
                                EMODIF,N,MAT,95

*ELSEIF,EXAMPLE(N,1),LT,25.75
                                        EMODIF,N,MAT,96

*ELSEIF,EXAMPLE(N,1),LT,26

EMODIF,N,MAT,97
```

```
*ELSEIF,EXAMPLE(N,1),LT,26.25

EMODIF,N,MAT,98

*ELSEIF,EXAMPLE(N,1),LT,26.25

EMODIF,N,MAT,99


*ELSEIF,EXAMPLE(N,1),LT,26.75

EMODIF,N,MAT,100


          *ELSEIF,EXAMPLE(N,1),LT,27
                    EMODIF,N,MAT,101

                *ELSEIF,EXAMPLE(N,1),LT,27.25
                 EMODIF,N,MAT,102

                  *ELSEIF,EXAMPLE(N,1),LT,27.5
                    EMODIF,N,MAT,103

                    *ELSEIF,EXAMPLE(N,1),LT,27.75
                         EMODIF,N,MAT,104

                         *ELSEIF,EXAMPLE(N,1),LT,28
                              EMODIF,N,MAT,105


*ELSEIF,EXAMPLE(N,1),LT,28.25
                                        EMODIF,N,MAT,106


*ELSEIF,EXAMPLE(N,1),LT,28.5

EMODIF,N,MAT,107


*ELSEIF,EXAMPLE(N,1),LT,28.75

EMODIF,N,MAT,108


*ELSEIF,EXAMPLE(N,1),LT,29
```

```
EMODIF,N,MAT,109


*ELSEIF,EXAMPLE(N,1),LT,29.25

EMODIF,N,MAT,110


          *ELSEIF,EXAMPLE(N,1),LT,29.5
                  EMODIF,N,MAT,111

                *ELSEIF,EXAMPLE(N,1),LT,29.75
                 EMODIF,N,MAT,112

                  *ELSEIF,EXAMPLE(N,1),LT,30
                    EMODIF,N,MAT,113

                    *ELSEIF,EXAMPLE(N,1),LT,30.25
                         EMODIF,N,MAT,114


*ELSEIF,EXAMPLE(N,1),LT,30.5
                                EMODIF,N,MAT,115


*ELSEIF,EXAMPLE(N,1),LT,30.75
                                       EMODIF,N,MAT,116


*ELSEIF,EXAMPLE(N,1),LT,31

EMODIF,N,MAT,117


*ELSEIF,EXAMPLE(N,1),LT,31.25

EMODIF,N,MAT,118


*ELSEIF,EXAMPLE(N,1),LT,31.5

EMODIF,N,MAT,119


*ELSEIF,EXAMPLE(N,1),LT,31.75
```

```
EMODIF,N,MAT,120


          *ELSEIF,EXAMPLE(N,1),LT,32
                    EMODIF,N,MAT,121

                *ELSEIF,EXAMPLE(N,1),LT,32.25
                 EMODIF,N,MAT,122

                   *ELSEIF,EXAMPLE(N,1),LT,32.5
                     EMODIF,N,MAT,123

                     *ELSEIF,EXAMPLE(N,1),LT,32.75
                          EMODIF,N,MAT,124

                          *ELSEIF,EXAMPLE(N,1),LT,33
                               EMODIF,N,MAT,125


*ELSEIF,EXAMPLE(N,1),LT,33.25
                                        EMODIF,N,MAT,126


*ELSEIF,EXAMPLE(N,1),LT,33.5

EMODIF,N,MAT,127


*ELSEIF,EXAMPLE(N,1),LT,33.75

EMODIF,N,MAT,128


*ELSEIF,EXAMPLE(N,1),LT,34

EMODIF,N,MAT,129



*ELSEIF,EXAMPLE(N,1),LT,34.25

EMODIF,N,MAT,130

          *ELSEIF,EXAMPLE(N,1),LT,34.5
                    EMODIF,N,MAT,131

                *ELSEIF,EXAMPLE(N,1),LT,34.75
                 EMODIF,N,MAT,132

                   *ELSEIF,EXAMPLE(N,1),LT,35
```

```
                    EMODIF,N,MAT,133

                    *ELSEIF,EXAMPLE(N,1),LT,35.25
                         EMODIF,N,MAT,134


*ELSEIF,EXAMPLE(N,1),LT,35.5
                                  EMODIF,N,MAT,135


*ELSEIF,EXAMPLE(N,1),LT,35.75
                                       EMODIF,N,MAT,136


*ELSEIF,EXAMPLE(N,1),LT,36

EMODIF,N,MAT,137


*ELSEIF,EXAMPLE(N,1),LT,36.25

EMODIF,N,MAT,138


*ELSEIF,EXAMPLE(N,1),LT,36.5

EMODIF,N,MAT,139


*ELSEIF,EXAMPLE(N,1),LT,36.75

EMODIF,N,MAT,140


          *ELSEIF,EXAMPLE(N,1),LT,37
                    EMODIF,N,MAT,141

               *ELSEIF,EXAMPLE(N,1),LT,37.25
                EMODIF,N,MAT,142

                 *ELSEIF,EXAMPLE(N,1),LT,37.5
                   EMODIF,N,MAT,143

                   *ELSEIF,EXAMPLE(N,1),LT,37.75
                        EMODIF,N,MAT,144

                        *ELSEIF,EXAMPLE(N,1),LT,38
                             EMODIF,N,MAT,145
```

```
*ELSEIF,EXAMPLE(N,1),LT,38.25
                                        EMODIF,N,MAT,146

*ELSEIF,EXAMPLE(N,1),LT,38.5

EMODIF,N,MAT,147

*ELSEIF,EXAMPLE(N,1),LT,38.75

EMODIF,N,MAT,148

*ELSEIF,EXAMPLE(N,1),LT,39

EMODIF,N,MAT,149


*ELSEIF,EXAMPLE(N,1),LT,39.25

EMODIF,N,MAT,150


            *ELSEIF,EXAMPLE(N,1),LT,39.5
                EMODIF,N,MAT,151

                *ELSEIF,EXAMPLE(N,1),LT,39.75
                EMODIF,N,MAT,152

                  *ELSEIF,EXAMPLE(N,1),LT,40
                    EMODIF,N,MAT,153

! Increments of 2 GPa from 40 to 70 GPa

                      *ELSEIF,EXAMPLE(N,1),LT,42
                          EMODIF,N,MAT,154

                           *ELSEIF,EXAMPLE(N,1),LT,44
                               EMODIF,N,MAT,155


*ELSEIF,EXAMPLE(N,1),LT,46
                                        EMODIF,N,MAT,156

*ELSEIF,EXAMPLE(N,1),LT,48

EMODIF,N,MAT,157
```

```
      *ELSEIF,EXAMPLE(N,1),LT,50

      EMODIF,N,MAT,158


      *ELSEIF,EXAMPLE(N,1),LT,52

      EMODIF,N,MAT,159


      *ELSEIF,EXAMPLE(N,1),LT,54

      EMODIF,N,MAT,160


                *ELSEIF,EXAMPLE(N,1),LT,56
                        EMODIF,N,MAT,161

                      *ELSEIF,EXAMPLE(N,1),LT,58
                       EMODIF,N,MAT,162

                        *ELSEIF,EXAMPLE(N,1),LT,60
                          EMODIF,N,MAT,163

                          *ELSEIF,EXAMPLE(N,1),LT,62
                               EMODIF,N,MAT,164

                               *ELSEIF,EXAMPLE(N,1),LT,64
                                    EMODIF,N,MAT,165


      *ELSEIF,EXAMPLE(N,1),LT,66
                                              EMODIF,N,MAT,166


      *ELSEIF,EXAMPLE(N,1),LT,68

      EMODIF,N,MAT,167


          *ELSE
            EMODIF,N,MAT,168 ! Greater than or equal to
70.

   *ENDIF

*ENDDO
```

```
FINISH

/SOL
/STATUS,SOLU
SOLVE
save,arg1,db,,all


finish

!POST PROCESSING

/POST1
SET,FIRST
! Output images of results
! Window controls Window options

/PLOPTS,INFO,1
/PLOPTS,LEG1,1
/PLOPTS,LEG2,0
/PLOPTS,LEG3,1
/PLOPTS,FRAME,0
/PLOPTS,TITLE,0
/PLOPTS,MINM,1
/PLOPTS,FILE,1
/PLOPTS,LOGO,1
/PLOPTS,WINS,1
/PLOPTS,WP,0
/PLOPTS,DATE,2
/TRIAD,OFF
/REPLOT

! A way of making the plot fit in window
/DIST,1,0.924021086472,1
/REP,FAST
/DIST,1,0.924021086472,1
/REP,FAST
/AUTO, 1
/REP

!Remove view of elements in plot style edge options
/GLINE,1,-1

! Set up contours for stress plot
/CONT,1,8,0, ,50
/REPLOT

!Equivalent Stress Plot
AVPRIN,0,
PLESOL, S,EQV, 0,1.0
```

```
! Redirect plot to tiff file white background
/SHOW,TIFF
TIFF,COMP,1
TIFF,ORIENT,HORIZ
TIFF,COLOR,2
TIFF,TMOD,1
/GFILE,800,
!*
/CMAP,_TEMPCMAP_,CMP,,SAVE
/RGB,INDEX,100,100,100,0
/RGB,INDEX,0,0,0,15
/REPLOT
/CMAP,_TEMPCMAP_,CMP
/DELETE,_TEMPCMAP_,CMP
/SHOW,CLOSE
/DEVICE,VECTOR,0
!*

!Set up Contours for strain plot
/CONT,1,10,0, ,0.003
/REPLOT

! Equivalent strain plot
AVPRIN,0,
PLESOL, EPTO,EQV, 0,1.0

! Redirect plot to tiff file white background
/SHOW,TIFF
TIFF,COMP,1
TIFF,ORIENT,HORIZ
TIFF,COLOR,2
TIFF,TMOD,1
/GFILE,800,
!*
/CMAP,_TEMPCMAP_,CMP,,SAVE
/RGB,INDEX,100,100,100,0
/RGB,INDEX,0,0,0,15
/REPLOT
/CMAP,_TEMPCMAP_,CMP
/DELETE,_TEMPCMAP_,CMP
/SHOW,CLOSE
/DEVICE,VECTOR,0
!*


! Set up to plot materials
!*
/PNUM,KP,0
/PNUM,LINE,0
/PNUM,AREA,0
/PNUM,VOLU,0
```

```
/PNUM,NODE,0
/PNUM,TABN,0
/PNUM,SVAL,0
/NUMBER,1
!*
/PNUM,MAT,1
/REPLOT
!*

! Plot Materials

EPLOT


! Redirect plot to tiff file white background
/SHOW,TIFF
TIFF,COMP,1
TIFF,ORIENT,HORIZ
TIFF,COLOR,2
TIFF,TMOD,1
/GFILE,800,
!*
/CMAP,_TEMPCMAP_,CMP,,SAVE
/RGB,INDEX,100,100,100,0
/RGB,INDEX,0,0,0,15
/REPLOT
/CMAP,_TEMPCMAP_,CMP
/DELETE,_TEMPCMAP_,CMP
/SHOW,CLOSE
/DEVICE,VECTOR,0
!*

!Output stress and strain to text files

!Equivalent Stress

ETABLE,sseqv,S,EQV
*DIM,alpha,ARRAY,5151,1,1, , ,
!*
*VGET,alpha,ELEM,1-5151,ETAB,sseqv, ,2

*CFOPEN,arg1,'sseqv',' '
*VWRITE,alpha(1), , , , , , , , ,
(F10.6)
*CFCLOS

!Principal Stress

ETABLE,ssp1,S,1
*DIM,beta,ARRAY,5151,1,1, , ,
!*
```

```
*VGET,beta,ELEM,1-5151,ETAB,ssp1, ,2

*CFOPEN,arg1,'ssp1',' '
*VWRITE,beta(1), , , , , , , , ,
(F10.6)
*CFCLOS

!Equivalent Strain

ETABLE,sneqv,EPTO,EQV
*DIM,gamma,ARRAY,5151,1,1, , ,
!*
*VGET,gamma,ELEM,1-5151,ETAB,sneqv, ,2

*CFOPEN,arg1,'sneqv',' '
*VWRITE,gamma(1), , , , , , , , ,
(F10.6)
*CFCLOS

!Principal Strain

ETABLE,snp1,EPTO,1
*DIM,delta,ARRAY,5151,1,1, , ,
!*
*VGET,delta,ELEM,1-5151,ETAB,snp1, ,2

*CFOPEN,arg1,'snp1',' '
*VWRITE,delta(1), , , , , , , , ,
(F10.6)
*CFCLOS

finish

/prep7
! Remove Arrays ALPHA BETA GAMMA DELTA EXAMPLE
alpha=
beta=
gamma=
delta=
example=

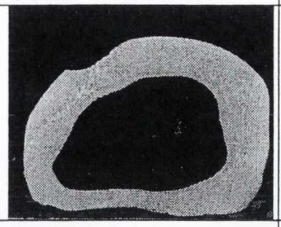
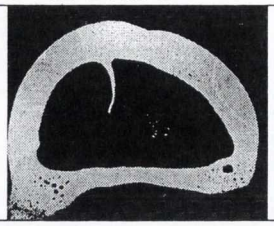
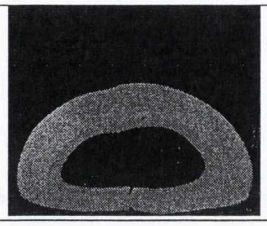
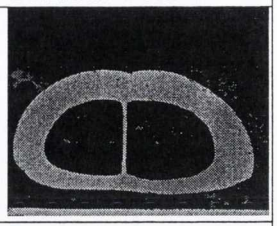
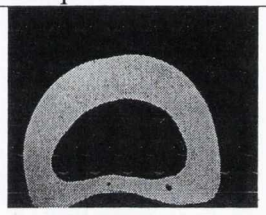
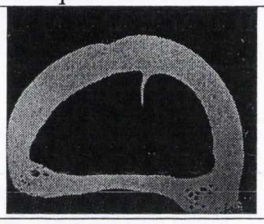
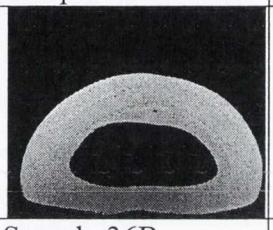
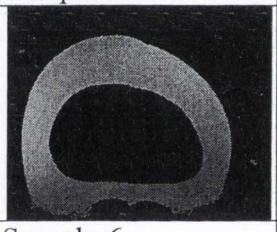
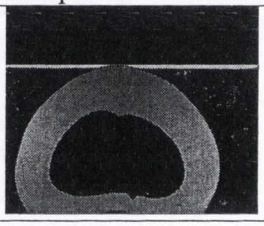
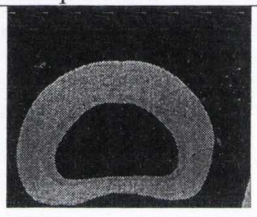
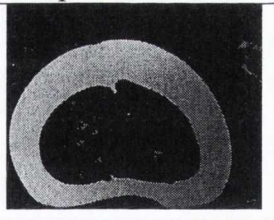
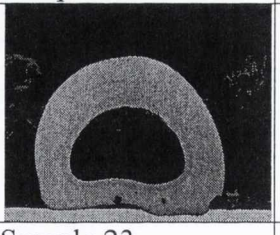
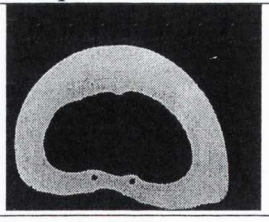
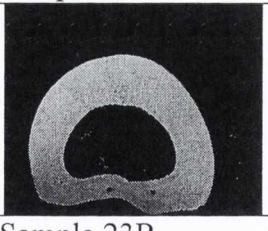
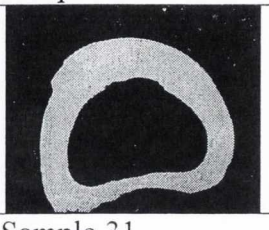
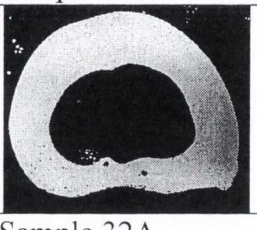
finish
```

7.3 SAM Reflectance Images

Shown below in table are the original unprocessed images. The images used in this study were scanned on the two days indicated. Three other SAM imaging sessions were also carried previous to these.

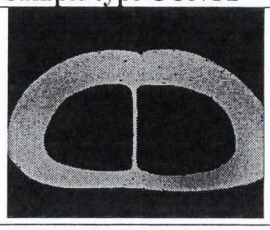
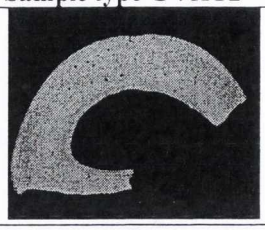
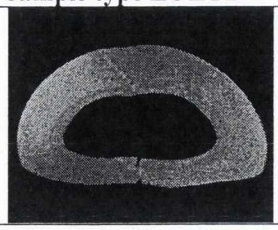
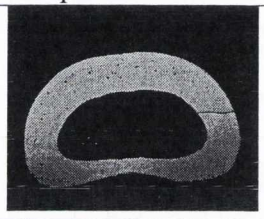
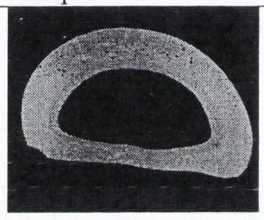
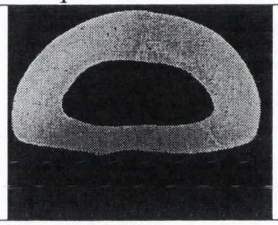
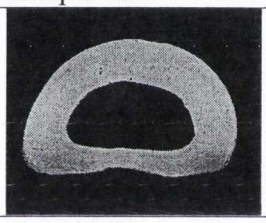
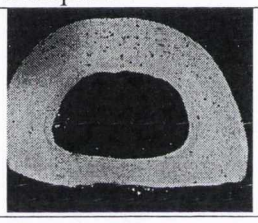
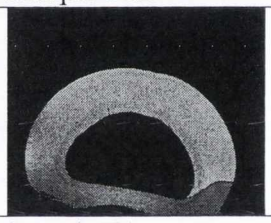
7.3.1 11th December 2009

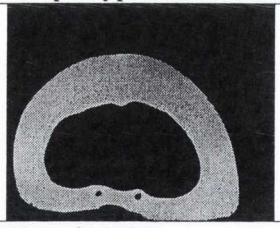
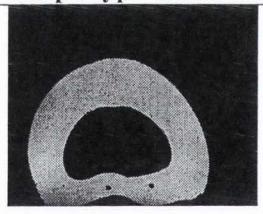
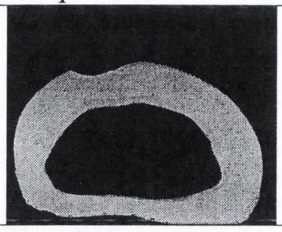
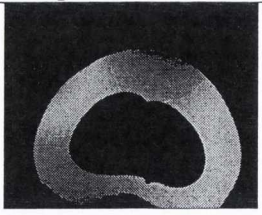
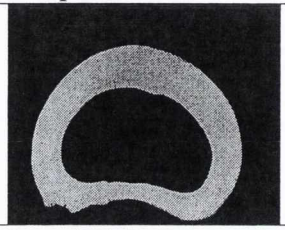
The samples imaged consisted of Year 1 and Year 2 samples.

Control Year 1	OVX Year 1	OVX-ZOL Year 2	Control Year 2
			
Sample 2	Sample4A	Sample 36A	Sample 40
			
Sample5B	Sample4B	Sample 36B	
			
Sample 6	Sample 15	Sample 51	
			
Sample 20	Sample 23		
			
Sample 22B	Sample 23B		
			
Sample 31	Sample 32A		

7.3.2 30th September 2011

In this study more year 2 samples were imaged.

Sample type CONY2	Sample type OVXY2	Sample type ZOLY2
		
Sample 40	Sample 45b	Sample 36A
		
Sample 52	Sample 54	Sample 36B
		
Sample 67	Sample 58	Sample 51

Sample type CON Y1	Sample type OVX Y1
	
Sample 22B	Sample 23B
	
Sample 2	Sample 15
	
Sample 31	

7.4 Sample Preparation Procedure

Sample Preparation Procedure

Samples initially cut using Struers Minitom Diamond Saw at 250rpm irrigated with water.

Samples were then cleaned of all non bone material.

Samples were polished using 4 micron diamond paste (Struers) on a DAP2 polishing wheel.

Samples were then ultrasonically cleaned for 2 minutes.

Samples were examined under a light microscope (Leica DMLM 10x viewfinder 5x Objective) for debris etc.

Samples were polished using 1 micron diamond paste (Struers) on a DAP2 polishing wheel.

Samples were then ultrasonically cleaned for one minute.

Samples were examined under a light microscope (Leica DMLM 10x viewfinder 5x Objective) for debris etc.

Samples were packed into numbered containers under water.

Samples were placed in freezer at –18 degrees C.

7.5 Ultrasonic Tranducers

In this section we will examine the concepts behind the piezo-electric effect and its application to the design of transducers for the generation and reception of ultrasonic signals. We will also discuss the application of ultrasonic beam theory to the design of suitable acoustic lenss.

7.5.1 Piezoelectricity and transducer design

The generation and reception of ultrasonic waves is accomplished using piezoelectric crystals. Most ultrasonic transducers are made out of lead zirconate titanate called PZT. ((Quartz, lithium Niobate (Hill 1986)) This crystal is energised into transmission by the application of an electrical voltage across its electrodes that cause it to deform slightly in thickness. When the electrical signal is removed the crystal tries to return to its original shape. Hence an ultrasonic pulse is generated. One pulse goes towards the boundary layer and the other goes into the crystal. A resonance condition may be set up where the longitudinal waves reflect back and forth from the electroded surface. This condition can occur where crystal thickness is a half an acoustic wavelength or odd multiples of this frequency. A backing layer is also included to dampen down vibration of the ultrasonic crystal transducer (Goldstein 2000).

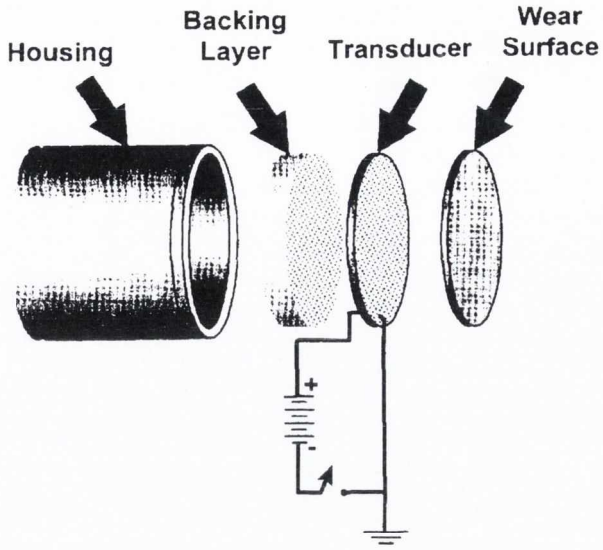


Figure 59 Basic structure of an ultrasonic transducer (Goldstein 2000) .

The other side of the crystal can be fitted with an acoustic lens made out of a material such as sapphire. This propagates the ultrasonic wave into the medium or sample. A spherical acoustic lens can also be fitted to this to focus the ultrasonic pulse into a pencil shape beam (Briggs 1992).

A matching layer is often included on the transducer window. This is usually a quarter of a wavelength thick and of a material with an acoustic impedance between that of the acoustic lens and the medium in which the ultrasound is travelling through. This limits the amount of wave energy reflected back at the interface (Hill 1986).

7.5.2 Bandwidth of transducer

It is not possible for various reasons to produce a pure ultrasonic signal at a specific frequency. Usually the best that can be done is to get a signal with the narrowest bandwidth possible. Ultrasonic pulses have a centre frequency f_c which is close to the half-wavelength resonance condition of the transducer and a bandwidth $\boldsymbol{B}$.

There is a requirement to have the ultrasonic pulse as short as possible. This allows us to switch the transducer in to receive mode as quickly as possible. This relationship between pulse length and pulse frequency broadening can be describe as:

$$\Delta t \cdot \Delta f \cong 1 \qquad \textit{Equation 7-1}$$

The interpretation of this equation is that short (***Δt***) ultrasonic pulses will have a wider bandwidth than a long ultrasonic pulses.

The transducer can be considered as a pass band filter in both transmit and receive mode. There is always a conflict in optimising the design of transducers. As stated earlier there is a requirement for short pulses but in doing this the efficiency of the transducer is reduced. This is specified as the quality factor ***Q***

$$Q=f_c/B \qquad \textit{Equation 7-2}$$

The efficiency of a transducer is described by its fractional bandwidth:

$$FB=100/Q \qquad \textit{Equation 7-3}$$

Early single element transducers had a fractional bandwidth of 40% (Goldstein 2000).

7.5.3 Ultrasonic field beam characteristics

The ultrasonic field of a transducer describes the spatial distribution of its radiated energy. This field is identical during transmission and receiving of ultrasound energy.

The ultrasound beam shape produced by transducer is complex. In the idealised case of a circular transducer generating a continuous wave of ultrasound, the beam shape can be considered to have two distinct regions.

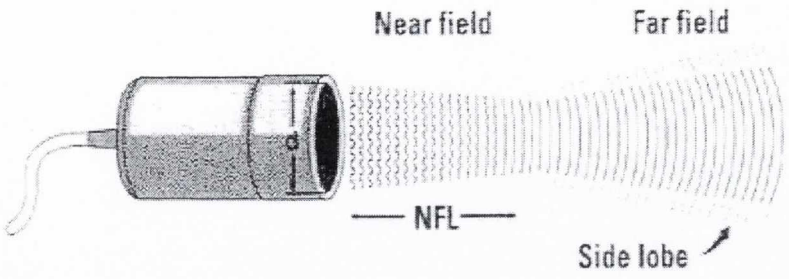


Figure 60 Schematic of an ultrasonic transducer showing the near and far field regions.

In the near field (or Fresnel zone) the ultrasound beam is approximately cylindrical with a diameter roughly equal to the transducer diameter. The near field extends for a distance of $D^2/4\lambda$ from the transducer face, where D is the transducer diameter and λ is the wavelength of the ultrasound. In the far field (or Fraunhofer zone) the beam diverges with an angle given by $\sin\theta = 1.22\lambda/D$.

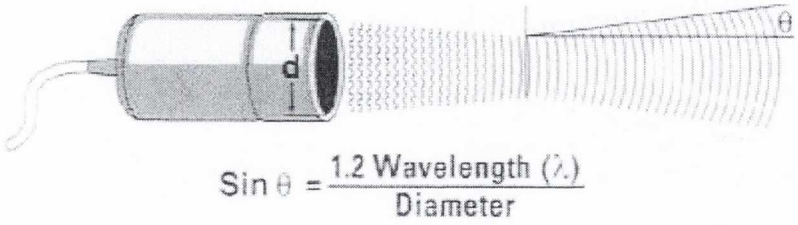


Figure 61 Schematic showing the far field region of ultrasonic transducer.

However, within these two regions the beam intensity is not uniform. The situation becomes more complex with the use of rectangular, focused and pulsed transducers.

A more accurate estimation of the field of a transducer can be obtained by considering the surface of the transducer to be an array of separate elements each radiating spherical waves. By estimating the points where the waves maxima and minima meet,

points of constructive and destructive interference can be established, and the ultrasonic field estimated.

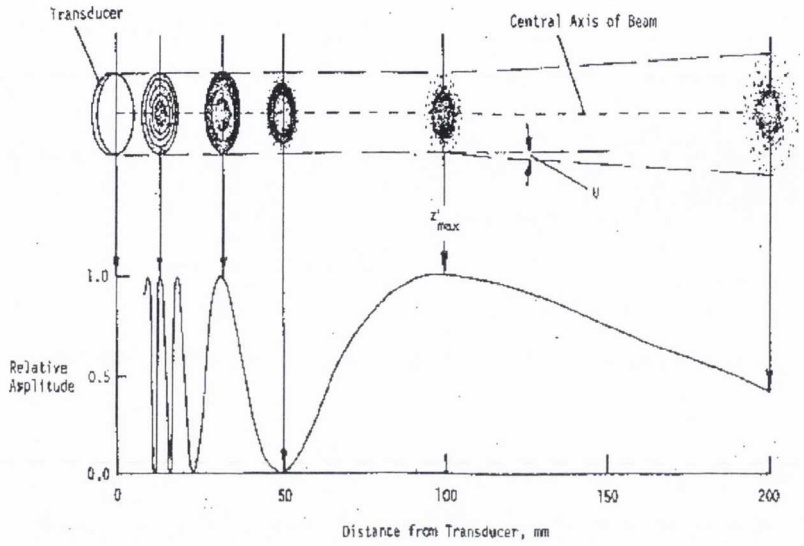


Figure 62 Schematic showing the relative amplitude as a function of distance from the transducer.

The theoretical field for a circular transducer is shown above. Moving along the central axis of the beam away from the transducer in the near zone, the intensity shows successive axial maxima and minima which become further apart away from the transducer. There are also several maxima across the beam diameter. The last axial maximum occurs at the end of the near zone (at a distance of $D^2/4\lambda$). Beyond this in the far zone the central axis intensity decreases and the beam diverges. Rectangular transducers and pulsed ultrasound complicate these fields.

Lateral Resolution

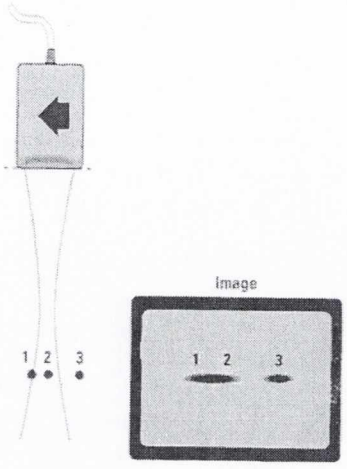


Figure 63 Schematic of maximum resolution being a function of beam width.

The ability to distinguish structures lying across the beam depends on the ultrasound beam width. Theory predicts that the separation which can be just resolved, ***d***, is equal to half the beam width i.e. to resolve $d \geq D/2$ where ***D*** is transducer diameter. The beam width and hence lateral resolution varies with range and may be improved by focusing. Lateral resolution will depend on other factors e.g. number of scan lines, signal processing etc. In general lateral resolution is worse than axial resolution.

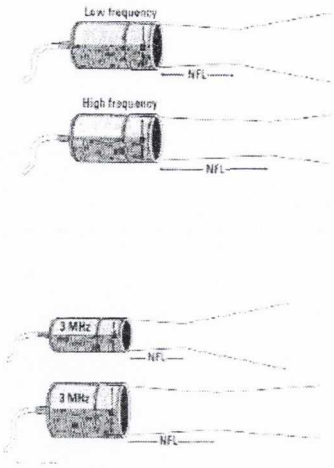


Figure 64 Comparison of transducers with different transducer diameters. The effect of higher frequency is to reduce the size of the narrow field.

f(MHz)	1	3	10
λ (mm)	1.5	0.5	0.15
D (cm) typical	3	1	0.3
Axial Resolution (mm)	6	2	0.6
Field Length (mm)	33.75	1.25	0.03375
Lateral Resolution (mm)	15	5	1.5

Table 38 Flat transducers typical properties

It is important to note that lower frequency probes have less attenuation and require longer near field lengths ($D^2/4\lambda$), therefore tend to use larger transducers.

It is normal practice to operate ultrasound systems in the near field region in order to have a narrow beam width (good lateral resolution) with little divergence. Ultrasound can only penetrate a limited depth therefore transducers are usually designed so that the end of the near field corresponds to the limit of penetration.

Smaller diameter crystals produce a narrower beam but at the expense of a shorter near field and greater divergence in the far field. Higher operating frequencies give a

longer near field, but unfortunately higher frequencies have a higher attenuation so the penetration is less. Transducer design is therefore a trade-off involving many conflicting goals (Browne 2006).

Focused transducers

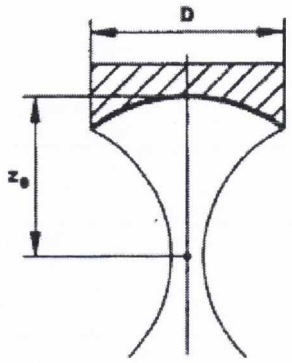


Figure 65 Geometry of a focussed transducer(Passmann 1994).

$F = \frac{z_0}{D}$ $\delta_{lat} = 1.02c\frac{F}{f_c}$ $\delta_{ax} = 2c\ln 2\frac{1}{\pi\Delta f}$	c: speed of sound. f_c: Center frequency. Δf: Bandwidth. F : Focussing of transducer. δ_{lat}: Lateral resolution of transducer. δ_{ax}: Axial resolution of transducer.

Table 39 Equations describing the F number, lateral and axial resolution of a focused transducer.

The absolute best resolution achievable is given by the equation below: Res=0.51 Wavelength/Numerical aperture. But as frequency increases attenuation increases as the square of frequency. Liquid path has to be reduced as frequency increases (Yu *et al.* 1995).

Frequency MHz	**Resolution microns**	**Penetration Depth**
20	100	4mm
200	8	300 microns
1000	1.5	25 microns
2000	0.7	10 microns

Table 40 Typical values for laterial resolution and penetration depth of a transducer for a range of ultrasonic frequencies.

To get better lateral resolution from a transducer a focussed transducer is used. The two key determinants of lateral resolution are the centre frequency and the F number of the transducer. The axial resolution however is dependent only on the bandwidth. Therefore to obtain very high resolution the centre frequency and the bandwidth have to be chosen as high as possible and the focal area as narrow as possible. There is a compromise because with high frequency comes poor penetration and with narrow focussing comes a short usable depth.

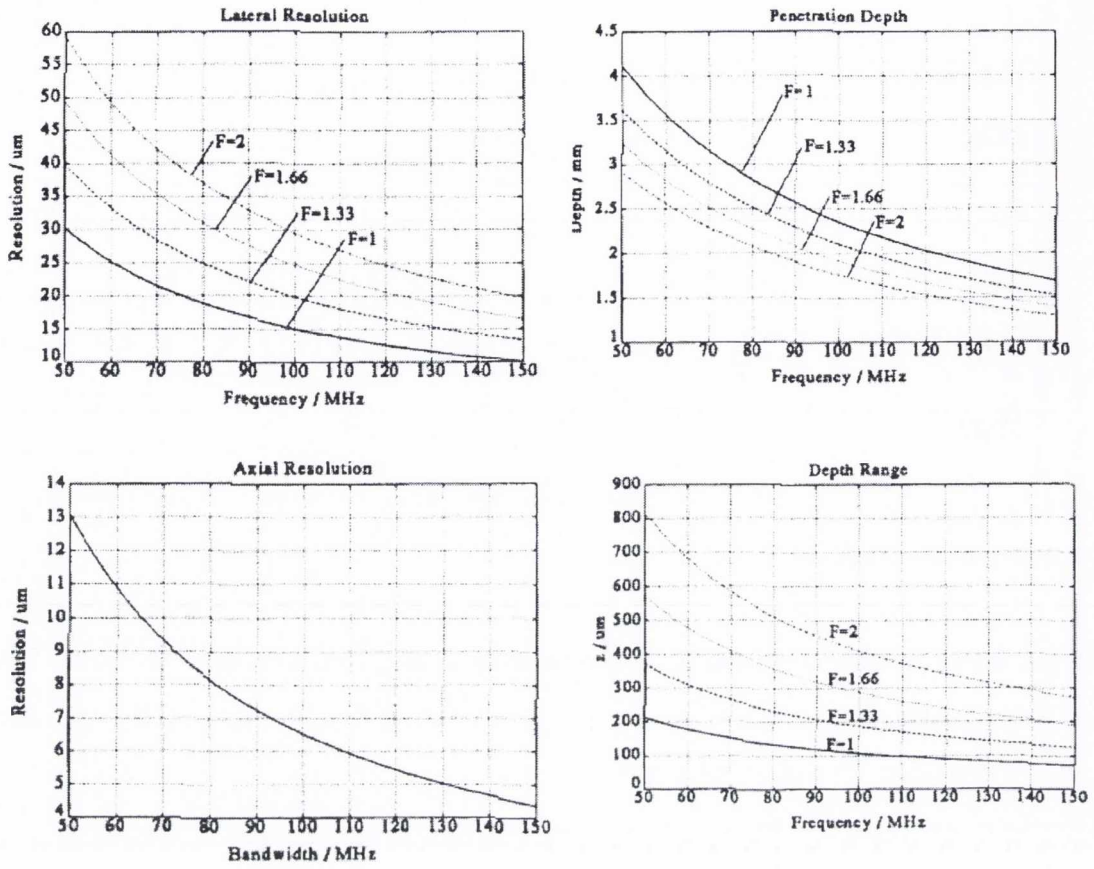


Figure 66 Top left: Lateral Resolution Depending on Center-Frequency and F-Number. Top right: Penetration Depth Depending on Center-Frequency and F-Number. Bottom left: Axial Resolution Depending on Bandwidth. Bottom right: Useable Depth Range for Imaging Depending on Center-Frequency and F-Number(Passmann 1993) .

The penetration depth depends mainly on the centre frequency, the F number, the transducer insertion loss (a_{ins}), the tissue attenuation (a_t) and the dynamic range of the system (***DR***, the ratio of the transmitted signal amplitude to the smallest detectable signal).

$$DR = a_{ins} + a_t \cdot f \cdot 2 \cdot z_p - gain(F, f_c)$$

$$z_p = (DR - a_{ins} + 20\log\left(\frac{\pi z_0 f}{4F^2 c}\right)/(2a_t f) \qquad \textit{Equation 7-4}$$

$$z_d = 7.2c\frac{F^2}{f}$$

Here z_p and z_d are the depth of penetration and the depth range. These equations were used to generate the graphs in Figure 14 above (Passmann 1993).

7.6 References

Abdel-Wahab, A. A., Maligno, A. R. ,Silberschmidt, V. V. (2011) Micro-scale modelling of bovine cortical bone fracture: Analysis of crack propagation and microstructure using X-FEM. *Computational Materials Science*: In Press.

Abrahamsen, B., Van Staa, T., Ariely, R., Olson, M. ,Cooper, C. (2009) Excess mortality following hip fracture: a systematic epidemiological review. *Osteoporosis International* **20**(10): 1633-1650.

Anonymous (1993) Consensus development conference: diagnosis, prophylaxis and treatment of o steoporosis. *American Journal of Medicine* **94**: 4.

Anonymous (2000) Osteoporosis prevention, Diagnosis, and Therapy. *NIH Consensus Statement* **17**(1): 1-36.

Anonymous (2007) *WHO SCIENTIFIC GROUP ON THE ASSESSMENT OF OSTEOPOROSIS AT PRIMARY HEALTH CARE LEVEL*. Brussels, Belgium, 5-7 May 2004 World Health Organization.

ANSYS (2004) *ANSYS Release 8.1 Documentation*. Canonsburg, PA, USA, ANSYS Inc.

Arden, N., Cooper C., (1994) Present and future osteoporsis: epidemiology. *Osteoporosis: diagnosis and management*. Meunier, P. J. London, Martin Dunitz Ltd: 1-16.

Ardizzoni, A. (2001) Osteocyte lacunar size-lamellar thickness relationships in human secondary osteons. *Bone* **28**(2): 215-219.

Bamber, J. C. (1986) Attenuation and absorption. *Physical principles of medical ultrasonics*. Hill, C. R. London, John Wiley and Sons: 120-199.

Basillais, A., Bensamoun, S., Chappard, C., Brunet-Imbault, B., Lemineur, G., Ilharreborde, B., Tho, M.-C. H. B. ,Benhamou, C.-L. (2007) Three-dimensional characterization of cortical bone microstructure by microcomputed tomography: validation with ultrasonic and microscopic measurements. *J Orthop Sci* **12**(2): 141-148.

Basso, N. ,Heersche, J. N. (2002) Characteristics of in vitro osteoblastic cell loading models. *Bone* **30**(2): 347-351.

Benford, H., McGowan, N., Helfrich, M., Nuttall, M. ,Rogers, M. (2001) Visualization of bisphosphonate-induced caspase-3 activity in apoptotic osteoclasts in vitro. *Bone* **28**(5): 465-473.

Biot, M. A. (1956) Theory of propagation of elastic waves in a fluid-saturated porous solid. I. Low-frequency range. *J. Acoust. Soc. Am* **28**(2): 168-178.

Bolotin, H. (2007) DXA in vivo BMD methodology: an erroneous and misleading research and clinical gauge of bone mineral status, bone fragility, and bone remodelling. *Bone* **41**(1): 138-154.

Bonivtch, A. R., Bonewald, L. F. ,Nicolella, D. P. (2007) Tissue strain amplification at the osteocyte lacuna: a microstructural finite element analysis. *J Biomech* **40**(10): 2199-2206.

Bossy, E., Laugier, P., Peyrin, F.,Padilla, F. (2007)
Attenuation in trabecular bone: A comparison between numerical simulation a nd experimental results in human femur. *J. Acoust. Soc. Am.*(122): 6.

Brennan, O. (2008) *Bone Quality and its Relationship with Bone Fragility and Osteoporosis* PhD., Royal College of Surgeons in Ireland

Brennan, O., Kennedy, O. D., Lee, T. C., Rackard, S. M. ,O'Brien, F. J. (2008) ESTROGEN DEPLETION AND ZOLEDRONIC ACID THERAPY: EFFECTS ON OSTEOCYTE APOPTOSIS AND MICRODAMAGE. *Journal of Biomechanics* **41**: S127-S127.

Brennan, O., Kennedy, O. D., Lee, T. C., Rackard, S. M. ,O'Brien, F. J. (2011) Effects of estrogen deficiency and bisphosphonate therapy on osteocyte viability and microdamage accumulation in an ovine model of osteoporosis. *Journal of Orthopaedic Research* **29**(3): 419-424.

Briggs, A. (1992) *Acoustic Microscopy*. New York, Oxford University Press.

Browne, J. (2006) Private Correspondence.

Broz, J., Simske, S. ,Greenberg, A. (1995) Material and compositional properties of selectively demineralized cortical bone* 1. *Journal of Biomechanics* **28**(11): 1357-1368.

Bumrerraj, S. ,Katz, J. L. (2001) Scanning acoustic microscopy study of human cortical and trabecular bone. *Ann Biomed Eng* **29**(12): 1034-1042.

Burger, E. H. ,Klein-Nulen, J. (1999a) Responses of bone cells to biomechanical forces in vitro. *Adv Dent Res* **13**: 93-98.

Burger, E. H. ,Klein-Nulend, J. (1999b) Mechanotransduction in bone--role of the lacuno-canalicular network. *FASEB J* **13 Suppl**: S101-112.

Cardoso, L., Herman, B., Verborgt, O., Laudier, D., Majeska, R. ,Schaffler, M. (2009) Osteocyte apoptosis controls activation of intracortical resorption in response to bone fatigue. *Journal of Bone and Mineral Research* **24**(4): 597-605.

Chandelier, F., Leguerney, I., Raum, K., Talmant,M., Saied, A.,, Peyrin, F., Laugier,P., (2004) Assessment of cortical bone microstructure and material properties using high resolution scanning acoustic microscopy. *148th Meeting of the Acoustical Society of America*, San Diego.

Chen, J. H., Liu, C., You, L. ,Simmons, C. A. (2010) Boning up on Wolff's Law: Mechanical regulation of the cells that make and maintain bone. *Journal of Biomechanics* **43**(1): 108-118.

Cook, R., Malkus, D., Plesha, M. ,Witt, R. (2002) *Concepts and applications of finite element analysis*, Wiley, New York.

Cowin, S. (2002) Mechanosensation and fluid transport in living bone. *Journal of Musculoskeletal and Neuronal Interactions* **2**(3): 256-260.

Cowin, S. ,Hegedus, D. (1976) Bone remodeling I: theory of adaptive elasticity. *Journal of Elasticity* **6**(3): 313-326.

Cowin, S. C., Moss-Salentijn, L. ,Moss, M. L. (1991) Candidates for the mechanosensory system in bone. *J Biomech Eng* **113**(2): 191-197.

Cowin, S. C. ,Van Buskirk, W. C. (1986) Thermodynamic restrictions on the elastic constants of bone. *J Biomech* **19**(1): 85-87.

Dickinson, R. J. (1986) Reflection and Scattering. *Physical principles of medical ultrasonics*. Hill, C. R. London, John Wiley and Sons**:** 225-259.

Doblaré, M. ,Garcia, J. M. (2002) Anisotropic bone remodelling model based on a continuum damage-repair theory. *J Biomech* **35**(1): 1-17.

Dodds, M., Codd, M., Looney, A. ,Mulhall, K. (2009) Incidence of hip fracture in the Republic of Ireland and future projections: a population-based study. *Osteoporosis International* **20**(12): 2105-2110.

Dong, X. N. ,Guo, X. E. (2004) Geometric determinants to cement line debonding and osteonal lamellae failure in osteon pushout tests. *Journal of biomechanical engineering* **126**: 387.

Dong, X. N. ,Guo, X. E. (2006) Prediction of cortical bone elastic constants by a two-level micromechanical model using a generalized self-consistent method. *J Biomech Eng* **128**(3): 309-316.

Dulgar, A. (2007). "*Notes Nanostructured Materials MTLE 6340.*" Retrieved 5/5/, 2007, from http://web.archive.org/web/20080323115455/http://www.rpi.edu/dept/materials/COURSES/NANO/dulgar/nano_index.html.

Eckardt, I. ,Hein, H. J. (2001) Quantitative measurements of the mechanical properties of human bone tissues by scanning acoustic microscopy. *Ann Biomed Eng* **29**(12): 1043-1047.

Evans, J. ,Tavakoli, M. (1990) Ultrasonic attenuation and velocity in bone. *Physics in Medicine and Biology* **35**: 1387.

Felippa, C. (2011). "*Introduction to Finite Element Methods (ASEN 5007)* " Retrieved 9/9, 2011, from http://www.colorado.edu/engineering/CAS/courses.d/IFEM.d/Home.html.

Feynman, R., Leighton R. B., Sands, M. (2006) *The Feynman lectures on Physics, Definitive Edition,* , Pearson Addison Wesley.

Frost, H. (1997a) Defining osteopenias and osteoporoses: another view (with insights from a new paradigm). *Bone* **20**(5): 385-391.

Frost, H. (1997b) Why do marathon runners have less bone than weight lifters? A vital-biomechanical view and explanation. *Bone* **20**(3): 183-189.

Frost, H. M. (2004) A 2003 update of bone physiology and Wolff's Law for clinicians. *The Angle Orthodontist* **74**(1): 3.

Fung, Y. C. (1993) *Biomechanics: mechanical properties of living tissues.* . New York, Springer Verlag.

Garner, E., Lakes, R., Lee, T., Swan, C. ,Brand, R. (2000) Viscoelastic dissipation in compact bone: implications for stress-induced fluid flow in bone. *J Biomech Eng* **122**(2): 166-172.

Ghanbari, J. ,Naghdabadi, R. (2009) Nonlinear hierarchical multiscale modeling of cortical bone considering its nanoscale microstructure. *Journal of Biomechanics* **42**(10): 1560-1565.

Goldstein, A., Powis, R. L., (2000) Medical Ultrasonic Diagnostics. *Ultrasonic Instruments and Devices*. Papadakis, E. P., Academic Press: 46-184.

Hasegawa, K., Turner, C. H., Recker, R. R., Wu, E. ,Burr, D. B. (1995) Elastic properties of osteoporotic bone measured by scanning acoustic microscopy. *Bone* **16**(1): 85-90.

Hazenberg, J. G., Freeley, M., Foran, E., Lee, T. C. ,Taylor, D. (2006) Microdamage: a cell transducing mechanism based on ruptured osteocyte processes. *J Biomech* **39**(11): 2096-2103.

Hazenberg, J. G., Taylor, D. ,Lee, T. C. (2007) The role of osteocytes and bone microstructure in preventing osteoporotic fractures. *Osteoporosis International* **18**(1): 1-8.

Hill, C. R. (1986) The generation and structure of acoustic fields. *Physical principles of medical ultrasonics*. Hill, C. R. London, John Wiley and Sons: 68-92.

Hoffler, C. E., Zhang, N., Kozloff, K.M., Grimm, M.J., Goldstein, S.A. (1999) Comparison of scanning acoustic microscopy and nanoindentation measures of the elastic properties of human bone lamellae *ASME Bioengineering Conference* Big Sky Montana.

Hofmann, T., Heyroth, F., Meinhard, H., Franzel, W. ,Raum, K. (2006) Assessment of composition and anisotropic elastic properties of secondary osteon lamellae. *J Biomech* **39**(12): 2282-2294.

Hogan, H. A. (1992) Micromechanics modeling of Haversian cortical bone properties. *Journal of Biomechanics* **25**(5): 7.

Horne, W. C. (1995) Toward a more complete molecular description of the osteoclast. *Bone* **17**(2): 107-109.

Jacobs, C., Yellowley, C., Davis, B., Zhou, Z., Cimbala, J. ,Donahue, H. (1998) Differential effect of steady versus oscillating flow on bone cells. *Journal of Biomechanics* **31**(11): 969.

Jee, S. S. W. (2001) Integrated bone tissue physiology: Anatomy and physiology. *Bone mechanics handbook*. Cowin, S. C. New York, CRC Press.

Johnell, O. ,Kanis, J. A. (2006) An estimate of the worldwide prevalence and disability associated with osteoporotic fractures. *Osteoporosis International* **17**(12): 1726-1733.

Kanis, J. A. ,Johnell, O. (2005) Requirements for DXA for the management of osteoporosis in Europe. *Osteoporosis international : a journal established as result of cooperation between the European Foundation for Osteoporosis and the National Osteoporosis Foundation of the USA* **16**(3): 229-238.

Katz, J. L. ,Meunier, A. (1993) Scanning Acoustic Microscope Studies of the Elastic Properties of Osteons and Osteon Lamallae. *Journal of Biomechanical Engineering-Transactions of the Asme* **115**(4): 543-548.

Kennedy, O. (2007) *The Effect of Bone Turnover on Bone Quality and Material Properties*. Doctor in Philosophy, University of Dublin.

Kennedy, O. D., Brennan, O., Mauer, P., Rackard, S. M., O'Brien, F. J., Taylor, D. ,Lee, T. C. (2008) The effects of increased intracortical remodeling on microcrack behaviour in compact bone. *Bone* **43**(5): 889-893.

Kennedy, O. D., Brennan, O., Rackard, S. M., Staines, A., O'Brien, F. J., Taylor, D. ,Lee, T. C. (2009) Effects of ovariectomy on bone turnover, porosity, and biomechanical properties in ovine compact bone 12 months postsurgery. *J Orthop Res* **27**(3): 303-309.

Kuttruff, H. (1991) *Ultrasonic fundamentals & applications*, Kluwer Academic Publications.

Lakes, R., Yoon, H. S. ,Katz, J. L. (1986) Ultrasonic wave propagation and attenuation in wet bone. *J Biomed Eng* **8**(2): 143-148.

Lakes, R. S. Y., H . S. Katz, J. L. (1983) Slow Compressional Wave Propagation in Wet Human and Bovine Cortical Bone. *Science* **220**: 3.

Laugier, P. (1999) The basic physics of ultrasound. *Quantitative ultrasound: Assessment of osteoporosis and bone status*. Njeh, C. F., Hans, D., Fuerst, T., Gluer, C.C., Genant, H.K., . London, Martin Dunitz: 47-66.

Laugier, P. (2008) Instrumentation for in vivo ultrasonic characterization of bone strength. *Ultrasonics, Ferroelectrics and Frequency Control, IEEE Transactions on* **55**(6): 1179-1196.

Lee, T. C., McHugh, P. E., O'Brien, F. J., O'Mahoney, D. ,Taylor, D., Bruzzi, M., Rackard, S.M., Kennedy, O.D., Mahony, N.J., Harrison, N., Lohfield, S., Brennan, O., Gleeson, J., Hazenberg, J.G., Mullins, L., Tyndyk, M., McNamara, L.M., O'Kelly, K.U., Prendergast, P.J., (2004) Bone for Life: Osteoporosis, bone remodelling and computer simulation. *Topics in Bio-Mechanical Engineering*. Prendergast, P. J. McHugh, P. E. Dublin, TCBE &NCBES 58-93.

Lees, S., Klopholz, D.Z. (1992) Sonic velocity & attenuation in wet compact cow femur for the frequency range 5 to 100MHz. *Ultrasound Med. Biol.* **18**: 5.

Lees, S., Ahern, J. M. ,Leonard, M. (1983) Parameters influencing the sonic velocity in compact calcified tissues of various species. *J Acoust Soc Am* **74**(1): 28-33.

Lemons, R. A. ,Quate, C. F. (1974) Scanning Acoustic Microscope. *Ieee Transactions on Sonics and Ultrasonics* **Su21**(1): 69-69.

Looker, A. C., Orwoll, E. S., Johnston, C. C., Jr., Lindsay, R. L., Wahner, H. W., Dunn, W. L., Calvo, M. S., Harris, T. B. ,Heyse, S. P. (1997) Prevalence of low femoral bone density in older U.S. adults from NHANES III. *J Bone Miner Res* **12**(11): 1761-1768.

Lyles, K. W., Colón-Emeric, C. S., Magaziner, J. S., Adachi, J. D., Pieper, C. F., Mautalen, C., Hyldstrup, L., Recknor, C., Nordsletten, L. ,Moore, K. (2007) Zoledronic acid and clinical fractures and mortality after hip fracture. *N Engl J Med* **357**(18): 1799-1809.

Mann, S. ,Weiner, S. (1999) Biomineralization: structural questions at all length scales. *J Struct Biol* **126**(3): 179-181.

Martin, R. B. (2000a) Does osteocyte formation cause the nonlinear refilling of osteons? *Bone* **26**(1): 71-78.

Martin, R. B. (2000b) Toward a unifying theory of bone remodeling. *Bone* **26**(1): 1-6.

Martin, R. B. (2002) Is all cortical bone remodeling initiated by microdamage? *Bone* **30**(1): 8-13.

Martin, R. B., Burr, D.B., N.A. Sharkey (1998) *Skeletal tissue mechanics*. New York, Springer-Verlag.

McGarry, J. G., Klein-Nulend, J., Mullender, M. G. ,Prendergast, P. J. (2005) A comparison of strain and fluid shear stress in stimulating bone cell responses--a computational and experimental study. *FASEB J* **19**(3): 482-484.

McNamara, L. M. ,Prendergast, P. J. (2007) Bone remodelling algorithms incorporating both strain and microdamage stimuli. *J Biomech* **40**(6): 1381-1391.

Mehta, S. S., Oz, O. K. ,Antich, P. P. (1998) Bone elasticity and ultrasound velocity are affected by subtle changes in the organic matrix. *J Bone Miner Res* **13**(1): 114-121.

Merryman, D. ,Engler, A. J. (2010) Innovations in cell mechanobiology. *Journal of Biomechanics* **43**(1): 1-1.

Meunier, A., Riot, O., Christel, P., Katz, J.L., (1991) Characterization of local anisotropic elastic properties of femoral and tibial diaphysis using acoustic transmission measurements and acoustic microscopy. *Interfaces in Medicine and Mechanics* Toni, A., Middleton, J., Pallotti, G. . London, Elsevier Applied Science**:** 454-463.

Miller, S. C., de Saint-Georges, L., Bowman, B. ,Jee, W. (1989) Bone lining cells: structure and function. *Scanning microscopy* **3**(3): 953.

Mischinski, S. ,Ural, A. (2011) Finite Element Modeling of Microcrack Growth in Cortical Bone. *Journal of Applied Mechanics* **78**: 041016.

Moilanen, P.,
Talmant, M, Nicholson, P. H.F., Cheng, S., Timonen, J., Laugier, P., (2007) Ultrasonically determined thickness of long cortical bones: threedimensional s imulations of invitro experiments. *J. Acoust. Soc. Am.* **122**: 6.

Morse P. M., I., U (1987) *Theoretical Acoustics*. Princeton, Princeton University Press

Mulcahy, L. E., Taylor, D., Lee, C. T. ,Duffy, G. P. (2011) RANKL and OPG activity is regulated by injury size in networks of osteocyte-like cells. *Bone* **48**: 182-188.

Mulvihill, B. M. ,Prendergast, P. J. (2008) An algorithm for bone mechanoresponsiveness: implementation to study the effect of patient-specific cell mechanosensitivity on trabecular bone loss. *Comput Methods Biomech Biomed Engin* **11**(5): 8.

Mulvihill, B. M. ,Prendergast, P. J. (2010) Mechanobiological regulation of the remodelling cycle in trabecular bone and possible biomechanical pathways for osteoporosis. *Clin Biomech (Bristol, Avon)* **25**(5): 491-498.

Nicholson, P. H. F., Bouxsein, M.L., (1999) Ultrasonic studies of cortical bone in vitro. *Quantitative ultrasound: Assessment of osteoporosis and bone status*. Njeh, C. F., Hans, D., Fuerst, T., Gluer, C.C., Genant, H.K., . London, Martin Dunitz**:** 177-193.

Nicolella, D. P., Bonewald, L. F., Moravits, D. E. ,Lankford, J. (2005) Measurement of microstructural strain in cortical bone. *Eur J Morphol* **42**(1-2): 23-29.

Nicolella, D. P., Moravits, D. E., Gale, A. M., Bonewald, L. F. ,Lankford, J. (2006) Osteocyte lacunae tissue strain in cortical bone. *J Biomech* **39**(9): 1735-1743.

Nicolella, D. P., Nicholls, A.E., Lankford, J., Davy, D.T., (2001) Machine vision photogrammetry: a technique for measurement of microstructural strain in cortical bone. *J. Biomechanics* **34**: 135-139.

Njeh, C. F., Nicholson, P.H.F., Langton, C.M. (1999a) The physics of ultrasound applied to bone. *Quantitative ultrasound: Assessment of osteoporosis and bone status*. Njeh, C. F., Hans, D., Fuerst, T., Gluer, C.C., Genant, H.K.,. London, Martin Dunitz: 67-75.

Njeh, C. F., Xiao, G.C., Elliot, J.M., Meunier, P.J. (1999b) Bone, bone diseases and bone quality. *Quantitative ultrasound: Assessment of osteoporosis and bone status*. Njeh, C. F., Hans, D., Fuerst, T., Gluer, C.C., Genant, H.K., . Martin Dunitz, London.

O'Brien, F. J., Taylor, D. ,Clive Lee, T. (2007) Bone as a composite material: the role of osteons as barriers to crack growth in compact bone. *International journal of fatigue* **29**(6): 1051-1056.

O'Brien, F. J., Taylor, D. ,Lee, T. C. (2003) Microcrack accumulation at different intervals during fatigue testing of compact bone. *J Biomech* **36**(7): 973-980.

O'Donnell, M., Jaynes, E. ,Miller, J. (1981) Kramers-Kronig relationship between ultrasonic attenuation and phase velocity. *Acoustical Society of America, Journal* **69**: 696-701.

O'Neill, T. (2005) Looking back: developments in our understanding of the occurrence, aetiology and prognosis of osteoporosis over the last 50 years. *Rheumatology* **44**(suppl 4): iv33.

Oyen, M. L., Ferguson, V. L., Bembey, A. K., Bushby, A. J. ,Boyde, A. (2008) Composite bounds on the elastic modulus of bone. *J Biomech* **41**(11): 2585-2588.

Parfitt, A. M. (2002) Targeted and nontargeted bone remodeling: relationship to basic multicellular unit origination and progression. *Bone* **30**(1): 5-7.

Passmann, C., Ermert, H., Auer, T., Kaspar, K., el-Gammala, S., Altmeyer P., (1993) In vivo ultrasound biomicroscopy. *IEEE 1993 ULTRASONICS SYMPOSIUM*

Passmann, C. E. H. (*1994*) 150 MHz In Vivo Ultrasound of the Skin: Imaging Techniques and Signal Processing Procedures Targeting Homogeneous Resolution. *IEEE 1994 ULTRASONICS SYMPOSIUM*

Plotkin, L. I., Weinstein, R. S., Parfitt, A. M., Roberson, P. K., Manolagas, S. C. ,Bellido, T. (1999) Prevention of osteocyte and osteoblast apoptosis by bisphosphonates and calcitonin. *Journal of Clinical Investigation* **104**: 1363-1374.

Prendergast, P. (2001) An analysis of theories in biomechanics. *Engineering Transactions* **49**(2/3): 117-133.

Prendergast, P. J. ,Huiskes, R. (1996) Microdamage and osteocyte-lacuna strain in bone: a microstructural finite element analysis. *J Biomech Eng* **118**(2): 240-246.

Raum, K. (2008) Microelastic imaging of bone. *IEEE Trans Ultrason Ferroelectr Freq Control* **55**(7): 1417-1431.

Raum, K., Brandt, J., (*2003*) Simultaneous determination of acoustic impedance, longitudinal and lateral wave velocities for the characterization of the elastic microstructure of cortical bone. *WCU 2003*, Paris.

Raum, K., Cleveland, R. O., Peyrin, F. ,Laugier, P. (2006a) Derivation of elastic stiffness from site-matched mineral density and acoustic impedance maps. *Phys Med Biol* **51**(3): 747-758.

Raum, K., Jenderka, K.V. Klemenz, A., Brandt, J., (*2002a*) Topographically corrected acoustic impedance estimation in cortical bone at a microscopic scale. *2002 IEEE ULTRASONICS SYMPOSIUM.*

Raum, K., Leguerney, I., Chandelier, F., Talmant, M., Saied, A., Peyrin, F. ,Laugier, P. (2006b) Site-matched assessment of structural and tissue properties of cortical bone using scanning acoustic microscopy and synchrotron radiation muCT. *Phys Med Biol* **51**(3): 733-746.

Raum, K., Reisshauer, J. ,Brandt, J. (2004) Frequency and resolution dependence of the anisotropic impedance estimation in cortical bone using time-resolved scanning acoustic microscopy. *J Biomed Mater Res A* **71**(3): 430-438.

Raum, K., Reisshauer, J., Brandt, J., (2002b) Frequency dependence of the anisotropic impedance estimation in cortical bone using time resolved scanning acoustic microscopy. *2002 IEEE Ultrasonics Symposium.*

Reid, I. R., Brown, J. P., Burckhardt, P., Horowitz, Z., Richardson, P., Trechsel, U., Widmer, A., Devogelaer, J. P., Kaufman, J. M. ,Jaeger, P. (2002) INTRAVENOUS ZOLEDRONIC ACID IN POSTMENOPAUSAL WOMEN WITH LOW BONE MINERAL DENSITY. *N Engl J Med* **346**(9): 9.

Reilly, G. C. (2000) Observations of microdamage around osteocyte lacunae in bone. *J Biomech* **33**(9): 1131-1134.

Rho, J. Y. (1996) An ultrasonic method for measuring the elastic properties of human tibial cortical and cancellous bone. *Ultrasonics* **34**(8): 777-783.

Rho, J. Y., Kuhn-Spearing, L. ,Zioupos, P. (1998) Mechanical properties and the hierarchical structure of bone. *Med Eng Phys* **20**(2): 92-102.

Schiessl, H., Frost, H. ,Jee, W. (1998) Estrogen and bone-muscle strength and mass relationships. *Bone* **22**(1): 1-6.

Scholz, F. ,Stephens, M. (1987) K-sample Anderson-Darling tests. *Journal of the American Statistical Association*: 918-924.

Seeman, E. (2004) *Osteoporosis in Men, IOF.*

Seeman, E. (2007) Is a change in bone mineral density a sensitive and specific surrogate of anti-fracture efficacy? *Bone* **41**(3): 308-317.

Seeman, E. ,Delmas, P. D. (2006) MECHANISMS OF DISEASE: Bone Quality - The Material and Structural Basis of Bone Strength and Fragility. *The New England Journal of Medicine* **354**(21): 2250-2250-2261.

Sekhon, J. S. (2011) `Multivariate and Propensity Score Matching Software with Automated Balance Optimization: The Matching package for R. *Journal of Statistical Software* **42**(7): 1-52.

Shieh, S. J., Zimmerman, M. C. ,Langrana, N. A. (1995) The application of scanning acoustic microscopy in a bone remodeling study. *J Biomech Eng* **117**(3): 286-292.

Smitmans, L., Raum, K., Brandt, J., Klemenz, A. (2000) Variations in the microstructural acousto-mechanical properties of cortical bone revealed by quantitative acoustic microscopy study. *2000 IEEE Ultrasonics Symposium.*

Sonix (2005) Sonix Presentation: Scanning Acoustic Microscopy Training, Sonix Inc. .

Tavakoli, M. ,Evans, J. (1991) Dependence of the velocity and attenuation of ultrasound in bone on the mineral content. *Physics in Medicine and Biology* **36**: 1529.

Taylor, D., Hazenberg, J. G. ,Lee, T. C. (2007) Living with cracks: damage and repair in human bone. *Nature materials* **6**(4): 263-268.

Taylor, D. ,Prendergast, P. (1997) A model for fatigue crack propagation and remodelling in compact bone. *Proceedings of the Institution of Mechanical Engineers, Part H: Journal of Engineering in Medicine* **211**(5): 369-375.

Tomkinson, A., Reeve, J., Shaw, R. ,Noble, B. (1997) The death of osteocytes via apoptosis accompanies estrogen withdrawal in human bone. *Journal of Clinical Endocrinology & Metabolism* **82**(9): 3128.

Turner, C. H. (1998) Three rules for bone adaptation to mechanical stimuli. *Bone* **23**(5): 399-407.

Turner, C. H., Rho, J., Takano, Y., Tsui, T. Y. ,Pharr, G. M. (1999) The elastic properties of trabecular and cortical bone tissues are similar: results from two microscopic measurement techniques. *Journal of Biomechanics* **32**(4): 437-441.

van der Meulen, M. C. ,Huiskes, R. (2002) Why mechanobiology? A survey article. *J Biomech* **35**(4): 401-414.

van der Meulen, M. C. H. ,Prendergast, P. J. (2000) Mechanics in skeletal development, adaptation and disease. *Phil. Trans. R. Soc. Lond. A* **358**: 565-578.

Vashishth, D., Verborgt, O., Divine, G., Schaffler, M. B. ,Fyhrie, D. P. (2000) Decline in osteocyte lacunar density in human cortical bone is associated with accumulation of microcracks with age. *Bone* **26**(4): 375-380.

Wallace, J. M., Erickson, B., Les, C. M., Orr, B. G. ,Banaszak Holl, M. M. (2010) Distribution of type I collagen morphologies in bone: Relation to estrogen depletion. *Bone* **46**(5): 1349-1354.

Weiner, S. ,Traub, W. (1992) Bone structure: from angstroms to microns. *FASEB J* **6**(3): 879-885.

Weiner, S., Traub, W. ,Wagner, H. D. (1999) Lamellar bone: structure-function relations. *J Struct Biol* **126**(3): 241-255.

WHO (1994) Assessment of fracture risk and its application to screening for postmenopausal osteoporosis. *WHO technical report series No. 843*. Geneva.

Williams, J. L. (1992) Ultrasonic wave propagation in cancellous and cortical bone: prediction of some experimental results by Biot's theory. *J Acoust Soc Am* **91**(2): 1106-1112.

Yu, Z. ,Boseck, S. (1995) Scanning acoustic microscopy and its applications to material characterization. *Reviews of Modern Physics* **67**(4): 863-891.

Zimmerman, M. C., Harten R. D., Shieh S.J., Meunier, A., Katz, J.L., (2001) Techniques and Applications of Scanning Acoustic Microscopy in Bone Remodeling Studies. *Musculoskeletal models and techniques*. Leondes, C. Boca Raton, CRC Press: 4-1 - 4-34.